DISSERTATION

Concepts for novel oxidation resistant thin film materials

carried out for the purpose of obtaining the degree of Doctor technicae (Dr. techn.),
submitted at TU Wien, Faculty of Mechanical and Industrial Engineering,

by

Sophie RICHTER

Matr.Nr.: 01325250
Schleifmühlgasse 11/33
1040 Vienna, Austria

under the supervision of

Ass. Prof. Dipl.-Ing. Dr.techn. Helmut Riedl-Tragenreif
Projektass. Dipl.-Ing. Dr.techn. Rainer Hahn

Institute of Materials Science and Technology - E308-01-2
Applied Surface and Coating Technology

Vienna, March 2025

reviewed by

Prof. Dr. Erik Lewin
Department of Chemistry
Uppsala University
75121 Uppsala, Sweden

Prof. Dr. Ivan Petrov
Department of Materials Science
University of Illinois
61801 Urbana, Illinois

The financial support by the Austrian Federal Ministry for Digital and Economic Affairs, the National Foundation for Research, Technology and Development and the Christian Doppler Research Association is gratefully acknowledged (Christian Doppler Laboratory "Surface Engineering of high-performance Components"). We also thank for the financial support of Plansee SE, Plansee Composite Materials GmbH, and Oerlikon Balzers, Oerlikon Surface Solutions AG. In addition, the Theodor Körner Fonds is gratefully recognized for its invaluable support in the completion of this work.

Affidavit:

I declare in lieu of oath, that I wrote this thesis and performed the associated research myself, using only literature cited in this volume. If text passages from sources are used literally, they are marked as such. I confirm that this work is original and has not been submitted elsewhere for any examination, nor is it currently under consideration for a thesis elsewhere. I acknowledge that the submitted work will be checked electronically-technically using suitable and state-of-the-art means (plagiarism detection software). On the one hand, this ensures that the submitted work was prepared according to the high-quality standards within the applicable rules to ensure good scientific practice "Code of Conduct" at the TU Wien. On the other hand, a comparison with other student theses avoids violations of my personal copyright.

Date *Signature*

Acknowledgements

Concluding my dissertation, I took some moments to reflect on an incredibly rewarding and exciting journey that began in June 2022 when I started my PhD studies. I am deeply grateful for the support and encouragement I have received from so many people along the way, and I would like to take this opportunity to express my sincere thanks to a couple of important friends and colleagues.

First, I would like to express my gratitude to **Ass. Prof. Dr. Helmut Riedl-Tragenreif**, my supervisor, head of the Applied Surface and Coating Technology team, and head of the CDL-SEC. **Helmut**, thank you for giving me the opportunity to join your team and for your consistent support throughout my academic journey - from my bachelor and master studies to my PhD program. Your mentorship, insightful discussion, and willingness to share your extensive expertise and network have been a great support to me over the years.

In addition, I would like to express my gratitude to **Projektass. Dipl.-Ing. Dr.techn. Rainer Hahn** for co-supervising my thesis. **Rainer**, thank you for your support throughout my time in the CD lab. I truly appreciate the enjoyable moments we shared, from conference trips to our daily lunches.

I am also very grateful to my CDL-SEC colleagues: **Anna**, **Norma**, **Arno**, **Phillip**, **Philip**, and **Tomasz**. You made these past three years enjoyable and enriching. Special thanks to **Anna** - we began our PhD studies together, and I have lots of great memories on our fun hours we shared together in the office and on conference trips. Thank you for being a great friend. **Philip** and **Tomasz**, you were a great support in your countless hours of TEM preparation and analysis. Furthermore, I want to thank my (former) colleagues from the CDL-SEC team - **Lukas**, **Thomas**, **Ahmed**, **Christoph**, and **Oliver** - for introducing me to the fascinating world of thin film materials science and providing me with a great kick-start into my PhD. Besides that, an important contribution to this PhD experience provided my current colleagues in the research group - **Christian**, **Samira**, **Dominik**, **Daniel**, **Stefan**, **Wei**, **David**, **Philipp**, **Jakob**, **Maximilian**, **Florentine**, **Elias**, and **Philip** – thank you for the engaging talks during lunch and coffee breaks, for all the fun moments we shared. A special acknowledgement deserves **Christian** for his assistance with the computational work and DFT calculations. Your expertise and time were a valuable addition to shape my research.

Besides the group I also would like to mention the entire **Materials Science Division** for the wonderful time we spent together in the office and lab. A special thanks to **Balint**, whose enjoyable chats in the lab offered much-needed breaks from technical discussions.

This research would not have been possible without the generous support of our industry partners, **Plansee Composite GmbH** and **Oerlikon Balzers**, who made significant contributions to the work done in the CD Lab. I am particularly grateful to **Dr. Jürgen Ramm**, who was always available for a discussion, shared his year-long knowledge on thin films, and helped in shaping my research. Furthermore, **Dr. Peter Polcik** – thanks for your support and the vivid exchange at various conferences and meetings. My sincere thanks also go to **Dr. Szilárd Kolozsvári**, whose encouragement was fundamental to my decision to pursue a PhD. I will always appreciate the support you gave me during my time as an intern at Plansee, which ultimately guided me onto this path.

I would like to acknowledge the **Christian Doppler Gesellschaft** for their financial support, which enabled my research. I am also deeply grateful to the **Theodor Körner Fonds** for recognizing my achievements and supporting my research in the final months of my PhD.

Finally, I would like to express my deepest gratitude to my family and friends, whose unwavering support has been the foundation of this journey. Without your encouragement, this accomplishment would not have been possible.

Contents

List of Figures

Abstract

This thesis explores different strategies to improve the oxidation resistance of novel protective ceramic thin film materials. Material degradation in extreme environments poses a critical challenge in aerospace, energy, and other high-temperature applications. The durability and operational efficiency of components exposed to oxidative environments/conditions can be significantly improved through advanced deposition techniques, optimized coating architectures, and tailored material compositions. This work systematically investigates three key approaches: $MoSi_2$-based coatings as stand-alone protective coating materials, architectural coating concepts incorporating protective Al-Si-O and Si-O top coatings, and alloying strategies to improve the oxidation behavior of transition metal carbides and borides.

The study of $MoSi_2$-based coatings focused on their phase formation and oxidation resistance, using both direct current magnetron sputtering (DCMS) and high-power pulsed magnetron sputtering (HPPMS). The microstructural evolution of these coatings has been studied based on their deposition parameters, revealing that HPPMS synthesized thin films exhibiting improved density and oxidation resistance at high temperatures (above 1200 °C). These results highlight the formation of a continuous protective silica scale that effectively limits oxygen diffusion, preventing accelerated oxidation and oxygen inward diffusion. However, oxidation performance at lower temperatures (around 600 °C) remains a challenge due to the so-called pesting phenomenon, where competing MoO_x and SiO_x oxide formation results in porous, non-protective oxide scales. Despite this minor limitation, HPPMS deposited coatings exhibit superior performance (only 650 nm oxide scale after 100 h at 1200 °C), highlighting the critical influence of deposition parameters and microstructure in optimizing the oxidation resistance of $MoSi_2$-based coatings.

To further improve the oxidation resistance of oxidation-prone thin film materials, architectural coating concepts using Al-Si-N, Al-Si-O, and Si-O protective top coatings on transition metal diborides (TM = W, Ti, Hf) were explored. A Si interlayer was introduced between the oxide-based top coatings and the diborides to prevent in-situ oxidation during growth by reactive (plasma enhanced) cathodic arc evaporation. Experimental results show that Si-O and Al-Si-O top coatings provide exceptional oxidation resistance for $TiB_{2.7}$ and $HfB_{2.4}$ diborides, maintaining stability up to 1200 °C. Transmission electron microscopy (TEM) analysis confirmed the stability of the dense oxide scales that effectively block oxygen diffusion, highlighting the superior resistance against oxygen inward diffusion of these coatings. In contrast, Al-Si-N top coatings exhibited accelerated oxidation above 1000 °C. However, the results underscore that Al-Si-O and Si-O protective top coatings provide excellent long term oxidation resistance (up to 30 h at 1200 °C) for transition metal diborides that are otherwise highly susceptible to oxidation.

The final part of this study focused on alloying strategies for transition metal carbides (TMCs) and borides (TMB_2) to enhance their oxidation resistance. As a first step, a high-throughput combinatorial approach was used to investigate ternary TM-X-C (TM = Ti, Zr, Hf, Ta, W and X = Al, Si) thin films. Experimental results, supported by density functional theory (DFT) calculations, confirmed that metastable face-centered cubic (fcc) solid solutions with Al and Si alloying up to 25/30 at.% could be synthesized. The oxidation behavior of these coatings was subsequently investigated, revealing that TMCs alloyed with Al and Si demonstrated significantly improved oxidation resistance at 750 °C. A two-layer scale consisting of a metal oxycarbide layer followed by an outer mixed Ti-(Al/Si) scale was exemplarily proven on top of the unoxidized Ti-Al/Si-C films. In comparison, their binary counterparts oxidized at temperatures below 600 °C. A similar alloying strategy was applied to TMB_2, where ternary Cr-Al-B, Cr-Si-B, and quaternary Cr-Al-Si-B thin films were synthesized by combinatorial co-sputtering. Si showed a limited solubility limit of about 4 at.% in the AlB_2-structured thin films. Beyond this threshold, the formation of a secondary $CrSi_2$ phase was observed in the ternary and quaternary coatings. Isothermal oxidation at 1200 °C for 1 h proved the crucial role of Si in improving the oxidation resistance. While binary CrB_2-based systems oxidize at around 600 °C, Cr-Al-B was unable to withstand these conditions. However, in the quaternary Cr-Al-Si-B system, Si also acts as a key element, facilitating the formation of protective alumina scales. TEM analysis confirmed a layered oxide structure in the quaternary system, consisting of Si-O, Cr-O, and Al-O, which contributed to the improved oxidation resistance of TMB_2.

Overall, this thesis provides a comprehensive evaluation of novel coating materials, architectural approaches and alloying concepts to enhance oxidation resistance of protective ceramic coating materials. These findings contribute to the development of advanced high-temperature materials for applications in extreme environments, offering pathways to increase component lifetimes and improve operational efficiency in diverse high-temperature applications.

Chapter 1

Introduction

For millions of years, innovation has been closely linked to the discovery of new materials: From 2.5 million years BCE, when wood and stones were used as tools, to coal, iron, brass and bronze at the end of the 18th century, which enabled industrial growth and steam power, to today's Industry 4.0, which is driven, for example, by optical and sensing materials that empower connectivity, autonomy, big data and artificial intelligence [1]. Research into new materials has the potential to set new technological standards. By using advanced material systems and continuously improving their properties, it is possible to achieve higher operating temperatures and thus unlock new efficiency windows in industrial processes. One example is gas-fired power plants [2, 3]. Gas turbines are still indispensable today, as more than 20 % of the world's electricity is still generated with gas [4–6], also because gas-fired power plants can primarily compensate the fluctuations in the variable deficit of renewable energies and enable the balancing of load peaks [7, 8]. As the efficiency levels achieved to date are only around 60 % (i.e., at large combined-cycle gas turbine plants [9, 10]), there is still an open window for improvement and a clear need to make this energy conversion more sustainable. The call for sustainable development has also been explicitly made by the United Nations and emphasizes the need to improve gas turbines. In 2015, they have called on all participating countries to achieve 17 goals by 2030, with major emphasis on the three key topics: *Ensuring sustainable production and consumption*, *Creating sustainable industrialization*, *Ensuring access to sustainable energy for all* [11, 12]. These three points highlight how important it is for the industry to push the boundaries of existing technologies, products and materials to new limits and overcome challenges such as ensuring efficiency and longevity.

Protective coatings that form a robust barrier against corrosion, oxidation, wear and other forms of degradation are an important solution to meet these challenges by improving the performance of products/materials/turbine components and extending their lifetime, such as for Ni-based superalloys. Ni-based superalloys are still used today for turbine blades and have limitations mainly related to their low creep, diffusion and temperature resistance. To overcome this problem and increase the maximum operation temperature from 900 °C to 1100 °C, an initial improvement was achieved by alloying with refractory metals [13, 14]. Even higher operating temperatures of up to 1500 °C were achieved through targeted forced cooling of the components [15] and the application of thermal barrier coatings (TBCs). TBCs play a decisive role in shielding component surfaces from extreme temperatures. They usually consist of a top layer of yttrium-stabilized zirconia (YSZ), characterized by excellent heat resistance and low thermal conductivity, and a bonding layer of NiCrAlY or NiCoCrAlY, which acts as corrosion barrier [14]. The presence of a thin thermally grown oxide (TGO) layer can further increase the high-temperature oxidation resistance of the compound layer.

To achieve higher operating temperatures in aero engines such as gas turbines ($>$ 1500 °C) and thus directly increase performance/efficiency, research is currently being conducted into ultra-high temperature resistant ceramic-based materials (e.g., ceramic matrix composites (CMC)) [16, 17]. In the context of gas turbines used in the transportation sector and aerospace, NASA also reports [18] that reduced emissions and fuel savings of 10 % are possible by the use of CMCs in gas turbines. Ceramic-based materials are significantly lighter [19] compared to currently used Ni-based superalloys and are known for their ultra-high temperature stability [20], promoting new operation temperatures and a higher level of efficiency. CMCs usually consist of ceramic fibers embedded in a ceramic matrix. Due to their structural composition/design, CMCs are known by their high strength, improved crack resistance and fracture toughness [20]. Common material classes for the fibers and the surrounding matrix are carbon-based materials, especially SiC, alumina and mullite [20]. However, the challenge is to improve the poor oxidation resistance of carbon-based ceramic bulk materials, characterized for excellent mechanical stability, and protect them from the operating environment while maintaining high strength. Based on that, research nowadays is pursued into environmental barrier coatings (EBCs) [21, 22]. The second generation of EBCs currently in use consists of mono- and disilicate top layers of rare earths with a silicon (Si) interlayer that serves as an adhesion layer [23]. However, since Si has a relatively low melting point of 1414 °C, it acts as the limiting factor [23]. More recent investigations with higher temperature resistant bond coatings are necessary as even higher operating temperatures (i.e., $T > 1500$ °C) are desired.

Therefore, there is still a great need for research into new material systems acting as protective coatings, and novel coating architectures to enable the full potential of carbon-based bulk materials. The class of ultra-high temperature ceramics (UHTCs) represents an interesting material class in that regard, especially due to similar coefficient of thermal expansion (CTE). In general, UHTCs are a group of refractory ceramics formed from an early Group IV or V transition metal (e.g. Ti, Zr, Hf, Nb, Ta) and a non-metal (e.g., B, C, N). Theses transition metal borides, carbides or nitrides (also carbonitrides) are characterized by their high melting points of over 3000 °C [24].

This study investigates different alloying approaches (for finding new material families) and coating concepts, that significantly improve the oxidation behavior of UHTCs under harsh conditions. Therefore, the influence of strong oxide formers (e.g., Al, Si), different coating architectures and other promising material systems (e.g., $MoSi_2$) are screened. However, a strong focus of this work is on the comprehensively researched novel material class of fcc-structured alloyed transition metal carbides (TM-X-C). They differ significantly from MAX phases based on their crystal structure but are similar in their chemical composition. The great advantage of fcc solid solution TM-X-C films is that they are correctly structured directly in the as deposited state and the crystal structure does not have to be formed by heat treatment and annealing tests. Physical vapor deposition (PVD) technology was used to produce and characterize these wide variety of coatings. They were thoroughly examined for their structural-mechanical properties and their oxidation characteristics.

Chapter 2

Oxides as protective surface layers

The range of application of metallic components, alloys and especially UHTCs at high temperatures can be considerably extended if their corrosion and oxidation behavior is improved [25]. Protective surface oxides, which essentially have high melting points, are phase-stable at high temperatures, have good adhesion (i.e., similar CTEs), and are free of cracks and pores are suitable for improving oxidation resistance [26, 27]. In general, protective surface oxides can be divided into two categories based on their formation mechanism [28].

Firstly, protective top coatings, also known as *overlay coatings*, in which the protective layer is applied directly onto the substrate. A commonly used deposition technique for this is physical vapor deposition, in which a variety of compositions can be specifically adjusted [28].

Secondly, *diffusion coatings* in which the substrate/coatings are enriched/alloyed with the protective/oxide-forming element (e.g., chromium, aluminum, silicon). The alloyed coatings are integrated into the process of forming thermally grown oxides (TGOs) by forming a diffusion zone. This alloying approach not only provides useful storage of the protective element, but also protects against renewed breakthrough oxidation, as a new scale can form again [28]. For practical applications, it is therefore important to understand a basic understanding of the oxidation mechanism and key concepts such as oxidation rate and reaction conditions [25].

2.1 Fundamentals in oxidation mechanisms

In general, oxidation is driven by a negative Gibbs free energy [28], and occurs at the atomic level where chemical bonds are broken, atomic diffusion takes place and a new surface structure is formed [29]. PVD thin films often contain a high concentration of defects, such as vacancies, dislocations or grain boundaries (see Fig. 2.1), which result from the vapor condensation process and enable diffusion [30]. The oxidation mechanism primarily takes place at interfaces I and II (see Fig. 2.1), where the thin film (for simplicity, the oxidation of metals M is described in the following) interacts with oxygen O_2, leading to the formation of an oxide layer (metal oxide, MO) between the interfaces.

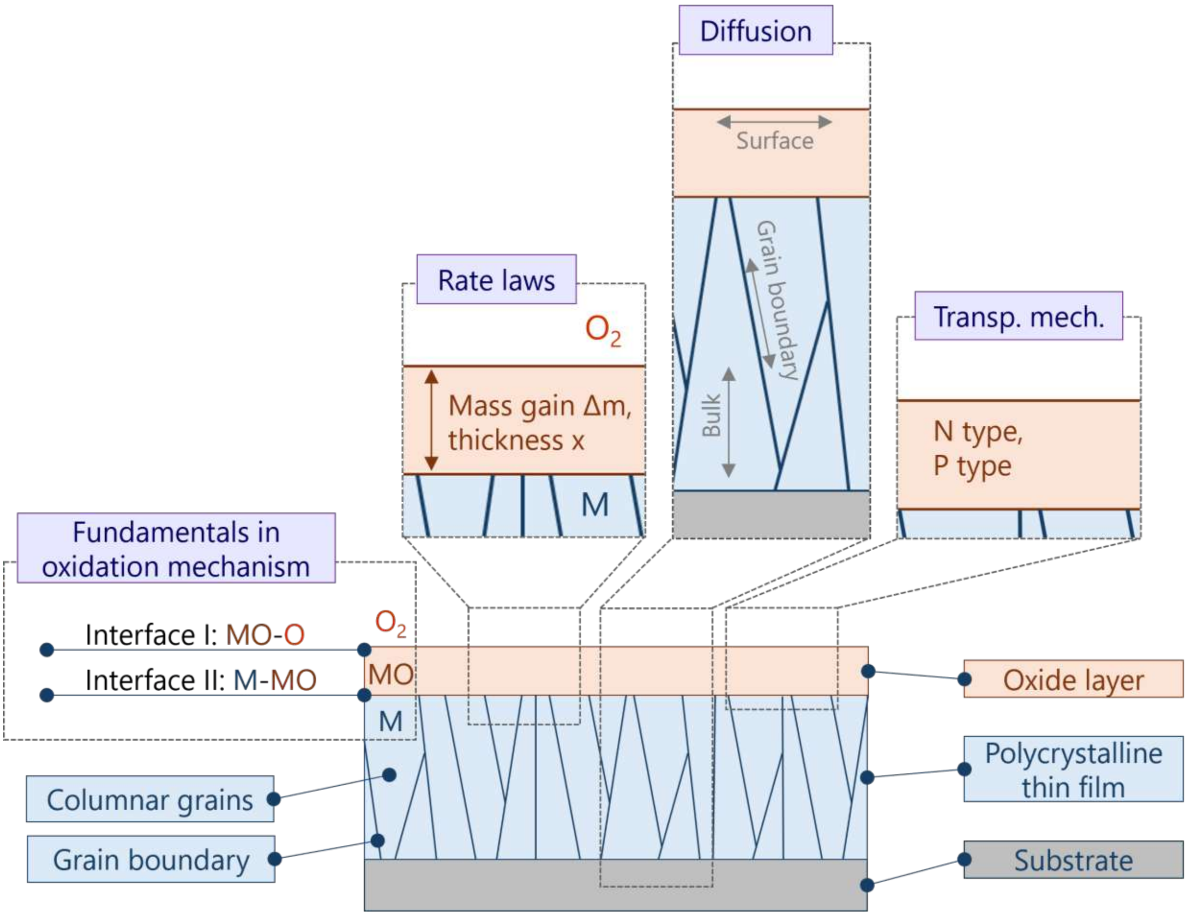

Figure 2.1: Schematic sketch of a thin film morphology, highlighting interfaces I and II, relevant for understanding the oxidation mechanism. Oxidation is based on diffusion processes; scale formation is based on rate laws; on small scale, transport mechanisms determine scale formation.

If, as in Fig. 2.1, a thin film or a metal M comes into contact with oxygen-containing atmosphere, the reaction that occurs can be explained using the following reaction equation Eq. 2.1 [27, 28]:

$$M + \frac{1}{2}O_2 \rightarrow MO \tag{2.1}$$

After the reaction of a (divalent) metal M with oxygen O_2, the reaction product MO is formed in between, on top of the metal [27, 28]. The above reaction equation Eq. 2.1 is a redox reaction that can be divided into an oxidation and a reduction term. The oxidation reaction describes the formation of the metal ions and takes place at the interface between M and MO (Eq. 2.2) [27].

$$M \rightarrow M^{2+} + 2e^{-} \tag{2.2}$$

The reduction equation describes the formation of oxygen anions and takes place at the interface between MO and the atmosphere/oxygen (Eq. 2.3) [27].

$$\frac{1}{2}O_2 + 2e^{-} \rightarrow O^{2-} \tag{2.3}$$

Fig. 2.2 shows a schematic overview of the processes involved [28].

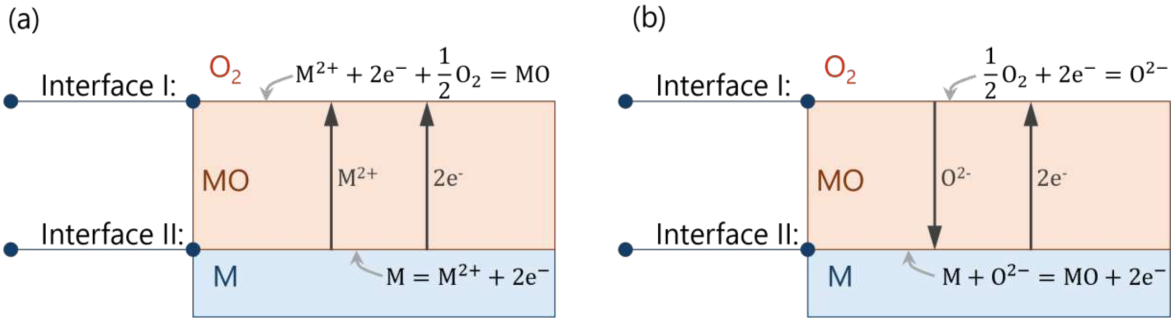

Figure 2.2: Overview of the reactions that take place during high-temperature oxidation. (a) shows the cation mobility and (b) the anion transport. Both figures are adapted from [28].

For the oxidation to continue, at least one reactant (i.e., M^{2+} or O^{2-}) must be able to diffuse through the scale. In addition, the electrons must be conducted to the MO/atmosphere interface. An oxide layer can therefore protect metals from further oxidation if it acts as diffusion barrier and electrical insulator – the diffusivity though the reaction product MO is a key characteristic of how quickly oxidation takes place [27, 28].

2.1.1 Ion diffusion in thin films

Diffusion in thin films occurs by two primary mechanisms: *vacancy* and *interstitial diffusion*. For both mechanisms, the atom must have sufficient energy (vibrational energy) for the change of position, so that bonding can be broken and any disturbances in lattice structure during movement can be overcome. In addition, an unoccupied, neighboring lattice position or interstitial site must also exist, so that the movement of atoms across lattice defects can take place [27].

The cause of macroscopic transport and position changes of atoms – diffusion – is the thermodynamic disequilibrium of a material system. This imbalance can arise from compositional inhomogeneities, where the free energy on a microscopic scale differs from point to point. With these atomic concentration gradients, a force emerges that drives the material systems towards equilibrium. A. Fick established a relationship between the concentration gradient $\frac{dc}{dx}$ and the diffusional transport through Fick's first law [27, 30]:

$$J = -D\frac{dc}{dx} \tag{2.4}$$

In Eq. 2.4, the minus sign results from the fact that the concentration gradient points in the opposite direction to the diffusion current density J $[kgm^{-2}s^{-1}]$ (diffusion takes place in the direction of decreasing concentration). The proportionality factor D is referred to as the diffusion coefficient $[m^2s^{-1}]$ and c is the concentration $[kgm^{-3}]$. Fick's first law is valid if the diffusion current density is time independent – stationary diffusion. However, since most of the occurring processes are non-stationary, it should be noted that the diffusion current density as well as the concentration gradient are time-dependent quantities. This non-stationary process is described by Fick's second law [27]:

$$\frac{dc}{dt} = D\frac{d^2c}{dx^2} \tag{2.5}$$

Eq. 2.5 can be used to determine the concentration as a function of time and position. With specific assumptions and boundary conditions (e.g., consideration of a semi-infinite solid, diffusion process begins at $t = 0$, $c = c_0$ at $t = 0$: a concentration c_0 is already evenly distributed in the solid at $t = 0$, etc.), the following solution of Eq. 2.5 can be determined [27]:

$$\frac{c_x - c_0}{c_s - c_v} = 1 - erf(\frac{x}{2\sqrt{Dt}}) \tag{2.6}$$

In Eq. 2.6, c_x stands for the concentration at position x after the time t has passed, c_s is the surface concentration, t stands for the time, and $erf(\frac{x}{2\sqrt{Dt}})$ is the Gaussian error function. Since the left-hand side of Eq. 2.6 is a constant for a specific concentration $c_x = c_1$, the right-hand side of the equation must also be a constant and the following relationship can be found [27]. Eq. 2.7 enables the calculation of diffusion processes.

$$\frac{x}{2\sqrt{Dt}} = constant \tag{2.7}$$

In general, diffusion is the result of random movement of many individual atoms. As already mentioned, these atoms oscillate in their equilibrium state with a characteristic lattice frequency (vibrational/oscillation frequency). With sufficiently high vibrational energy, it is possible for an atom to actually jump from one position to another. In this respect, the diffusion coefficient D provides an indication of the rate of atomic transports/jumps [27, 30]:

$$D = D_0 exp(-\frac{Q_D}{RT}) \tag{2.8}$$

In Eq. 2.8 D_0 is the temperature independent pre-exponential factor $[m^2 s^{-1}]$, Q_D is the activation energy for diffusion $[Jmol^{-1}]$, R is the universal gas constant $[Jmol^{-1}K^{-1}]$ and T the temperature $[K]$. Eq. 2.8 shows that the temperature has a strong influence on the diffusion rate. The Boltzmann factor $exp(-\frac{Q_D}{RT})$ can be regarded as the fraction of atoms with sufficient energy for jumps (diffusion) in the crystal [27, 30]. The diffusion rate is largest along surfaces, followed by phase and grain boundary diffusion, dislocation and bulk diffusion: $D_{surface} > D_{phaseboundary} > D_{grainboundary} > D_{discloation} > D_{volume/bulk}$ [31].

2.1.2 Rate laws of oxidation kinetics

The rate laws describe the rate of oxidation and thus the kinetics of oxidation. The rate of an oxidation reaction is considered to be the increase in thickness/mass of the reaction product MO per unit time or area. As mentioned above, in the oxidation process, the two reactants M and O_2 are separated by the reaction product MO. For oxidation to occur, ionic and electronic transport through MO must be possible. Consequently, the diffusion of ions and electrons is the driving force behind the formation of an oxide scale [27, 28].

Assuming that the diffusion of the ions determines the rate of oxide growth, and assuming a thermodynamic equilibrium on each interface (scale-gas and scale-metal), the outward cation flux $j_{M^{2+}}$ must be equal to the opposite occurrence of metal vacancies j_{V_M} (inward flux of cation defects). This relationship can be expressed as follows [28]:

$$j_{M^{2+}} = -j_{V_M} = D_{V_M} \frac{C''_{V_M} - C'_{V_M}}{x} \tag{2.9}$$

In Eq. 2.9, D_{V_M} is the cation vacancy diffusion coefficient, C'_{V_M} and C''_{V_M} represent the vacancy concentrations at the two interfaces, and x is the scale thickness. Eq. 2.9 can be further expressed to become Eq. 2.10, where V_{ox} is the molar oxide volume [28]:

$$j_{M^{2+}} = \frac{1}{V_{ox}} \frac{dx}{dt} = D_{V_M} \frac{C''_{V_M} - C'_{V_M}}{x} \tag{2.10}$$

Eq. 2.10 includes the fact that with increasing scale growth $\frac{dx}{dt}$ per molar oxide volume, the outward cation flux increases and vice versa. Assuming the thermodynamic equilibrium at the two interfaces $C''_{V_M} - C'_{V_M}$ is constant, the following Eq. 2.11 can be obtained, which indicates the rate of oxide growth [28]:

$$\frac{dx}{dt} = \frac{k'}{x} \tag{2.11}$$

with

$$k' = D_{V_M} V_{ox}(C''_{V_M} - C'_{V_M})$$

Integrating Eq. 2.11 and considering that at time $t = 0$ the scale thickness is still $x = 0$ leads to Eq. 2.12 [28]:

$$x^2 = 2k't \tag{2.12}$$

Eq. 2.12 is also known as the common parabolic rate law (see Eq. 2.13) [27, 28]:

$$x^2 = k_p t \tag{2.13}$$

In Eq. 2.13 x is the scale thickness, k_p is the parabolic rate constant, which is also dependent on the oxygen partial pressure and the temperature, and t is the time. And of course, the smaller k_p the better the protective properties of a scale. This theory is called *Wagner's theory of oxidation* [32], which states that ionic and electronic transport are the rate-controlling factors for oxide scale formation [28, 31].

However, if oxide formation follows a constant rate step, such as in the initial stages of an oxidation process, or if the oxide thickness is very thin, the scale formation obeys a linear rate law, which can be expressed by Eq. 2.14 [27, 28, 31]:

$$x = k_l t \tag{2.14}$$

In Eq. 2.14 x is the scale thickness, k_l is the linear rate constant and t is the time. With linear oxidation kinetics, the scale cannot inhibit the diffusion of ions or electrons, as in the case with porous oxides for example [28, 31]. When metals are for example oxidized at low temperatures (up to 400 °C), or even during the initial formation of oxides (up to about 1000 Å, scale formation and oxidation kinetics are governed by a logarithmic rate law, see Eq. 2.15, where A and t_0 are constants at constant temperatures, and k_{log} is the logarithmic rate constant [28]:

$$x = k_{log} \log{(t + t_0)} + A \tag{2.15}$$

All these trends in oxide scale growth and the associated kinetics are sketched in Fig. 2.3 [33]. As shown in Fig. 2.3, break-away oxidation can also occur. In this case, scale formation follows the parabolic rate law. However, spalling occurs (e.g., due to compressive stress) and some of the metal is again exposed to the gas (e.g., oxygen). This again means accelerated oxidation according to the parabolic law until spalling occurs again. This behavior must be avoided at all costs, as it can lead to significant material loss and damage [31].

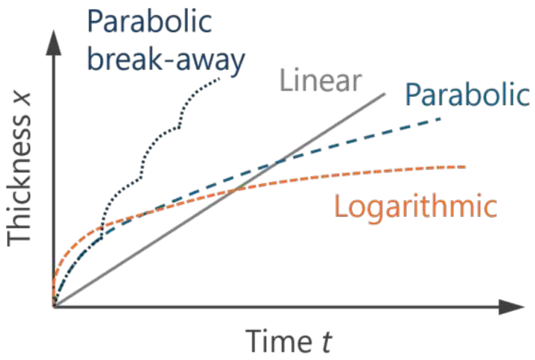

Figure 2.3: Schematical illustration of the rates of oxidation. The figure is adapted from [33].

In addition to the three rate laws described (parabolic, linear and logarithmic), metals can also follow other rate laws. These trends can be described by a general power rate kinetic, see Eq. 2.16, where x is the layer thickness, k' is the power law rate constant, t is time and n is the power law exponent for the scale growth [34].

$$x = k't^n \tag{2.16}$$

In addition to diffusivity and kinetics, the Pilling-Bedworth ratio (PBR) is a parameter that describes the ability of the scale to protect the metal from further oxidation so that no parabolic break-away oxidation takes place [27]:

$$PBR = \frac{V_{oxide}}{nV_{metal}} = \frac{M_{oxide}\rho_{metal}}{M_{metal}n\rho_{oxide}} \tag{2.17}$$

In Eq. 2.17, M denotes the molar mass, ρ the density, V the (molar) volume, and n the number of metal atoms in the sum formula of the oxides. The scales can therefore be divided into well-protective ($PBR = 1 - 2$) and non-protective ($PBR < 1$, $PBR > 2$). $PBR < 1$ means that the metal oxide does not cover the surface of the metals well, or the scale is porous. If $PBR > 1$, this means that compressive stresses are occurring (up to a certain degree this is conducive to dense film growth). However, if the PBR is too high ($PBR > 2$), the compressive stress can lead to cracking or flaking of the oxide scale. Strong oxide formers such as Al, Cr, and Si have $PBRs$ of 1.28, 2.07, and 2.27, respectively [27, 31].

2.1.3 Transport mechanism

Metal oxides are usually ionically bound. It therefore makes sense to describe the transport of ions instead of elements (natural metals, etc.). In general, defects in the crystal are responsible for the transport mechanism, as free sites enable the transport and diffusion of ions. For stoichiometric MO reaction products with ionic bonding, *Schottky* (i.e., equal number of cation and anion vacancies) and *Frankel* (i.e., cation vacancies with cation interstitials) defects are the most common. Depending on which defects are present, the diffusion capacity of the cations or the mobility of the anions can be increased. This leads either to M^{2+} diffusion out and forming a compound with O_2 on the MO/O_2 interface, or O^{2-} diffusion in and forming the oxide at the interface with the metal. However, since electrons must also diffuse through for the reaction to take place, it must be assumed that the ionic MO reactants do not have to be stoichiometric and can be described as *negative* (n-type) or *positive* (p-type) semiconductors. Non-stoichiometry in this case means that the ratio of metal to non-metal deviates from the chemical formula, while still being electrically neutral, and has an anionic or cationic variable valence (metals or cations tend to have a variable valence more likely) [28].

Negative (n-type) semiconductors

N-type semiconductors are formed by MO reaction products with metal excess or non-metal deficiency. The chemical formula is therefore $M_{1+x}O$. In this type of semiconductor, the electrical charge is transferred by negative charge carriers, when electrons are entering the conduction band [28].

If the MO reaction product has metal excess, interstitial cations (e.g., M_i^+, M_i^{2+} for single or doubly charged interstitial cations) with the same number of electrons (e.g., e^-, $2e^-$) are present. These *excess* electrons are transferred to the conduction band and become *quasi-free* electrons. However, this defect can be associated with absence of oxygen (when having a perfect MO crystal) and can be described by Eq. 2.18, which is valid for doubly charged cation interstitials [28]:

$$MO = M_i^{2+} + 2e^- + \frac{1}{2}O_2 \tag{2.18}$$

Eq. 2.19 applies equally to singly charged cation interstitials:

$$MO = M_i^{+} + e^- + \frac{1}{2}O_2 \tag{2.19}$$

Similarly, the absence of the non-metal (absence of an incorporated oxygen ion in the oxide) creates an oxygen vacancy, $2e^-$ *quasi-free* electrons can enter the conduction band, and oxygen is released as $\frac{1}{2}O_2$. It should be noted that there can also be singly and doubly charged vacancies, as the cations can attract electrons and as a result only one quasi-free electron can enter the conduction band [28].

In the following, the equilibrium condition for metal excess in Eq. 2.18 (and Eq. 2.19) are used to derive the dependence between the electron concentration and the oxygen partial pressure, obtaining the same results for non-metal deficiency. Based on Eq. 2.18 as well as using thermodynamic and *Henry's laws* (the partial pressure of a gas in a liquid is directly proportional to the concentration of the gas in the liquid [35]), the following relationship (Eq. 2.20) can be found where the concentration of the cation interstitials $C_{M_i^{2+}}$ and the concentration of the electrons C_{e^-} are correlated with the partial pressure of O_2 [28].

$$K_1 = C_{M_i^{2+}} C_{e^-}^2 p_{O_2}^{\frac{1}{2}} \tag{2.20}$$

Considering the fact that $2C_{M_i^{2+}} = C_{e^-}$ and adding up the constants, C_{e^-} is proportional to $p_{O_2}^{-\frac{1}{6}}$ for doubly charged anion interstitials.

The following relationship (Eq. 2.21) can be stated for singly ($n = 4$) and doubly ($n = 6$) charged n-type semiconductors, where the electrical conductivity κ is proportional to the electron concentration and this is inverse proportional to the oxygen partial pressure [28].

$$\kappa \propto C_{e^-} \propto p_{O_2}^{-\frac{1}{n}} \tag{2.21}$$

This means that the electron concentration is the highest where the partial pressure of oxygen is low (at the interface between the metal and the MO). The difference in the electron concentration between the metal-MO and atmosphere-MO interfaces is also the decisive reason why the diffusion of electron and ions take place [28].

Positive (p-type) semiconductors

In contrast to the n-type semiconductor, a p-type semiconductor is formed in the absence of metal or an excess of the non-metal, and the charge transfer takes place through positive charges. The chemical formular for the metal oxide is $M_{1-x}O$, with well-known examples being chromium oxide Cr_2O_3 or alumina Al_2O_3 [28].

The principle is because metals can occur in different valance states. Transition metals in particular are known to be able to change from M^{2+} to M^{3+}, for example, relatively easily with the release of electrons. If $\frac{1}{2}O_2$ adsorbs to a perfect MO crystal (consisting of M^{2+} and O^{2-}), chemisorption occurs, in which (two) existing M^{2+} transfer electrons to the now incorporated oxygen ion in the oxide, and as a result O^{2-} is formed. This creates two so-called electron holes (two M^{3+}, which present low energy positions for electrons) and a vacancy in the cation lattice as one M^{2+} moves to the new O^{2-}. These vacancies in the cation lattice and the electron holes enable electrical conductivity for a p-type semiconductor. In general, the process can be described by Eq. 2.22, where an incoming $\frac{1}{2}O_2$ leads to an incorporated oxygen ion in the oxide O_O, (two) positively charged electron holes ($2h^+$) and negatively charged metal vacancies (V_M^{2-}) [28].

$$\frac{1}{2}O_2 = O_O + 2h^+ + V_M^{2-} \tag{2.22}$$

In the case that a cation vacancy attaches to an electron hole, Eq. 2.22 is adjusted to one electron hole (h^+) with a singly charged metal vacancy (V_M^-). The equilibrium condition from Eq. 2.22 can be assumed again with the use of *Henry's laws* [35] as follows (Eq. 2.23) [28]:

$$C_{h^+}^2 C_{V_M^{2-}} = K_2 p_{O_2}^{\frac{1}{2}} \tag{2.23}$$

Assuming electrical neutrality, $C_{h^+} = 2C_{V_M^{2-}}$, and summarizing the constants it follows for n-type semiconductors that the electrical conductivity κ is directly related to the electron-hole concentration and this is directly related to the oxygen partial pressure, see Eq. 2.24. It should be noted that the power of the oxygen partial pressure is positive and $n = 4$ for single electron holes and $n = 6$ for double electron holes/doubly charged cation vacancies [28].

$$\kappa \propto C_{h^+} \propto p_{O_2}^{\frac{1}{n}} \tag{2.24}$$

In addition to the classic n-type and p-type approaches, there are also so-called *intrinsic* or *transitional* semiconductors, in which the electrical conductivity does not depend on the oxygen partial pressure. In this case, an electron is transferred from the valence band to the conduction band (excitation) and an electron hole is created at the same time [28].

2.2 Strong oxide formers

Strong oxide formers are characterized by the fact that the associated oxides have strong protective properties. These include thermodynamic stability, phase stability (e.g., phase transition within the oxide could cause detrimental volume changes) and proper oxidation kinetics. Such properties are exhibited by Al/Al_2O_3, Cr/Cr_2O_3, and Si/SiO_2. Their oxidation kinetics are characterized by the parabolic rate law, where the diffusion of the ions through the scale is the rate determining step. Fick's first law (diffusion) can be used to establish the relationship to the parabolic rate law constant k_p [31]:

$$k_p = k_0 e^{-\frac{Q}{RT}} \tag{2.25}$$

In Eq. 2.25 k_0 is a constant, Q is the activation energy, R is the universal gas constant and T is temperature. The oxidation rate is therefore an exponential function of the activation energy and temperature and can be represented using an Arrhenius plot, see Fig. 2.4 [28, 31].

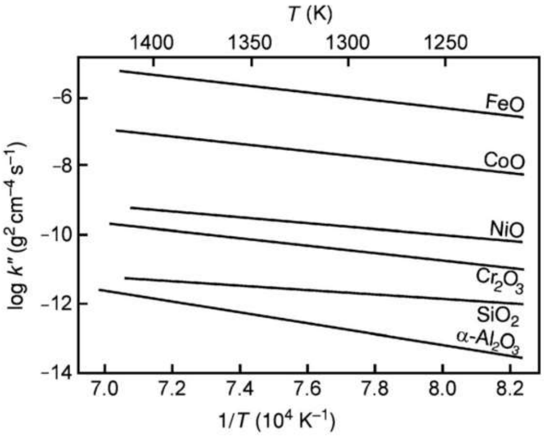

Figure 2.4: Logarithmic plot of parabolic rate constants for several oxide growths [28].

The larger k_p, the faster oxidation occurs; the smaller k_p, the greater the protection effectiveness of the corresponding oxide. As can be seen in Fig. 2.4, Al_2O_3, SiO_2 and Cr_2O_3 have a low k_p, which stands for slow growing oxides and their protective properties. Therefore, in this subchapter, the three strong oxide formers aluminum, silicon and chromium are described [28, 31]. In addition, mullite, a compound formed out of alumina (Al_2O_3) and silica (SiO_2), is described.

2.2.1 Aluminum

The investigation of bare aluminum (Al) substrates and Al-alloys that tend to form passivating protective scales based on Al_2O_3 has been part of many scientific efforts. The process of oxidation is complex and depends on many factors such as chemical composition (alloy content), microstructure or oxidation kinetics. Understanding the characteristics of the growth and structure of an Al_2O_3 layer is crucial to derive significant benefits from passivating scale formation for industrial applications (e.g., gas turbines). In addition, it is important that these forming scales are resistant to mechanical stress to ensure the longevity of the scale [36].

Recent studies on the growth kinetics and mechanisms of alumina (Al_2O_3) formed by thermal oxidation of aluminum substrates have provided valuable insights into the oxidation process and its dependence on temperature. When aluminum is exposed to oxygen at temperatures above 300 °C, oxide islands form on the surface, which indicate that the process involves lateral diffusion of mobile oxygen species over the bare aluminum surface. At temperatures below 200 °C, the mobility of the oxygen species is low, so that island formation is hindered.

As a result, the bare Al substrate becomes covered with a uniform oxide film that is 2-3 monolayers thick (approximately 0.4 to 0.6 *nm*). As the temperature increases, the lateral diffusion and the rate of oxide formation increases, resulting in a decrease in the density of oxide islands. At temperatures of 300 °C and above, a closed oxide film forms over the entire surface of the Al substrate. Thereby, a uniformly thick scale establishes (of approximately 10 to 30 *nm*), still having local leftovers of the initial island-by-layer growth mechanism. Once a closed oxide film has formed on an aluminum substrate, the growth of the oxide film requires transportation of Al substrate atoms and/or chemisorbed oxygen atoms through the establishing scale. This movement typically involves ionic species [37]. Polycrystalline alumina thereby can exhibit both, n-type or p-type behavior, which depends on the local oxygen potential. Due to the large oxygen gradient along the forming scale, a p- to n-type transition can occur within the growing Al_2O_3. Therefore, the electronic structure of the forming alumina is directly relevant to its oxidation resistance [36].

To achieve oxidation at high temperatures (i.e., 700 to 1200 °C), typically Al-based alloys are examined (the melting point of pure Al is already at 660 °C). The formation of a protective α-Al_2O_3-based thermally grown oxide (TGO) provides excellent oxidation resistance in this high temperature regime. However, before the stable α-phase (high-temperature phase) is formed, several other phases of aluminum oxides are often formed in the early stages of the oxidation process, such as δ-Al_2O_3 (tetragonal), ε-Al_2O_3 (hexagonal), γ-Al_2O_3 (cubic), θ-Al_2O_3 (monoclinic). The transformations between the polymorphs and the stable α-phase are associated with structural changes such as volume changes, which are accompanied by mechanical stresses within the forming scale and can weaken the protective properties [26, 36].

The oxidation kinetics of the forming alumina is largely determined by the oxygen partial pressure and morphology-dependent factors such as diffusion at grain boundaries. In general, the morphology of the Al-alloyed bulk materials is characterized by a columnar structure. Through targeted grain boundary design, i.e. by alloying *reactive* elements, which usually sit at grain boundaries and act as diffusion blockade. Alloying with these *reactive* elements such as yttrium (Y), zirconium (Zr) and hafnium (Hf) can therefore increase the oxidation resistance. By that, the diffusion of aluminum to the outside, the oxidation process and thus the oxidation kinetics can be slowed down significantly [36].

Aluminum is also often alloyed into thin film materials to improve their resistance to oxidation at high temperatures. Again, this is primarily due to the ability of Al to form a protective alumina-based scale (Al_2O_3) that acts as a barrier to further oxidation. Bakhit et al. improved the oxidation resistance of Al alloyed TiB_2 thin films [38]. While the unalloyed $TiB_{2.4}$ coating forms a porous Ti-based scale (mainly due to the evaporation of B_2O_3) of about 1900 *nm* during oxidation at 800 °C for 30 *min*, a $Ti_{0.68}Al_{0.32}B_{1.35}$ thin film forms a thinner Al-containing scale of approximately 470 *nm* under the same air-annealing conditions.

Similar results and an improvement in oxidation resistance at 600 °C were also obtained for $Ti_{0.9}Al_{0.1}B_{1.3}$ and $Ti_{0.9}Al_{0.1}B_{1.4}$ thin films, forming a mixed Al_2O_3-TiO_2 scale by Thörnberg et al. [39]. Banakh et al. additionally demonstrated an improvement in the oxidation of Al-alloyed CrN thin films, where he showed that Al helps to increase the oxidation properties with contents between $0.2 < x < 0.6$ at.% of Al on the metal sublattice [40].

2.2.2 Silicon

Silica, which has the chemical formula SiO_2, has a covalent bonding nature and is a natural occurring material. Under atmospheric pressure and depending on temperature conditions, a distinction is made between the crystalline α-quartz structure ($T < 870$ °C), tridymite (870 – 1470 °C) and the β-cristobalite ($T > 1470$ °C) phase. The high-temperature phase β-cristobalite is stable till 1700 °C and transforms into amorphous silica glass at higher temperatures [41]. Silica is mainly used in semiconductor technology as an oxide layer for insulation protection, and, due to its dense crystal structure, it is widely used as diffusion barrier for corrosion protection [42].

The dry oxidation of silicon takes place in a pure oxygen atmosphere according to Eq. 2.26. Common production variants of silica are produced by thermal oxidation or separated from the gas phase (e.g., sputtering or thermal evaporation). After synthesis of silicon dioxide layers, e.g. by PVD processes, the films are usually in an amorphous, glassy-like state [42].

$$Si + O_2 \rightarrow SiO_2 \tag{2.26}$$

The oxide growth is limited by the oxygen diffusion through the already existing oxide to the reaction partner (silicon). The oxidation process can be described by a simple model consisting of a parabolic and a linear part (Eq. 2.27) [42].

$$d_{ox}^2 + \alpha \; d_{ox} = \beta(t + t_0) \tag{2.27}$$

Here, α and β are temperature-dependent variables. β describes the parabolic growth and $\frac{\beta}{\alpha}$ the linear growth. t_0 is also used to take into account the already existing (negligible) surface oxides [42].

The diffusion of oxygen through SiO_2 is very different from Al_2O_3-based oxides, where ion transport takes place. For SiO_2, oxygen diffusion is dominated by O_2 molecules. This was shown in a theoretical study by Hoshino et al. [43], who determined the activation energy for atomic (O) and molecular (O_2) oxygen diffusion through the α-quartz and the β-cristobalite SiO_2 structure. For both crystalline phases, O_2 diffusion is associated with a significantly lower activation energy, which does not require to break the existing covalent Si-O bonds in the SiO_2 phase.

Figure 2.5 shows the diffusion of the O_2 molecule through the cristobalite SiO_2 structure. In (a), the O_2 molecule is embedded in the stable SiO_2 state. The numerical values in the figure also describe the bond length of the individual compounds, whereby that of O-O is approximately 1.21 Å. (b) describes the unstable transition state, in which the O_2 molecule migrates through a 12-atom Si-O ring and then reintegrates into the stable state in (c), whereby no new chemical compounds need to be formed. Therefore, the activation energy is also relatively low (approximately 0.3 eV for molecular O_2 diffusion and approximately 1.3 eV for atomic oxygen diffusion) [43].

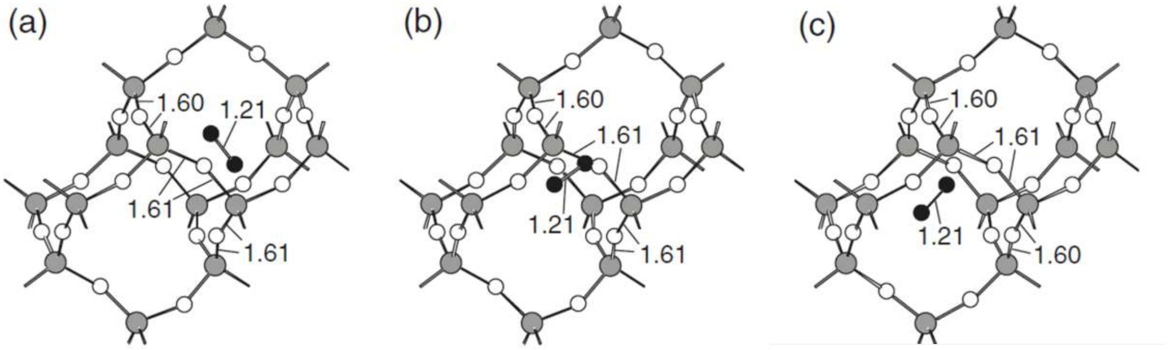

Figure 2.5: Schematic representation of the diffusion of an O_2 molecule through SiO_2 and the associated atomic changes. The numerical values represent the bond length of the individual compounds. (a) represents the stable state, where an O_2 molecule is embedded in the SiO_2 structure. (b) shows the unstable transition state. In (c), again a stable state is formed [43].

2.2.3 Chromium

Chromium is well known for its protective properties, especially in stainless steel, protecting it from oxidation by forming a passivating Cr_2O_3 layer [44, 45]. It is also widely used as an excellent alloying element for thin films to improve corrosion and oxidation properties [46, 47], and also has been used in thermal barrier coatings [48–50].

In general, the oxidation of pure chromium (Cr) is primarily characterized by the formation of a single oxide, Cr_2O_3. Under certain conditions, however, this seemingly straightforward process becomes complex. These complications are crucial for technical alloys whose oxidation resistance depends on a Cr_2O_3 protective layer. The main challenges are the thinning of the oxide layer due to the evaporation of CrO_3 at high oxygen partial pressures, which can be described by Eq. 2.28 [28].

$$Cr_2O_3\,(s) + \frac{3}{2}O_2\,(g) = 2CrO_3(g) \tag{2.28}$$

The formation of CrO_3 occurs at elevated temperatures (above approximately 1000 °C) and high oxygen partial pressures, which leads to a thinning of the chromia (Cr_2O_3) scale, which in turn enables faster ion diffusion through the scale and increase the oxidation rate, displayed by Figure 2.6. This process of volatilization significantly influences the kinetics of oxidation [28, 51].

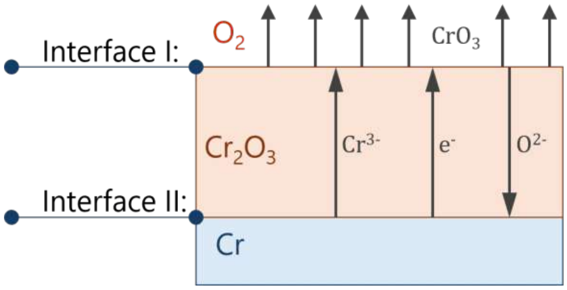

Figure 2.6: Schematic representation of the CrO_3 volatilization. The figure is adapted from [28].

The change in oxide thickness over time is influenced by two processes: *Thickening* (oxide growth) by diffusion and *thinning* by volatilization. Initially, diffusion is the predominant process as the oxide layer grows and the effects of CrO_3 volatilization are negligible. However, as the scale becomes thicker, the rate of CrO_3 volatilization begins to match the rate of oxide growth, leading to a phenomenon known as *paralinear* oxidation, which establishes a limiting thickness of the oxide. This limiting thickness x_0 is determined by the ratio between the diffusion constant k_d and the volatilization constant k_s [28].

Although reaching a limiting thickness of the oxide layer means effective protection, it can also lead to increased metal consumption. Once the oxide layer has reached its limiting thickness, the metal substrate continues to be consumed at a constant rate. This problem is particularly problematic in environments with fast-moving gases and is a significant limitation for the use of Cr_2O_3-forming alloys at high temperatures [28].

Another important problem with chromium oxidation is the development of compressive stresses within the chromia scale that leads to buckling, sketched in Fig. 2.7. In general, the type of surface preparation affects both the rate of oxidation and the build-up of stresses. Electropolished chromium samples tend to oxidize faster and develop compressive stresses within the polycrystalline Cr_2O_3 scale. In contrast, etched samples can form thinner, single-crystalline Cr_2O_3 scales with less compressive stresses [28, 51, 52]. This studies carried out by Caplan and Sproule [52] have shown that polycrystalline oxides grow by transporting cations outward and anions inward. The anion transport takes place along the grain boundaries in the oxide and generates compressive stresses though the oxide formation at the metal-oxide interface [28, 51].

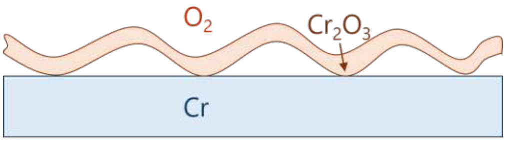

Figure 2.7: Schematic representation of the buckling of a chromia scale. The figure is adapted from [28].

2.2.4 Mullite

Mullite is a silicate mineral and a compound formed out of alumina and silica, see phase diagram Fig. 2.8. It has remarkable properties, such as low density ($\sim 3.2\ gcm^{-3}$ [53]), high strength ($\sim 200\ MPa$), low thermal conductivity, good fracture toughness ($K_{Ic} \sim 2.5\ MPa\sqrt{m}$ [53]), and excellent thermal stability ($T_M \sim 1830\ °C$ [53]) as well as high chemical resistance at high temperatures [53–55].

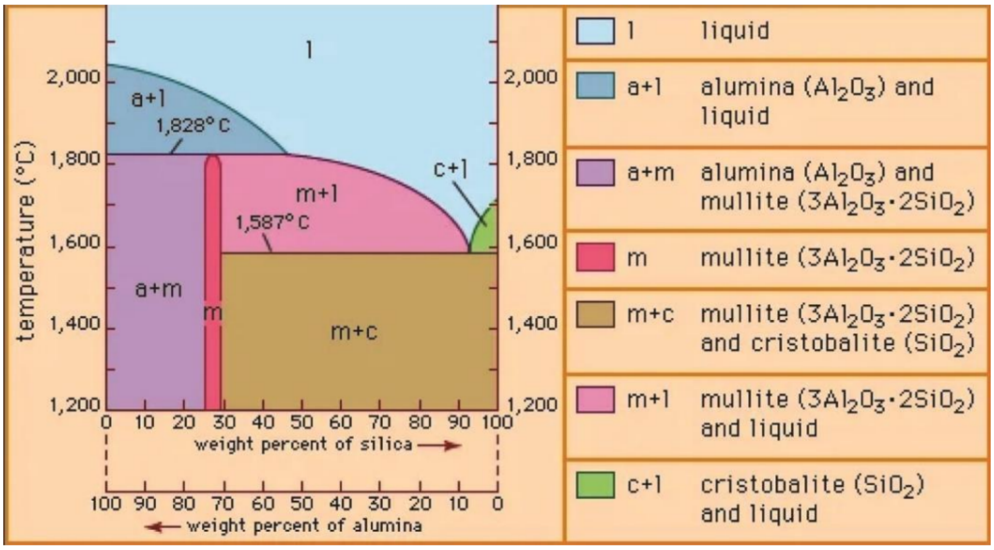

Figure 2.8: Phase diagram Al_2O_3-SiO_2 showing the mullite phase [54].

The crystal structure of mullite, characterized by Fischer and Schneider [56, 57], is based on chains of edge-sharing octahedra in tetragonal arrangement within a orthorhombic aluminosilicate system, see Fig. 2.9.

The fundamental building blocks of mullite are AlO_6 octahedral chains running parallel to the c-axis, connected by doubly chains of $(Al,Si)O_4$ tetrahedra. The structure is defective, allowing compositional variation between $2Al_2O_3 \cdot SiO_2$ (called 2/1 mullite) and $3Al_2O_3 \cdot 2SiO_2$ (3/2 mullite), mostly dependent on the synthesis temperature [54].

In the past two decades, advanced mullite ceramics have become increasingly important, particularly in high-temperature applications such as composite matrix materials and protective coatings. Mullite can be synthesized using the sintering method or melted in an electric furnace to produce fused mullite. Multi fibers, usually manufactured by the sol-gel method,

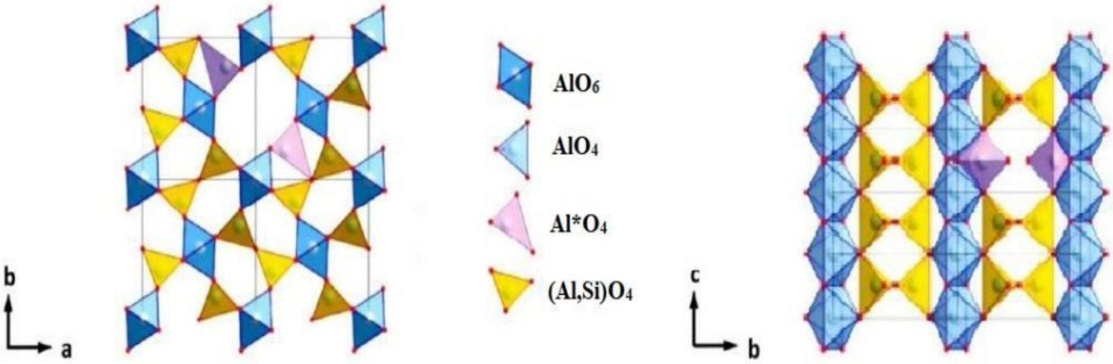

Figure 2.9: Schematic representation of the crystal structure of mullite [54].

offer excellent high-temperature insulation used for electrical insulation. Mullite whiskers, a bundle of mullite fibers is often employed as reinforcement in ceramics or metals. Monolithic bulk mullite ceramics are suitable for silicon solar cells or even refractories, crucibles and hot gas filters [53, 54, 56].

Mullite has also attracted significant interest as a material for environmental barrier coatings (EBCs), particularly for protecting silicon-based ceramics and composites used for components in the hottest regions in gas turbines [58–60]. Mullite coatings are highly beneficial because of its unique combination of properties including excellent oxidation as well as hot-corrosion resistance (for example in Na_2SO_4-rich environment) [56]. Additionally, mullite can maintain stability in water vapor-rich conditions (stationary systems at low pressures). Although mullite's constituents (Al_2O_3 and SiO_2) can form volatile (oxy-)hydroxides, but the high chemical activity of silica lead to the preferred formation of Si-O-H species on top of mullite. This release creates a gas boundary layer that slows further decomposition [56].

Mullite coatings can be synthesized via chemical vapor deposition (CVD) with aluminum and silicon chlorides as starting materials, in combination with CO_2 and H_2 [61–63], or plasma- and flame-sprayed [64–67]. For both deposition techniques, SiC could effectively be protected from rapid oxidation up to 1500 °C, even in water vapor (H_2O) environment (at 1200 °C), highlighting its applicability for diffusion barriers in environmental barrier coatings. The low thermal expansion of mullite ($\sim 4.5 \cdot 10^{-6}\ °C^{-1}$ between 20-1400 °C [53]) also minimizes the risk of delamination or spallation at high temperatures when the material is subjected to temperature shocks. Additional its low fracture toughness helps to resist cracking and mechanical damage, helping to enhance the durability [54, 56].

Chapter 3

High-performance ceramic coating materials

This chapter presents the material systems investigated in this study, with a focus on molybdenum disilicide ($MoSi_2$), transition metal diborides (TMB_2) and transition metal carbides (TMC). These materials were synthesized by physical vapor deposition (PVD), particularly by magnetron sputtering. Various strategies have been applied to improve their high temperature oxidation resistance by using strong oxide formers, as explained in Chapter 2. The $MoSi_2$ phase benefits from Si contained in its structure. In contrast, the transition metal carbides and diborides, which are more susceptible to oxidation, have been improved in terms of oxidation resistance by various alloying processes and architectural designs (application of top coatings). These approaches aimed to utilize the properties of the material systems to create a protective oxide barrier and thereby improve their overall performance et elevated temperatures.

3.1 Molybdenum disilicide ($MoSi_2$)

Molybdenum disilicide ($MoSi_2$) is a transition metal silicide valued for its unique combination of metallic and ceramic properties that make it ideal for high temperature applications. Its structure includes a metal bond between molybdenum atoms and a covalent bond between molybdenum and silicon atoms [68], which gives $MoSi_2$ excellent chemical stability, oxidation and corrosion resistance, as well as good electrical conductivity [69].

An important property of $MoSi_2$ is its excellent oxidation resistance at elevated temperatures. Additionally, it is characterized by its high melting point of approximately 2030 °C [68]. Above 800 °C, $MoSi_2$ forms a protective silica scale (SiO_2), which prevents further oxidation of the underlying material. This process is described by the following reaction equation Eq. 3.1 [68].

$$5MoSi_2 + 7O_2 \rightarrow Mo_5Si_3 + 7SiO_2 \tag{3.1}$$

The silica scale effectively protects $MoSi_2$ from oxygen [70, 71], making it highly suitable for high-temperature applications such as heating elements and aerospace components [72, 73].

However, $MoSi_2$ is not without its limitations. At medium temperatures (300 to 800 °C), an unfavorable oxidation mechanism can occur due to the mixed oxide scale formation of molybdenum trioxide (MoO_3) and silica, described by Eq. 3.2 [68]. This so-called *pesting* behavior, a destructive oxidation mechanism, occurs most likely at defects such as pores and grain boundaries. This reaction leads to volume expansion, which destroys the protective SiO_2 scale and makes the material susceptible to further oxidation [68, 74].

$$2MoSi_2 + 7O_2 \rightarrow 2MoO_3 + 4SiO_2 \tag{3.2}$$

$MoSi_2$ exists in two crystallographic forms: α-$MoSi_2$ (body-centered tetragonal type C11b structure) and β-$MoSi_2$ (hexagonal type C40 structure), as displayed in Figure 3.1 [75]. The α-phase is stable at low temperatures, while the β-phase transitions at 1877 °C and is stable at high temperatures [76]. $MoSi_2$ is known for its strength at high temperatures and its brittleness at room temperature. The transition from brittle to ductile occurs at around 1000 °C [68, 77].

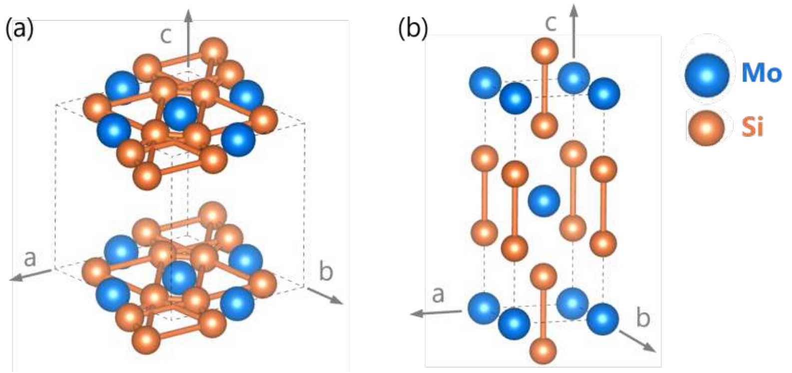

Figure 3.1: Schematic respresentation of the crystal strucutre of (a) hexagonal $MoSi_2$ (beta, SG180, $CrSi_2$ prototype) and (b) tetragonal $MoSi_2$ (alpha, SG139, $MoSi_2$ prototype).

In practice, $MoSi_2$ is often used in thin-film technology for protective coatings. Various deposition methods are used, including plasma spraying, hot-dip siliconizing, chemical vapor deposition, and physical vapor deposition (PVD) [70, 78–81]. PVD, particularly magnetron sputtering, has been shown to produce $MoSi_2$ coatings with excellent oxidation resistance [70]. The sputtered films, which are initially amorphous, can be crystallized by annealing. Annealing at around 700 °C achieves the metastable β-$MoSi_2$ phase, while higher temperatures (800 °C) produce stable α-$MoSi_2$ and Mo_5Si_3 phases [82]. Further research is needed to improve the oxidation resistance of $MoSi_2$ and to optimize deposition parameters and techniques for even better performance.

3.2 Transition metal diborides (TMB_2)

Transition metal diborides (TMB_2) are of great interest due to their potential as coatings for refractory metals and high-temperature structural materials [38, 83–85]. In particular, the compounds of group IV to VI transition metal diborides are the focus of interest, which can have a primitive hexagonal crystal structure known as the AlB_2 type (α-structure). This structure is shown schematically in Fig. 3.2, and consists of alternating layers of boron atoms arranged in two-dimensional graphite-like networks and metal atoms in a hexagonally close-packed formation [83, 85, 86].

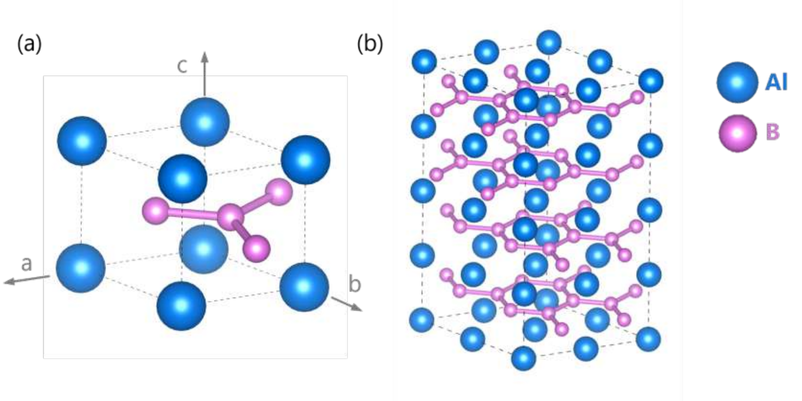

Figure 3.2: Schematic representation of the AlB_2 prototype crystal structure (SG191). In (a) the unit cell is shown, in (b) the 2x2x4 supercell, with the hexagonal B-networks highlighted.

Interestingly, early TMB_2 (e.g., TiB_2, VB_2) are more stable in the AlB_2 structure, while late TMB_2 (e.g., WB_2, ReB_2) prefer the W_2B_5-based structure (ω-type). Point defects like vacancies can significantly impact phase stability and structural preferences (AlB_2 or W_2B_5-based structure). Additionally, metastable diboride structures are generally more ductile than their stable forms [87]. The bonds in TMB_2 are complex and include covalent, ionic and metallic bonds. The strong covalent bonds between the boron atoms (B-B) contribute significantly to the high strength and hardness of the material. The bonds between the transition metals and boron (TM-B) are a combination of ionic and covalent bonds, and a metallic bonding nature predominates between the transition metals (TM-TM), providing moderate fracture toughness [84, 88]. Hexagonal TMB_2 thin films exhibit remarkable hardness anisotropy. In coatings such as α-stabilized $WB_{2\text{-}z}$ coatings, the hardness is significantly influenced by the crystal orientation. Thereby, the (0001)-orientation is preferred (with super-hardness values above 40 GPa), while the $(10\bar{1}1)$-orientation has a significantly lower hardness around 25 GPa [89].

TMB_2 coatings exhibit excellent mechanical properties, but also have some limitations. While they are highly valued for their high hardness and thermal stability, their oxidation resistance is limited due to the competing formation of porous TM-based oxides (TMO_x) and volatile boron oxides (B_2O_3) at temperatures up to 1000 °C [90]. Boron-rich tissue phases, typical for magnetron sputtered diborides, additionally promote the evaporation of B_2O_3 along grain boundaries and strongly affect the oxidation kinetics. X. Cai and S. Dorri [91, 92] have shown that TiB_2 for example can achieve a stable oxide formation at around 600 °C, as Ti forms a dense crystalline TiO_2 scale covered by an amorphous B_2O_3 layer. At higher oxidation temperatures, between 1000 and 1800 °C, a different scale formation occurs as B_2O_3 evaporates and a partly porous TMO_x is remaining [90]. To improve the oxidation properties of TMB_2, studies have already suggested that alloying with Al and Si could increase the oxidation resistance and improve performance at higher temperatures ($T < 1000$ °C). For example for chromium diboride, alloying 16 at.% Si shifts the oxidation onset temperature form 600 °C ($CrB_{2.27}$) to 1300 °C [93], while the addition of Al improves the oxidation resistance of TiB_2 at 800 °C as the scale thickness is reduced to ∼470 nm compared to ∼1900 nm for $TiB_{2.4}$ [38].

3.3 Transition metal carbides (TMC)

Transition metal carbides (TMC), which are formed by group IV to VI TM, are known for their high hardness, brittleness, high melting points and their electrical and thermal conductivity. Their diverse properties result from a mixture of covalent, ionic and metallic bonds [94]. The growing interest in TMC can be attributed to several factors, above all the demand for the aerospace industry for next-generation high-temperature materials. These carbides include compounds such as the solid solution TaC-HfC, which has the highest known melting point of around 4000 °C. Its exceptional hardness, which is already used in the abrasives industry, underlines its potential as material for high-temperature applications [94, 95].

TMC exhibit a range of structures from simple to complex. Simple structures include body-centered cubic (bcc), face-centered cubic (fcc), hexagonal close-packed (hcp) and simple hexagonal (sh) arrangements. Complex structures include, for example: TM_3C_2, TM_3C, TM_5C_2, TM_7C_3, $TM_{23}C_6$, TM_6C. Group IV transition metals such as Ti, Zr, and Hf generally form carbides of the fcc group, while group V TM form carbides of both the fcc and hcp structures. Mo and W from group VI are known to form carbides with fcc, hcp, sh structures and Cr forms complex carbide structures (e.g., Cr_3C_2, Cr_7C_3, $Cr_{23}C_6$), see Tab. 3.1 [94].

The structure of fcc-type carbides (exemplified by TiC) is illustrated in the next Fig. 3.3, where metal atoms are shown as blue circles and carbon atoms occupy the positions of the smaller grey circles in the octahedral interstices [94].

Table 3.1: Overview of TMC structures [94].

Group IV TM (Ti, Zr, Hf)	Group V TM (V, Nb, Ta)			Group VI TM (Cr, Mo, W)			
fcc	bcc	fcc	hcp	fcc	hcp	sh	complex
TiC ZrC HfC	- - $Ta_{0.64}C$	VC NbC TaC	V_2C Nb_2C Ta_2C	(CrC) α-MoC_x β-W_2C	- β-Mo_2C α-W_2C	- γ-MoC WC	Cr_3C_2, Cr_7C_3, $Cr_{23}C_6$ η-MoC_x, γ-MoC (W_5C_3)

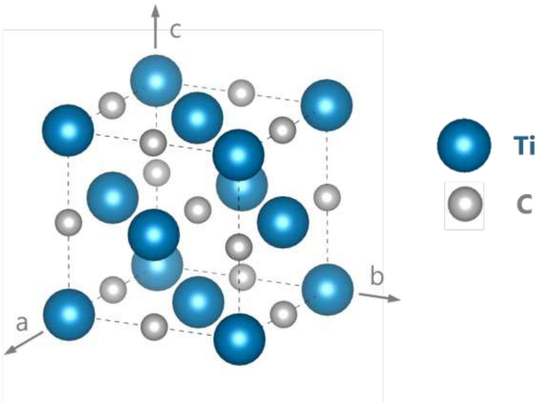

Figure 3.3: Schematic representation of the crystal structure of fcc TiC (SG225, NaCl prototype).

For stoichiometric TMC, all octahedral sites are filled with carbon, resulting in a NaCl-type structure. Typically, NaCl-type carbides exhibit a range of chemical compositions and are typically non-stoichiometric, see Tab. 3.2. Additionally, as can be seen in Tab. 3.2, the lattice parameter increases with carbon content, reaching up to 50 at.% C. Generally, their chemical formula is represented as TMC_x (where $x \leq 1$), indicating that some octahedral interstices remain unoccupied [94].

Table 3.2: Overview of the crystallographic data of fcc-TMC [94].

Carbide	Composition range (at.% C)	Type	Lattice parameter (Å)
TiC	33 to 50	fcc	4.296 to 4.326
ZrC	35 to 50	fcc	4.677 to 4.696
HfC	37 to 50	fcc	4.614 to 4.631
VC	38.6 to 44.1	fcc	4.118 to 4.141
NbC	41.8 to 49.7	fcc	4.443 to 4.470
TaC	41.5 to 49.5	fcc	4.410 to 4.456

Chapter 4

Coating synthesis

This chapter describes the method used to synthesize the thin films investigated in this thesis. The focus is on magnetron sputtering, a physical vapor deposition (PVD) process. In PVD, atoms or molecules are transferred from a material source (target) to a substrate through a vacuum by physical processes such as ion bombardment with high energy, evaporation, sublimation or condensation. In this process, a continuous film with a few nano- to micrometers is deposited, with a deposition rate between 1 to 10 nanometers per second. Common PVD processes include vacuum/thermal evaporation, sputtering, cathodic arc evaporation and ion plating [96–98]. PVD can be carried out in inert atmospheres such as argon or helium, or with reactive gases such as nitrogen, acetylene, silane or oxygen to deposit compounds like nitrides, carbides, silicides, or oxides, respectively. The PVD process comprises three main steps: the *generation of the vapor phase*, the *material transport* to the substrate and the *nucleation and growth* of the thin film [98].

4.1 Direct current magnetron sputtering (DCMS)

In sputter deposition, atoms or molecules are vaporized from a target through a *physical* process. In this process, the target atoms are ejected by momentum transfer when high-energy ions from a surrounding plasma are accelerated towards the target and bombard the target surface [97, 98], see Figure 4.1.

Direct current magnetron sputtering (DCMS) is a common method in which a negative DC voltage of several hundred volts is applied to the cathode, which is normally located behind the target, while the chamber wall serves as the anode. In this setup, the plasma is generated by passing an electric current through the sputtering gas, usually argon, resulting in a glow discharge between the electrodes [98, 100]. The high-energy ions (e.g., Ar^+) are attracted by the cathode and hit the surface of the target and cause atoms to be ejected and deposited on a substrate, creating a thin film. This requires that the target material must have a certain

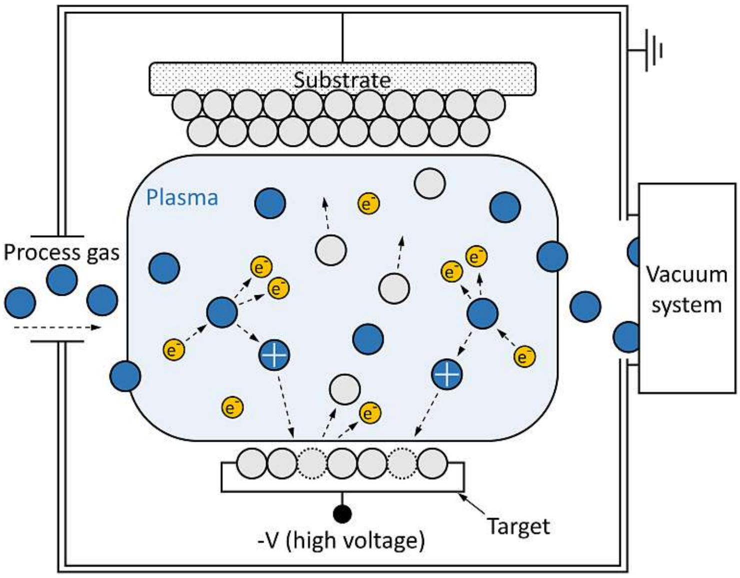

Figure 4.1: Schematic representation of the sputter process [99].

electrical conductivity. In DCMS, additional magnets are placed behind the target to keep the electrons close to the target surface and therefore enhance the efficiency of the plasma generation and increase the sputtering rate. The applied magnetic field cause the electrons to move in a circular/helical motion along the target surface, which is described by the *Lorentz force* ($\vec{F} = q(\vec{E} + \vec{v} \times \vec{B})$, with $\vec{E}$ the electrical field, $\vec{B}$ the magnetic field, $\vec{v}$ the electron velocity and q the negative charge of the electron) and results in the formation of a racetrack on the target surface (e.g., planar magnetron and target configuration) [98]. A schematic illustration of a planar magnetron is given in Fig. 4.2.

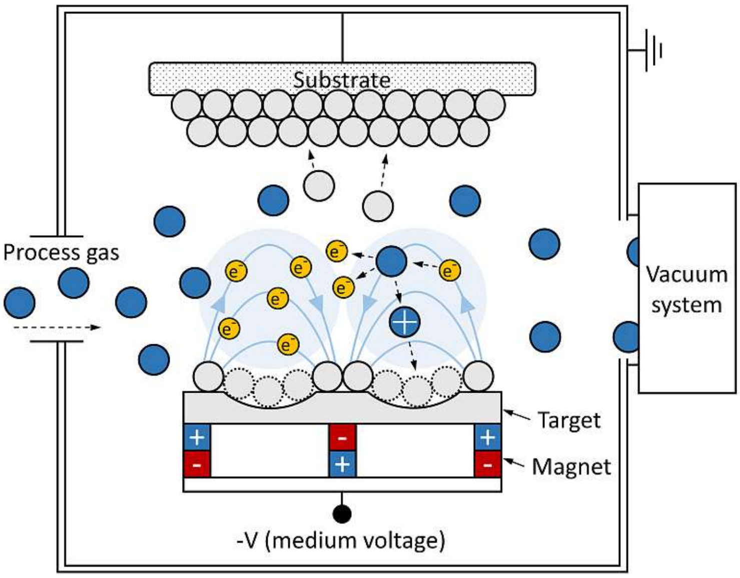

Figure 4.2: Schematic representation of a planar magnetron configuration [99].

After the sputtered atoms leave the target, they are transported through the gas phase before reaching the substrate. On their way, gas scattering can occur. The degree of gas scattering depends on several factors, including the target to substrate angle, the distance between them, or the deposition pressure in the chamber. Gas scattering effects are particularly pronounced when sputtering a compound target, such as transition metal borides or carbides, where the elements have significantly different masses and atomic radii. These differences can significantly affect the chemical composition of the deposited thin film. This phenomenon was investigated by studying Ti-B thin films deposited from a compound target, where the chemical composition could be controlled by adjusting parameters such as pressure, distance, and target to substrate angle. For instance, by varying the target to substrate distance alone, Ti/B ratios in the deposited thin film could be tuned within a range of approximately 1.3 to 2.1, sputtering a target with a Ti/B ratio of 1.66 [101]. Similar effects have also been observed in sputtering a TiB_2 target. A flux of B is directed centrally, while Ti experiences a larger sputtering angle [102].

Applying a negative bias potential to the substrate during thin film deposition can additionally influence thin film growth by directing argon ions onto the substrate. The negative potential applied is significantly lower than the potential applied to the cathode. This ion bombardment transfers the kinetic energy to the sputtered adatoms and thus promotes their diffusion ability, which can contribute to the formation of dense coatings. However, a too high bias voltage can lead to argon implantation, which causes defects, stresses and lower film quality. Alternatively, substrate heating can also control the energy and mobility of the adatoms and thus the morphology of the growing thin film [97, 98, 103]. All these properties of thin film growth are described in the structure zone diagram by A. Anders, see Fig. 4.3 [104]. On the y-axis, Anders plots the normalized energy flux E^*, which represents the energy of the incoming particles on the substrate, influencing the layer growth. This energy flux is particularly relevant for techniques such as arc evaporation or advanced high power pulsed magnetron sputtering (discussed in the next section), where highly ionized species can be attracted to the substrate (e.g., with a bias potential). On the x-axis, Anders represents the generalized temperature T^*, which reflects the thermal energy during film growth. The z-axis corresponds to the film thickness t^*. The etching zone is shown as the red area, indicating that excessive E^* can lead to material removal. In the structure zone diagram, our magnetron sputtered thin films are mainly located in the transition zone T and zone 2, where dense, columnar grains are formed [104].

4.2 High power pulsed magnetron sputtering (HPPMS)

High power pulsed magnetron sputtering (HPPMS) is an advanced version of magnetron sputtering. This method operates with short pulses, low duty cycles (usually below 10 %) and frequencies (usually below 10 kHz), resulting in high peak power densities on the target

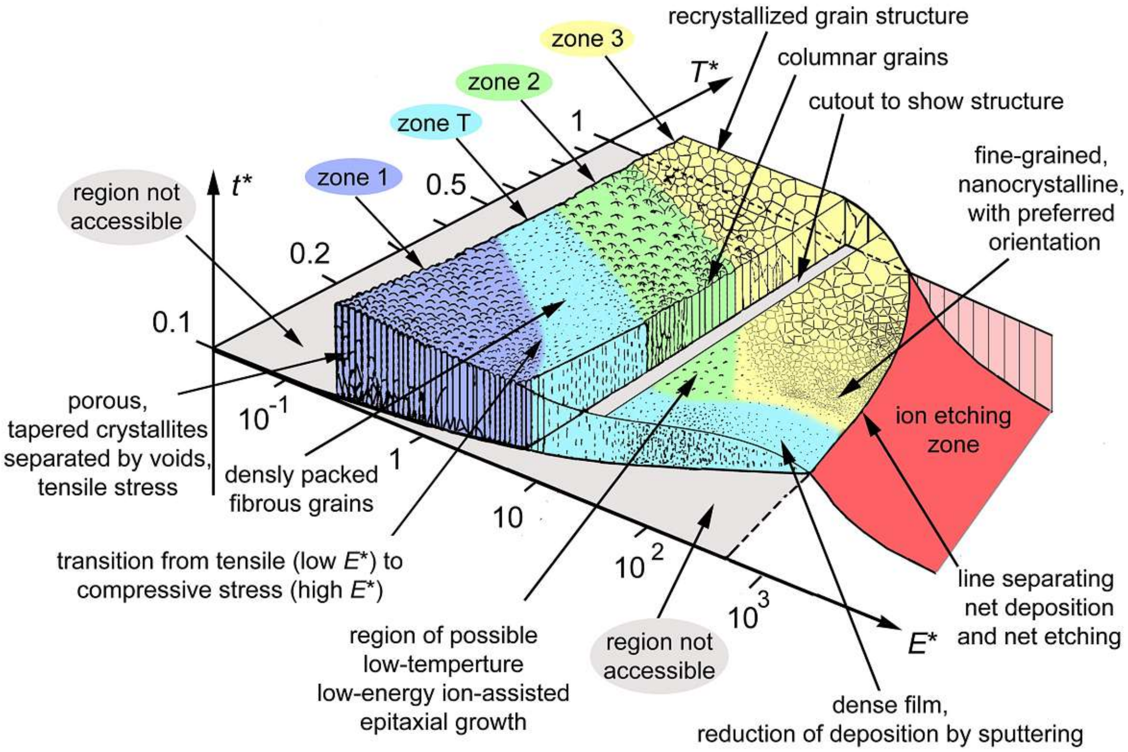

Figure 4.3: Structure zone diagram by A. Anders [104].

(several $kW\ cm^{-2}$) [103]. The peak powers achieved can be 2-3 orders of magnitude higher than with conventional sputtering (see Fig. 4.4 [105]), which is advantageous for the target due to the lower thermal load.

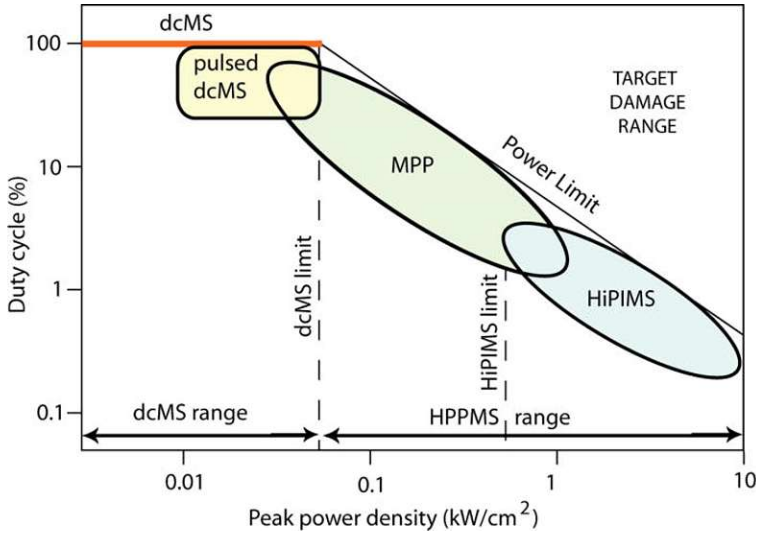

Figure 4.4: Classification for DCMS and pulsed power sputtering techniques [105].

Using HPPMS, ultra-dense plasmas are created with almost complete ionization of the sputtered atoms [103, 105]. Additionally, applying a negative bias potential to the substrate enables precise control of the film growth due to the ionized sputtered species (e.g., TM^+), which is a key benefit of HPPMS and a big advantage over conventional magnetron sputtering, in which mainly neutral species are sputtered [105, 106]. HPPMS thin films generally have a dense and strong pronounced columnar structure. One disadvantage of HPPMS is the lower deposition rate compared to DCMS at the same average power. One possible explanation for this is self-sputtering, where atoms that have already arrived at the substrate are re-sputtered due to the high energy input from the ionized incoming species [105]. The deposition characteristics for HPPMS are strongly influenced by pulse parameters, including the on-time t_{on}, off-time t_{off}, pulse duty cycle ($\frac{t_{on}}{T}$, with the pulse duration T), and frequency f. These parameters play a crucial role in shaping the HPPMS signal (target current, target voltage), which is illustrated in Fig. 4.5 [103].

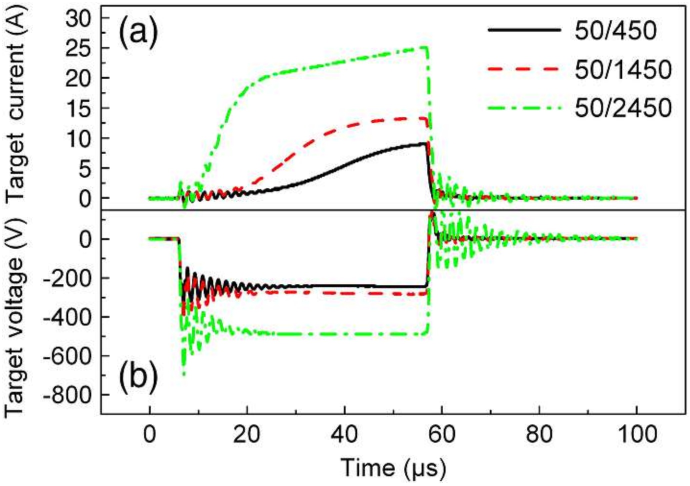

Figure 4.5: HPPMS signal including target voltage and target current at different on-/off-time configurations [103].

4.3 Growth concepts for oxidation resistant coatings

This section discusses various alloying strategies and explores additional methods, such as architectural design of thin films, which aim to protect oxidation-sensitive materials and thin films from high-temperature oxidation. When low-melting materials such as Al, Si, and Cr are alloyed into refractory ceramics (considering bulk materials), several challenges can arise. One key issue is the difference in sintering behavior, as low-melting metals often have different sintering behavior than ceramics. While ceramics typically require much higher sintering temperatures, the metals may already be melting at these high temperatures, which can lead to inhomogeneous densification. In addition, differences in the CTE of metals and ceramics can cause significant stress, potentially leading to cracking. Furthermore, the contrasting thermal conductivities of the metals and refractories can further complicate the sintering process, which in turn can lead to cracking due to differences in thermal shock resistance. PVD synthesis offers the advantage of overcoming these difficulties [107–109]. Therefore, several approaches to improve oxidation resistance have been investigated and tested in this work and are briefly discussed in the following subsections. Tab. 4.1 gives an overview of the melting points of Al, Si, Cr and some of the refractory ceramics synthesized in this work.

Table 4.1: Melting points of elements and compounds.

Element/compound	Bulk melting points (°C)
Al	660 °C [110]
Si	1414 °C [110]
Cr	1907 °C [110]
SiC	2730 °C [111]
$MoSi_2$	2030 °C [68]
TiB_2	2980 °C [83]
HfB_2	3250 °C [83]
CrB_2	2170 °C [83]
TiC	3067 °C [83]
ZrC	3420 °C [83]
HfC	3928 °C [83]
TaC	3950 °C [83]

4.3.1 Non-reactive DCMS/HPPMS

One approach to alloying low-melting strong oxide formers (Al, Cr, Si) into ceramics by PVD synthesis techniques includes the target production and magnetron co-sputtering. These methods do not require a reactive gas, such as silane for alloying silicon, and are therefore classified as non-reactive deposition techniques. A brief overview of these processes is provided in the following subchapters.

Target production

The addition of Al or Si in ceramics can be achieved during target production. Common manufacturing processes for producing ceramic targets (bulk materials) include hot pressing (HP) and spark plasma sintering (SPS). SPS, an electric field assisted joining technique, is widely used to produce (joint) carbides, borides, nitrides, or oxides [112–116]. In SPS, the starting materials (powder) are placed in graphite molds, and a high current (1500-2000 $mA\,mm^{-2}$) is passed through the material. The electrical resistance of the materials generates significant heat, leading to atomic diffusion and chemical reactions whereby (dense) targets and bulk materials can be formed. These processes are typically very fast, often taking less than an hour, with temperatures ranging from 1100-2000 °C during the process [112, 117].

At these high temperatures, metals such as Al and Si would melt (see Tab. 4.1). Because of the high temperatures involved, materials such as SiC, which have a much higher melting point of 2730 °C, are often used as alloying partner for ceramics [118]. This high melting point allows for densification with other ceramic precursors. Another potential candidate is $MoSi_2$ [119], which also has a high melting point of over 2000 °C.

Using this target production method, thin films can then be deposited by PVD (magnetron sputtering), allowing elements such as Si to be alloyed into borides or carbides in a non-reactive deposition process. To evaluate the alloying properties of $MoSi_2$ (acting as a strong alloying partner), this study primarily examines the oxidation resistance of $MoSi_2$ coatings.

Co-sputtering

Co-sputtering is an effective method for synthesizing different alloying states, making it ideal for exploring the properties and phase formation of different (novel) chemical compositions. A magnetron configuration, such as the one used to synthesize the thin films investigated in this work, had a target to substrate arrangement schematically shown in Fig. 4.6.

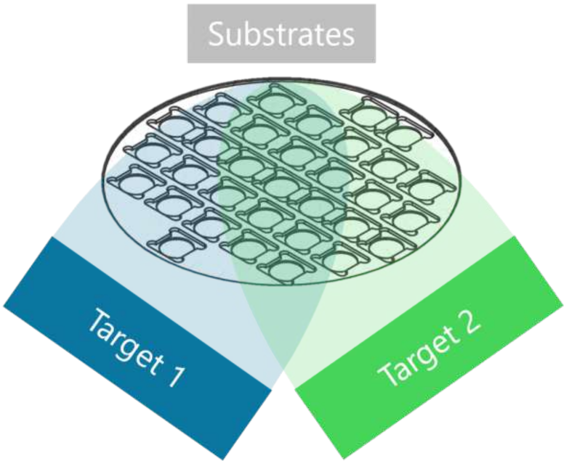

Figure 4.6: Schematic illustration of the target to substrate (thin films) arrangement during magnetron co-sputtering.

In recent years, the co-sputtering technique has been successfully used to alloy Al or Si into nitrides or borides using pure Al, Si or AlB_2 and SiB_2 compound targets [120–122]. In another study, Cr-B-C thin films were synthesized by co-sputtering from pure B and a compound CrB_2 target [123]. These examples highlight the growing trend of material systems in which co-sputtering is used to deposit various elemental configurations. A common feature of these studies is that co-sputtering allows precise control over the chemical composition of the deposited materials.

In this study, we used the co-sputtering technique, and additionally kept the substrate holder (and the targets) stationary during the deposition process, creating a compositional gradient across the substrates. This approach allows the study of multiple chemical compositions within a single deposition run, providing an efficient method for screening and researching novel coating materials. Furthermore, the technique poses no target fabrication challenges, as it can easily be performed using a variety of targets with different melting points, allowing the alloying of materials without technical complications.

4.3.2 Plasma enhanced deposition

In this work, plasma enhanced deposition was used as an additional method for alloying Si into ceramic thin films using silane (SiH_4) as a reactive gas and Si precursor. This technique was also applied to deposit Al-Si-based oxides and nitrides. The deposition process combines PVD and chemical vapor deposition (CVD) and was performed on a modified Oerlikon Balzers Innova system at Oerlikon Surface and Solutions AG. Both CVD and PVD can also be used independently to deposit thin films (and with other reactive gases such as oxygen and nitrogen) [124, 125].

This enhanced deposition technique introduces a low-voltage arc discharge in the center of the chamber, significantly increasing the plasma intensity beyond the levels achieved in standard sputtering processes. The high plasma density results in enhanced ionization, excitation, and dissociation of molecular species (silane) [125]. The deposition process is shown schematically in Fig. 4.7. In this figure, position 1 represents the center of the chamber where the low-voltage arc discharge occurs between the auxiliary anode at the bottom and the electron filament at the top. The targets are arranged in a 90° configuration. The (cathodic arc) evaporated target atoms then combine with silicon from the silane source, for example, and form the thin film material, which is then transported to the substrate (see position 2 in Fig. 4.7), where it condenses. With this advanced technique, for example, $Yb_2Si_2O_7/Si$ bilayer stacks have been successfully deposited on SiC to serve as an EBC [126], that withstood cyclic oxidation in water vapor (1000 cycles for 1 h each) at 1316 °C. For the deposition, an ytterbium Yb target was subjected to arc evaporation, while Si and O were introduced though silane and oxygen reactive gases. The Si layer was deposited only using the CVD process, while for the $Yb_2Si_2O_7$ the combined version of PVD/CVD was used.

4.3.3 Architectural design – top coatings

An architectural design of thin films involves the development of a layered structure. This approach also includes the application of top coatings to oxidation-prone base materials to provide protection against high-temperature oxidation, see Fig. 4.8. In this figure, the TM boride represents the oxidation-sensitive base material (blue), which is layered with a Si interlayer (orange) and a protective top coating (yellow). The motivation behind this strategy is inspired by TBCs and EBCs, which have a multi-layered structure. The current generation of EBCs, for example, are typically composed of rare earth (Re) mono- or disilicates (Re_2SiO_5 for mono- and $Re_2Si_2O_7$ for disilicates, Re = yttrium, ytterbium, scandium, or lutetium)

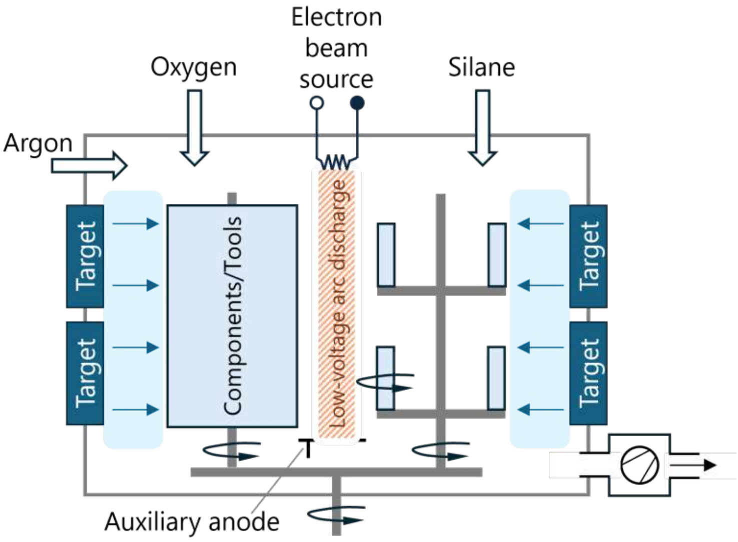

Figure 4.7: Schematic representation of plasma enhanced deposition. The figure is adapted from [125].

with a Si interlayer, which provides enhanced adhesion to the CMC substrate and acts as a diffusion barrier to protect the substrate from oxidation [127]. In contrast to thermally grown oxides (TGOs), sharp interfaces occur here, which can offer a significant advantage by acting as an effective (oxygen) diffusion barrier.

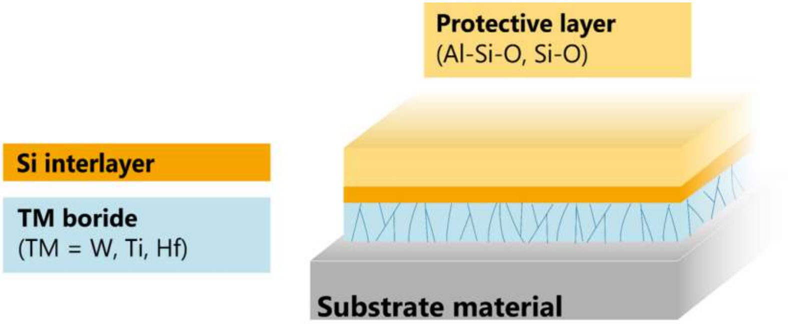

Figure 4.8: Architectural concept of protective coatings: Designing a layered coating architecture.

Chapter 5

Chemical analysis: challenges in heavy-light atomic mass combinations

This chapter deals specifically with the methods used to determine the chemical composition of the coatings investigated within this thesis. The fundamentals and the basic principles are explained in each case. The X-ray fluorescence (XRF) analysis was performed at the TU Wien, while the Rutherford backscattering spectroscopy (RBS) and the Elastic recoil detection analysis (ERDA) were performed at the Tandem Laboratory at the Uppsala University [128].

5.1 X-ray fluorescence (XRF)

X-ray fluorescence (XRF) is a highly effective method for identifying and quantifying almost all elements in a sample, from Be with the atomic number 4 to U with the atomic number 92. The technique is particularly valued for its non-destructive analysis, its high precision and its ability to analyze multiple elements simultaneously with a short irradiation time, enabling high sample throughput. In XRF, the material is irradiated with high-energy X-rays (photons) that penetrate the material and interact with the atoms in the sample. This interaction also leads to the ionization of electrons from the inner shell (K, L, M, etc.). The majority of the electrons remain in the bulk of the analyzed sample, and a few are emitted via the photoelectric effect (see Fig. 5.1), creating vacancies. When electrons from the outer shell fill these vacancies, they emit a characteristic fluorescence radiation that is specific to each element and enables their identification [129].

In addition to the emission of characteristic X-rays during the relaxation process, there is another possibility: the emission of Auger electrons. Typically the generation of Auger electrons is more likely for lighter elements, while the emission of X-ray fluorescence is more dominant for heavier elements [129].

In general, the interaction between the high-energy X-ray photons and the inner-shell electrons

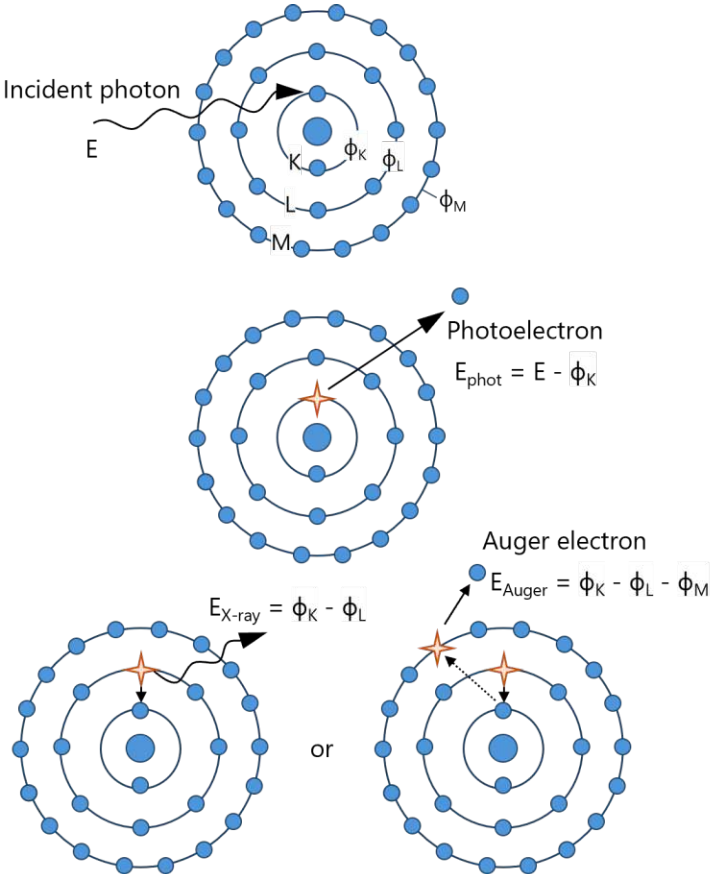

Figure 5.1: Schematic representation of photoelectric ionization resulting in the emission of characteristic fluorescent X-rays or Auger electrons. The figure is adapted from [129].

of the atoms (photoelectric effect) relies on the principle that the energy of the incident photon must be equal or greater than the binding energy of the electron for this to happen. The energy E of an X-ray photon is inversely proportional to its wavelength λ, expressed by the following Eq. 5.1, and typical radiation within XRF is between 1 and 50 keV (1 to 0.02 nm) [129].

$$\lambda\,(nm) = \frac{1.24}{E(keV)} \tag{5.1}$$

XRF analysis can be performed using either *wavelength* dispersive (WDXRF) or *energy* dispersive (EDXRF) spectrometers. In WDXRF, the intensity of the emitted X-rays is measured as a function of the wavelength, while in EDXRF the photons are sorted according to their energy [129].

5.2 Rutherford backscattering spectroscopy (RBS)

Rutherford backscattering spectroscopy (RBS) is a widely used method for quantitatively assessing the composition, thickness and depth profiles of thin films and bulk materials, especially near their surfaces. RBS has become an important technique for material characterization, valued for its accuracy and its ability to set standards for other techniques. In this technique a beam of monoenergetic ions (e.g., H^+, He^+) with energies between 0.5 and 2.5 MeV is focused on the sample. When these ions collide with the atoms of the sample, they are scattered back and their energy after scattering is measured. The scattering is elastic and occurs between the nuclei of the incoming ion (e.g., He^+) and the target atom. The ratio between the energy of the scattered ions E_1 and the original energy of the incident ions E_0 is expressed by the kinematic factor K, which originate from the theory of binary collisions (elastic scattering), see Eq. 5.2 [130].

$$K = \frac{E_1}{E_0} = (\frac{(M_2^2 - M_1^2 sin^2\theta)^{\frac{1}{2}} + M_1 cos\theta}{M_1 + M_2})^2 \tag{5.2}$$

In Eq. 5.2, M_1 and M_2 are the masses of the incident ion and the sample atom, respectively, and θ is the scattering angle. This equation shows that the energy of the backscattered ion results only from the masses involved and the scattering angle, so if M_1, E_0 and θ are given, M_2 can be calculated and identified as the sample element [130].

If $\theta = 180°$, the energy ratio is simplified to Eq. 5.3 [130].

$$K = \frac{E_1}{E_0} = (\frac{M_2 - M_1}{M_2 + M_1})^2 \tag{5.3}$$

This equation states that if the masses of the incident ion and the sample atom are the same, $M_1 = M_2$, the incident ion transfers its entire energy to the sample atom. Additionally, also important for RBS, if $M_2 < M_1$, no backscattering occurs [130].

With RBS, it must also be considered that the incident ions are not only scattered back from the atoms on the sample surface, but also from internal atoms along the direction of the ion beam. Thereby, the ions lose energy on their way due to interactions with electrons (e.g., excitation or ionization of the sample atoms). This energy loss, known as stopping power $(\frac{dE}{dx})$, leads to a broadening of the peaks in the RBS spectrum, as illustrated in Fig. 5.2 [130].

RBS is particularly sensitive to heavy elements, which can be understood by the Rutherford scattering cross-section σ_R, see Eq. 5.4. The scattering cross section σ_R indicates the probability that an incident projectile (M_1, Z_1, E_1) is scattered by a target atom (M_2, Z_2) by an angle θ (into a given area dQ), and the sensitivity of RBS per se depends on the scattering cross section. Since the scattering cross section is proportional/linear to Z_2^2, this means that

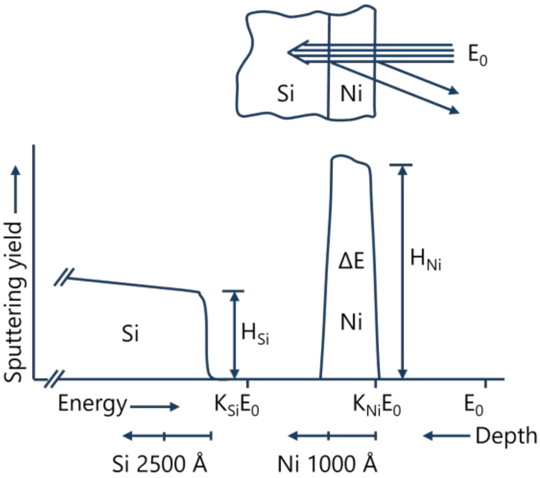

Figure 5.2: Schematic illustration of an RBS spectrum, where a 100 nm Ni thin film deposited on an Si substrate was analyzed using an MeV He$^+$ ion beam. ΔE represents the film thickness. K_{Si} is smaller than K_{Ni} because of the mass difference. The Si signal approaches 0 because of an infinite depth. The figure is adapted from [130].

the scattering cross section is larger for heavier elements (and also varies with the mass and energy of the incoming ions) [130].

$$\sigma_R = 5.18 \times 10^{-27} \left(\frac{Z_1 Z_2 (M_1 + M_2)^2}{M_2 E_1}\right)^2 \frac{1}{cos^3\theta} \tag{5.4}$$

5.3 Elastic recoil detection analysis (ERDA)

Elastic recoil detection analysis (ERDA) is another technique that enables quantitative elemental analysis and elemental depth distribution of thin films. While RBS analyzes backscattered ions (which are lighter compared to the sample atoms) at an angle of more than 90°, ERDA focuses on backscattered sample atoms that are directed forward by an incident ion ($\theta < 90°$). Since the scattered incident ions also move in the forward direction, the analysis of ERDA spectra is complex due to the overlap of the energy spectra of both the recoiled sample atoms and the scattered ions. Therefore, the ERDA spectra must be split into these two spectra: the $\Delta E - E$ *method* that uses the specific energy loss of the particles ΔE to determine their atomic number, and the *time-of-flight (TOF) method*, which distinguishes the particles based on their velocity. While RBS also provides simpler depth profiles, the complexity of ERDA often requires computational analysis to accurately evaluate the spectra. However, the big advantage of ERDA is that it can profile light elements, which is almost impossible with RBS [130].

Like RBS, also ERDA relies on important physical mechanisms such as the kinematic factor, which describes the two-body collision, and the stopping power to quantify the depth profiles.

ERDA is versatile and uses different incident ions with different energies depending on the sample elements to be analyzed: From light projectiles (e.g., He, C ions with 2-10 MeV) for analyzing very light elements (e.g., H), to medium ions (e.g., Cl with 30 MeV) for light elements (where the TOF method is commonly used), to heavy projectiles (e.g., Au with >100 MeV) for a wide range of elements where the $\Delta E - E$ method is typically used [130].

The schematic representation of an ERDA geometry setup is shown in Fig. 5.3 and includes an incident ion beam hitting a sample at an incident angle α. After the ions collide with the atoms of the sample, they are either recoiled or scattered and are detected at an angle β. θ represents the scattering angle [130].

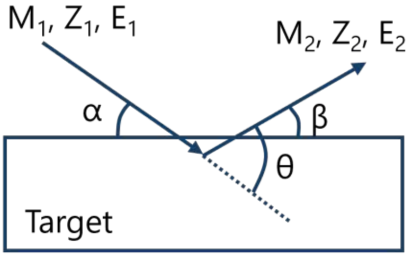

Figure 5.3: Schematic representation of the ERDA geometry setup. The figure is adapted from [130].

In ERDA, the kinematic factor for elastic recoil K_R can be determined by the conservation of energy and momentum during the two-body collision and is expressed in the following Eq. 5.5 [130].

$$K_R = \frac{E_2}{E_1} = \frac{4M_1M_2}{(M_1+M_2)} cos^2\theta \tag{5.5}$$

In Eq. 5.5, M_1, E_1, and Z_1 stand for the mass, the energy and the atomic number of the incident ion, respectively, see also Fig. 5.3. After the collision, the sample atom emerges with the mass M_2, atomic number Z_2, and energy E_2. This equation illustrates how the energy transfer depends on the masses of the incident ion and the sample atom as well as the scattering angle θ. The maximum recoil energy occurs when the mass of the sample atom is equal to the ion mass ($M_1 = M_2$), represented by $E_2^{max} = E_1 cos^2\theta$. In addition, scattered ions have a higher energy than recoils when $M_2 > M_1$, making heavy ions ideal for analyzing elements in the surface region [130].

Another important parameter, which emphasizes that even particularly light elements (e.g., C) can be detected well with ERDA, is the recoil cross-section, which represents the probability of the recoil effect/indicates how likely the recoil by the incident ion occurs at a certain scattering angle θ. With considerable deviations, the recoil cross-section for Rutherford scattering σ_R can be considered, see Eq. 5.4 [130].

The cross-section is proportional to $(\frac{Z_2}{M_2})^2$ for light elements (where $M_2 \ll M_1$) and almost constant because the ratio $\frac{Z_2}{M_2}$ is roughly 0.5 for all elements. This makes ERDA with heavy ions an effective tool for profiling different elements (also light elements), although specific deviations from this ideal Rutherford cross-section can occur due to nuclear interactions or other effects [130].

Bibliography

[1] M. F. Ashby, en*Materials and Sustainable Development* (Butterworth-Heinemann, 2022).

[2] A. Saini and T. Pollock, MRS Bull. **37**, 550 (2012).

[3] Z. Huda, T. Zaharinie, and H. A. Al-Ansary, Nucl. Eng. Des./Fusion **9**, 2 (2014).

[4] International Energy Agency: IEA, "Natural gas," `https://www.iea.org/energy-system/fossil-fuels/natural-gas` (2023), accessed: 2024-7-15.

[5] N. Armaroli and V. Balzani, Energy Environ. Sci. **4**, 3193 (2011).

[6] M. Hasanuzzaman, U. S. Zubir, N. I. Ilham, and H. Seng Che, Wiley Interdiscip. Rev. Energy Environ. **6**, e222 (2017).

[7] G. Wang, M. Bi, H. Fan, Y. Fan, C. Huang, Y. Shi, W. Liu, D. Liu, and H. Hua, IET Cyber-Phys. Syst. Theory Appl. (2022).

[8] N. Keyaerts, E. Delarue, Y. Rombauts, and W. D'haeseleer, Appl. Energy **119**, 266 (2014).

[9] J. Winters, en"Energy blog: Gas power plants are efficiency giants," `https://www.asme.org/topics-resources/content/blog-gas-power-plants-are-efficiency-giants` (2023), accessed: 2025-1-4.

[10] C. Carcasci and B. Facchini, Energy Convers. Manage. **41**, 757 (2000).

[11] United Nations, `https://sdgs.un.org/2030agenda` (2015), accessed: 2024-12-7.

[12] C. Mohan, J. Robinson, L. Vodwal, and N. Kumari, in *Green Chemistry Approaches to Environmental Sustainability*, edited by V. K. Garg, A. Yadav, C. Mohan, S. Yadav, and N. Kumari (Elsevier, 2024) pp. 357–374.

[13] M. J. Pomeroy, Mater. Des. **26**, 223 (2005).

[14] I. Barwinska, M. Kopec, D. Kukla, C. Senderowski, and Z. L. Kowalewski, Coat. World **13**, 769 (2023).

[15] J. H. Perepezko, Science **326**, 1068 (2009).

[16] G. Canale, F. Rubino, and R. Citarella, Forces Mech. **14**, 100251 (2024).

[17] P. Spriet, in *Ceramic Matrix Composites* (John Wiley & Sons, Inc., Hoboken, NJ, USA, 2014) pp. 591–608.

[18] National Aeronautics and Space Administration, Agency Licensing Concierge, Glenn Research Center, "Environmental barrier coatings for ceramic matrix composites," `https://technology.nasa.gov/patent/LEW-TOPS-136`, accessed: 2024-2-23.

[19] P. Wehrel, "Technological level of CMC components for stationary gas turbines and aero-engines, DLR report, DLR-IB-AT-KP-2022-32," (2022).

[20] F. Christin, en*Ceramic matrix composites: Fiber reinforced ceramics and their applications*, 1st ed., edited by W. Krenkel (Wiley-VCH Verlag, Weinheim, Germany, 2008).

[21] D. Casari, X. Maeder, D. Chen, B. Widrig, and J. Ramm, J. Eur. Ceram. Soc. **44**, 6367 (2024).

[22] M. Ridley, D. M. Lance, T. Aguirre, K. Kane, and B. A. Pint, J. Eng. Gas Turbine. Power , 1 (2024).

[23] S. K. Mital and S. M. Arnold, (2024).

[24] B. C. Wyatt, S. K. Nemani, G. E. Hilmas, E. J. Opila, and B. Anasori, Nature Reviews Materials , 1 (2023).

[25] D. J. Young, en*High Temperature Oxidation and Corrosion of Metals* (Elsevier, 2016).

[26] R. Prescott and M. J. Graham, Oxid. Met. **38**, 233 (1992).

[27] W. D. Callister and D. G. Rethwisch, de*Materialwissenschaften und Werkstofftechnik: Eine Einführung* (John Wiley & Sons, 2012).

[28] N. Birks, G. H. Meier, and F. S. Pettit, en*Introduction to the High Temperature Oxidation of Metals* (Cambridge University Press, 2006).

[29] X. Zhang, P. Zheng, Y. Ma, Y. Jiang, and H. Li, Mater. Des. **217**, 110605 (2022).

[30] M. Ohring, en*The materials science of thin films* (Academic Press, San Diego, CA, 1992).

[31] P. H. Mayrhofer, “Script surface technology,” (2020).

[32] C. Wagner, Z. Phys. Chem. (N F) **21B**, 25 (1933).

[33] R. E. Smallman and R. J. Bishop, en*Modern Physical Metallurgy and Materials Engineering* (Elsevier, 1999).

[34] D. J. Tallman, B. Anasori, and M. W. Barsoum, Mater. Res. Lett. **1**, 115 (2013).

[35] W. Henry, Philos. Trans. R. Soc. Lond. **93**, 29 (1803).

[36] A. H. Heuer, D. B. Hovis, J. L. Smialek, and B. Gleeson, J. Am. Ceram. Soc. **94**, s146 (2011).

[37] L. Jeurgens, W. Sloof, F. Tichelaar, and E. Mittemeijer, J. Appl. Phys. **92**, 1649 (2002).

[38] B. Bakhit, J. Palisaitis, J. Thörnberg, J. Rosen, P. O. Persson, L. Hultman, I. Petrov, J. E. Greene, and G. Greczynski, Acta Mater. **196**, 677 (2020).

[39] J. Thörnberg, S. Mráz, J. Palisaitis, F. F. Klimashin, P. Ondracka, B. Bakhit, P. Polcik, S. Kolozsvari, L. Hultman, I. Petrov, P. O. Persson, J. M. Schneider, and J. Rosen, Surf. Coat. Technol. **442**, 128187 (2022).

[40] O. Banakh, P. E. Schmid, R. Sanjinés, and F. Lévy, Surf. Coat. Technol. **163-164**, 57 (2003).

[41] E. F. Vansant, P. Van Der Voort, and K. C. Vrancken, en*Characterization and Chemical Modification of the Silica Surface* (Elsevier, 1995).

[42] U. Hilleringmann, de*Silizium-Halbleitertechnologie: Grundlagen mikroelektronischer Integrationstechnik* (Springer-Verlag, 2018).

[43] T. Hoshino, M. Hata, S. Neya, Y. Nishioka, T. Watanabe, K. Tatsumura, and I. Ohdomari, Jpn. J. Appl. Phys. **42**, 3560 (2003).

[44] T. Ohmi, Y. Nakagawa, M. Nakamura, A. Ohki, and T. Koyama, J. Vac. Sci. Technol. B Nanotechnol. Microelectron. **14**, 2505 (1996).

[45] J. Sun, H. Tang, C. Wang, Z. Han, and S. Li, Steel Res. Int. **93**, 2100450 (2022).

[46] D. Wang, M. Hu, D. Jiang, Y. Fu, Q. Wang, J. Yang, J. Sun, and L. Weng, Vacuum **143**, 329 (2017).

[47] B. Bakhit, S. Dorri, A. Kooijman, Z. Wu, J. Lu, J. Rosen, J. M. C. Mol, L. Hultman, I. Petrov, J. E. Greene, and G. Greczynski, Vacuum **185**, 109990 (2021).

[48] W. Zhang, J. Zhang, H. Wang, W. Lou, and X. Liu, Coat. World **8**, 195 (2018).

[49] P. J. R. Smith, M. P. Taylor, H. E. Evans, N. E. Murray, C. McMillan, and J. Cherrington, Oxid. Met. **81**, 47 (2014).

[50] W. J. Quadakkers, V. Shemet, D. Sebold, R. Anton, E. Wessel, and L. Singheiser, Surf. Coat. Technol. **199**, 77 (2005).

[51] D. J. Young, in *High Temperature Oxidation and Corrosion of Metals (Second Edition)*, edited by D. J. Young (Elsevier, 2016) pp. 85–144.

[52] D. Caplan and G. I. Sproule, Oxid. Met. **9**, 459 (1975).

[53] H. Schneider, J. Schreuer, and B. Hildmann, J. Eur. Ceram. Soc. **28**, 329 (2008).

[54] R. Roy, D. Das, and P. K. Rout, Engineered Science **18 (June 2022)**, 20 (2021).

[55] L. K. S. Lima, K. R. Silva, R. R. Menezes, L. N. L. Santana, and H. L. Lira, Cerâmica **68**, 126 (2022).

[56] H. Schneider and S. Komarneni, en*Mullite* (John Wiley & Sons, 2006).

[57] R. X. Fischer, A. Gaede-Köhler, J. Birkenstock, and H. Schneider, Int. J. Mater. Res. **103**, 402 (2012).

[58] H.-I. Seo, D. Kim, and K. S. Lee, Coat. World **9**, 585 (2019).

[59] C. A. Botero, E. Jimenez-Piqué, R. Martín, T. Kulkarni, V. K. Sarin, and L. Llanes, International Journal of Refractory Metals and Hard Materials **49**, 383 (2015).

[60] K. N. Lee, D. S. Fox, J. I. Eldridge, D. Zhu, R. C. Robinson, N. P. Bansal, and R. A. Miller, J. Am. Ceram. Soc. **86**, 1299 (2003).

[61] P. Hou, S. N. Basu, and V. K. Sarin, International Journal of Refractory Metals and Hard Materials **19**, 467 (2001).

[62] M. L. Auger and V. K. Sarin, Surf. Coat. Technol. **94-95**, 46 (1997).

[63] J. A. Haynes, M. J. Lance, K. M. Cooley, M. K. Ferber, R. A. Lowden, and D. P. Stinton, J. Am. Ceram. Soc. **83**, 657 (2004).

[64] P. Ramaswamy, S. Seetharamu, K. J. Rao, and K. B. R. Varma, J. Therm. Spray Technol. **7**, 497 (1998).

[65] G. Di Girolamo, C. Blasi, L. Pilloni, and M. Schioppa, Ceram. Int. **36**, 1389 (2010).

[66] C. Cano, E. Garcia, A. L. Fernandes, M. I. Osendi, and P. Miranzo, J. Eur. Ceram. Soc. **28**, 2191 (2008).

[67] C. Ma, H. Li, H. Wu, Q. Fu, C. Sun, X. Shi, Y. Zhang, Z. Zhang, J. Tao, and Z. Han, J. Mater. Sci. Technol. **29**, 29 (2013).

[68] S. K. Ramasesha, P. S. Tantri, and A. K. Bhattacharya, Met. Mater. Process. **12**, 181 (2000).

[69] X. Chen and C. Liang, Catalysis Science & Technology **9**, 4785 (2019).

[70] A. Bahr, S. Richter, R. Hahn, T. Wojcik, M. Podsednik, A. Limbeck, J. Ramm, O. Hunold, S. Kolozsvári, and H. Riedl, J. Alloys Compd. **931**, 167532 (2023).

[71] G. Sauthoff, en*Intermetallics* (Wiley, 1995).

[72] L. Zhang, Z. Tong, R. He, C. Xie, X. Bai, Y. Yang, and D. Fang, J. Alloys Compd. **780**, 156 (2019).

[73] M. C. Kushan, Y. Uzunonat, S. C. Uzgur, and F. Diltemiz, Recent Advances in Aircraft Technology (2012).

[74] S. Chevalier, F. Bernard, E. Gaffet, S. Paris, Z. A. Munir, and J. P. Larpin, in *Materials Science Forum*, Vol. 461 (2004) pp. 439–446.

[75] X. Y. Wang, I. T. H. Chang, and M. Aindow, Intermetallics **10**, 829 (2002).

[76] P. S. Frankwicz and J. H. Perepezko, Materials Science and Engineering: A **246**, 199 (1998).

[77] J. J. Petrovic, MRS Bull. **18**, 35 (1993).

[78] X. Fei, Y. Niu, H. Ji, L. Huang, and X. Zheng, Ceram. Int. **37**, 813 (2011).

[79] J. Sun, T. Li, and G.-P. Zhang, Corros. Sci. **155**, 146 (2019).

[80] E. K. Nyutu, M. A. Kmetz, and S. L. Suib, Surf. Coat. Technol. **200**, 3980 (2006).

[81] Y. Zhang, J. Zhao, J. Li, J. Lei, and X. Cheng, Ceram. Int. **45**, 5588 (2019).

[82] T. C. Chou and T. G. Nieh, "Phase transformation and mechanical properties of thin MoSi2 films produced by sputter deposition," (1992).

[83] M. Magnuson, L. Hultman, and H. Högberg, Vacuum **196**, 110567 (2022).

[84] W. G. Fahrenholtz, E. J. Wuchina, W. E. Lee, and Y. Zhou, en*Ultra-High Temperature Ceramics: Materials for Extreme Environment Applications* (John Wiley & Sons, 2014).

[85] S. Chen, X. Qiu, B. Zhang, J. Xu, F. Zhong, B. Zhu, Y. Zhang, J. Ou-Yang, and X. Yang, J. Alloys Compd. **886**, 161143 (2021).

[86] B. R. Golla, A. Mukhopadhyay, B. Basu, and S. K. Thimmappa, Prog. Mater Sci. **111**, 100651 (2020).

[87] V. Moraes, H. Riedl, C. Fuger, P. Polcik, H. Bolvardi, D. Holec, and P. H. Mayrhofer, Sci. Rep. **8**, 9288 (2018).

[88] Y. Zhou, J. Wang, Z. Li, X. Zhan, and J. Wang, in *Ultra-High Temperature Ceramics* (John Wiley & Sons, Inc, Hoboken, NJ, 2014) pp. 60–82.

[89] C. Fuger, R. Hahn, L. Zauner, T. Wojcik, M. Weiss, A. Limbeck, O. Hunold, P. Polcik, and H. Riedl, Materials Research Letters **10**, 70 (2022).

[90] T. A. Parthasarathy, R. A. Rapp, M. Opeka, and R. J. Kerans, Acta Mater. **55**, 5999 (2007).

[91] X. Cai, S. Ding, K. Wen, L. Xu, H. Xue, S. Xin, and T. Shen, J. Eur. Ceram. Soc. **41**, 5100 (2021).

[92] S. Dorri, J. Palisaitis, G. Greczynski, I. Petrov, J. Birch, L. Hultman, and B. Bakhit, Corros. Sci. **206**, 110493 (2022).

[93] T. Glechner, H. G. Oemer, T. Wojcik, M. Weiss, A. Limbeck, J. Ramm, P. Polcik, and H. Riedl, Surf. Coat. Technol. **434**, 128178 (2022).

[94] S. Nagakura and S. Oketani, Transactions of the Iron and Steel Institute of Japan **8**, 265 (1968).

[95] W. S. Williams, Prog. Solid State Chem. **6**, 57 (1971).

[96] L. B. Freund and S. Suresh, en*Thin Film Materials: Stress, Defect Formation and Surface Evolution* (Cambridge University Press, 2003).

[97] D. M. Mattox, en*Handbook of Physical Vapor Deposition (PVD) Processing* (William Andrew, 2010).

[98] P. M. Martin, en*Handbook of Deposition Technologies for Films and Coatings: Science, Applications and Technology* (William Andrew, 2009).

[99] L. Zauner, Diploma thesis, TU Wien (2019).

[100] Gencoa Ltd, “The basic theory of magnetron sputtering,” `https://www.gencoa.com/the-basic-theory-of-magnetron-sputtering` (2024), accessed: 2024-9-8.

[101] J. Neidhardt, S. Mráz, J. M. Schneider, E. Strub, W. Bohne, B. Liedke, W. Möller, and C. Mitterer, J. Appl. Phys. **104**, 063304 (2008).

[102] C. Fuger, R. Hahn, A. Hirle, P. Kutrowatz, M. Weiss, A. Limbeck, O. Hunold, P. Polcik, and H. Riedl, Surf. Coat. Technol. **446**, 128806 (2022).

[103] K. Sarakinos, J. Alami, and S. Konstantinidis, Surf. Coat. Technol. **204**, 1661 (2010).

[104] A. Anders, Thin Solid Films **518**, 4087 (2010).

[105] J. T. Gudmundsson, N. Brenning, D. Lundin, and U. Helmersson, J. Vac. Sci. Technol. A **30**, 030801 (2012).

[106] U. Helmersson, M. Lattemann, J. Bohlmark, A. P. Ehiasarian, and J. T. Gudmundsson, Thin Solid Films **513**, 1 (2006).

[107] M. B. Uday, M. N. Ahmad-Fauzi, A. M. Noor, and S. Rajoo, in *Joining Technologies* (InTech, 2016).

[108] M. Nakahashi, Weld. Int. **10**, 765 (1996).

[109] Y. Zhang, D. Feng, Z.-Y. He, and X.-C. Chen, J. Iron Steel Res. Int. **13**, 1 (2006).

[110] American Elements, "Melting point of common metals, alloys, & other materials," `https://www.americanelements.com/meltingpoint.html` (2024), accessed: 2024-12-30.

[111] American Elements, "Silicon carbide," `https://www.americanelements.com/silicon-carbide-409-21-2#:~:text=Silicon%20Carbide%20is%20a%20ceramic,nanopowder%20forms%20may%20be%20considered.` (2024), accessed: 2024-12-30.

[112] J. Xia, T. Ding, W. Ren, X. Zhao, K. Ren, and Y. Wang, J. Eur. Ceram. Soc. **43**, 5061 (2023).

[113] K. Kohama and K. Ito, Mater. Des. **110**, 888 (2016).

[114] T. Okuni, Y. Miyamoto, H. Abe, and M. Naito, Ceram. Int. **40**, 1359 (2014).

[115] A. Nisar, T. Dolmetsch, T. Paul, C. Zhang, B. Boesl, and A. Agarwal, J. Am. Ceram. Soc. **104**, 2483 (2021).

[116] L.-L. Zhu, M.-M. Dai, X. Xu, C.-C. Zhao, G.-X. Zhang, Y.-J. Jian, W.-M. Guo, and H.-T. Lin, Ceram. Int. **47**, 30838 (2021).

[117] H. U. Kessel, J. Hennicke, J. Schmidt, T. Weißgräber, B. F. Kieback, M. Herrmann, and J. Räthel, *Feldaktives Sintern FAST - ein neues Verfahren zur Herstellung metallischer und keramischer Sinterwerkstoffe*, edited by H. Kolaska (Heimdall Verlag Witten, Pulvermetallurgie in Wissenschaft und Praxis 22 - Pulvermetallurgie - Kompetenz und Perspektive, 2006).

[118] Y.-H. Seong, C. Baek, J.-H. Kim, J. H. Kong, D. S. Kim, S.-H. Lee, and D. K. Kim, Ceram. Int. **44**, 8505 (2018).

[119] A. Bahr, T. Glechner, A. Grimmer, T. Wojcik, R. Hahn, P. Kutrowatz, M. Podsednik, A. Limbeck, M. Heller, J. Ramm, O. Hunold, S. Kolozsvári, P. Polcik, E. Ntemou, D. Primetzhofer, P. Felfer, and H. Riedl, Surf. Coat. Technol. **468**, 129733 (2023).

[120] A. Lange and R. Braun, Corros. Sci. **84**, 74 (2014).

[121] G. Greczynski, J. Lu, J. Jensen, S. Bolz, W. Kölker, C. Schiffers, O. Lemmer, J. E. Greene, and L. Hultman, Surf. Coat. Technol. **257**, 15 (2014).

[122] C. Hu, S. Lin, M. Podsednik, S. Mráz, T. Wojcik, A. Limbeck, N. Koutná, and P. H. Mayrhofer, Mater. Res. Lett. **12**, 561 (2024).

[123] N. Nedfors, D. Primetzhofer, L. Wang, J. Lu, L. Hultman, and U. Jansson, Surf. Coat. Technol. **266**, 167 (2015).

[124] Oerlikon-Balzers, "PACVD plasma-assisted chemical vapour deposition," `https://www.oerlikon.com/balzers/global/en/portfolio/surface-technologies/pacvd/` (2024), accessed: 2024-8-13.

[125] Oerlikon-Balzers, "Enhanced sputtering," `https://www.oerlikon.com/balzers/us/en/portfolio/surface-technologies/pvd-based-processes/enhanced-sputtering/` (2024), accessed: 2024-8-13.

[126] D. Chen, X. Maeder, B. Widrig, J. Ramm, and D. De Wet, Vacuum **213**, 112098 (2023).

[127] M. J. Presby, J. L. Stokes, and B. J. Harder, J. Am. Ceram. Soc. **107**, 1776 (2024).

[128] P. Ström and D. Primetzhofer, J. Instrum. **17**, P04011 (2022).

[129] G. Gauglitz and D. S. Moore, en*Handbook of spectroscopy: Second, enlarged edition*, 2nd ed., edited by G. Gauglitz, T. Vo-Dinh, and D. S. Moore (Wiley-VCH Verlag, Weinheim, Germany, 2012).

[130] G. Friedbacher and H. Bubert, en*Surface and Thin Film Analysis: A Compendium of Principles, Instrumentation, and Applications* (John Wiley & Sons, 2011).

Chapter 6

Scientific Contributions

This chapter presents the publications resulting from this work, each accompanied by a brief description. The publications are divided into three sections. The first section focuses on a disilicide-based material and its exceptional oxidation resistance. The second section investigates layered coating systems (architectural coatings), and the third section examines alloying approaches, both sections designed to improve oxidation resistance of oxidation prone materials (transition metal borides and carbides). In addition, the chapter includes a co-authored peer-reviewed publication, a patent, the list of students supervised and a summary of international conferences attended.

6.1 Silicides as stand-alone protective coating materials

Publication I

Tuning microstructural and oxidative characteristics of direct current- and high-power pulsed magnetron sputtered $MoSi_2$-based thin films

S. Richter, A. Bahr, P. Kutrowatz, T. Wojcik, S. Kolozsvári, P. Polcik, C. Jerg, J. Ramm, H. Riedl, *J. Vac. Sci. Technol. A* 42, 053407 (2024).

This study investigates the microstructural evolution and oxidation behavior of $MoSi_2$-based thin films deposited by direct current magnetron sputtering (DCMS) and high-power pulsed magnetron sputtering (HPPMS). This research explores how deposition parameters such as substrate temperature and plasma ionization affect the phase composition, microstructure, mechanical properties and oxidation resistance of the thin films, especially under extreme conditions up to 1500 °C. In general, $MoSi_2$ is well known for its high temperature stability and excellent high-temperature oxidation resistance, mainly due to the formation of a protective silica (SiO_2) scale. However, at lower temperatures, a so-called pesting phenomenon, characterized by mixed MoO_x and SiO_x oxide growth, poses a challenge.

Using DCMS, amorphous thin films could be synthesized at a substrate temperature of 200 °C, with a transition to hexagonal $MoSi_2$ as the substrate temperature increases to 300-400 °C. At temperatures above 500 °C, dual-phase structures consisting of hexagonal $MoSi_2$ and tetragonal Mo_5Si_3 are formed. HPPMS, on the other hand, provides better control over phase formation and allows the deposition of very dense thin films. In detail, coatings deposited at 1000 Hz exhibit a dense microstructure with a hexagonal $MoSi_2$ phase. Mechanical testing (nanoindentation) also showed differences between the two sputtering modes. The highest hardness of 22.8 GPa was measured in the HPPMS thin films deposited at 1000 Hz, which correlates with their fine-grained, dense morphology. Young's modulus values for the crystalline films consistently ranged from 360 to 400 GPa.

Long-term oxidation tests were carried out at 600 °C, 850 °C, and 1200 °C for up to 100 h. At 600 °C, pesting-related phenomena such as small cracks and porous oxide scales were observed. At 850 °C, the oxide scale consisted of amorphous SiO_x with embedded MoO_x clusters. At 1200 °C, all coatings showed excellent oxidation resistance and protection due to the formation of a dense SiO_2 scale. Among the coatings tested, the dense HPPMS thin film grown at 1000 Hz exhibited the lowest scale thickness of approximately 650 nm. The HPPMS coating grown at 500 Hz was further tested up to 1500 °C for 1 h. Even with a Si substoichiometry (Si/Mo ratio of 1.86), the coating showed excellent oxidation resistance under these extreme conditions. This highlights the potential of HPPMS to grow dense, single-phase hexagonal $MoSi_2$ coatings with exceptional oxidation resistance and mechanical properties. In addition, the results demonstrate that $MoSi_2$-based materials are suitable for applications in ultra-high temperature environments.

6.2 Architectural concepts for enhancing oxidation resistance

Publication II

Reactively grown Al/Si-based top coatings protecting TM-diborides (TM = W, Ti, Hf) against high-temperature oxidation

S. Richter, T. Glechner, T. Wojcik, B. Widrig, S. Kolozsvári, P. Polcik, O. Hunold, L. Zauner, J. Ramm, H. Riedl, *Surface & Coatings Technology* 476 (2024) 130191.

This study investigates architectural coating concepts to improve the high temperature oxidation resistance of transition metal diboride (TMB_2, TM = W, Ti, Hf) thin films. The poor oxidation resistance of TMB_2, caused by volatilization of B_2O_3 and the formation of porous transition metal oxides, is addressed by the application of reactively grown Al-Si-N, Al-Si-O, and Si-O protective top coatings. These topcoats are applied to sputter deposited $WB_{1.9}$, $TiB_{2.7}$, $HfB_{2.4}$ thin films and designed to suppress oxidation while maintaining superior mechanical properties of TMB_2 under extreme conditions. The investigated coating architecture includes a Si interlayer for the oxide-based top coatings to enhance adhesion and prevent in-situ oxidation during deposition. Structural characterization of the as deposited thin films revealed a α-TMB_2 phase formation for the diboride base layer and amorphous Al- and Si-containing top layer, with the Si interlayer exhibiting a partial crystalline structure. The study analyzed the oxidation performance of the coatings through dynamic oxidation tests up to 1400 °C and isothermal oxidation tests at 1200 °C up to 30 h.

Dynamic oxidation tests showed that Al-Si-N top coatings provided limited protection, with oxidation resistance decreasing above 1000 °C due to accelerated mass increase/oxide growth. Contrary, Al-Si-O and Si-O top coatings showed excellent performance with minimal mass changes and the formation of a (stable) protective scale. Isothermal oxidation experiments at 1200 °C revealed significant differences between the TMB_2 systems: The $WB_{1.9}$ thin films experienced delamination due to poor film adhesion. However, $TiB_{2.7}$ and $HfB_{2.4}$ retained their layered structures with excellent adhesion and stability against the high temperature oxidation conditions. Detailed microstructural TEM analysis of the $HfB_{2.4}$ sample showed that the Al-Si-O layer formed a porous Al_2O_3-SiO_2 mullite structure, while the Si-O top layer remained dense and amorphous with embedded SiO_2 crystallites. Notably, the Si-O layer inhibited the recrystallization of the $HfB_{2.4}$ base layer, maintaining its fine columnar morphology. These results demonstrate that Al-Si-O and Si-O protective top coatings, especially with a Si interlayer, provide outstanding high-temperature oxidation resistance for oxidation prone TMB_2 thin films. Both Al-Si-O and Si-O top coatings are promising candidates for extending the operating limits of TMB_2 in extreme environments such as aerospace and energy applications.

6.3 Alloying approach to enhance oxidation properties

Publication III

High-throughput phase exploration of ternary transition metal carbide TM-X-C (X=Al/Si) thin films

S. Richter, C. Gutschka, D. Danner, R. Hahn, T. Wojcik, E. Ntemou, C. Jerg, J. Ramm, P. Polcik, S. Kolozsvári, D. Primetzhofer, H. Riedl, under review at *Acta Materialia* A-24-4225R1 (2025).

Transition metal carbides (TMCs) are of great interest due to their high thermal stability, exceptional hardness and resistance to mechanical wear, making them crucial for extreme environments such as aerospace and high-performance tooling applications. However, their sensitivity to oxidation requires research into solutions to overcome this problem. Therefore, the motivation was to study Al and Si alloyed ternary TM-X-C (TM = Ti, Zr, Hf, Ta, W and X = Al, Si) systems. In this study, as a first step, the phase formation is systematically investigated by combining density functional theory (DFT) calculations with X-ray diffraction (XRD) analysis of magnetron sputtered thin films. In addition, the mechanical properties are investigated by nanoindentation.

Theoretical predictions were used to determine trends and solubility limits of metastable Al and Si alloying in face-centered cubic (fcc) TM-X-C (solid solutions) based on the energy of formation and lattice parameter/cubic cell symmetry. DFT calculations suggested that Si preferentially occupies both transition metal (TM) and carbon sites, while Al primarily substitutes sites on the TM sublattice. Experimentally, over 260 different chemical compositions were synthesized by combinatorial sputtering. Structural analysis confirmed the formation of single-phase fcc TM-X-C solid solutions up to 25-30 at.% Al/Si. Beyond this threshold, amorphization or the formation of second (metallic) phases was observed. In contrast, DFT predictions for W-X-C did not emphasize the formation of fcc solid solutions (hexagonal W_2C is the stable ground state structure). XRD analysis also showed that the W-X-C systems form a nanocrystalline – even amorphous – structure. Mechanical testing by nanoindentation revealed a strong correlation between phase stability and mechanical properties. The highest hardness values of 30 to 40 GPa were observed for fcc-structured TM-X-C thin films, especially for Ta-X-C and Hf-X-C systems. However, when the Al or Si content exceeded the solubility limits, the hardness decreased significantly due to a more metallic character of the thin films or amorphous coating states. The Young's modulus followed a similar trend, with values around 500 GPa for single-phase Hf-X-C and Ta-X-C coatings but decreased for dual-/multi-phase or amorphous thin films. These results from a high-throughput phase screening provide a systematic mapping of physical vapor deposited (PVD) ternary carbide phase formation. Using this information, further research is being conducted to evaluate their oxidation behavior to further expand their application potential in high temperature and extreme environments.

Publication IV

Exploring the oxidation characteristics of binary and ternary transition metal carbide coatings

S. Richter, P. Kutrowatz, T. Wojcik, S. Kolozsvári, P. Polcik, C. Jerg, J. Ramm, H. Riedl, *Plansee Seminar* Conference Proceeding (2025).

Transition metal carbides (TMCs) are widely recognized for their ultra-high temperature stability and exceptional mechanical properties, making them critical for aerospace, energy and advanced tooling applications. However, their poor oxidation resistance remains a major drawback. This study systematically investigates the oxidation behavior of binary TMC and ternary TM-X-C thin films, where TM = Ti, Zr, Hf, Ta, W and X = Al, Si, serving as a strong oxide-forming element.

Dynamic thermogravimetric analysis (TGA) up to 1400 °C revealed that most binary TMC oxidized below 600 °C. To improve the oxidation resistance, Al and Si alloyed TM-X-C coatings were synthesized by a combinatorial deposition approach (stationary co-sputtering of TMC and Al or Si targets). Subsequently, the oxidation behavior of the ternary systems was investigated by performing isothermal oxidation tests at 750 °C for 1 h. The results show that Al and Si alloying significantly improves the oxidation resistance: For Al alloyed thin films, Ti-Al-C and Ta-Al-C emerged as the most promising systems, forming protective oxide scales < 750 nm with alloying contents above 25 at.%. For the Si alloyed coatings, Ti-Si-C thin films withstood the annealing conditions as well as the high alloyed dual-phased $Zr_{0.22}Si_{0.46}C_{0.32}$ sample. In contrast, Ta-Si-C and W-Al/Si-C coatings failed at 750 °C (spallation of the coatings), highlighting the different oxidation performance of the different transition metal systems. Transmission electron microscopy (TEM) and electron energy loss spectroscopy (EELS) analyses of $Ti_{0.26}Al_{0.32}C_{0.42}$ and $Ti_{0.29}Si_{0.26}C_{0.45}$ provided further insight into the oxidation mechanisms. A two-layer scale structure was observed, consisting of a metal oxycarbide ($MC_{1-x}O_x$) at the interface to the nonporous, unoxidized Ti-X-C film, followed by a Ti-(Al/Si)-oxide based scale. While both Al and Si effectively inhibited complete oxidation of the thin films, the Al-alloyed coatings exhibited lower oxygen inward diffusion, suggesting a stronger protective effect.

Publication V

Assessing the effectiveness of strong oxide formers (Cr, Si, Al) in diboride thin films

S. Richter, A. Bahr, T. Wojcik, E. Ntemou, S. Kolozsvári, P. Polcik, J. Ramm, D. Primetzhofer, H. Riedl, Manuscript draft for *Materials Research Letters* (2025).

Transition metal diborides (TMB_2), such as CrB_2, are widely used for high temperature applications due to their exceptional hardness, wear resistance and thermal stability. However, their oxidation resistance remains a limiting factor, especially for thin films in temperature regions above 500 to 600 °C, where B_2O_3 gets volatile and porous (transition metal) based oxide scales are formed leading to accelerated degradation. This study systematically investigates the effect of strong oxide formers (Si, Al) in CrB_2-based thin films to enhance the oxidation resistance. The coatings were synthesized using a combinatorial magnetron sputtering approach to deposit ternary (Cr-Al-B, Cr-Si-B) and quaternary (Cr-Al-Si-B) coatings. X-ray diffraction (XRD) analysis confirmed that all coatings crystallized predominantly in the AlB_2 prototype structure, with Si solubility limits of about 4 at.%. At higher Si alloy contents, secondary $CrSi_2$ phases were observed. Thermogravimetric analysis (TGA) in synthetic air up to 1400 °C showed that CrB_2 films alloyed with $>$ 20 at.% Al exhibited an improved oxidation onset temperature of approximately 800 °C (compared to around 600 °C for almost unalloyed CrB_2 thin films, e.g. $Cr_{0.52}Al_{0.01}B_{0.47}$ and $Cr_{0.48}Si_{0.01}B_{0.51}$). In contrast, Cr-Si-B coatings with $>$ 11 at.% Si exhibited exceptional oxidation resistance up to 1300 °C, due to the formation of a dense silica (SiO_2)-based protective scale. The quaternary Cr-Al-Si-B ($Cr_{0.29}Al_{0.18}Si_{0.10}B_{0.43}$) also showed outstanding resistance during dynamic oxidation testing up to 1300 °C (almost stable mass signal over the entire temperature range tested). Isothermal oxidation at 1200 °C for 1 h provided further insight into scale formation: Transmission electron microscopy (TEM) and electron energy loss spectroscopy (EELS) analyses of $Cr_{0.35}Si_{0.16}B_{0.49}$ and $Cr_{0.27}Al_{0.22}Si_{0.09}B_{0.42}$ revealed a layered scale structure, with a Si-O scale forming directly above the diboride film, followed by Cr-O and Al-O in the quaternary systems. Notably, Cr-Si-B exhibited localized Si clustering, but the coating remained structurally intact. Cr-Al-Si-B showed a reduced recrystallization compared to Cr-Si-B. At higher temperatures (1300 and 1400 °C), Cr-Al-Si-B experienced spallation, while Cr-Si-B withstood 1300 °C before complete oxidation at 1400 °C. In summary, Si acts as a perfect alloying element in terms of enhancing oxidation resistance of TMB_2 thin films, outperforming Al. Furthermore, small additions (approx. 8 at.%) in Cr-Al-Si-B coatings promoted additional Al_2O_3 scale formation, highlighting the key effect of Si in diborides. These findings provide a basis for designing oxidation resistant diboride coatings. Especially Al-alloying could be beneficial when considering environments with water vapor.

6.4 Further peer-reviewed publications

Oxidation behaviour and mechanical properties of sputter-deposited $TMSi_2$ coatings (TM = Mo, Ta, Nb), A. Bahr, **S. Richter**, R. Hahn, T. Wojcik, M. Podsednik, A. Limbeck, J. Ramm, O. Hunold, S. Kolozsvári, H. Riedl, *J. Alloys Compd.* 931 (2023) 167532.

6.5 Patents

Si- and Al/Si-containing top coatings
PCT/EP2024/063821, filed: 17.5.2024
S. Richter, L. Zauner, H. Riedl, B. Widrig, J. Ramm

6.6 Supervised students

Norma Salvadores Farran
Oxidation behavior and mechanical properties of Al alloyed HfC thin films
Master's student (Intern)
Finished 09/2022

Andrew Rofaiel
Oxidation behavior and mechanical properties of Si alloyed HfC thin films
Bachelor thesis
Finished 09/2023

David Danner
Exploration of Hf-Al-C thin films for high-temperature applications
Bachelor thesis
Finished 09/2023

Tobias Reining
WC-based thin films synthesized by PVD techniques
Master's student (project work)
Finished 02/2024

Nikolaus Tonn
Exploration of ternary and quaternary Cr-Al-Si-B thin films
Bachelor thesis
Finished 09/2024

David Danner
Mechanical properties and oxidation resistance of $MoSi_2$ *alloyed TMC thin films (TM = Ti, Zr, Hf, Ta, W)*
Master thesis
Ongoing, expected graduation 09/2025

6.7 Participation at international conferences

ÖGV Seminar 2022
Leoben, Austria, 11.07.2022
Mechanical properties and high-temperature behavior of non-reactive synthesized $MoSi_2$ *thin films by PVD techniques*
S. Richter, A. Bahr, T. Wojcik, J. Ramm, O. Hunold, P. Polcik, S. Kolozsvári, H. Riedl

Junior Euromat 2022
Coimbra, Portugal, 19.-22.07.2022
Phase formation and oxidation resistance of physical vapor deposited $MoSi_2$ *thin films*
S. Richter, A. Bahr, T. Wojcik, J. Ramm, O. Hunold, P. Polcik, S. Kolozsvári, H. Riedl

PSE 2022
Erfurt, Germany, 12.-15.09.2022
Mechanical properties and oxidation resistance of sputter deposited $MoSi_2$ *thin films*
S. Richter, A. Bahr, T. Wojcik, J. Ramm, O. Hunold, P. Polcik, S. Kolozsvári, H. Riedl

Heart of Europe – Thin Films Workshop 2023
Bratislava, Slovakia, 13.-14.03.2023
Mechanical properties and oxidation resistance of sputter deposited $MoSi_2$ *thin films*
S. Richter, A. Bahr, T. Wojcik, J. Ramm, O. Hunold, P. Polcik, S. Kolozsvári, H. Riedl

ICMCTF 2023
San Diego, USA, 21.-26.05.2023
The architectural design of high-temperature protective coatings: Improving the oxidation resistance of TMB_2 $(TM = Hf, Ti, W)$ *thin films*
S. Richter, T. Glechner, L. Zauner, T. Wojcik, B. Widrig, O. Hunold, S. Kolozsvári, P. Polcik, J. Ramm, H. Riedl

High-temperature stability and mechanical properties of non-reactive PVD-synthesized $MoSi_2$ *coatings*
S. Richter, A. Bahr, T. Wojcik, O. Hunold, S. Kolozsvári, P. Polcik, J. Ramm, H. Riedl

ÖGV Seminar 2023

Vienna, Austria, 13.06.2023

Oxidation-prone TMB_2 (TM = Hf, Ti, W) thin films protected with Al/Si-based top coatings

S. Richter, T. Glechner, L. Zauner, T. Wojcik, B. Widrig, O. Hunold, S. Kolozsvári, P. Polcik, J. Ramm, H. Riedl

IUVSTA Workshop 2023

Seggau, Austria, 15.-19.10.2023

Analysing the pore formation in ternary and quaternary diborides during high-temperature oxidation

S. Richter, A. Bahr, L. Zauner, T. Wojcik, S. Kolozsvári, P. Polcik, O. Hunold, J. Ramm, H. Riedl

ICACC 2024

Daytona, USA, 28.01.-02.02.2024

Architectural coating design to improve the oxidation resistance of TMB_2 (TM = Hf, Ti, W) thin films at harsh conditions

S. Richter, T. Glechner, L. Zauner, T. Wojcik, B. Widrig, O. Hunold, S. Kolozsvári, P. Polcik, J. Ramm, H. Riedl

ICMCTF 2024

San Diego, USA, 19.-24.05.2024

Structural evolution and oxidation resistance of Al/Si alloyed transition metal carbide thin films

S. Richter, E. Ntemou, D. Primetzhofer, T. Wojcik, O. Hunold, S. Kolozsvári, P. Polcik, J. Ramm, H. Riedl

Unravelling diffusion processes and morphology changes of ternary and quaternary diborides during high-temperature oxidation

S. Richter, A. Bahr, T. Glechner, T. Wojcik, S. Kolozsvári, P. Polcik, O. Hunold, J. Ramm, D. Primetzhofer, P. Felfer, H. Riedl

PSE 2024

Erfurt, Germany, 02.-05.09.2024

Exploring the phase space and oxidation mechanisms of TM-X-C thin films

S. Richter, D. Danner, R. Hahn, E. Ntemou, D. Primetzhofer, T. Wojcik, S. Kolozsvári, P. Polcik, C. Jerg, J. Ramm, H. Riedl

ICACC 2025

Daytona, USA, 26.-31.01.2025

Phase exploration of TM-X-C (X = Al, Si) thin film materials: Correlation between theory and experiments

S. Richter, C. Gutschka, R. Hahn, T. Wojcik, E. Ntemou, D. Primetzhofer, S. Kolozsvári, P. Polcik, C. Jerg, J. Ramm, H. Riedl

Chapter 7

Concluding Remarks

The development of protective coatings for high temperature applications is essential to improve the durability and performance of components exposed to extreme (oxidative) environments. High-temperature oxidation can cause severe material degradation, affecting the functionality and lifetime of critical components, particular in aerospace applications, automotive or tooling industries. To address this challenge, this thesis investigates novel thin film materials, alloying strategies, and coating architectures designed to improve oxidation resistance.

The first part, **Publication I**, focuses on $MoSi_2$-based thin films, which belong to the disilicide family and are known for their excellent high temperature oxidation resistance (even above 1600 °C) and suitable mechanical properties. However, at lower temperatures (around 600 °C) $MoSi_2$ suffers from poor oxidation resistance due to the pesting phenomenon, where mixed oxides (e.g., MoO_x and SiO_x) grow simultaneously, resulting in internal stresses due to the significant volume expansion and hence to cracking and porous scale formation. Despite this limitation, $MoSi_2$ remains a promising stand-alone protective coating material for high temperature applications. This study investigates how deposition parameters – such as substrate temperature and ionization – affect the phase formation, microstructure and oxidation resistance of $MoSi_2$ thin films using DCMS and HPPMS. The results prove that amorphous coating states are formed at a substrate temperature of 200 °C, while dense hexagonal $MoSi_2$ structures are formed between 300 and 400 °C as well as with HPPMS at 1000 Hz (2.5 to 10 % duty cycle). At higher temperatures (500 to 600 °C) and enhanced plasma states (500 Hz, 2.5 to 10 % duty cycle), dual phase coatings consisting of hexagonal $MoSi_2$ and tetragonal Mo_5Si_3 with underdense grain boundary regions are observed. In particular, the application of HPPMS at 1000 Hz significantly increases the film density, leading to highest hardness values (22.8 GPa). The oxidation behavior was studied from 600 to 1500 °C, revealing minor cracks at 600 °C and a combination of amorphous SiO_x and MoO_x clusters at 850 °C, indicating some pesting. Above 1200 °C, especially films with a predominant hexagonal $MoSi_2$ phase constitution and a highly dense microstructure demonstrated excellent oxidation resistance with thin SiO_2 scales (650 nm after 100 h at 1200 °C). Even at high temperatures up to 1500 °C, effective protective mechanisms were observed for short-term oxidation tests with 30 min. In conclusion, a predominant hexagonal $MoSi_2$ structure and a highly dense morphology are the keys to excellent oxidation protection.

The second part, **Publication II**, investigates architectural coating concepts, specifically Al-Si-N, Al-Si-O, and Si-O protective top coatings for oxidation prone transition metal diborides (TM = W, Ti, Hf). These reactively (plasma enhanced) cathodic arc evaporated top coatings were applied to sputter-deposited diboride thin films, with a Si interlayer introduced to prevent in-situ oxidation of the diborides during the growth of the oxide-based top coatings and to improve film adhesion. While Al-Si-N coatings undergo accelerated oxidation at temperatures above 800 to 1000 °C, TGA highlighted that Si-O and Al-Si-O coatings significantly improved the oxidation resistance of the underlying diborides up to 1400 °C. Long-term oxidation tests at 1200 °C for up to 30 h further confirmed the resilience of Si/Al-Si-O and Si/Si-O top coatings, especially for the $TiB_{2.7}$ and $HfB_{2.4}$ samples. TEM analysis showed that the Al-Si-O protective layer formed a porous Al_2O_3-SiO_2 mullite structure and the Si-O layer remained dense, where SiO_2 crystallites are embedded in an amorphous Si-O matrix. Nevertheless, both top coating approaches (Si/Al-Si-O and Si/Si-O) acted as an excellent oxygen diffusion barrier, protecting the underlying TMB_2 thin film.

The third section explores alloying strategies to improve the oxidation resistance of transition metal carbides and borides. **Publications III and IV** use a high-throughput combinatorial screening approach to effectively investigate a broad compositional range of ternary transition metal carbide thin films, where TM = Ti, Zr, Hf, Ta, W and X = Al, Si. As a first step, **Publication III** explores the phase formation and mechanical properties of more than 260 different chemical compositions. Density functional theory (DFT) calculations, together with structural analysis by X-ray diffraction (XRD), confirm that Al and Si can be alloyed up to about 25 to 30 at.% in fcc TM-X-C thin films. However, in W-X-C films, a nanocomposite or even amorphous structure is predominant. At higher Al and Si concentrations, additional metallic phases are prevalent or the coatings transition to an XRD amorphous state. Nanoindentation shows a strong correlation between phase formation and mechanical properties, with fcc-structured TM-X-C thin films achieving the highest hardness values of 30 to 40 GPa. Reaching the transition zone between single phased fcc-TM-X-C solid solutions and dual phased or amorphous states, the hardness decreases to about 10 to 20 GPa. Building on these findings, **Publication IV** focuses on the oxidation mechanisms of ternary TM-X-C thin films. While binary TMC systems oxidize at temperatures below 600 °C, ternary films successfully withstand isothermal oxidation tests at 750 °C for 1 h. The most promising material systems are Ti-Al-C, Ta-Al-C, and Ti-Si-C. For the Al alloyed thin films, compositions containing 25 at.% Al improve oxidation resistance by protective oxide scales

$<$ 750 nm. Similarly, Ti-Si-C coatings show improvements in oxidation resistance starting at 20 at.% Si. TEM analysis of oxidized $Ti_{0.26}Al_{0.32}C_{0.42}$ and $Ti_{0.29}Si_{0.26}C_{0.45}$ coatings, reveals a two-layer scale formation consisting of a metal oxycarbide layer on top of the unoxidized, non-porous Ti-X-C thin film, followed by an outer mixed Ti-(Al/Si) oxide scale. Electron energy loss spectroscopy (EELS) line scans indicate that Al provides a superior oxygen diffusion barrier, as no oxygen gradient is detected within the underlying film proven for Ti-Al-C.

In **Publication V**, the oxidation behavior of Al and Si alloyed CrB_2 thin films was investigated. A similar high throughput deposition approach allowed the synthesis of ternary Cr-Al-B, Cr-Si-B and quaternary Cr-Al-Si-B thin films by co-sputtering a CrB_2, AlB_2, and Si target. Structural analysis confirmed that all films crystallized predominantly in the hexagonal AlB_2 prototype structure. Si exhibited low solubility in the hexagonal CrB_2 structure, with a maximum of approximately 4 at.%. Beyond this limit, additional $CrSi_2$ phases were observed. Al alloying above 20 at.% increased the oxidation onset temperature of CrB_2 from 600 °C to about 800 °C. Notably, Si alloying above 11 at.% significantly improved the oxidation resistance, with TGA demonstrating stability up to 1300 °C. This highlights Si as a key protective oxide forming element in diboride structures. Interestingly, Si also promoted alumina formation, which improved the oxidation resistance of the quaternary $Cr_{0.29}Al_{0.18}Si_{0.10}B_{0.43}$ up to 1300 °C, as confirmed by TGA. Detailed TEM analysis of isothermally oxidized $Cr_{0.35}Si_{0.16}B_{0.49}$ and $Cr_{0.27}Al_{0.22}Si_{0.09}B_{0.42}$ at 1200 °C for 1 h revealed a layered oxide growth. The Cr-Si-B developed a Si-O layer on top of the diboride, followed by a Cr-O scale. The quaternary Cr-Al-Si-B systems formed an additional Al-O on the outer surface. Both coatings exhibited excellent high temperature oxidation resistance at 1200 °C, demonstrating the potential of PVD to alloy low melting metals into ceramic diboride based phases.

In summary, this thesis presents a comprehensive evaluation of coating strategies designed to enhance the oxidation resistance of ceramic thin film materials. By utilizing advanced deposition techniques, alloying approaches, and architectural coating concepts, this work has demonstrated significant advances in the development of protective coatings for high temperature oxidative environments. Through the studies, Si has emerged as a critical element for improving the oxidation resistance of ceramic thin films. From $MoSi_2$-based coatings over Si-O top coatings to the improved oxidation performance of Cr-Si-B thin films, Si played a key role due to its ability to form rapidly protective silica-based oxide scales. In addition, Si contributed to the improved oxidation resistance of Al-containing thin films, as observed in Al-Si-O top coatings where mullite structures (Al_2O_3-SiO_2) formed, and in the quaternary Cr-Al-Si-B system where Si enhanced the effectiveness of protective alumina scales. While transition metal carbides have so far demonstrated greater oxidation resistance with Al, there remains significant potential for further research, particularly to optimize the oxidation kinetics of TMCs at even higher temperatures. These results provide a robust basis for future research and create new possibilities for developing advanced high-temperature oxidation resistant coating materials. Ultimately, this work paves the way for innovations that could significantly impact various industries.

Publication I

Tuning microstructural and oxidative characteristics of direct current- and high-power pulsed magnetron sputtered $MoSi_2$-based thin films

S. Richter, A. Bahr, P. Kutrowatz, T. Wojcik, S. Kolozsvári, P. Polcik, C. Jerg, J. Ramm, H. Riedl

J. Vac. Sci. Technol. A, 42, 053407 (2024).

Journal of Vacuum Science and Technology A

RESEARCH ARTICLE | AUGUST 21 2024

Tuning microstructural and oxidative characteristics of direct current- and high-power pulsed magnetron sputtered $MoSi_2$-based thin films

Special Collection: Celebrating the Achievements and Life of Joe Greene

Sophie Richter ; Ahmed Bahr ; Philip Kutrowatz; Tomasz Wojcik ; Szilárd Kolozsvári ;
Peter Polcik ; Carmen Jerg ; Jürgen Ramm ; Helmut Riedl

Check for updates

J. Vac. Sci. Technol. A 42, 053407 (2024)
https://doi.org/10.1116/6.0003833

View Online

Export Citation

JVST A Journal of Vacuum Science & Technology A
ARTICLE
pubs.aip.org/avs/jva

Tuning microstructural and oxidative characteristics of direct current- and high-power pulsed magnetron sputtered $MoSi_2$-based thin films

Cite as: J. Vac. Sci. Technol. A **42**, 053407 (2024); doi: 10.1116/6.0003833
Submitted: 16 June 2024 · Accepted: 31 July 2024 ·
Published Online: 21 August 2024

Sophie Richter,[1,a)] Ahmed Bahr,[1] Philip Kutrowatz,[1] Tomasz Wojcik,[1] Szilárd Kolozsvári,[2] Peter Polcik,[2] Carmen Jerg,[3] Jürgen Ramm,[3] and Helmut Riedl[1,4]

AFFILIATIONS

[1] Christian Doppler Laboratory for Surface Engineering of High-Performance Components, TU Wien, A-1060 Wien, Austria
[2] Plansee Composite Materials GmbH, D-86983 Lechbruck am See, Germany
[3] Oerlikon Balzers, Oerlikon Surface Solutions AG, FL-9496 Balzers, Liechtenstein
[4] Institute of Materials Science and Technology, TU Wien, A-1060 Wien, Austria

Note: This paper is part of the Special Topic Collection Celebrating the Achievements and Life of Joe Greene.

[a)] **Author to whom correspondence should be addressed:** sophie.richter@tuwien.ac.at

ABSTRACT

A comparative study on nonreactively direct current magnetron sputtered (DCMS) and high-power pulsed magnetron sputtered (HPPMS) $MoSi_2$-based coatings has been implemented with the objective of advancing the knowledge on the growth conditions and oxidation resistance of $MoSi_2$ thin films. The energy supplied during the growth process (i.e., deposition temperature and ionization degree) exerts a significant influence on the phase formation and morphology. At 200 °C, highly dense but x-ray amorphous films are prevalent, whereas an increase up to 400 °C leads to dense and fine-columnar structured hexagonal $MoSi_2$ films. Increased growth temperatures (≥500 °C for DCMS) and strongly ionized plasma states result in the formation of dual-phase structures (h-$MoSi_2$ and t-Mo_5Si_3), accompanied by slightly underdense but strongly columnar grains. The $MoSi_{1.92}$ HPPMS film (1000 Hz, 10% duty cycle) grown at 500 °C exhibits the maximum hardness of 22.8 GPa and an elastic modulus of approximately 400 GPa. In long-term oxidation tests conducted at 600, 850, and 1200 °C (up to 100 h), all $MoSi_2$-based films exhibited a temperature-dependent scale formation. Up to 850 °C, the formation of a continuous, dense protective scale is disrupted by the competing growth of MoO_x and SiO_x. At temperatures exceeding 1200 °C, all $MoSi_2$-based coatings analyzed demonstrate exceptional oxidation resistance, resulting in the formation of a continuous, dense SiO_2 scale. At 1500 °C for 30 min, the initially slightly underdense and dual-phased $MoSi_{1.92}$ coating achieved a scale thickness of only 670 nm, thereby demonstrating the exceptional oxidation resistance capabilities of HPPMS-grown $MoSi_2$-based coatings.

I. INTRODUCTION

The potential of intermetallic Mo-Si compounds as ultrahigh temperature materials has attracted the attention of researchers due to their exceptional thermal properties beyond 1600 °C.[1] Given their versatile properties, including extremely high phase stability, tribological characteristics,[2,3] and optoelectronic properties,[4,5] Mo-Si-based materials are suitable for a wide range of applications. The binary Mo-Si system comprises three distinct intermetallic compounds: $MoSi_2$, Mo_5Si_3, and Mo_3Si, respectively. While the Mo-rich phases, such as Mo_5Si_3 and Mo_3Si, exhibit superior

JVST A
Journal of Vacuum Science & Technology A
ARTICLE
pubs.aip.org/avs/jva

mechanical properties, the Si-rich phase, $MoSi_2$, displays enhanced oxidation resistance.[1] The oxidation behavior of $MoSi_2$ has been extensively studied for bulk materials, with the formation of a highly protective silica scale (SiO_2) being responsible for the enhanced oxidation resistance.[6–9] It is evident that $MoSi_2$ materials display unfavorable oxidation resistance at low temperatures (below 600 °C), which can be attributed to the so-called pesting phenomenon, well-known for Mo-based alloys.[10–12] The pesting phenomenon typically manifests when mixed oxides (e.g., metallic and silica-based) grow simultaneously, resulting in internal stresses due to the significant volume expansion of the respective oxides.[8] A substantial body of research has demonstrated that microstructure and structural defects exert a profound influence on the pesting behavior of $MoSi_2$ bulk and coating materials. Typically, accelerated oxidation occurs as a result of the formation of cracks and pores, which leads to the formation of a poorly protective and porous oxide layer comprising mixed amorphous Si- and Mo-containing oxidation products.[13,14] Nevertheless, the remarkable high-temperature oxidation resistance of $MoSi_2$—which forms a dense and protective scale that inhibits oxygen inward diffusion up to 1400 °C—indicates that it is a promising candidate for applications at elevated temperatures.[15]

The value of this feature has been demonstrated in numerous studies of $MoSi_2$ coating materials produced through a variety of deposition techniques, including chemical vapor deposition,[16] as well as vacuum and atmospheric plasma spraying.[17–20] Nevertheless, these deposition techniques are not without limitations. In plasma spraying, the unintended addition of oxygen during film growth, which is provided by atmospheric conditions, weakens the protective effect of the coatings with regard to oxygen. Moreover, the formation of a uniform $MoSi_2$ phase throughout the entire film thickness has not been demonstrated to be a straightforward process in hot dipping siliconizing.[21] This inconsistency results in a limited oxidation resistance, as reported by Liu *et al.*[22] Magnetron sputtering, a physical vapor deposition (PVD) technique, represents an alternative approach for the synthesis of $MoSi_2$ thin films. While the existing literature addresses the mechanical properties and phase formation of direct current magnetron sputtered (DCMS) $MoSi_2$ thin films,[23–25] there are no reports on the growth of $MoSi_2$ films using other PVD methods, such as high-power pulsed magnetron sputtering (HPPMS). In the comparative study conducted by Bahr *et al.*, DCMS-grown $TaSi_2$, $NbSi_2$, and $MoSi_2$ were primarily investigated with regard to long-term oxidation kinetics at 1200 °C.[15]

In the context of oxidation resistance, HPPMS-grown $MoSi_2$ thin films are of interest as highly ionized plasmas have the potential to positively influence the microstructure. A densified and more perfect morphology may prove to be a crucial factor during scale formation (e.g., pesting behavior) and retarded oxygen inward diffusion. The objective of this study is to gain a deeper understanding of the growth and oxidation characteristics of nonreactively sputtered $MoSi_2$ thin films using different sputtering techniques (i.e., HPPMS versus DCMS). Furthermore, the objective is to examine the coating performance of even higher oxidation temperatures, up to 1500 °C, with the aim of providing a comprehensive characterization of the observed phenomena.

II. EXPERIMENTAL

A. Deposition process

All $MoSi_2$-based thin films were synthesized in a laboratory-scale magnetron sputtering system. A 3″ $MoSi_2$ compound target with a purity of 99.34%, provided by Plansee Composite Materials GmbH,[26] was operated in DC- and HPPMS modes with 99.999% pure argon as the working gas. Prior to all deposition processes, a base pressure of less than 4×10^{-4} Pa was attained. For DCMS depositions, the substrate temperature was varied from 200 to 600 ° C, while the bias potential was maintained at −50 V. The target power density for DCMS was kept at 5.6 W/cm^2, and the deposition pressure was set at 0.4 Pa by introducing 21 sccm of argon. Moreover, two HPPMS series were synthesized, with the frequencies varying from 500 to 1000 Hz, and the pulse duty cycles (t_{on}/T) adjusted to 2.5%, 5%, and 10%, respectively. All HPPMS films were deposited at a substrate temperature of 500 °C and a DC bias potential of −50 V. The resulting peak power density for the HPPMS films exhibited a range of 150–600 W/cm^2, based on an average power of 7.8 W/cm^2 set at the generator. The deposition pressure was maintained at a constant value of 0.4 Pa by introducing a flow rate of 21 sccm of argon. Single-crystalline silicon (100 orientation, $20 \times 7 \times 0.38$ mm), single-crystalline Al_2O_3 (sapphire, 1-102 orientation, $10 \times 10 \times 0.53$ mm), and polycrystalline Al_2O_3 ($20 \times 7 \times 0.38$ mm) substrates were positioned parallel to the target at a distance of 70 mm and rotated at 0.23 Hz. Prior to the deposition process, an ultrasonic bath was utilized to clean the substrates in acetone and ethanol for a duration of 5 min each. Subsequently, an argon ion etching step was conducted, lasting for 15 min and employing a substrate bias potential of −800 V, along with an argon flow rate of 180 sccm. The resulting etching pressure was approximately 4.9 Pa. Prior to deposition, the target surface was subjected to presputtering at a power density of approximately 2.2 W/cm^2 for the final 2 min, with the shutters closed. The deposition time for the samples in the DCMS series was 30 min, with the exception of the thin film deposited at 500 °C, which required 60 min. The deposition time for the HPPMS coatings was 60 min, except in the case of coatings deposited at 500 Hz with a 10% duty cycle, where the deposition time was 45 min. Overall, the deposition times were adjusted to achieve film thicknesses between 3 and 4 μm.

B. Coating characterization

A microstructural analysis of the $MoSi_2$ films was conducted using a scanning electron microscope (SEM) instrument of varying specifications. The analysis was performed on cross sections of the films in their both as-deposited and annealed states. The SEM instruments utilized were the FEI Quanta 200 FEGSEM, operating at 10 kV, and the Zeiss Sigma 500 VP SEM, operating at 3 kV. Additional cross sections of the oxidized samples were prepared using a dual-beam focused ion beam/scanning electron microscope (FIB-SEM) system (Thermo Scientific Scios 2). The cross sections were prepared using Ga^+ ions at an acceleration voltage of 30 kV and an ion beam current of 7–15 nA for rough milling. The final fine milling was conducted with a beam current of 1 nA. The chemical composition was analyzed by energy-dispersive x-ray spectroscopy (EDX) using a FEI Philips XL30 scanning electron microscope (SEM) operated at an accelerating voltage of 20 kV. For the transmission electron microscopy (TEM) analysis, a FEI TECNAI F20 microscope equipped with a field emission gun was utilized to generate bright-field (BF) images. The TEM lamellas were prepared with the same dual-beam FIB-SEM system that was used for the preparation of the oxidized samples. To analyze the phase evolution of the deposited $MoSi_2$ films, a Panalytical X'Pert Pro MPD X-ray diffractometer was employed in a Bragg Brentano configuration with a Cu-Kα radiation source (wavelength $\lambda = 1.5418$ Å). All measurements on coated single-crystalline Al_2O_3 were conducted with an offset of 3° to reduce the influence of substrate peaks.

The mechanical properties, including hardness and elastic modulus, were determined by nanoindentation on sapphire substrates using an Ultra Micro Indentation System (UMIS) with a Berkovich diamond tip. In order to calculate the respective modulus, the Poisson's ratio of $MoSi_2$ was assumed to be $\nu = 0.25$. A line measurement of 30 indentations at various loads between 3 and 45 mN was conducted to ensure that the penetration depths did not exceed 10% of the film thickness, thereby minimizing the influence of the substrate. The load-displacement curves were evaluated in accordance with the methodology proposed by Oliver and Pharr.[27,28]

Long-term oxidation tests were conducted on single-crystalline Al_2O_3 substrates in ambient air at temperatures of 600, 850, and 1200 °C for 100 h in a conventional furnace. To gain further insight into the high-temperature oxidation behavior, selected coatings on polycrystalline Al_2O_3 substrates were subjected to a synthetic air atmosphere in a Netzsch STA 449 F1 setup with a rhodium furnace. The isothermal oxidation tests were conducted at temperatures of 1300, 1400, and 1500 °C. The annealing time was 60 min, except in the case of the test at 1500 °C, where the annealing time was reduced to 30 min to prevent the system and equipment from overheating. During the oxidation test, a constant supply of oxygen (50 ml/min) and helium (20 ml/min) was maintained, the latter with the objective of protecting the oxide scale formation.

III. RESULTS AND DISCUSSION

A. Phase evolution and morphology

To study the microstructure and growth morphology of the as-deposited $MoSi_2$-based thin films, SEM cross sections have been prepared for all DCMS and HPPMS coatings. Figure 1 depicts the cross-sectional morphology of the DCMS $MoSi_2$ films deposited at varying substrate temperatures (with a constant DC bias potential of −50 V for all conditions). The dashed line represents the interface between the Si substrate and the respective coatings [Figs. 1(a)–1(e)]. The chemical composition of selected coatings was determined by EDX and is presented in Fig. 1. Additional TEM lamellae were prepared for the coating deposited at 400 and 500 °C, respectively.

The cross section in Fig. 1(a) displays a featureless, dense $MoSi_2$ thin film, which exhibits a slight Si super-stoichiometry. As the substrate temperature exceeds 300 °C, the morphological appearance changes to a more columnar state, indicative of a mixed island growth mode of crystalline features, see Figs. 1(b)–1(e). In all observed columnar morphologies, the grains are arranged in a fibrous shape, perpendicular to the substrate according to the growth direction. The coatings deposited at 300 and 400 °C appear denser in comparison to those grown at higher temperatures, as the columns are closely arranged, leaving no pores. In contrast, the coatings depicted in Figs. 1(d) and 1(e) exhibit straight and more continuous columns but with small open porosities in-between. In more detail, this can be also seen by the TEM bright-field images in Fig. 1(f) (400 °C) and Fig. 1(g) (500 °C). In particular, the coating depicted in Fig. 1(g) exhibits larger and continuous columns with underdense grain boundary regions. These morphological changes are related to enhanced diffusion processes with increasing temperatures, whereas in the medium temperature range, a competitive growth between different oriented nuclei promotes the formation of densely overgrown grains. At higher temperatures, recrystallization and restructuring lead to the elimination of overgrown and closest arranged features. In accordance with the temperature-related alterations in the growth mode, the coatings deposited at 300 and 400 °C exhibit a more fine-grained morphology in the vicinity of the substrate, thereby corroborating the aforementioned competitive growth. From a compositional standpoint, a slight decline in the Si/Mo ratio can be discerned with rising temperature.

The influence of ionized species within the plasma on microstructural evolution is illustrated in Fig. 2, presenting fracture cross sections of the as-deposited HPPMS $MoSi_2$ thin films. Once more, the bias voltage and substrate temperature were maintained at 500 °C and −50 V, respectively, for all HPPMS films. The coatings depicted in Figs. 2(a)–2(c) were synthesized at a pulse frequency of 500 Hz, with duty cycles of 2.5%, 5%, and 10%, respectively (as indicated in the lower right corner of each cross section). The morphologies of these coatings are comparable to those of the DCMS coatings grown at 500 and 600 °C, as evidenced by the presence of straight columns with grain boundaries that are not fully dense. The combination of the enhanced plasma conditions accompanied by the relatively high deposition temperature predominates the growth mode. Nevertheless, increased duty cycles, such as 10%, maintain decreased peak power densities, which result in slightly denser morphologies by retarding morphological reorganization effects. Furthermore, all coatings grown at 500 Hz display slight indications of a finer morphology in the substrate interface region. In comparison, the films deposited at 1000 Hz exhibit notable differences in their appearance, as illustrated in Figs. 2(d)–2(f). The growth morphology is more densely arranged, with columns of a smaller size. The small, interrupted features suggest the presence of a more competitive growth mode involving the overgrowth of multiple nuclei, which is analogous to the DCMS coatings deposited at 300 and 400 °C. However, the mean column size appears to be even smaller.

The diverse growth conditions, encompassing the deposition temperatures for DCMS and the ionization degree through varying parameters for the HPPMS states, exert a considerable influence on the phase formation of $MoSi_2$-based thin films. The phase evolution of all as-deposited thin films was investigated via x-ray diffraction in Bragg–Brentano geometry (offset of 3°) on single-crystalline Al_2O_3 substrates, as illustrated in Fig. 3.

While an x-ray amorphous state was only observed for the films grown at 200 °C, higher deposition temperatures resulted in

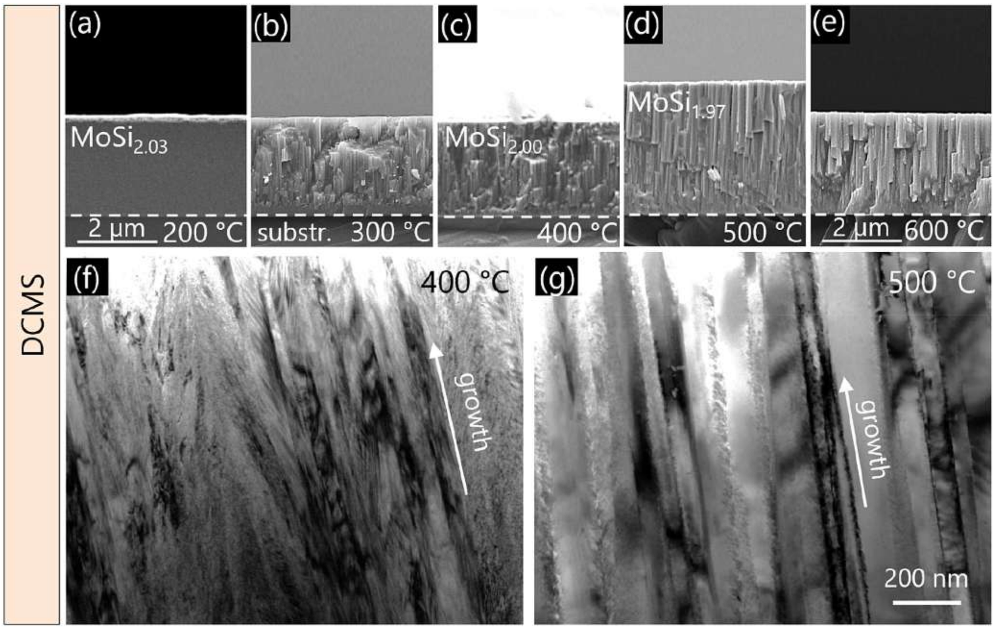

FIG. 1. SEM cross sections of the as-deposited DCMS $MoSi_2$-based thin films at different substrate temperatures are presented, with the chemical compositions (analyzed by EDX) indicated for selected states. The temperatures are (a) 200, (b) 300, (c) 400, (d) 500, and (e) 600 °C, respectively. Additional TEM cross sections are presented in (f) and (g), which depict the coatings deposited at 400 and 500 °C, respectively.

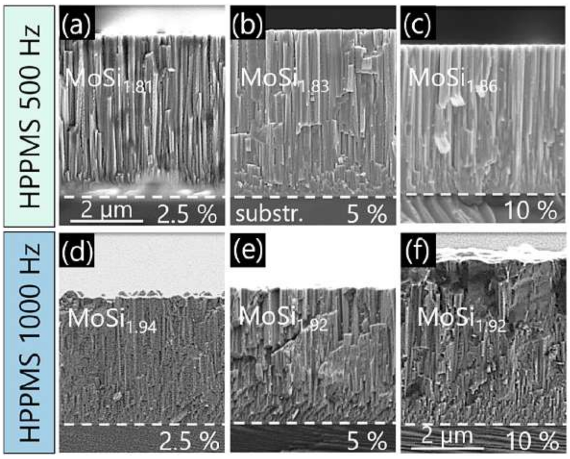

FIG. 2. SEM cross sections of the as-deposited HPPMS $MoSi_2$ thin films. The specific HPPMS parameters utilized are indicated on the left-hand side of the figure as well as within the cross sections. The first line represents the 500 Hz sample synthesized with a (a) 2.5%, (b) 5%, and (c) 10% duty cycle, respectively. The second line displays the 1000 Hz sample, again with a (d) 2.5%, (e) 5%, and (f) 10% duty cycle, respectively. The interface between the substrate (Si) and the coating is delineated by the dashed line.

the formation of single- or dual-phase structures. The predominant phases are also indicated on the right-hand side of all diffractograms. The evident structural evolution from x-ray amorphous to a single-crystalline hexagonal (h) $MoSi_2$ phase at 300 °C is in accordance with the morphology observed in Fig. 1.

At temperatures between 300 and 400 °C, the $MoSi_2$-based films can be assigned to the metastable h-$MoSi_2$ phase. Nevertheless, there are already peak overlaps with Mo_5Si_3, as evidenced by the peak observed at 26.1°. However, all other orientations exhibit perfect alignment with the hexagonal structure, and the observed stoichiometry strongly suggests the formation of the h-$MoSi_2$ phase. Even so, there is a slight indication of the formation of the tetragonal (t) Mo_5Si_3 phase, albeit in small quantities, at 29°. Moreover, the metastable h-$MoSi_2$ phase exhibits different orientations as a result of a predominant competitive growth mode.

An additional increase in deposition temperature results in the formation of a dual-phase structure comprising h-$MoSi_2$ and t-Mo_5Si_3, which aligns with the chemical changes observed in Fig. 1. This trend is also observed in the peak intensities of the Mo_5Si_3 phase, which increases with temperature. The pronounced preferred orientation of the 600 °C film at 41.5° is particularly noteworthy, aligning with the morphological changes observed (Fig. 1). However, due to peak overlap, it is challenging to definitely assign a specific phase. This is because the (202) orientation of the t-Mo_5Si_3 phase partially overlaps with the (111) h-$MoSi_2$ phase. Nevertheless, a more detailed examination of the peak shoulder

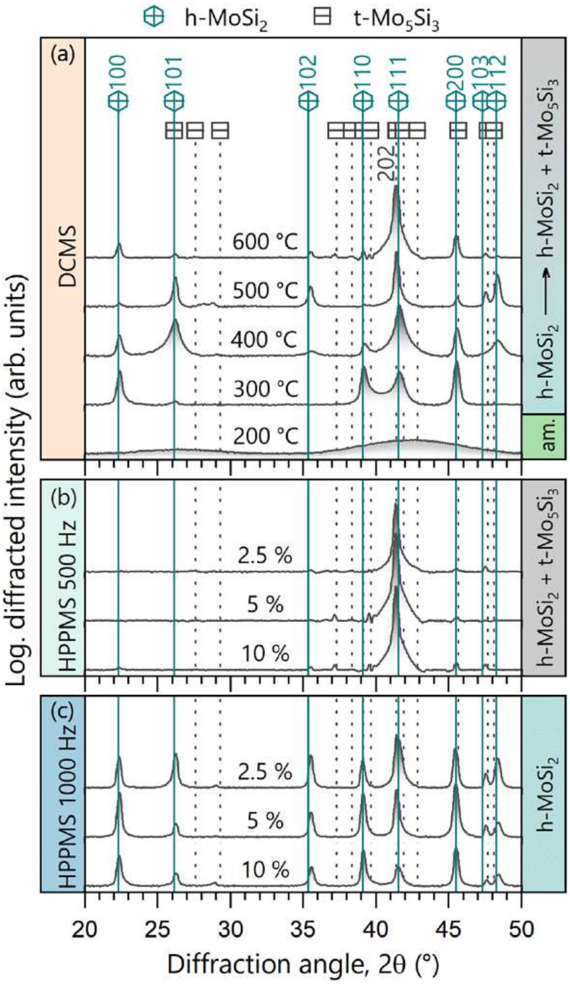

FIG. 3. X-ray diffractograms of the as-deposited $MoSi_2$ coatings are presented in (a) as a function of the substrate temperature during DCMS deposition. The various HPPMS films are illustrated in (b) for 500 Hz and (c) for 1000 Hz, with different duty cycles varying from 2.5% to 10%, respectively. The reference patterns for the hexagonal beta $MoSi_2$ (C40, $CrSi_2$ prototype) phases are represented by hexagons and continuous lines, as referenced in Ref. 29, whereas the tetragonal Mo_5Si_3 (D8 m, W_5Si_3 prototype) phase is labeled by squares with dashed lines, as referenced in Ref. 30.

indicates the presence of a dual-phase structure. Furthermore, the tetragonal Mo_5Si_3 phase is thermodynamically stable, and there is a tendency for Si to form substoichiometric compositions at higher temperatures.[15]

Figures 3(b) and 3(c) illustrate the phase evolution of the HPPMS coatings. In accordance with their morphological appearance, the 500 Hz coatings also exhibit comparable crystal structures and diffractograms to those of the DCMS grown at 600 °C. All coating states are predominantly dual-phase structured, comprising primarily h-$MoSi_2$ and t-Mo_5Si_3. The predominant growth orientation (as indicated by the peak at 41.5°) is consistent with the observed pronounced columnar morphology. In contrast, the 1000 Hz HPPMS coatings obtain h-$MoSi_2$ predominated structures with small indications of the t-Mo_5Si_3 phase for the 2.5% and 10% duty cycle states, respectively. All three coatings grown at 1000 Hz exhibit a random oriented structure [see Fig. 3(c)].

B. Mechanical properties

The morphological and structural differences of the as-deposited $MoSi_2$ films, resulting from the distinct synthesis routes (DCMS and HPPMS), are clearly reflected in their mechanical properties. Figure 4 illustrates the hardness (depicted on the left axis, represented by square symbols) and elastic modulus (depicted on the right axis, represented by circles) of the various $MoSi_2$ films.

The amorphous coating deposited at 200 °C exhibits low hardness (13.8 ± 0.7 GPa) in combination with a low elastic modulus (275 ± 20 GPa) [see Fig. 1(a)]. This finding aligns with the data presented by Chou and Nieh,[23] who determined a hardness of 10–12 GPa and a modulus of 225–232 GPa for amorphous sputtered $MoSi_2$ films. The elastic modulus exhibits a notable increase with the formation of the hexagonal $MoSi_2$ structure, reaching approximately 400 GPa for all crystalline $MoSi_2$-based films. In contrast, the hardness is found to exhibit a stronger dependence on the substrate temperature and the prevailing phases. The coatings deposited at 300 and 400 °C exhibit a peak hardness within the DCMS series, with values of 22.3 ± 1.6 and 21.4 ± 1.9 GPa, respectively. Subsequently, there is a notable decline in hardness to approximately 18 GPa at 600 °C. This finding is in good agreement with the phase evolution observed in Fig. 3 and the morphological

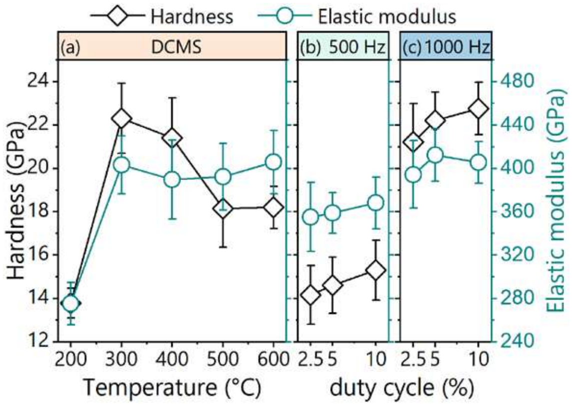

FIG. 4. Depiction of the hardness (on the left axis) and elastic modulus (on the right axis) of the (a) DCMS and (b) and (c) HPPMS coatings as a function of substrate temperature and duty cycle variation for different frequencies, 500 and 1000 Hz, respectively.

JVST A
Journal of Vacuum Science & Technology A
ARTICLE
pubs.aip.org/avs/jva

changes in Fig. 1. The formation of dual-phase structures (h-$MoSi_2$ and t-Mo_5Si_3) and larger grain/column sizes with underdense grain boundary regions, resulting from the enhanced surface diffusion, contribute to a decrease in hardness values. Nevertheless, it is challenging to discern the impact of orientation relations in the context of phase changes and overlapping peak positions.

For the HPPMS coatings, please refer to Figs. 4(b) and 4(c). The elastic modulus is approximately 400 GPa for the 1000 Hz series, which is comparable to the crystalline films produced by the DCMS series. Additionally, the 500 Hz series exhibits an elastic modulus of 360 GPa. The observed trend is in accordance with the phase evolution, as the 1000 Hz coatings and DCMS at 300 and 400 °C are predominantly randomly oriented h-$MoSi_2$ structured. The decline to 360 GPa for the predominantly t-Mo_5Si_3 structured 500 Hz series can be attributed to the phase transition. However, this phenomenon is not discernible for the DCMS coatings at temperatures ranging from 500 to 600 °C.

In terms of hardness, a more pronounced difference is evident between the two HPPMS series at 500 and 1000 Hz, as illustrated in Figs. 4(b) and 4(c). The highest hardness, 22.8 ± 1.2 GPa, is observed for an h-$MoSi_2$ structure coating grown at 1000 Hz and a duty cycle of 10%, respectively. In contrast, the same duty cycle at 500 Hz results in significantly lower hardness values, namely, 15.3 ± 1.4 GPa. The discrepancy of approximately 8 GPa between the two HPPMS series can be primarily attributed to their disparate morphologies. The films deposited at 1000 Hz exhibit a denser and finer morphology compared to those grown at 500 Hz (see also Fig. 2).

In addition to the observed morphological differences, the measured hardness and modulus values are also dependent on the crystal structure and texture. It was observed that films exhibiting dual-phase structures demonstrated lower hardness values than films displaying a predominant h-$MoSi_2$ phase and random orientation. The highest hardness values were observed for the DCMS thin film deposited at 300 °C and the 1000 Hz 10% duty cycle coating. Both exhibited an h-$MoSi_2$ dominated structure with a more or less random orientation but also contained the (100) orientation.

C. Oxidation characteristics

The objective of this investigation was to examine the long-term oxidation resistance of selected $MoSi_2$ films exposed to ambient air at temperatures of 600, 850, and 1200 °C for 100 h. To provide a variation in different morphologies and predominant crystal structures, two HPPMS coatings deposited at 500 and 1000 Hz, each with a 10% duty cycle, and the DCMS coating grown at 500 °C was selected for analysis. The 1000 Hz 10% duty cycle $MoSi_{1.92}$ is primarily h-$MoSi_2$ structured with a dense, small-grained morphology, as illustrated in Figs. 5(a)–5(c). In contrast, the DCMS coating grown at 500 °C [Figs. 5(d) and 5(e)] exhibits a dual-phase h-$MoSi_2$/t-Mo_5Si_3 structure with a partly open-porous morphology. Figures 5(g)–5(i) depict the dual-phase coating grown at 500 Hz and 10% duty cycle after oxidation at different temperatures. It is noteworthy that all of the coatings exhibited robust adhesion to the substrate (sapphire) throughout the oxidation process.

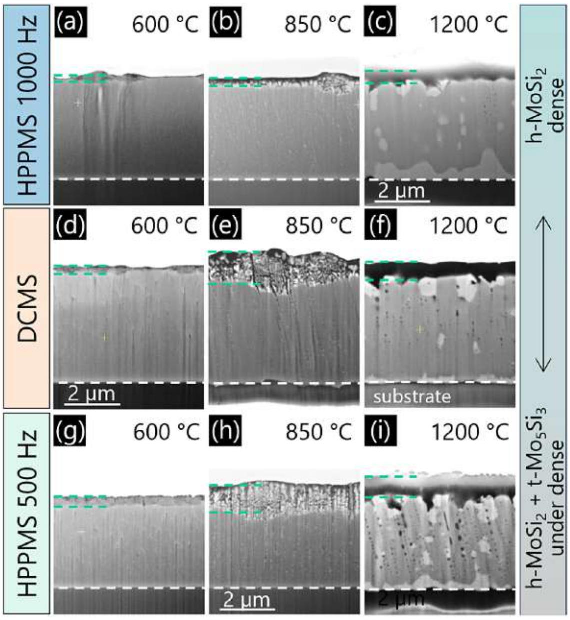

FIG. 5. FIB-prepared cross sections of isothermally oxidized $MoSi_2$ thin films grown on sapphire substrates for 100 h in ambient air at temperatures of 600, 850, and 1200 °C were analyzed. The first line depicts the HPPMS coating at 1000 Hz and a 10% duty cycle [(a) 600, (b) 850, and (c) 1200 °C], the middle row represents the DCMS coating deposited at 500 °C [(d) 600, (e) 850, and (f) 1200 °C], and the bottom row illustrates the HPPMS coating at 500 Hz and a 10% duty cycle, respectively [(g) 600, (h) 850, and (i) 1200 °C]. The interface between the substrate and the coating is indicated by a white dashed line. The oxide scale is delineated by two short, dashed lines.

Following the oxidation of the coatings at 600 °C for 100 h, an oxide layer was observed to form on the surface of all selected $MoSi_2$ coatings, as indicated by the turquoise dashed lines. It is notable that the 500 Hz HPPMS series sample, as illustrated in Fig. 5(g), exhibited the most substantial oxide layer, reaching approximately 400 nm in thickness. Furthermore, the film displayed a relatively underdense morphology and a low Si content of $MoSi_{1.86}$ in comparison to the DCMS sample (i.e., a Si/Mo ratio of 1.97) and the 1000 Hz sample (i.e., a Si/Mo ratio of 1.92). However, the $MoSi_{1.86}$ film is the only one to exhibit the formation of cracks within the oxide layer when subjected to oxidation at 600 °C. This behavior is consistent with the observed morphology and may indicate the presence of slight pesting phenomena. In this lower temperature range (approximately 600 °C), the interaction between MoO_x and SiO_x impedes the formation of a continuous, dense protective oxide layer. The disparities in thermal and volume expansion between these oxides contributed to the instability of the oxide scale, as evidenced by previous research.[8,31–33] Typically, the onset of pesting in $MoSi_2$ is triggered by local microstructural irregularities, such as cracks, pores, or grain boundaries, which subsequently affect the entire sample. It is imperative to minimize these defects in $MoSi_2$ in order to prevent the pesting phenomenon.[34] During the pesting process, $MoSi_2$ may also decompose into so-called pest oxide products, which contain amorphous SiO_2 and MoO_x clusters.[33,34] These products were not observed at 600 °C. In contrast to the 500 Hz HPPMS sample, the DCMS $MoSi_{1.97}$ and the 1000 Hz $MoSi_{1.92}$ coating state exhibited enhanced resistance to crack formation and deterioration in oxidation behavior, which can be attributed to their superior structural, chemical, and particularly morphological design.

In contrast to the oxidation behavior observed at 600 °C, the coatings oxidized at 850 °C exhibit a slightly different behavior, with considerably thicker oxide scales. This is illustrated in Figs. 5(b), 5(e), and 5(h). In detail, the dual-phased states that are less dense [see Figs. 5(e) and 5(h)] demonstrate a notable increase in oxide scale thicknesses and an open porous scale formation. These observations are related to a slight pesting behavior, whereby the competing formation of MoO_x and SiO_x scales result in the formation of a rugged scale. The morphological appearance suggests that the SiO_x is glassy in nature and contains inclusions of molten MoO_x clusters (the melting point of MoO_3 is approximately 795 °C[35]). The HPPMS coating, which was grown at 1000 Hz and a 10% duty cycle, exhibited superior performance relative to the other coatings, as evidenced by a markedly reduced scale thickness. Nevertheless, it displayed a comparable scale formation pattern to the other coatings to a certain degree. In general, the oxide scales formed at 850 °C on the three different coatings do not appear completely dense at first glance. However, upon closer examination of the FIB cross sections, it becomes evident that the underlying coating is adequately protected, resulting in the $MoSi_2$-based coating surviving for up to 100 h.

At elevated temperatures (1200 °C), all $MoSi_2$-based coatings demonstrate exceptional oxidation resistance, which is attributed to the formation of a continuous, dense SiO_2 layer of approximately 500 nm. Any MoO_3 products that form at high temperatures evaporate rapidly (the boiling point of MoO_3 is approximately 1155 °C[35]), leaving a protective SiO_2 scale.[32,34] A comparison of the three oxidized samples at 1200 °C reveals notable contrasts with regard to the structural and morphological differences observed in the as-deposited state. Of particular note is the formation of pores, which was predominantly observed in the HPPMS 500 Hz 10% duty cycle sample [see Fig. 5(i)]. This phenomenon is attributed to the outward diffusion of silicon and the inward diffusion of oxygen along underdense column boundaries,[15] which is consistent with the observed slight underdense morphology. In contrast, the formation of pores was markedly diminished in the 1000 Hz sample subjected to 1200 °C, as illustrated in Fig. 5(c). This is also due to the notable improvement in the microstructure of the 1000 Hz series sample, as evidenced by a denser film in the as-deposited state [see Figs. 2(c) and 2(f)]. Furthermore, the lower Si content in the 500 Hz film results in a reduced capacity for Si to form a protective scale in comparison to the 1000 Hz film. A greater flux of Si outward diffusion is necessary for the formation of a protective SiO_2 scale. The DCMS coating [see Fig. 5(f)] exhibits an intermediate behavior, as the microstructure and phase evolution in the as-deposited state are well situated between the other two samples.

A further notable observation is the existence of discrete regions of darker and brighter appearing contrast within the residual $MoSi_2$ coating beneath the formed oxide scale. This effect is associated with the formation of Mo-rich Mo_5Si_3 (brighter areas based on mass contrast), which persists in the coating due to Si outward diffusion.[15] These observations indicate that the decomposition and phase formation of Mo_5Si_3 associated with Si deficiency can be observed not only during the deposition process (as evidenced by the 500 Hz and 500–600 °C DCMS states) but also during annealing treatments. This finding is substantiated by the observation that the as-deposited 1000 Hz 10% duty cycle coating is predominantly composed of h-$MoSi_2$ and that brighter Si-depleted areas form subsequent to the oxidation experiment [see Fig. 3(c)].

The presence of Mo-rich phase (Mo_5Si_3) in the long-term annealed coatings is further corroborated by XRD analysis. Figure 6 depicts the diffractograms of all long-term annealed samples at varying temperatures (600, 850, and 1200 °C) for 100 h.

Figure 6(a) provides a summary of the phase evolution of the long-term (100 h) oxidized 1000 Hz HPPMS sample. Following annealing at 600 °C, the $MoSi_2$ thin film continues to exhibit the metastable hexagonal $MoSi_2$ phase, with the presence of additional tetragonal Mo_5Si_3. Following annealing at 850 °C, a phase transition from hexagonal to the stable tetragonal $MoSi_2$ phase occurs. Even at 1200 °C, the stable tetragonal $MoSi_2$ phase remains the dominant phase, accompanied by the formation of the Mo_5Si_3 phase due to Si outward diffusion. Furthermore, additional minor peaks can be attributed to the cristobalite SiO_2 phase following annealing at 1200 °C. These peaks are distinctly present at diffraction angles (2Θ) of 21.9°, 31.5°, and 36.1° and are not superimposed upon any other peaks belonging to the tetragonal $MoSi_2$ or Mo_5Si_3 phase. The phase evolution resulting from the oxidation of the DCMS and 500 Hz HPPMS thin films is illustrated in Figs. 6(b) and 6(c), respectively. In general, a comparable trend is observed, albeit with slightly disparate initial conditions, as a result of the different phase constitution of the as-deposited state in comparison to the 1000 Hz HPPMS coating. Following oxidation at 600 °C, both coatings exhibited a mixture of h-$MoSi_2$ and t-Mo_5Si_3. It is notable that the HPPMS 500 Hz sample [Fig. 6(c)] retains a pronounced orientated structure, as evidenced by the peak at 41.5° that emerges following oxidation at 600 °C for 100 h in ambient air. Both the DCMS and the 500 Hz HPPMS coating then undergo the same phase transformation into tetragonal $MoSi_2$ after oxidation at 850 °C, with the additional Mo_5Si_3 still present. Following annealing at 1200 °C, the samples also exhibited the tetragonal $MoSi_2$ and Mo_5Si_3 peaks, as observed in the 1000 Hz HPPMS sample. Furthermore, the initial indications of a crystalline SiO_2 oxide layer can be identified through the presence of tetragonal cristobalite SiO_2 peaks.

To gain insights into extreme oxidation conditions, the HPPMS coating, which was grown at 500 Hz and a 10% duty cycle, was selected for investigation of its oxidation behavior and scale formation even at higher temperatures (1300, 1400, and 1500 °C). Despite the suboptimal initial condition, characterized by an underdense morphology and Si deficiency, the experiments should yield the exceptional oxidation behavior of $MoSi_2$-based coating. It should be noted that the measurement at 1500 °C was limited to

JVST A
Journal of Vacuum Science & Technology A
ARTICLE
pubs.aip.org/avs/jva

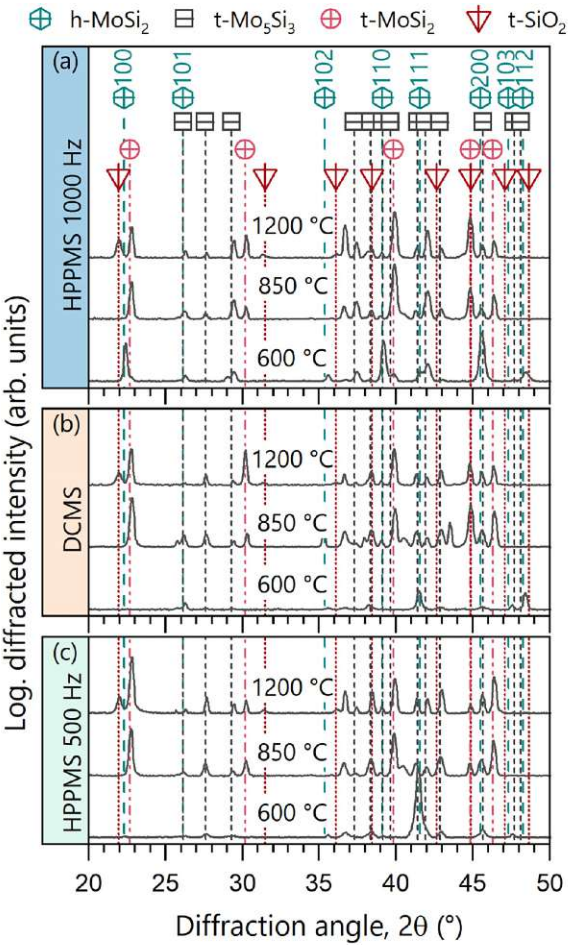

FIG. 6. X-ray diffractograms presented here depict the phase formation of long-term annealed MoSi$_2$-based coatings in ambient air for 100 h. The samples were annealed at 600, 850, and 1200 °C. Panel (a) depicts the diffractograms of the annealed 1000 Hz HPPMS films synthesized with a duty cycle of 10%, (b) of the annealed DCMS samples deposited at a substrate temperature of 500 °C, and (c) the data of the annealed 500 Hz films synthesized with a duty cycle of 10%. All measurements were conducted on coated single-crystalline Al$_2$O$_3$ substrates in Bragg–Brentano configuration with an offset of 3°. Hexagonal MoSi$_2$ is represented by hexagons (Ref. 29), tetragonal MoSi$_2$ by circles (Ref. 36), tetragonal Mo$_5$Si$_3$ by squares (Ref. 30), and tetragonal SiO$_2$ (cristobalite) by triangles. (Ref. 37).

30 min to protect the heating system, in comparison to 60 min for the other temperatures. Following the completion of the annealing tests, SEM cross sections were prepared and are presented in Fig. 7.

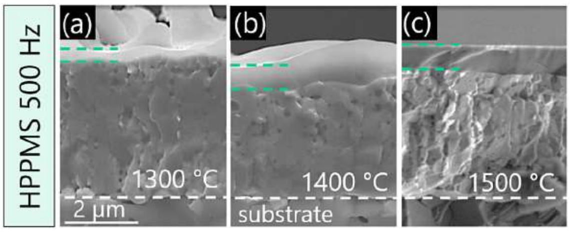

FIG. 7. SEM cross sections of an annealed MoSi$_2$-based thin film deposited on a polycrystalline Al$_2$O$_3$ substrate at 500 Hz and a duty cycle of 10%. Oxidation experiments were conducted in synthetic air at (a) 1300 °C (60 min), (b) 1400 °C (60 min), and (c) 1500 °C (30 min). The interface between the substrate and the coating is delineated by the white dashed line. The oxide scale formed is indicated by two short, dashed lines.

As illustrated in Fig. 7, the cross sections after oxidation demonstrate the exceptional oxidation resistance of the coating following exposure to these extreme conditions, despite a discernible substoichiometry of Si (Si/Mo ratio of 1.86). The thickness of the oxide layer exhibits a slight increase with elevated temperatures. The scale formation on the sample oxidized at 1300 and 1400 °C exhibits a glassy, wavy character, whereas the scale on the sample oxidized at 1500 °C displays a more uniform appearance. Additionally, the SEM images in Fig. 7 demonstrate minimal pore

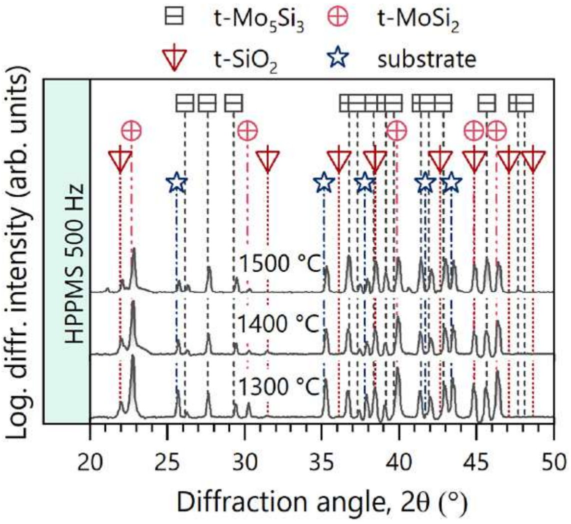

FIG. 8. X-ray diffractograms of oxidized MoSi$_2$-based coatings deposited at 500 Hz and a duty cycle of 10%. The oxidation experiments were conducted in synthetic air environment at 1300 °C (60 min), 1400 °C (60 min), and 1500 °C (30 min). All measurements were conducted on coated polycrystalline Al$_2$O$_3$ substrates [depicted by star symbols, as referenced in (Ref. 38)] utilizing a Bragg–Brentano configuration. The circles represent tetragonal MoSi$_2$ (Ref. 36), the squares represent tetragonal Mo$_5$Si$_3$ (Ref. 30), and the triangles represent tetragonal SiO$_2$ (cristobalite) (Ref. 37).

formation in comparison to the FIB-prepared cross section in Fig. 5(f), indicating an enhanced Si outward diffusion at elevated temperatures. Moreover, following isothermal testing at temperatures up to 1500 °C, all annealed coatings demonstrated robust adhesion to the polycrystalline Al_2O_3 substrate.

Following the high-temperature oxidation tests, the samples were also subjected to phase analysis. This was conducted to investigate the formation of oxide phases and to ascertain the phase stability of $MoSi_2$. As illustrated in Fig. 8, the XRD analysis clearly demonstrates the stability of the tetragonal $MoSi_2$ phase up to 1500 °C. Furthermore, the tetragonal Mo_5Si_3 phase was formed, as previously observed during the 100 h oxidation at 1200 °C. At all temperatures up to 1500 °C, the cristobalite SiO_2 phase could be clearly identified, particularly by the peaks at around 21.9°, 31.5°, and 36.1°, a peak shoulder at 42.6°, and possibly further overlapping peaks with the Mo_5Si_3 phase.

IV. CONCLUSIONS

The objective of this study was to conduct a comprehensive investigation on the phase formation, structure-mechanical properties, and high-temperature oxidation resistance of DCMS and HPPMS $MoSi_2$-based coatings. A particular emphasis was placed on the utilization of HPPMS in comparison to DCMS, which enabled the deposition of dense, h-$MoSi_2$ dominated thin films through the precise regulation of the ionization degree. Subsequently, the coatings were evaluated for their oxidation properties, which exhibited protective characteristics even at temperatures up to 1500 °C.

For DCMS, crystalline $MoSi_2$ films could be deposited at a substrate temperature of 300 °C and above, while x-ray amorphous films were only obtained below this temperature threshold. In their as-deposited state, films grown at temperatures between 300 and 400 °C predominantly crystallize in the hexagonal $MoSi_2$ structure. A higher substrate temperature (500–600 °C) is conducive to the formation of dual-phase coatings (h-$MoSi_2$ and t-Mo_5Si_3) and a Si substoichiometry. The 500 Hz HPPMS coatings exhibit a comparable phase formation and morphology to the DCMS coatings grown at 600 °C, predominantly featuring the additional t-Mo_5Si_3 structure and a pronounced columnar morphology. In contrast, the 1000 Hz HPPMS coatings are primarily composed of the h-$MoSi_2$ structure and exhibit a more randomly oriented texture.

The highest hardness was observed within the 1000 Hz HPPMS series for the random oriented h-$MoSi_{1.92}$ film, which exhibited a densely packed morphology, reaching 22.8 ± 1.2 GPa. The elastic modulus for all crystalline coatings was in the range of 360–400 GPa.

The oxidation behavior of the $MoSi_2$-based films was comprehensively investigated across a range of temperatures (650–1500 °C) over an extended period (up to 100 h). During oxidation at 600 °C, the formation of minor cracks in the oxide scales on top of the coatings was observed, indicating the presence of the pesting phenomenon. At 850 °C, the scales contain both amorphous SiO_x and MoO_x clusters, which are still indicative of a slight pesting-like behavior. The excellent oxidation resistance of $MoSi_2$ has been confirmed above 1200 °C, with an extremely thin scale of approximately 650 nm established for the HPPMS thin film deposited at a frequency of 1000 Hz with a 10% duty cycle. The formation of pores was markedly diminished through the strategic implementation of HPPMS. With regard to the outward diffusion of Si during oxidation, the formation of Mo_5Si_3-rich phase regions has been confirmed through structural analysis. Short-term tests (up to one hour) in the high temperature regime from 1300 to 1500 °C revealed effective protective oxidation mechanisms, namely, the formation of dense SiO_2 scales below 670 nm. This was observed even in films with a Si substoichiometry (Si/Mo ratio of 1.86).

The findings underscore the exceptional oxidation resistance up to 1500 °C and the valuable mechanical properties of nonreactively grown $MoSi_2$-based coatings, particularly for films deposited via HPPMS at 1000 Hz. In conclusion, the primary determinants of these remarkable properties are a predominant hexagonal $MoSi_2$ phase constitution and a highly dense microstructure.

ACKNOWLEDGMENTS

The financial support by the Austrian Federal Ministry for Digital and Economic Affairs, the National Foundation for Research, Technology and Development, and the Christian Doppler Research Association is gratefully acknowledged (Christian Doppler Laboratory “Surface Engineering of high-performance Components”). We also thank Plansee SE, Plansee Composite Materials GmbH, and Oerlikon Balzers, Oerlikon Surface Solutions AG for financial support. We also thank the X-ray center (XRC) of TU Wien for beam time and the electron microscopy center—USTEM TU Wien—for using the SEM and TEM facilities. Finally, we acknowledge TU Wien Bibliothek for financial support through its Open Access Funding Programme.

AUTHOR DECLARATIONS

Conflict of Interest

The authors have no conflicts to disclose.

Author Contributions

Sophie Richter: Conceptualization (lead); Data curation (lead); Formal analysis (lead); Investigation (lead); Methodology (lead); Project administration (equal); Visualization (lead); Writing – original draft (lead). **Ahmed Bahr:** Investigation (supporting); Methodology (supporting). **Philip Kutrowatz:** Investigation (supporting); Methodology (supporting). **Tomasz Wojcik:** Investigation (supporting); Methodology (supporting). **Szilárd Kolozsvári:** Funding acquisition (supporting); Writing – review & editing (supporting). **Peter Polcik:** Funding acquisition (supporting); Writing – review & editing (supporting). **Carmen Jerg:** Funding acquisition (supporting); Writing – review & editing (supporting). **Jürgen Ramm:** Funding acquisition (supporting); Writing – review & editing (equal). **Helmut Riedl:** Funding acquisition (lead); Project administration (equal); Supervision (lead); Writing – review & editing (equal).

DATA AVAILABILITY

The data that support the findings of this study are available from the corresponding author upon reasonable request.

JVST A
Journal of Vacuum Science & Technology A
ARTICLE
pubs.aip.org/avs/jva

REFERENCES

[1] L. Jiang, B. Zheng, C. Wu, P. Li, T. Xue, J. Wu, F. Han, and Y. Chen, Processes **10**, 1772 (2022).

[2] T. S. R. C. Murthy, B. Basu, A. Srivastava, R. Balasubramaniam, and A. K. Suri, J. Eur. Ceram. Soc. **26**, 1293 (2006).

[3] J. Lu, J.-B. Wang, S.-R. Yang, and Q.-J. Xue, Mocaxue Xuebao/Tribol. **23**(5), 361 (2003).

[4] F. Ferrieu, C. Viguier, A. Cros, A. Humbert, O. Thomas, R. Madar, and J. P. Senateur, Solid State Commun. **62**, 455 (1987).

[5] M. N. H. Liton, M. A. Helal, M. K. R. Khan, M. Kamruzzaman, and A. K. M. Farid Ul Islam, Indian J. Phys. **96**, 4155 (2022).

[6] A. A. Sharif, J. Mater. Sci. **45**, 865 (2010).

[7] Y. Q. Liu, G. Shao, and P. Tsakiropoulos, Intermetallics **9**, 125 (2001).

[8] D. A. Berztiss, R. R. Cerchiara, E. A. Gulbransen, F. S. Pettit, and G. H. Meier, Mater. Sci. Eng. A **155**, 165 (1992).

[9] S. Lohfeld and M. Schütze, Mater. Corros. **56**, 93 (2005).

[10] G. Sauthoff, *Intermetallics* (Wiley-VCH, Weinheim, Germany, 1995).

[11] J. J. Petrovic, MRS Bull. **18**, 35 (1993).

[12] S. Chevalier, F. Bernard, E. Gaffet, S. Paris, Z. A. Munir, and J. P. Larpin, "Effect of microstructure on the high temperature oxidation and pesting behaviour of $MoSi_2$," in *Materials Science Forum* (Trans Tech, Switzerland, 2004), pp. 439–446.

[13] H. J. Grabke and G. H. Meier, Oxid. Met. **44**, 147 (1995).

[14] F. Zhang, L. T. Zhang, A. D. Shan, and J. S. Wu, J. Alloys Compd. **422**, 308 (2006).

[15] A. Bahr *et al.*, J. Alloys Compd. **931**, 167532 (2023).

[16] E. K. Nyutu, M. A. Kmetz, and S. L. Suib, Surf. Coat. Technol. **200**, 3980 (2006).

[17] J. Yan, Y. Wang, L. Liu, Y. Wang, and F. Chen, J. Therm. Spray Technol. **24**, 1093 (2015).

[18] Y. Wang, D. Wang, J. Yan, and A. Sun, Appl. Surf. Sci. **284**, 881 (2013).

[19] X. Fei, Y. Niu, H. Ji, L. Huang, and X. Zheng, Ceram. Int. **37**, 813 (2011).

[20] J. Sun, T. Li, and G.-P. Zhang, Corros. Sci. **155**, 146 (2019).

[21] Y. Zhang, J. Zhao, J. Li, J. Lei, and X. Cheng, Ceram. Int. **45**, 5588 (2019).

[22] L. Liu, H. Q. Zhang, H. Lei, H. Q. Li, J. Gong, and C. Sun, Ceram. Int. **46**, 5993 (2020).

[23] T. C. Chou and T. G. Nieh, Thin Solid Films **214**, 48 (1992).

[24] P. V. Kiryukhantsev-Korneev and A. Potanin, Russ. J. Non-Ferr. Met. **59**, 698 (2018).

[25] W. Bretschneider and G. Beddies, Thin Solid Films **149**, 61 (1987).

[26] Plansee Composite Materials GmbH (2024).

[27] G. M. Pharr and W. C. Oliver, MRS Bull. **17**, 28 (1992).

[28] W. C. Oliver and G. M. Pharr, J. Mater. Res. **7**, 1564 (1992).

[29] International Center of Diffraction Data, Powder Diffraction File—hexagonal $MoSi_2$—04-018-0302 (2014).

[30] International Center of Diffraction Data, Powder Diffraction File—tetragonal Mo_5Si_3—04-005-9703 (2011).

[31] T. C. Chou and T. G. Nieh, JOM **45**, 15 (1993).

[32] C. Volders and P. Reinke, Surf. Sci. **681**, 134 (2019).

[33] T. C. Chou and T. G. Nieh, J. Mater. Res. **8**, 214 (1993).

[34] B. V. Cockeram, G. Wang, and R. A. Rapp, Oxid. Met. **45**, 77 (1996).

[35] American Elements (2024).

[36] International Center of Diffraction Data, Powder Diffraction File—tetragonal $MoSi_2$—00-006-0681 (1956).

[37] International Center of Diffraction Data, Powder Diffraction File—tetragonal SiO_2—00-011-0695 (1961).

[38] International Center of Diffraction Data, Powder Diffraction File—rhombohedral Al_2O_3—00-005-0712 (1955).

Publication II

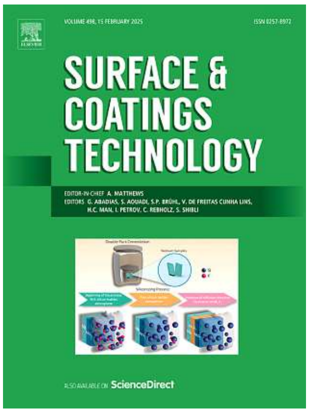
VOLUME 498, 15 FEBRUARY 2025 ISSN 0257-8972

SURFACE & COATINGS TECHNOLOGY

EDITOR-IN-CHIEF A. MATTHEWS
EDITORS G. ABADIAS, S. AOUADI, S.P. BRÜHL, V. DE FREITAS CUNHA LINS, H.C. MAN, I. PETROV, C. REBHOLZ, S. SHIBLI

ALSO AVAILABLE ON ScienceDirect

Reactively grown Al/Si-based top coatings protecting TM-diborides (TM = W, Ti, Hf) against high-temperature oxidation

S. Richter, T. Glechner, T. Wojcik, B. Widrig, S. Kolozsvári, P. Polcik, O. Hunold, L. Zauner, J. Ramm, H. Riedl

Surface & Coatings Technology, 476 (2024) 130191.

Surface & Coatings Technology 476 (2024) 130191

Contents lists available at ScienceDirect

Surface & Coatings Technology

journal homepage: www.elsevier.com/locate/surfcoat

Reactively grown Al/Si-based top coatings protecting TM-diborides (TM = W, Ti, Hf) against high-temperature oxidation

S. Richter [a,*], T. Glechner [a], T. Wojcik [a], B. Widrig [b], S. Kolozsvári [c], P. Polcik [c], O. Hunold [b], L. Zauner [a], J. Ramm [b], H. Riedl [a,d]

[a] *Christian Doppler Laboratory for Surface Engineering of high-performance Components, TU Wien, A-1060 Wien, Austria*
[b] *Oerlikon Balzers, Oerlikon Surface Solutions AG, FL-9496 Balzers, Liechtenstein*
[c] *Plansee Composite Materials GmbH, D-86983 Lechbruck am See, Germany*
[d] *Institute of Materials Science and Technology, TU Wien, A-1060 Wien, Austria*

ARTICLE INFO

Keywords:
Diborides
PVD
Protective coatings
Oxidation
Silane

ABSTRACT

Architectural designs involving Al- and/or Si-containing top coatings present an effective approach to protect oxidation-sensitive materials such as binary transition metal (TM) diborides against high-temperature oxidation. Using reactive arc evaporation, Al-Si-N, Al-Si-O, and Si-O top coatings were applied on sputter-deposited $WB_{1.9}$, $TiB_{2.7}$, and $HfB_{2.4}$ thin films, respectively. A pure Si adhesion layer was introduced prior to the deposition of both oxide-based top coatings (Al-Si-O & Si-O) to prevent *in-situ* oxidation of the diboride base layers. During thermal annealing up to 1200 °C, Al-Si-O and Si-O provided outstanding oxidation resistance on top of $TiB_{2.7}$ and $HfB_{2.4}$, while limited adhesion was observed on $WB_{1.9}$ at elevated temperatures. Contrary, Al-Si-N protected architectures suffered from accelerated oxidation beyond 800 to 1000 °C. Isothermal annealing in ambient air at 1200 °C for 30 h confirmed the long-term stability of the oxide-based top coatings, revealing no decohesion or oxygen inward diffusion beyond the Si interlayer. Complementary TEM analysis showed that the Si-O top coating forms a dense SiO_2 scale above the columnar $HfB_{2.4}$, while the formation of a mullite scale ($3Al_2O_3{\cdot}2SiO_2$) and pronounced recrystallization is recorded for the Al-Si-O protected $HfB_{2.4}$. In summary, the Al-Si-O- and Si-O-based top coatings demonstrated exceptional high-temperature oxidation resistance, fully protecting the TM-diborides from oxidative attack.

1. Introduction

Decreasing the environmental footprint is of utmost importance when striving for more sustainable industrial processes and products. Besides the focus on decarbonization and reduced primary energy consumption, extending the lifetime of high-performance components is considered as a highly efficient approach [1]. In this context, physical vapor deposited protective coatings offer attractive possibilities to extend the operating range of highly stressed materials by enhancing the surface hardness, corrosion-, wear-, and in particular the high-temperature oxidation resistance [2].

Research on novel protective coatings withstanding extreme mechanical and thermal loads is strongly focused on the class of ultra-high temperature ceramics (UHTCs) such as transition metal diborides. In addition to their outstanding thermal stability with melting temperatures beyond 3000 °C, TM-diborides feature excellent wear and creep resistance, as well as super-hardness and chemical inertness [3–6]. Their suitability for applications under extreme thermal and mechanical loads [7,8] is proven by today's use in *e.g.*, atmospheric reentry vehicles, gas turbine combustors, or rocket engine nozzles [4–6,9].

Despite their outstanding mechanical properties, the application of TM-diborides as protective thin films is generally limited due to their poor oxidation resistance related to the competitive growth of volatile boron- and porous TM-oxides [10]. For unalloyed diboride based thin films, the adverse volatilization of B_2O_3 as well as the formation of porous TM-oxides is predominantly observed between 400 and 800 °C [11–13]. Interestingly, these environmental reactions are shifted to higher temperatures for bulk TM-diborides, which is mainly attributed to altered oxidation kinetics and microstructural differences (*i.e.*, boron-rich grain boundary phases) [14–17].

To improve the oxidation resistance of bulk TM-diborides, an approach *via* co-sintering of Si-based compounds (*e.g.*, *SiC*, $MoSi_2$, *etc.*) is

---

[*] Corresponding author.
E-mail address: sophie.richter@tuwien.ac.at (S. Richter).

https://doi.org/10.1016/j.surfcoat.2023.130191
Received 24 July 2023; Received in revised form 27 October 2023; Accepted 9 November 2023

commonly selected [15,18]. This enhances the oxidation resistance significantly through the formation of a dense SiO_x-based scale. Similarly, for PVD synthesized TM-diboride thin films, Al- and Si-based alloying showed great potential in improving the high-temperature oxidation behavior [12,19]. Contrary to bulk materials, these concepts usually target the formation of AlB_2-structured solid solutions to maintain sufficiently high mechanical properties [20]. Glechner et al. [19,21,22] showed that Si alloying in transition metal diborides (TMB_2) increases the oxidation onset temperature by around 400 °C providing long-term oxidation resistance at 1200 °C for up to 100 h. Moreover, TiB_2 thin films alloyed with Al in [12] were investigated up to 800 °C, demonstrating a reduction in oxide scale growth by 75 % after isothermal annealing for 30 min. A particular disadvantage of solid-solution alloying routes is, however, the accompanying pore formation within the unaffected material upon extended oxidation periods, which is caused by the outward diffusion of the protective scale forming elements (*i.e.*, Al or Si) [19,20,23]. In order to avoid this chemical/microstructural separation, Wu et al. used a multilayered coating architecture of sputtered TiB_2 and Cr, achieving slightly improved low-temperature oxidation resistance up to 600 °C due to the direct supply of Cr to the coating surface [24].

Within this work, we suggest an alternative architectural approach consisting of a single protective thin film applied on top of TM-diboride base layers to drastically improve their long-term oxidation resistance. For this purpose, a matrix screening involving three TM-diborides (*i.e.*, WB_2, TiB_2, and HfB_2) and three Al- and/or Si-based top coatings (*i.e.*, Al-Si-N, Al-Si-O, and Si-O) is studied in detail.

2. Experimental

2.1. Deposition process

All coatings were deposited on single-crystalline ($1\bar{1}02$, 10 × 10 × 0.53 mm) and polycrystalline Al_2O_3 (20 × 7 × 0.38 mm) substrates, which were ultrasonically cleaned in acetone and ethanol for 10 min before all depositions. The coating process was conducted in two steps, starting with the synthesis of three different TM-diboride thin films, followed by the deposition of three different Al- and/or Si-based protective top layers. Overall, nine different coating architectures were investigated.

The synthesis of the TM-diboride thin films (*i.e.*, WB_2, TiB_2, or HfB_2) was performed in a laboratory-scale magnetron sputtering system using the corresponding 3-inch compound target (Plansee Composite Materials GmbH [25]). The targets were powered in direct current mode (DCMS) at around 4.8 W/cm^2 using Argon (purity of 99.999 %, Linde Gas GmbH) as a working gas. A base pressure below $3\cdot10^{-4}$ Pa was ensured before all depositions. Prior to the coating processes, the substrates were additionally cleaned through an Ar-ion etching step for 10 min, conducted at a total Ar pressure of 5 Pa and a substrate bias potential of −800 V. The target surface was further sputter-cleaned during the final 3 min of the Ar-etching sequence with a shutter placed between the target and substrate. The coating process was operated at a target-to-substrate distance of 90 mm at a constant substrate temperature of 550 °C. The substrates were placed in a rotating substrate holder (0.25 Hz) with a constant substrate bias potential of −40 V. The deposition pressure was maintained at 0.56 Pa. The coating times varied depending on the material system to obtain a consistent thickness of 2 μm, being 80 min for WB_2 and HfB_2, as well as 180 min for TiB_2.

An industrial-scale Oerlikon Balzers INNOVA system was used to deposit the Al- and/or Si-based top layers (*i.e.*, Al-Si-N, Al-Si-O, and Si-O) onto the TM-diboride thin films. For all top coatings a base pressure below 0.05 Pa was provided. The substrates were rotated using a two-fold rotating carousel. The chamber was heated to a substrate temperature of 450 °C for the deposition of the Si-O and Al-Si-N coatings, whereas a temperature of 550 °C was used to deposit the Al-Si-O top coating. To protect the TM-diboride thin films from immediate oxidation during the reactive deposition of Al-Si-O and Si-O as well as to achieve enhanced adhesion on the coating-coating interface, a 0.45 μm thick Si interlayer was introduced. The Si layer was deposited in a reactive process based on the Oerlikon Blazers central beam technology (average current of 120 A) using a mixture of silane and argon gas (90 sccm SiH_4, 80 sccm Ar, 99.999 % purity from Linde Gas GmbH). A bipolar substrate bias with a potential of ±40 V was utilized during the deposition.

The deposition conditions of the Si-O layer were analogous to the Si interlayer, however 180 sccm of O_2 were additionally introduced. The Al-Si-O and Al-Si-N top coatings were produced by reactive arc evaporation without the central beam technology using a pure Al target (purity of 99.5 %, Plansee Composite Materials GmbH) operated with a source current of 140 A. Si was added *via* SiH_4 gas at a flow rate of 50 sccm. A bipolar substrate bias potential of ±60 V was applied for the deposition of Al-Si-O, with again an oxygen flow rate of 180 sccm. Moreover, the Al-Si-N layer was synthesized using a bipolar substrate potential of ±40 V, with the nitrogen introduced at a constant pressure of 2 Pa. The deposition conditions of the individual top layers were determined in pre-studies on monolithic coatings.

2.2. Coating characterization

The chemical composition of the TM-diboride thin films was determined using inductively coupled plasma optical emission spectroscopy (ICP-OES) prior to the deposition of all top coatings. Details on the procedure can be found in Ref. [19]. Additionally, the chemical composition of the top layers was determined by standard-free energy dispersive X-ray spectroscopy (EDS) in top-view using a FEI Quanta 200 FEGSEM system at an acceleration voltage of 10.0 kV.

Cross-sectional characterization of the as-deposited coating architecture and growth morphology was performed by scanning electron microscopy (SEM) using a Zeiss Sigma 500 VO. Investigations of the thin films after oxidation treatments were conducted using a FEI Quanta 200 FEGSEM system. The fracture cross sections of all samples were investigated with an acceleration voltage of 5.0 kV to minimize charge build-up. Additionally, to examine the structure and pore formation of the oxidized coatings, focused ion beam (FIB) cross sections were prepared using a FIB-SEM dual beam system (ThermoFisher Scientific Scios 2). The cross sections were milled by a Ga^+ ion beam with currents ranging from 7 to 17 nA for fine milling, at an acceleration voltage of 30 kV.

Structural information as well as the phase composition of as-deposited and oxidized samples was obtained by X-ray diffraction (XRD) using a Panalytical X'Pert Pro MPD system operated in Bragg-Brentano geometry with Cu-K$_\alpha$ radiation (wavelength $\lambda = 1.5418$ Å).

To investigate the high-temperature behavior, dynamic oxidation tests in a mixture of synthetic air (50 ml/min) and helium protective gas (20 ml/min) were carried out in a combined DSC/TGA system (Netzsch STA 449 F1) equipped with a Rhodium furnace (TGA signals were processed only). The dynamic oxidation tests were performed from room temperature up to 1400 °C with a heating rate of 10 °C/min. Before each sample measurement, a baseline measurement was carried out with an empty crucible under equivalent conditions. The TGA data was recorded from coatings synthesized on pre-weighed polycrystalline Al_2O_3 substrates, which allowed for a precise measurement of the coating-only mass after the deposition process. Since the substrate material is inert in the investigated temperature range [19], any mass-change is directly related to oxidation/spallation/evaporation effects of the actual thin film material.

Additional long-term oxidation experiments up to 30 h were conducted in a conventional box furnace in ambient air at 1200 °C. The samples were placed directly into the preheated oven, removed from the high-temperature chamber after 30 h, and then allowed to cool to room temperature. Before these isothermal experiments, the adhesion between the TM-diboride and the protective layer was increased through vacuum annealing at 800 °C for 30 min. The annealing was conducted in a CENTORR VI LF Series vacuum furnace at a heating rate of 20 °C/min and a base pressure below $1{\cdot}10^{-3}$ Pa.

Finally, transmission electron microscopy (TEM) of two selected samples was performed to investigate the oxide-scale formation and coating architecture after long-term oxidation treatments using a FEI TECNAI F20 (S)TEM system (operated at 200 kV acceleration voltage). Selected area electron diffraction (SAED) images were taken for crystallographic analysis. The TEM lamellae were prepared *via* a standardized focused ion beam (FIB) lift out procedure on a ThermoFisher Scios II. The local chemical composition was further determined by electron energy loss spectroscopy (EELS). The EELS data was quantified using the Digital Micrograph software package (Gatan Microscopy Suite, version 3.22).

3. Results and discussion

In Fig. 1 the architectural design of the three different TM-diborides (TM = W, Ti, Hf, blue layer) in combination with the three different protective top layers is summarized (yellow layer). As mentioned above, an intermediate Si layer was introduced for the oxide-based top layers to prevent *in-situ* oxidation of the diboride thin films during the reactive deposition process, as well as to improve adhesion (see Fig. 1, orange layer). The following sections contain a comprehensive analysis of all sample configurations with respect to their growth morphology and oxidation resistance in high-temperature oxidative environments.

3.1. Chemical composition & growth morphology

The chemical composition of the TM-diborides was determined by ICP-OES, revealing a slight boron deficiency for the $WB_{1.9}$ layer, while both the $TiB_{2.7}$ and $HfB_{2.4}$ thin films contain excess boron. Hence, it can be expected that especially the latter two variants exhibit boron-enriched grain boundary sites – typically susceptible to B_2O_3 volatilization [26,27]. These deviations from the stoichiometric TMB_2 structure in the target materials originate from different scattering angles and mass ratios between the involved species, as previously detailed by Neidhardt et al. [20,26,28]. Additionally, the chemical composition of the top layer was determined using standard-free EDS, which resulted in an Al-Si-N layer composition of $Al_{0.20}Si_{0.15}N_{0.65}$, an Al-Si-O composition of $Al_{0.22}Si_{0.09}O_{0.69}$, and a Si-O composition of $Si_{0.22}O_{0.78}$. For further use in the text, the abbreviated form (*i.e.*, Al-Si-N, Al-Si-O, and Si-O) is used.

In Fig. 2 the SEM fracture cross sections of all coating configurations are shown in the as-deposited state. The layered structure is indicated with colored dashed lines on the left side of each image as a guide to the eye. The single-crystalline Al_2O_3 substrate is followed by the TM-diboride layer ($WB_{1.9}$ in Fig. 2a-c, $TiB_{2.7}$ in Fig. 2d-f, and $HfB_{2.4}$ in Fig. 2g-i), a Si interlayer (only present for Al-Si-O and Si-O top layers) and the protective surface layers (Al-Si-N in the left column, Al-Si-O in the center column, and Si-O in the right column).

All TMB_2 coatings show a dense and rather featureless morphology. $TiB_{2.7}$ exhibits slight indications for a columnar morphology in top most regions. The average thickness of the TM-diboride films was determined with 2.3, 1.7, and 1.8 µm for $WB_{1.9}$, $TiB_{2.7}$, and $HfB_{2.4}$, respectively. The Si interlayer introduced for all samples with Al-Si-O and Si-O top layers were grown to a thickness of ~450 nm. Moreover, the different protective top layers were determined with an average thickness of 4.5, 3.6, and 4.8 µm for Al-Si-N, Al-Si-O, and Si-O, respectively. The top coatings further appear as homogenous and dense without any texture on all TM-diboride thin films. In contrast to the $TiB_{2.7}$ and $HfB_{2.4}$ thin films, pores can be observed at the coating-coating interface between the Al-Si-N and $WB_{1.9}$ coating, indicating poor layer adhesion. In addition, due to the arc evaporation process from elemental Al targets, both the Al-Si-N and Al-Si-O coatings contain metallic macro particles which contribute to increased surface roughness.

3.2. Phase formation

The phase formation of each layer during the successive deposition stages was investigated by X-ray diffraction in Bragg-Brentano geometry, as presented in Fig. 3. The diffractograms are grouped according to the TM-diboride base layer, with the data in Fig. 3a corresponding to $WB_{1.9}$, in Fig. 3b to $TiB_{2.7}$, and in Fig. 3c to $HfB_{2.4}$, respectively. In addition, each subfigure is arranged from bottom to top, starting with the bare TM-diboride followed by the samples having an additional Al-Si-N, Si/Al-Si-O, or Si/Si-O top coating. All TM-diborides were synthesized as single-phased, α-TMB_2-structured (AlB_2 prototype) thin films. In particular, $WB_{1.9}$ and $TiB_{2.7}$ exhibit a clearly preferred (001) growth orientation. Contrary, the $HfB_{2.4}$ containing samples reveal a polycrystalline grain orientation. Both sample configurations with the Si interlayer further contain diffraction peaks corresponding to pure Si, suggesting that the Si interlayer is in a partly crystalline state.

However, the most striking observation in the diffractograms is that irrespective of the TM-diboride, all protective top layer variants were deposited in a fully X-ray amorphous state, as suggested by the lack of additional diffraction peaks. Solely two reflexes indicative of metallic Al [29] are observed for the samples containing Al-Si-N and Si/Al-Si-O top coatings. Following the SEM fracture cross section in Fig. 2, these peaks can be assigned to Al-rich macro-particles formed during the arc evaporation process.

3.3. Dynamic oxidation

The oxidation behavior of all coating variants including the bare TMB_2 thin films without protective top layer was investigated by dynamic oxidation experiments in synthetic air up to 1400 °C (10 °C/min heating rate). Fig. 4 presents the mass change of the coating material normalized to the coated area as function of the temperature. Please note, that the inert substrate material does not contribute to the recorded mass signal.

The reference measurements of the bare TMB_2 thin films clearly highlight the necessity for additional measures to sustain these materials in oxygen containing environments at elevated temperatures. While $WB_{1.9}$ and $TiB_{2.7}$ reveal a similar oxidation onset temperature of about 500 °C (see Fig. 4a-b), $HfB_{2.4}$ is able to tolerate temperatures between

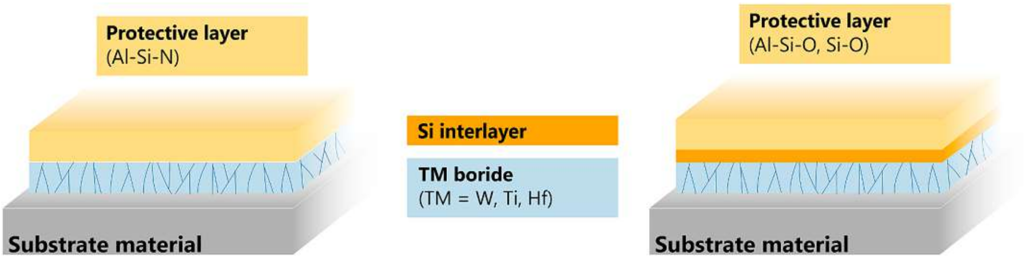

Fig. 1. Architectural design preserving $TMB_{2\pm z}$ coatings against high-temperature oxidation by introducing different protective top layers. The Si interlayer is solely present for Al-Si-O and Si-O top layers.

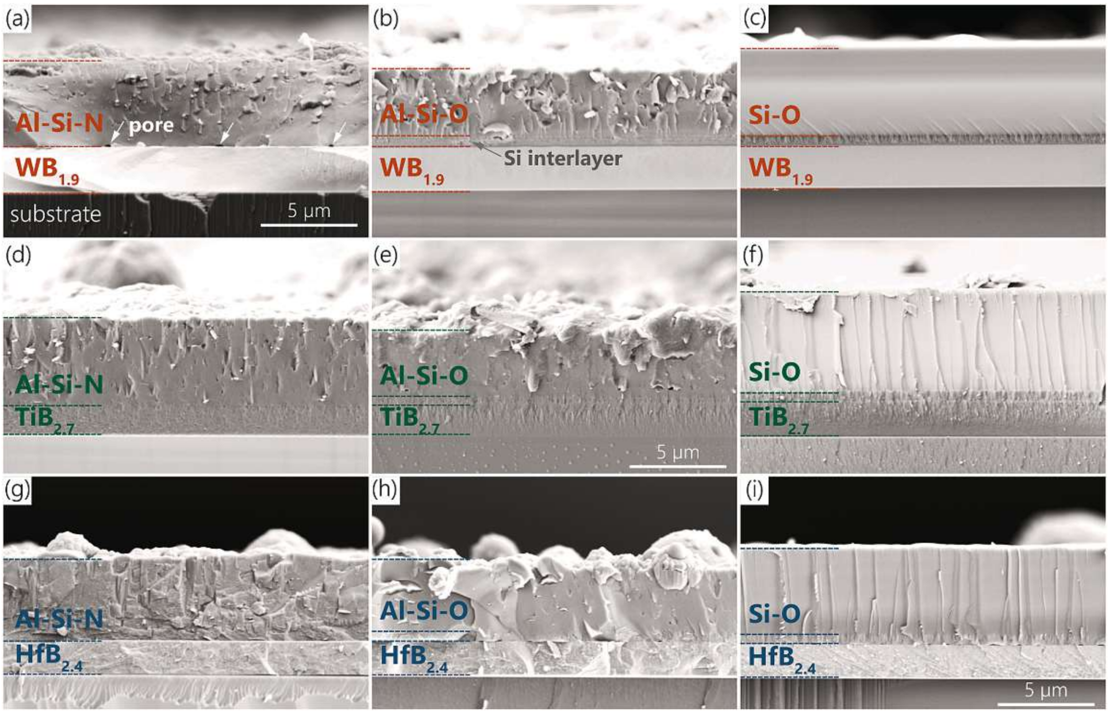

Fig. 2. SEM fracture cross sections of the as-deposited coatings on single-crystalline Al_2O_3 substrate. The upper image row depicts the $WB_{1.9}$-based thin films with an (a) Al-Si-N, (b) Al-Si-O, and (c) Si-O protective top layer. The center and bottom image rows display the same top layer sequence for (d-f) $TiB_{2.7}$ and (g-i) $HfB_{2.4}$ thin films, respectively. White arrows in (a) indicate small pores at the interface between the Al-Si-N and the $WB_{1.9}$ layer. An additional Si interlayer (as exemplarily marked in (b)) is present for all Al-Si-O and Si-O top layers.

700 and 750 °C before noticable mass gain is recorded (see Fig. 4c). The data confirms that the bare diboride materials (irrespective of the stoichiometry) are incapable of forming protective oxide scales, with the coating mass increasing to a respective maxima between 900 and 1200 °C. At temperatures beyond 1200 °C all TMB_2 thin films show a decreasing mass signal, which correlates to the volatilization of B_2O_3 [16,19].

Adding a protective Al-Si-N top coating to the TMB_2 thin films results in increased oxidation resistance for all samples, visible in a pronounced shift of the oxidation onset temperature to the range between 800 and 1000 °C. Interestingly, not only the oxidation onset temperature varies between the samples, also the recorded oxidation kinetics are markedly different. While the Al-Si-N coating on $WB_{1.9}$ suffers from accelerated mass gain – even exceeding the $WB_{1.9}$ reference data above 950 °C (see Fig. 4a) – the identical coating on $TiB_{2.7}$ and $HfB_{2.4}$ allows for enhanced oxidation resistance up to ~1000 °C before continued oxide scale growth is observed (see Fig. 4b-c). This drastic oxidation of the Al-Si-N on top of $WB_{1.9}$ is suggested to be caused by any unobserved microstructural defect/feature causing this kind of break away oxidation. The variations in CTE values (α_a and α_c, with a and c standing for the different crystallographic directions within the hexagonal system) among the three different diborides concerning the Al_2O_3 substrate may also play a role in the observed discrepancies in the oxidation kinetics. Considering theses distinctions (WB_2: $6.0 \cdot 10^{-6}$ and $9.4 \cdot 10^{-6}$ K^{-1} at 300 K for α_a and α_c, respectively; TiB_2: $5.9 \cdot 10^{-6}$ and $8.5 \cdot 10^{-6}$ K^{-1} at 300 K for α_a and α_c, respectively; HfB_2: $5.2 \cdot 10^{-6}$ and $6.0 \cdot 10^{-6}$ K^{-1} at 300 K for α_a and α_c, respectively [30,31]; Al_2O_3: $7 \cdot 10^{-6}$ K^{-1} at 300 K [32]), it is reasonable that WB_2 exhibits the least favorable substrate adhesion. Furthermore, the difference between the top layers/Si and the diborides also influence the behavior (Si: $2.6 \cdot 10^{-6}$ K^{-1} at 300 K [33]; AlN: $4.2 \cdot 10^{-6}$ and $5.3 \cdot 10^{-6}$ K^{-1} at 300 K for α_a and α_c, respectively [34]; Al-Si-O (mullite): 4–$6 \cdot 10^{-6}$ K^{-1} at 300 K [35,36]; SiO_2: $0.6 \cdot 10^{-6}$ K^{-1} at 300 K [37]). In addition, the small pores at the interface further supports rapid scale formation of the underlying boride, see cross section in Fig. 2a. Moreover, the Al-Si-N protected $TiB_{2.7}$ reveals a step-wise oxidation behavior with a stable mass plateau of ~0.10 mg/cm^2 between 850 and 1050 °C (see Fig. 4b), suggesting the temporary formation of a stable oxide scale prior to a full oxidation of the remaining coating material. In general, the step-wise oxidation is a combined process of an initial oxidation and a subsequent break away phenomenon. The general difference in oxidation behavior between these samples may be seen in varying growth morphologies of the Al-Si-N coating – note the absence of a uniform interlayer in the architecture – as well as from differences in thermal expansion to the base TMB_2 coatings. Overall, the dynamic oxidation tests involving Al-Si-N protective top layers did not result in the formation of a sufficient oxygen barrier above 1000 °C, hence these sample configurations were excluded from the following isothermal oxidation treatments (see Section 3.4).

In clear contrast to the Al-Si-N coated TMB_2 samples, both the Si/Al-Si-O and Si/Si-O coatings enable outstanding oxidation resistance irrespective of the diboride base layer, as indicated by negligible mass gain/loss over the entire temperature range. In detail, thin films with a protective Si/Al-Si-O top layer experience a total mass gain between 0.05 and 0.07 mg/cm^2, particularly in the temperature range above 1150 °C. This performance is even exceeded by Si/Si-O coated samples, which reveal a maximum mass change of 0.02 mg/cm^2. These results suggest that both protection layer concepts provide a stable, dense scale formation which prevents a continued and fast oxygen inward diffusion towards the unaffected coating material.

3.4. Isothermal oxidation

The long-term performance of the Si/Al-Si-O and Si/Si-O top coatings was further assessed by isothermal oxidation tests at 1200 °C for 3

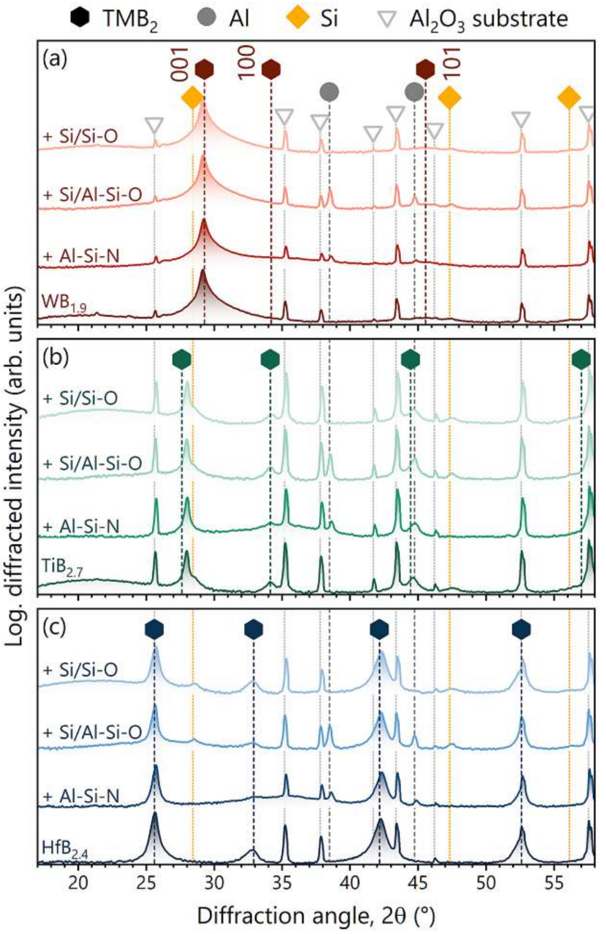

Fig. 3. X-ray diffractograms of all samples with (a) WB$_{1.9}$ (red hexagon, α-structure, [38]), (b) TiB$_{2.7}$ (green hexagon, α-structure, [39]), or (c) HfB$_{2.4}$ (blue hexagon, α-structure, [40]) coating as base layer. Each subfigure is arranged from bottom to top, starting with the pure TM-diboride coating followed by sample configurations with additional Al-Si-N, Si/Al-Si-O, or Si/Si-O top coating. All measurements were performed on coated polycrystalline Al$_2$O$_3$ substrates (light-grey triangle, [41]) in Bragg-Brentano geometry. Additional diffraction peaks correspond to metallic Al (dark grey circle, [29]) and Si (yellow diamond, [42]). (For interpretation of the references to colour in this figure legend, the reader is referred to the web version of this article.)

and 30 h in lab-air conditions, respectively. The resulting oxide scale formation was then investigated by cross-sectional microscopy analysis and in terms of phase formation by X-ray diffraction. Prior to these tests, vacuum annealing treatments were performed for 30 min at 800 °C to improve the adhesion of the Si interlayer to the TM-diboride as well as the protective top coating. This pretreatment was performed to minimize spallation of the oxide scale during sample cooling from 1200 °C. However, the oxidized WB$_{1.9}$-based samples were found to have fully delaminated from the polycrystalline Al$_2$O$_3$ substrates for both oxidation periods, indicating limited adhesion under the tested conditions and thus preventing further investigations. It should be noted, that WB$_2$ has the largest discrepancy of the CTE values in the c-axis direction, which may contribute to the observed delamination.

Fig. 5 displays the SEM fracture cross sections of all oxidized samples with a TiB$_{2.7}$ base layer. The upper image row (see Fig. 5a-c) corresponds to the Si/Al-Si-O top coating, whereas the bottom image row (see Fig. 5d-f) contains the Si/Si-O protected samples. From left-to-right the images are aligned with increasing duration of the oxidation treatment.

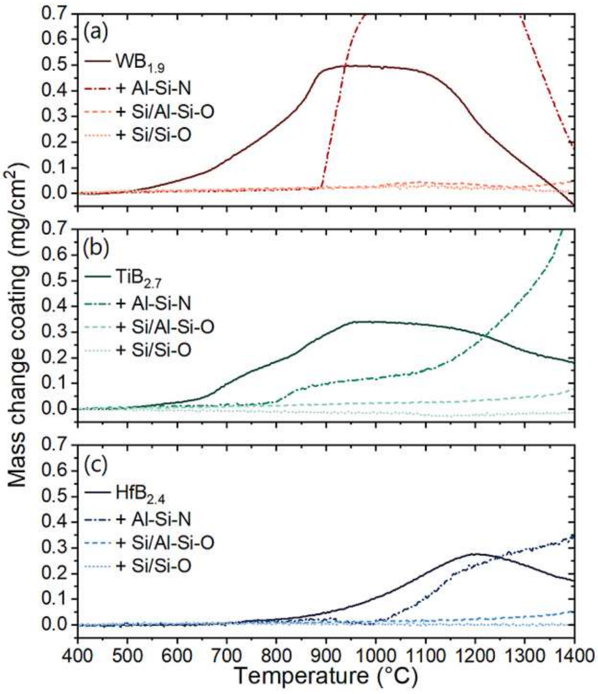

Fig. 4. Thermogravimetric analysis of the coating mass during dynamic oxidation up to 1400 °C in synthetic air. The data is grouped into (a) WB$_{1.9}$, (b) TiB$_{2.7}$, and (c) HfB$_{2.4}$ based coatings, with each section containing reference data of the bare TMB$_2$ thin film as well as with the three top layer variants Al-Si-N, Si/Al-Si-O, and Si/Si-O.

After 3 h of isothermal oxidation (see Fig. 5a-b), the protective Si/Al-Si-O layer exhibits a significant change in morphology. The protective coating shows increased porosity – in particular within the Si interlayer – and a pronounced increase in surface roughness when compared to the as-deposited state. The underlying TiB$_{2.7}$ coating, however, visually remains unchanged after the first annealing treatment. Furthermore, adhesion to the polycrystalline Al$_2$O$_3$ substrate appears to be intact. After 30 h oxidation at 1200 °C (see Fig. 5c), the pore formation within the Si interlayer progresses, whereas porosity in the Al-Si-O top coating appears reduced. Additional visual information is provided by FIB cross sections in the supplementary part (see Fig. S1), highlighting that fractured cross sections (as presented) in Fig. 5 also depend on the crack path compared to the FIB milled ones – obtaining a more continuous trend in scale thickness and pore formation.

Fig. 6a contains the corresponding X-Ray diffractograms, arranged from bottom to top with increasing oxidation time. The data recorded after 3 h already indicates the formation of several crystalline structures within the protective coating architecture. Comparison to standardized reference patterns suggests that the Al-Si-O coating crystallizes into an 3Al$_2$O$_3$·2SiO$_2$ mullite-based structure. In addition, the presence of both tetragonal and hexagonal SiO$_2$ as well as hints for a TiO$_2$ phase are observed. Also, the partly amorphous Si interlayer crystallizes at this temperature range. After 30 h, the intensity of all diffraction peaks including that of TiB$_2$ increases, suggesting continued crystallization and grain growth. Overall, the presence of the TiB$_2$ phase after the oxidation treatment shows the oxygen barrier capabilities of the protective layer concept.

The SEM images in Fig. 5d-f show TiB$_{2.7}$ coatings protected by Si/Si-O. The top coating has a dense, featureless morphology in the as-deposited state (see Fig. 5d), which is maintained throughout the oxidation treatment (see Fig. 5e-f). Moreover, the coating surface remains significantly smoother than for Si/Al-Si-O coated samples after

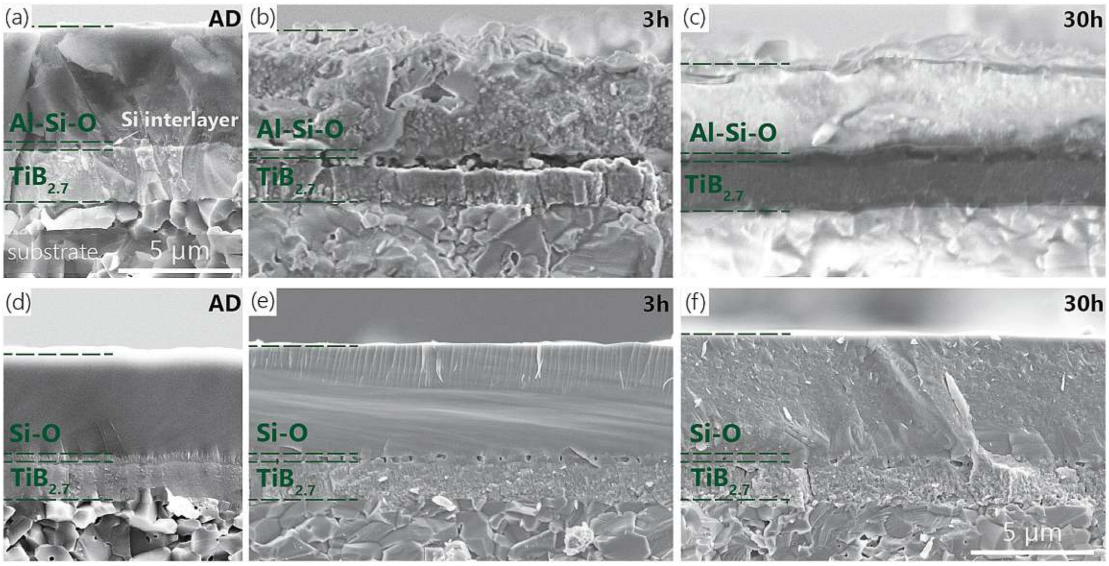

Fig. 5. SEM fracture cross sections of $TiB_{2.7}$ thin films protected with (a-c) Si/Al-Si-O and (d-f) Si/Si-O top coatings. (a) and (d) show the as-deposited state for reference (AD), (b) and (e) after 3 h, (c) and (f) after 30 h of isothermal oxidation at 1200 °C in ambient air. All images were recorded on coated polycrystalline Al_2O_3 substrates.

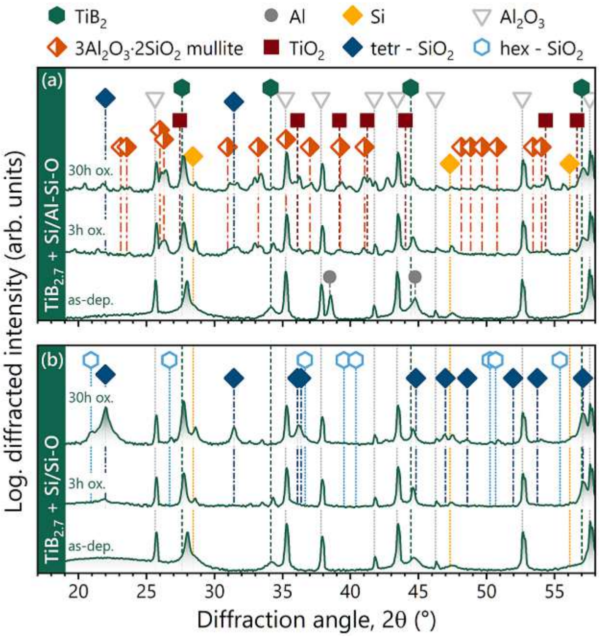

Fig. 6. XRD diffractographs of $TiB_{2.7}$ thin films protected with (a) Si/Al-Si-O and (b) Si/Si-O top coatings. In each group, the lower diffractograph represents the as-deposited state, followed by the data recorded after 3 and 30 h of isothermal oxidation at 1200 °C in ambient air, respectively. The data was collected from coated polycrystalline Al_2O_3 substrates (grey triangles, [41]). The following standardized reference patterns are included: hexagonal TiB_2 (green hexagon, α-structure, [39]), cubic Al (grey circle, [29]), cubic Si (yellow diamond, [42]), orthorhombic $3Al_2O_3{\cdot}2SiO_2$ (mullite, half-filled, orange diamond, [43]), tetragonal TiO_2 (dark red cube, [44]), tetragonal SiO_2 (blue diamond, [45]) and hexagonal SiO_2 (light blue, open hexagon, [46]). (For interpretation of the references to colour in this figure legend, the reader is referred to the web version of this article.)

oxidation. The data further shows that after 3 and 30 h, the Si interlayer exhibits initial signs of pore formation – indicative of accelerated diffusion processes – while the $TiB_{2.7}$ coating maintains a dense morphology throughout the full oxidation treatment. Overall, good adhesion between the individual layers is still recorded after 30 h at 1200 °C (see Fig. 5f), underlining the excellent protective character of the Si-O based top coat. The respective XRD data in Fig. 6b again shows the (re-)crystallization of all individual layers, with the initially amorphous Si/Si-O coating transforming into tetragonal- and hexagonal-structured SiO_2 next to the recrystallized Si interlayer after 3 and 30 h at 1200 °C, respectively.

Fig. 7 shows SEM fracture cross sections of the $HfB_{2.4}$-based coating architectures after identical isothermal oxidation treatments at 1200 °C for up to 30 h in ambient air. Following the arrangement of Fig. 5, all images corresponding to $HfB_{2.4}$ protected by Si/Al-Si-O top coatings are given in Fig. 7a-c, whereas the Si/Si-O coated samples are displayed in Fig. 7d-f. Moreover, from left-to-right the images refer to increasing durations of the oxidation treatment.

After 3 h of annealing at 1200 °C, $HfB_{2.4}$ protected by Si/Al-Si-O (see Fig. 7b), exhibits a more textured and granular morphology throughout all layers. In addition, the top surface of the protective Al-Si-O layer shows a pronounced increase in surface roughness. After 30 h of annealing (see Fig. 7c), all layers obtained a globular morphology with small pores formed throughout the $HfB_{2.4}$ as well as the Al-Si-O coating close to the Si interlayer. Additional visual support is provided by FIB cross sections, see Fig. S2 in the supplementary part. Nevertheless, the initial layered structure is distinctly maintained and the layer adhesion between the polycrystalline Al_2O_3 substrate and the subsequent layers is still given.

Similar to the $TiB_{2.7}$-based coating, the corresponding X-ray diffractograms in Fig. 8a reveal the formation of a crystalline $3Al_2O_3{\cdot}2SiO_2$ mullite phase after 3 and 30 h of isothermal annealing. Moreover, both the tetragonal- and hexagonal-structured variants of SiO_2 are formed next to hints for a monoclinic HfO_2 phase. Still, the hexagonal $HfB_{2.4}$ phase is well present after the entire annealing treatment, suggesting a recrystallization due to decreasing peak-width.

The final configuration of $HfB_{2.4}$ protected by a Si/Si-O coating is studied before and after oxidation in Fig. 7d-f. Analogous to the $TiB_{2.7}$-based coatings, both the Si-O and the TM-diboride layer maintain a

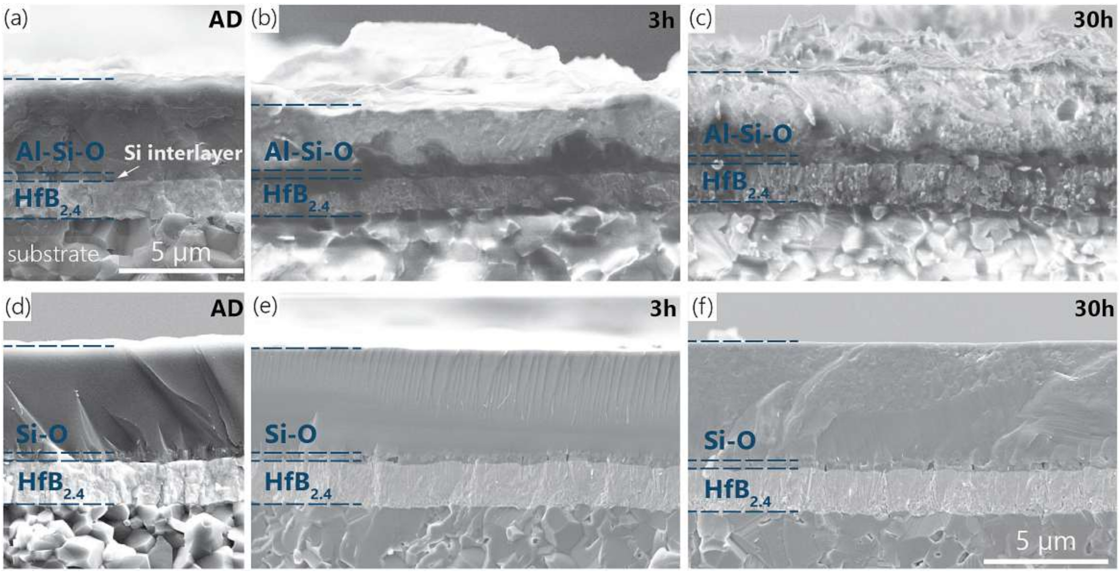

Fig. 7. SEM fracture cross sections of $HfB_{2.4}$ thin films protected with (a-c) Si/Al-Si-O and (d-f) Si/Si-O top coatings. (a) and (d) show the as-deposited state for reference (AD), (b) and (e) after 3 h, (c) and (f) after 30 h of isothermal oxidation at 1200 °C in ambient air. All images were recorded on coated polycrystalline Al_2O_3 substrates.

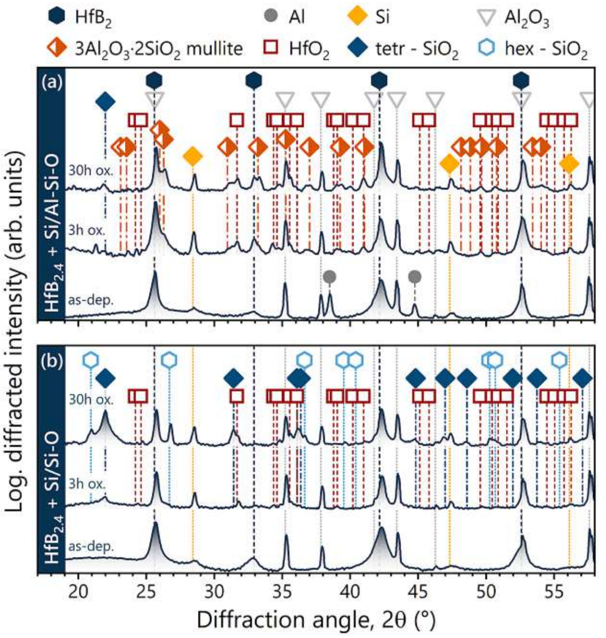

Fig. 8. XRD diffractographs of $HfB_{2.4}$ thin films protected with (a) Si/Al-Si-O and (b) Si/Si-O top coating. In each group, the lower diffractograph represents the as-deposited state, followed by the data recorded after 3 and 30 h of isothermal oxidation at 1200 °C in ambient air, respectively. The data was collected from coated polycrystalline Al_2O_3 substrates (grey triangles, [41]). The following standardized reference patterns are included: hexagonal HfB_2 (blue hexagon, α-structure, [40]), cubic Al (grey circle, [29]), cubic Si (yellow diamond, [42]), orthorhombic $3Al_2O_3{\cdot}2SiO_2$ (mullite, half-filled, orange diamond, [43]), monoclinic HfO_2 (dark red cube, [47]), tetragonal SiO_2 (blue diamond, [45]) and hexagonal SiO_2 (light blue, open hexagon, [46]). (For interpretation of the references to colour in this figure legend, the reader is referred to the web version of this article.)

highly dense morphology even after 30 h of annealing at 1200 °C. The porosity within the Si interlayer appears less pronounced, with excellent adhesion recorded for all layers.

Looking at the phase formation in Fig. 8b, next to an intact and recrystallized $HfB_{2.4}$ phase, again the formation of tetragonal and hexagonal SiO_2 is observed. In addition, the monoclinic HfO_2 structure appears to contribute to the excellent oxidation resistance observed for this coating architecture.

3.5. *Scale formation on $HfB_{2.4}$ at 1200 °C*

Based on the previously discussed dynamic and isothermal oxidation treatments, both the Si/Al-Si-O and Si/Si-O protective coatings showed exceptional high-temperature oxidation resistance up to 1200 °C on $TiB_{2.7}$ and $HfB_{2.4}$. In particular, the $HfB_{2.4}$ samples excelled with an intact layer structure, exceptional layer adhesion and a dense microstructure – especially within the Si interlayer – after annealing for 30 h in air at 1200 °C. Therefore, a more detailed investigation on the scale growth, chemical distribution, and microstructure was conducted on oxidized $HfB_{2.4}$ coatings with Si/Al-Si-O and Si/Si-O protective top coatings.

Fig. 9a shows a bright-field TEM micrograph of the $HfB_{2.4}$-Si/Al-Si-O coating architecture after 30 h of isothermal oxidation at 1200 °C. As suggested by the X-ray diffraction data (see Fig. 8a), large globular grains within the $HfB_{2.4}$ base layer confirm a recrystallization of the material, however, hardly any pores are visible within the diboride coating. The image also shows a perfectly continuous adhesion of the recrystallized Si interlayer to the $HfB_{2.4}$ and Al-Si-O coatings. Moreover, in agreement with previous SEM fracture cross sections (see Fig. 5a-c), the nanostructured protective top layer appears as rough and slightly porous, with large inclusions holding pure Si as determined by localized EDS analysis. The observed structure is strongly connected to the crystallization of the complex orthorhombic $3Al_2O_3{\cdot}2SiO_2$ mullite phase from the initially amorphous coating (compare with Fig. 8a).

To get an insight into the diffusion processes after annealing in the high-temperature regime, an EELS line-scan was recorded covering the entire coating architecture. In Fig. 9a the position and direction of the line-scan is indicated by a blue arrow. The chemical distribution

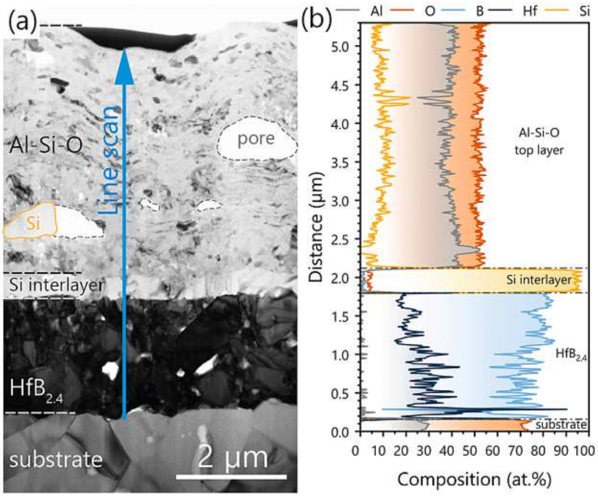

Fig. 9. TEM analysis of an oxidized $HfB_{2.4}$ thin film protected with an Al-Si-O top coating. The sample was annealed in ambient air at 1200 °C for 30 h. (a) Bright-field image of the sample cross section showing the polycrystalline Al_2O_3 substrate, the $HfB_{2.4}$ base layer, the Si interlayer, as well as the Al-Si-O protective coating from bottom to top. The blue arrow in (a) indicates the position and direction of the (b) EELS line-scan. (For interpretation of the references to colour in this figure legend, the reader is referred to the web version of this article.)

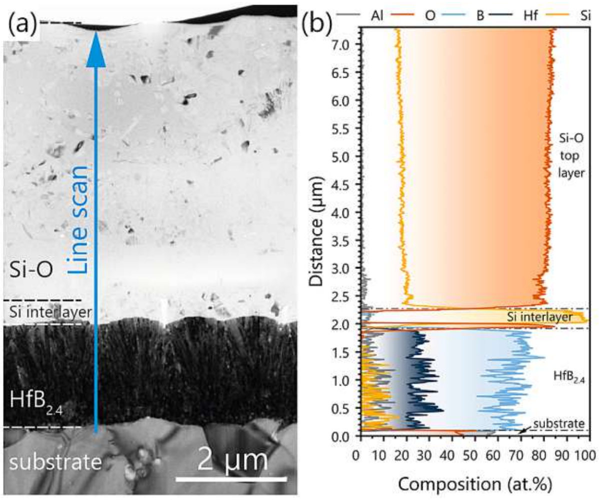

Fig. 10. TEM analysis of an oxidized $HfB_{2.4}$ thin film protected with a Si-O top coating. The sample was annealed in ambient air at 1200 °C for 30 h. (a) Bright-field image of the sample cross section showing the polycrystalline Al_2O_3 substrate, the $HfB_{2.4}$ base layer, the Si interlayer, as well as the Si-O protective coating from bottom to top. The blue arrow in (a) indicates the position and direction of the (b) EELS line-scan. (For interpretation of the references to colour in this figure legend, the reader is referred to the web version of this article.)

underlines an intact, layered structure after annealing at 1200 °C, with the individual coatings fully separated from each other. Hf appears to be slightly depleted towards the Si interlayer, with an average concentration of 30 at.% recorded close to the substrate near interface (note the close correlation with the chemistry determined by ICP-OES). Moreover, the HfO_2 observed during X-ray diffraction could not be identified in this localized analysis.

Furthermore, the line-scan shows a clear demarcation of the $HfB_{2.4}$ layer from the substrate and the adjacent Si interlayer. The absence of interdiffusion between HfB_2 and Si is in good correlation with previous works, where limited solubility was determined for Si in TMB_2 thin films, leading to a chemical separation upon thermal annealing [20,22]. Interestingly, the Al-Si-O-based protective layer shows pronounced porosity within the crystallized Al_2O_3-SiO_2 matrix. The pores are partly filled with Si, pointing towards excess Si (see Fig. 9b) within the mullite scale which subsequently concentrates in distinct locations.

Nevertheless, it can be stated that the selected coating system shows excellent oxidation resistance, tested at 1200 °C for up to 30 h. The oxygen diffusion into the diboride coating is fully suppressed, with only minor concentration detected within the Si interlayer. Hence, it can be concluded that the Al-Si-O layer served as a good protective barrier against oxygen at the tested conditions.

The bright-field image in Fig. 10a depicts the cross-sectional morphology of a $HfB_{2.4}$ thin film protected by a Si/Si-O top coating during 30 h of isothermal oxidation at 1200 °C. In contrast to the pronounced recrystallization of the diboride coating in Fig. 9a, the $HfB_{2.4}$ coating maintained a fine columnar morphology, typical for sputter-deposited thin films. Furthermore, the entire coating architecture appears as dense without noticeable pores in the microstructure or between the individual layers. Contrary to the Al-Si-O based top layer, the Si-O coating remained mostly amorphous with small SiO_2 crystallites embedded in the matrix.

As for the previously described sample with Al-Si-O top coating, an EELS line scan was recorded for $HfB_{2.4}$ protected with Si-O. Irrespective of the relative low Si solubility in TM diborides, a Si diffusion of about 5–10 at. % into the diboride layer can be indicated, which could possibly be the reason for inhibiting the recrystallization of the $HfB_{2.4}$ layer during the oxidation process. This is a highly interesting observation, as Si typically tends to separate within HfB_2 structures [22]. The ratio between B to Hf is nearly constant over the entire thickness of the diboride layer. At the interface to the Si layer, a very narrow O peak is visible, that may indicate a pore. Nevertheless, this layer also impressively withstood the challenging oxidative environment at 1200 °C since the diboride thin film remained entirely unaffected by O.

4. Conclusions

In this study, an effective architectural design is demonstrated to protect TM-diboride coatings against high-temperature oxidation. Reactively grown Al-Si-N, Al-Si-O, and Si-O top layer provide long-term stability for oxidation sensitive binary diborides up to 1200 °C. These architectural designs were applied to sputter deposited $WB_{1.9}$, $TiB_{2.7}$, and $HfB_{2.4}$ thin films. A pure Si adhesion layer was introduced to prevent *in-situ* oxidation during the synthesis of the oxide based top layers.

- Structural analysis of the as deposited coatings showed α-structured diborides in the base layers and X-ray amorphous top layers. The introduced Si adhesion layer obtained a crystalline character.
- During thermo-gravimetric screening up to 1400 °C, the Al-Si-N protective layers exhibited accelerated mass gain beyond 800–1000 °C, while Si-O and Al-Si-O experienced significantly fewer mass changes.
- In long-term isothermal oxidation tests as 1200 °C for 3 and 30 h, the $WB_{1.9}$ architectures delaminated. In contrast, the $TiB_{2.7}$ and $HfB_{2.4}$ thin films, protected by Al-Si-O and Si-O, maintained their layered structures even after 30 h.
- Detailed microstructural analysis of the $HfB_{2.4}$ based architectures confirmed the outstanding oxidation resistance, with no oxygen inward diffusion beyond the Si adhesion layer. The Al-Si-O layer on $HfB_{2.4}$ displayed more pronounced diffusion processes, forming a phase-separated Al_2O_3-SiO_2 scale. Additionally, the underlying $HfB_{2.4}$ was strongly recrystallized. In contrast, the fully dense Si-O

protective layer showed no pores, and the $HfB_{2.4}$ base layer remained unaffected.

CRediT authorship contribution statement

S. Richter: Conceptualization, Investigation, Data Analysis, Writing, Visualization, – original draft, **T. Glechner**: Conceptualization, Investigation, **T. Wojcik**: Investigation, **B. Widrig**: Investigation, **S. Kolozsvári**: Project Administration, Writing – Review & Editing, **P. Polcik**: Project Administration, Writing – Review & Editing, **O. Hunold**: Project Administration, Writing – Review & Editing, **L. Zauner**: Conceptualization, Data Analysis, Visualization, Writing – Review & Editing, **J. Ramm**: Conceptualization, Project Administration, Writing – Review & Editing, **H. Riedl**: Supervision, Conceptualization, Project Administration, Writing – Review & Editing.

Declaration of competing interest

The authors declare that they have no known competing financial interests or personal relationships that could have appeared to influence the work reported in this paper.

Data availability

Data will be made available on request.

Acknowledgments

The financial support by the Austrian Federal Ministry for Digital and Economic Affairs, the National Foundation for Research, Technology and Development and the Christian Doppler Research Association is gratefully acknowledged (Christian Doppler Laboratory "Surface Engineering of high-performance Components"). We also thank Plansee SE, Plansee Composite Materials GmbH, and Oerlikon Balzers, Oerlikon Surface Solutions AG for financial support. We also thank the X-ray center (XRC) of TU Wien for beam time and the electron microscopy center - USTEM TU Wien - for using the SEM and TEM facilities. Finally, we acknowledge TU Wien Bibliothek for financial support through its Open Access Funding Programme.

Appendix A

In addition, FIB cross sections were prepared of the samples oxidized at 1200 °C for 3 and 30 h in ambient air. In Fig. S1 as well as in Fig. S2, the layered structure consisting of TM diboride, Si interlayer and the two top coatings (Al-Si-O and Si-O) can be clearly seen, even after oxidation. The top layers are overexposed due to charging during imaging.

Based on the FIB cross sections, there is a clear tendency for the layer thickness to increase with increasing oxidation time. For the Al-Si-O top layer, more pronounced pore formation can be seen in (b–c) in both Fig. S1 and Fig. S2, which is partly due to phase transformation into the mullite structure $3Al_2O_3 \cdot 2SiO_2$. However, for the Si-O protected coatings, less pore formation is evident. In the oxidized state after 30 h, see (f) in Fig. S1 and Fig. S2, SiO_2 crystals are embedded in an amorphous Si-O matrix, which was verified by XRD and TEM investigations.

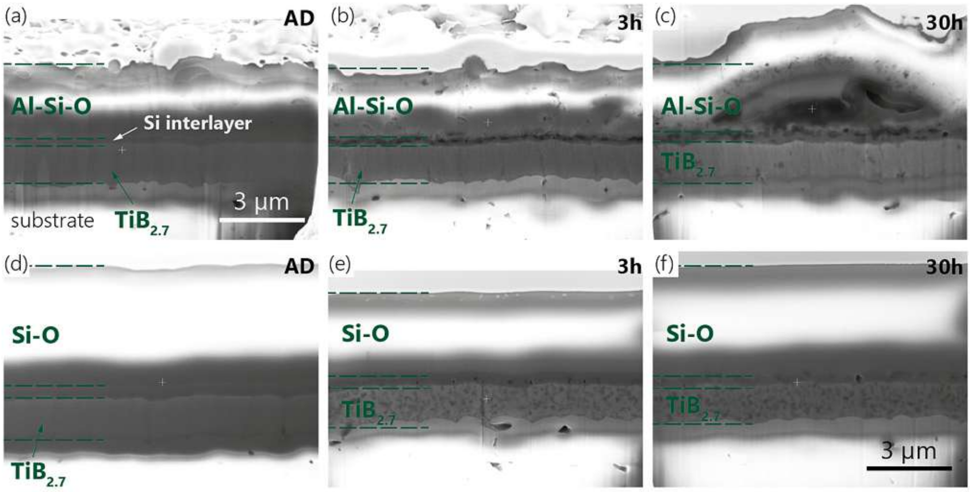

Fig. S1. FIB cross sections of $TiB_{2.7}$ thin films protected with (a–c) Si/Al-Si-O and (d–f) Si/Si-O top coatings. (a) and (d) show the as-deposited state for reference (AD), (b) and (e) after 3 h, (c) and (f) after 30 h of isothermal oxidation at 1200 °C in ambient air. All images were recorded on coated polycrystalline Al_2O_3 substrates.

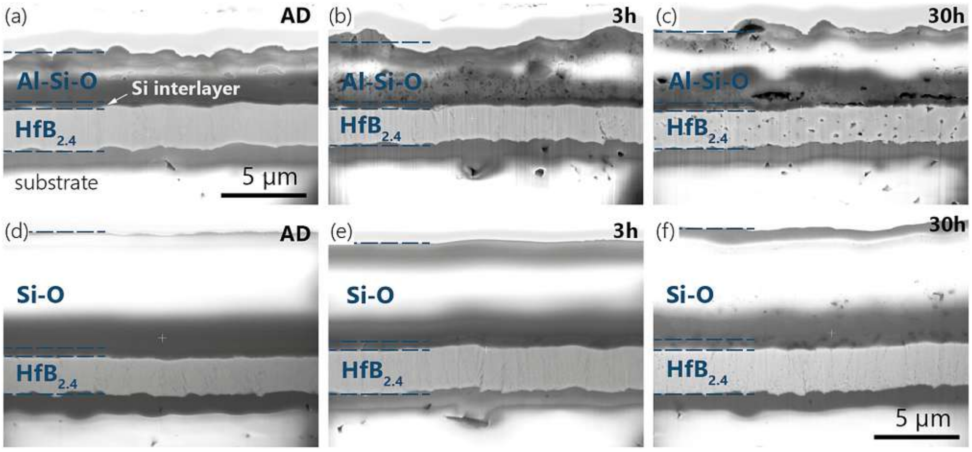

Fig. S2. FIB cross sections of $HfB_{2.4}$ thin films protected with (a–c) Si/Al-Si-O and (d–f) Si/Si-O top coatings. (a) and (d) show the as-deposited state for reference (AD), (b) and (e) after 3 h, (c) and (f) after 30 h of isothermal oxidation at 1200 °C in ambient air. All images were recorded on coated polycrystalline Al_2O_3 substrates.

References

[1] J.R. Rodgers, et al., Materials informatics, MRS Bull. 31 (2006) 975–980.

[2] B. Navinšek, et al., PVD coatings as an environmentally clean alternative to electroplating and electroless processes, Surf. Coat. Technol. 116–119 (1999) 476–487.

[3] S.-J. Lee, et al., Fabrication and properties of reactively hot pressed HfB_2-HfC ultra-high temperature ceramics, J. Korean Ceram. Soc. 47 (2010) 534–539, https://doi.org/10.4191/kcers.2010.47.6.534.

[4] W.G. Fahrenholtz, et al., Ultra-high temperature ceramics: materials for extreme environments, Scr. Mater. 129 (2017) 94–99.

[5] R. Savino, et al., Aero-thermo-chemical characterization of ultra-high-temperature ceramics for aerospace applications, J. Eur. Ceram. Soc. 38 (2018) 2937–2953.

[6] A. Nisar, et al., Ultra-high temperature ceramics: aspiration to overcome challenges in thermal protection systems, Ceram. Int. 48 (2022) 8852–8881.

[7] B.R. Golla, et al., Review on ultra-high temperature boride ceramics, Prog. Mater. Sci. 111 (2020), 100651.

[8] G.-J. Zhang, et al., Ultrahigh temperature ceramics (UHTCs) based on ZrB2 and HfB2 systems: powder synthesis, densification and mechanical properties, J. Phys. Conf. Ser. 176 (2009), 012041.

[9] W.G. Fahrenholtz, A historical perspective on research related to ultra-high temperature ceramics, in: Ultra-High Temperature Ceramics, John Wiley & Sons, Inc, Hoboken, NJ, 2014, pp. 6–32.

[10] M. Magnuson, et al., Review of transition-metal diboride thin films, Vacuum 196 (2022), 110567.

[11] X. Huang, et al., Investigation of mechanical properties and oxidation resistance of CVD TiB2 ceramic coating on molybdenum, J. Mater. Res. Technol. 9 (2020) 282–290.

[12] B. Bakhit, et al., Improving the high-temperature oxidation resistance of TiB2 thin films by alloying with Al, Acta Mater. 196 (2020) 677–689.

[13] T. Glechner, et al., Influence of the non-metal species on the oxidation kinetics of Hf, HfN, HfC, and HfB2 coatings, Mater. Des. 211 (2021), 110136.

[14] Y.-H. Koh, et al., Oxidation behavior of titanium boride at elevated temperatures, J. Am. Ceram. Soc. 84 (2001) 239–241.

[15] W.G. Fahrenholtz, et al., Oxidation of ultra-high temperature transition metal diboride ceramics, Int. Mater. Rev. 57 (2012) 61–72.

[16] T.A. Parthasarathy, et al., A model for the oxidation of ZrB2, HfB2 and TiB2, Acta Mater. 55 (2007) 5999–6010.

[17] R. Naraparaju, et al., Effect of moisture on the oxidation behavior of ZrB2, J. Am. Ceram. Soc. 104 (2021) 1058–1066.

[18] P. Sarin, et al., In situ studies of oxidation of ZrB2 and ZrB2–SiC composites at high temperatures, J. Eur. Ceram. Soc. 30 (2010) 2375–2386.

[19] T. Glechner, et al., Influence of Si on the oxidation behavior of TM-Si-B2±z coatings (TM = Ti, Cr, Hf, Ta, W), Surf. Coat. Technol. 434 (2022), 128178.

[20] L. Zauner, et al., Role of Si segregation in the structural, mechanical, and compositional evolution of high-temperature oxidation resistant Cr-Si-B2±z thin films, J. Alloys Compd. 944 (2023), 169203.

[21] T. Glechner, et al., Oxidation resistance of Si doped transition metal diborides at elevated temperatures, Int. J. Refract. Met. Hard Mater. 113 (2023), 106172.

[22] T. Glechner, et al., High temperature oxidation resistance of physical vapor deposited Hf-Si-B2±z thin films, Corros. Sci. 205 (2022), 110413.

[23] A. Bahr, et al., Oxidation behaviour and mechanical properties of sputter-deposited TMSi2 coatings (TM = Mo, Ta, Nb), J. Alloys Compd. 931 (2023), 167532.

[24] Z. Wu, et al., Improving oxidation and wear resistance of TiB2 films by nano-multilayering with Cr, Surf. Coat. Technol. 436 (2022), 128337.

[25] Plansee Composite Materials, Plansee Composite Materials. https://www.plansee.com/de/unternehmen/kontakt/deutschland.html (accessed January 10, 2023).

[26] C. Fuger, et al., Revisiting the origins of super-hardness in TiB2+z thin films – impact of growth conditions and anisotropy, Surf. Coat. Technol. 446 (2022), 128806.

[27] S. Dorri, et al., Oxidation kinetics of overstoichiometric TiB2 thin films grown by DC magnetron sputtering, Corros. Sci. 206 (2022), 110493.

[28] J. Neidhardt, et al., Experiment and simulation of the compositional evolution of Ti–B thin films deposited by sputtering of a compound target, J. Appl. Phys. 104 (2008), 063304.

[29] International Center of Diffraction Data, Powder Diffraction File - Cubic Al - 00-004-0787, 1954.

[30] B. Lönnberg, Thermal expansion studies on the group IV–VII transition metal diborides, J. Less Common Metals 141 (1988) 145–156.

[31] C.L. Jiang, et al., Determination of the thermal properties of AlB2-type WB2, Appl. Surf. Sci. 288 (2014) 324–330.

[32] CTE Al2O3 substrates, Kerafol. https://www.kerafol.com/_wpframe_custom/downloads/files/KERAFOL_Datenblatt_Keral99_07-17__095151-14012020.pdf (accessed September 4, 2023).

[33] H. Watanabe, et al., Linear thermal expansion coefficient of silicon from 293 to 1000 K, Int. J. Thermophys. 25 (2004) 221–236.

[34] H. Morkoç, Aluminum, gallium, and indium nitrides, in: Encyclopedia of Materials: Science And, 2001. https://ui.adsabs.harvard.edu/abs/2001emst.book..121M/abstract.

[35] J.S. Moya, et al., Sintering, in: R.A. Meyers (Ed.), Encyclopedia of Physical Science and Technology (Third Edition), Academic Press, New York, 2003, pp. 865–878.

[36] T.F. Choo, et al., A review on synthesis of mullite ceramics from industrial wastes, Recycl. Today 4 (2019) 39.

[37] L. Filipovic, Topography Simulation of Novel Processing Techniques, Technische Universität Wien, 2012. https://repositum.tuwien.at/handle/20.500.12708/13712. (Accessed 1 September 2023).

[38] International Center of Diffraction Data, Powder Diffraction File - Hexagonal WB2 - 04-003-6624, 2005.

[39] International Center of Diffraction Data, Powder Diffraction File - hexagonal TiB2 - 00-035-0741, 1985.

[40] International Center of Diffraction Data, Powder Diffraction File - Hexagonal HfB2 - 04-002-0174, 2005.

[41] International Center of Diffraction Data, Powder Diffraction File - Hexagonal Al2O3 - 01-088-5737, 2022.

[42] International Center of Diffraction Data, Powder Diffraction File - Cubic Si - 00-005-0565, 1955.

[43] International Center of Diffraction Data, Powder Diffraction File - Orthorhombic (Al2O3)3·2(SiO2) - 00-070-0189, 2020.

[44] International Center of Diffraction Data, Powder Diffraction File - Tetragonal TiO2 - 00-021-1276, 1970.

[45] International Center of Diffraction Data, Powder Diffraction File - Tetragonal SiO2 - 04-007-5015, 2005.

[46] International Center of Diffraction Data, Powder Diffraction File - hexagonal SiO2 - 01-085-0865, 1999.

[47] International Center of Diffraction Data, Powder Diffraction File - Monoclinic HfO2 - 00-034-0104, 1984.

Publication III

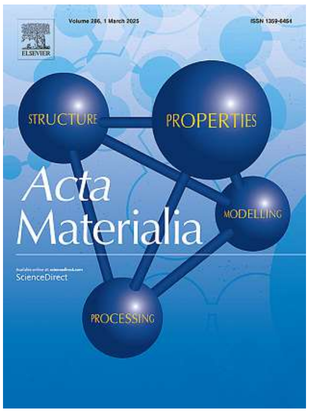

High-throughput phase exploration of ternary transition metal carbide TM-X-C (X=Al/Si) thin films

S. Richter, C. Gutschka, D. Danner, R. Hahn, T. Wojcik, E. Ntemou, C. Jerg, J. Ramm, P. Polcik, S. Kolozsvári, D. Primetzhofer, H. Riedl

Acta Materialia, 288 (2025) 120839.

Acta Materialia 288 (2025) 120839

Contents lists available at ScienceDirect

Acta Materialia

journal homepage: www.elsevier.com/locate/actamat

High-throughput phase exploration of ternary transition metal carbide TM-X-C (X=Al/Si) thin films

S. Richter [a,*], C. Gutschka [a], D. Danner [a], R. Hahn [a], T. Wojcik [a], E. Ntemou [b], C. Jerg [c], J. Ramm [c], P. Polcik [d], S. Kolozsvári [d], D. Primetzhofer [b], H. Riedl [a,e]

[a] *Christian Doppler Laboratory for Surface Engineering of High-Performance Components, TU Wien, Austria*
[b] *Department of Physics and Astronomy, Uppsala University, Uppsala 75120, Sweden*
[c] *Oerlikon Balzers, Oerlikon Surface Solutions AG, Balzers 9496, Liechtenstein*
[d] *Plansee Composite Materials GmbH, Lechbruck am See 86983, Germany*
[e] *Institute of Materials Science and Technology, TU Wien, Wien 1060, Austria*

ARTICLE INFO

Keywords:
Ternary carbides
PVD
Solid solutions
DFT
Phase analysis

ABSTRACT

Transition metal carbides (TMCs) are highly valued for their exceptional thermal stability (melting temperatures up to 4000 °C), refractory character, and outstanding mechanical properties, particularly hardness. These properties make TMCs crucial for applications in extreme conditions, such as in aerospace and tooling industries. Striving for novel oxidation-resistant ternary carbides, we systematically screened the phase formation of TM-X-C (where X = Al or Si) using a combined theoretical and experimental high-throughput approach. Density functional theory (DFT) calculations forecast the phase formation of (meta)stable TM-X-C solid solutions (with TM = Ti, Zr, Hf, Ta, W) using the formation energy and lattice constant ratios as structural key parameters. These theoretical predictions are experimentally validated by synthesizing over 260 compositions across the 10 different TM-X-C material systems by combinatorial magnetron sputtering. The DFT calculations indicated that Si preferentially occupies both C and TM sites, while Al tends to fill TM sites. Structural analysis experimentally confirmed the formation of face-centered-cubic TM-X-C solid solutions up to alloying contents of 25–30 at.% – for all material families except W-X-C. Additional TEM investigation confirmed the formation of fcc solid solutions. A strong correlation between prevalent phases and mechanical properties is observed, with the highest hardness values (30–40 GPa) found for fcc structured TM-X-C thin films, followed by a significant decrease entering multi-phased or amorphization phase regions – typically occurring above 25 at.% Al or Si. This comprehensive phase screening paves the way for a targeted development of novel TM-X-C ceramic thin film materials.

1. Introduction

Ultra-high temperature ceramics (UHTC) are a class of materials known for their exceptional thermal stability and mechanical strength, making them indispensable in extreme environments [1–3]. These ceramics, which comprise early transition metal (TM) borides, carbides, and nitrides, are typically defined by their melting temperatures above 3000 °C [2,4]. Among them, the solid solution system TaC-HfC ($Ta_{0.8}Hf_{0.2}C$) is particularly noteworthy as one of the highest known melting materials with T_M of almost 3960 to 4027 °C [5–9]. Next to this exceptional feature, UHTCs obtain further properties, making them resilient to extreme temperatures, heat fluxes, radiation levels, mechanical loads, and chemical attacks beyond the capabilities of existing materials. These remarkable characteristics of UHTCs are attributed to the strong covalent bonds between transition metal atoms and non-metals and the non-metals themselves [2,10]. Consequently, conventional UHTCs play a critical role in applications where temperatures exceed 2000 °C, such as aerospace (e.g., hypersonic vehicles, atmospheric re-entry vehicles), plasma-facing materials or cutting tools, where materials must maintain their strength under extreme conditions [1,11,12]. Although UHTCs are highly resistant to high temperatures and are characterized as refractory, they reflect a weakness: their poor oxidation resistance in O_2-containing atmospheres. Primarily TM carbides are known to form metal oxycarbides with O_2 environments, providing only partial protection, as gaseous volatilization of CO and CO_2 causes cracking even at low temperatures [13].

---

* Corresponding author.
E-mail address: sophie.richter@tuwien.ac.at (S. Richter).

https://doi.org/10.1016/j.actamat.2025.120839
Received 28 November 2024; Received in revised form 3 February 2025; Accepted 15 February 2025

Therefore, the exploration of novel oxidation resistant transition metal carbide-based materials is crucial to further increase their usability and fully utilize their potential. In this context, $M_{n+1}AX_n$ phases – a class of nano-layered (ternary) early transition metal carbides and nitrides with hexagonal structure (M refers to a transition metal, A is a metal mostly from groups IIIA or IVA, and X stands for carbon or nitrogen, $n = 1, 2, 3$, short form MAX) – have attracted attention due to their improved oxidation resistance, especially when A is aluminum or silicon [14–19]. Among MAX based materials [15,18,20–25], Ti_2AlC is extremely resistant as oxidation temperatures of about 1400 °C can be reached. However, MAX phases and protective coatings based on them usually need to be annealed after deposition to preserve their unique ordered crystal structure and associated properties [26,27].

A promising alternative is the creation of disordered face-centered cubic (fcc) solid solutions of transition metal carbides and strong oxide formers such as silicon and aluminum. Previous studies on plasma-sprayed TiC thin films alloyed with Si (Ti-Si-C system, using Ti and Si powders, as well as sucrose as carbon precursor) proved the formation of a TiC phase alongside Ti_5Si_3 and TiO_3 after fabrication (as deposited state) [28]. Wilhelmsson et al. [29] observed a solid solution for the Ti-Al-C system at low substrate temperatures (300 °C) during DC magnetron co-sputtering of Ti, Al, and C, respectively. At higher deposition temperatures, phase-pure MAX phases (Ti_3AlC_2 and Ti_2AlC) and Ti_3AlC (perovskite phase) could be stabilized. In another study by Lauridsen et al. [30], the formation of nanocrystalline TiC (single crystalline phase) together with amorphous C and SiC was demonstrated after magnetron sputtering of a Ti_3SiC_2 compound target. The formation of ternary fcc-structured TM-X-C solid solutions ($X =$ Al or Si) was highlighted in different studies [22,31–38] focusing on various synthesis routes and properties. However, for thin films a compositional variety up to 15 at. % was screened by various studies [39,40], obtaining predominantly amorphous structures. For example, Gaydaychuk et al. [38] have synthesized Hf-Al-C fcc solid solution thin films between 5 and 10 at.% Al, or Lindquist et al. [35] sputter deposited (Ti,Al)C nanocomposites in an amorphous C matrix targeting only one specific composition of about 29 at.% Al at 45 at.% C. Furthermore, Du et al. [34] have investigated the Ta-Si-C systems varying the Si content between 0 and 31 at. %, whereas Andersson et al. [41] focused on a similar range for Zr-Si-C. Nevertheless, the phase space of combining low melting materials such as Al and Si (and their ability to form strong oxides) with refractory transition metal carbide thin films is still uncharted and requires more in-depth exploration and therefore systematic screening.

Therefore, this work systematically explores the phase space through combinatorial sputtering of Si and Al alloyed TMC (TM = Ti, Zr, Hf, Ta, W) thin films, guided by density functional theory (DFT) calculations. Specifically, DFT is used to determine solubility trends for metastable solid solutions and the structural stability of the cells. A simple synthesis route using a combinatorial physical vapor deposition (PVD) approach is employed, allowing the sophisticated combination of low melting materials (Al, Si) and refractory TMCs based on conditions far from the thermodynamic equilibrium. This not only identifies new coating materials but also creates a comprehensive database. The study examines over 260 compositions describing the phase boundaries of face-centered cubic solid solutions using a high-throughput approach, comparing theoretical predictions with experimental observations of the phase evolution. Additionally, the findings are supplemented by mechanical property data, specifically hardness and Young's modulus, which were measured through nanoindentation experiments (CSM technique). This comprehensive approach enhances the understanding of novel UHT ceramics, TM-X-C solid solutions. These coatings have the potential for numerous applications, including implementation as adhesion layers in environmental barrier coatings [42] and as protective coatings in aerospace or tooling industry. By exploring the alloying behavior and the potential for incorporating Al and Si into TMCs, we aim to identify promising candidates for future studies focused on their oxidation behavior.

2. Methods

2.1. Computational details

In this study, 3 × 3 × 3 supercells were constructed from the carbide's primitive trigonal cells (space group 225), comprising 27 transition metal (TM) and 27 carbon sites. In these supercells, TMs comprise Ti, Zr, Hf, Ta, and W. The Special Quasi-random Structure (SQS) method [43] using the sqsgenerator python suit [44] was used to model the random alloying with Si or Al (denoted as X). The X atoms were distributed either on the transition metal sublattice or on the carbon sublattice. In addition, a mixed sublattice alloy was investigated in which the Si and Al were evenly distributed on both sublattices. The DFT calculations were performed using the Vienna Ab initio Simulation Package (VASP) [45] and the electron-electron exchange-correlation interactions were treated with the Generalized Gradient Approximation (GGA) [46]. Further details of the calculations are given in Appendix A.1.

The energies of formation E_f of the compounds were calculated by using the total energies per atom of hcp-Ti (SG 194), hcp-Zr (SG 194), hcp-Hf (SG 194), fcc-Ta (SG 225), bcc-W (SG 229), fcc-Al (SG 225), and diamond-Si (SG 227), respectively. A resulting negative E_f was used as an indicator for chemical (meta)stability, with respect to the unary elements. Deviations of the lattice symmetry were additionally used to track the distortion of the compounds, with a threshold of ±5 % of the ratio a/b or a/c set as a breakdown of a (meta)stable solid solution phase. However, a decomposition of the ternary compounds into binary and/or unary phases, according to the convex hull, was not taken into account in the discussion of this study.

2.2. Deposition process

All Al and Si alloyed TMC thin films were synthesized using an AJA Orion 5 [47] deposition system with 3" TMC targets. Stoichiometric powder metallurgically produced compound target materials including TiC, ZrC, HfC, and TaC, as well as a WC/C target (70/30 mol%) for W-X-C coatings have been utilized. The system was additionally equipped with two 2" cathodes, one for Al and the other for Si, respectively. The cathodes and targets were confocally aligned. All targets have been provided by Plansee Composite Materials GmbH [48] and operated in magnetron sputtering mode with Ar (purity of 99.999 %) as the working gas. Following a combinatorial screening approach to achieve a broad variety of chemical compositions within the ternary phase space, the TMC target was co-sputtered with Al or Si without substrate rotation, resulting in the formation of TM-Al/Si-C thin films. Further details of the coating synthesis are given in Appendix A.2.

2.3. Coating characterization

Time-of-Flight Elastic Recoil Detection Analysis (ToF-ERDA) and Elastic Backscattering Spectrometry (EBS) were used to obtain the chemical composition of selected TM-X-C thin films. The experiments were performed at the 5 MV Pelletron Tandem accelerator at Uppsala University [49]. Subsequently, ERDA-calibrated XRF measurements were performed at TU Wien to determine the chemical composition of all samples. The phase formation was determined using X-ray diffractometry in Bragg-Brentano geometry, the crystal structure and morphology were examined using transmission electron microscopy (TEM, FEI TECNAI F20). The mechanical properties such as hardness and Young's modulus were determined using an FT-I04 Femto-Indenter and the continuous stiffness measurement (CSM) technique. Further details of the coating characterization techniques can be found in Appendix A.3.

3. Results and discussion

Initially, DFT calculations for binary and ternary TM-X-C provided a crucial theoretical foundation for the experimental work. Using a combinatorial high-throughput approach, we synthesized and characterized over 260 samples across 10 material systems, which include 5 transition metals (TM = Ti, Zr, Hf, Ta, W) and 2 alloying elements (X = Al, Si) with varied compositions.

3.1. Phase boundary exploration by DFT

First-principles calculations serve as the basis to assess the phase boundaries of ternary fcc-structured TM-X-C ceramics, using simple measures such as the lattice parameters and energy of formation, E_f, as evaluation criteria. In the first step, the focus was set on stoichiometric compounds with a transition metal to carbon ratio TM to C of 1/1, without considering the presence of defects or non-stoichiometric variations. To gain insights for different sub-lattice occupations Al/Si have been positioned on the metal (TM) sites, resulting in the designation (TM,X)C, or on the non-metal sublattice (C sites), resulting in the labeling TM(X,C). In addition, a scenario in which both the TM and C sites were equally occupied by X (Al or Si) was studied, motivated through their high configurational entropy, labeled as (TM,X)(X,C).

Fig. 1 presents the theoretical solubility limits of Al and Si in the fcc NaCl structure of TiC, focusing on two important limiting cases: *(i)* chemical instability, where the E_f exceeds 0 eV/atom, and *(ii)* structural instability, where significant lattice distortion occurs, disrupting the fcc symmetry. Structural instability is identified by deviations of the lattice parameter ratios a/b or a/c from the ideal value of 1 ($a/b = a/c = 1$ for fcc), indicating the loss of fcc (meta)stability: a threshold of ±5% deviation from $a/b = a/c = 1$ was assumed. These limits for the structural stability was motivated by NaCl structured nitrides, such as TiAlN, ZrAlN and HfAlN, and their lattice parameter changes as a function of the AlN mole fraction with respect to decomposition [50]. The structural stability is illustrated in Fig. 1a, b for Ti-Al-C, where the green shaded areas represent the stability range of (meta)stable fcc phases.

Regarding the underlying structural meta(stability) criteria, Fig. 1a, b clearly proves that the fcc structure remains (meta)stable over a range of 0 to 45 at.% Al when Al replaces Ti atoms, indicated by almost constant a/b and a/c ratios close to 1. In contrast, when Al occupies both Ti and C lattice sites or C sites exclusively, the lattice is significantly distorted and the structure loses fcc symmetry – even at low Al concentrations (around 5 at.%). For the Ti-Al-C system, the solubility limit is not only constrained by structural instability but also by chemical instability. As illustrated in Fig. 1c, E_f for the (Ti,Al)C phase crosses 0 eV/atom at approximately 27 at.% Al, thereby defining the theoretical solubility limit with respect to the unary species. It is important to note that these calculations do not consider any potential competing phases and focus solely on the trends of the Ti-Al-C system. Fig. 1c also evidences that the formation energy for the binary TiC is −0.809 eV/atom and increases with increasing Al content for all different occupation types. Up to 10 at.% Al, the E_f for Al occupying Ti, C, or both sites is almost similar, with the differences becoming more pronounced with increasing Al content. These curves show lower E_f values than (Ti,Al)C but remain unstable due to the lack of fcc symmetry, consistent with the observed structural instability in Fig. 1a, b.

A similar trend is observed in the Ti-Si-C system. Fig. 1d, e illustrates the lattice parameter ratios (a/b and a/c) for Si alloying in the Ti-Si-C system over a range from 0 to 45 at.% Si. As shown in Fig. 1d, e, the fcc structure remains (meta)stable when Si replaces Ti atoms and maintains fcc symmetry over the entire composition range. The maximum solubility limit in this case is also defined by chemical instability, as highlighted in Fig. 1f, where the E_f for (Ti,Si)C at about 25 at.% exceeds 0 eV/atom. Remarkably, the (Ti,Si)(Si,C) curve also shows only small deviations from $a/b = 1$ in the low-alloyed region (< 20 at.%) and the E_f remains negative in this region, indicating that Si at low concentrations could occupy both Ti and C sites, with Ti sites being preferred. Similar to the Ti-Al-C system, the energy of formation in the Ti-Si-C increases with increasing Si content.

Fig. 2 illustrates the energy of formation for all further transition

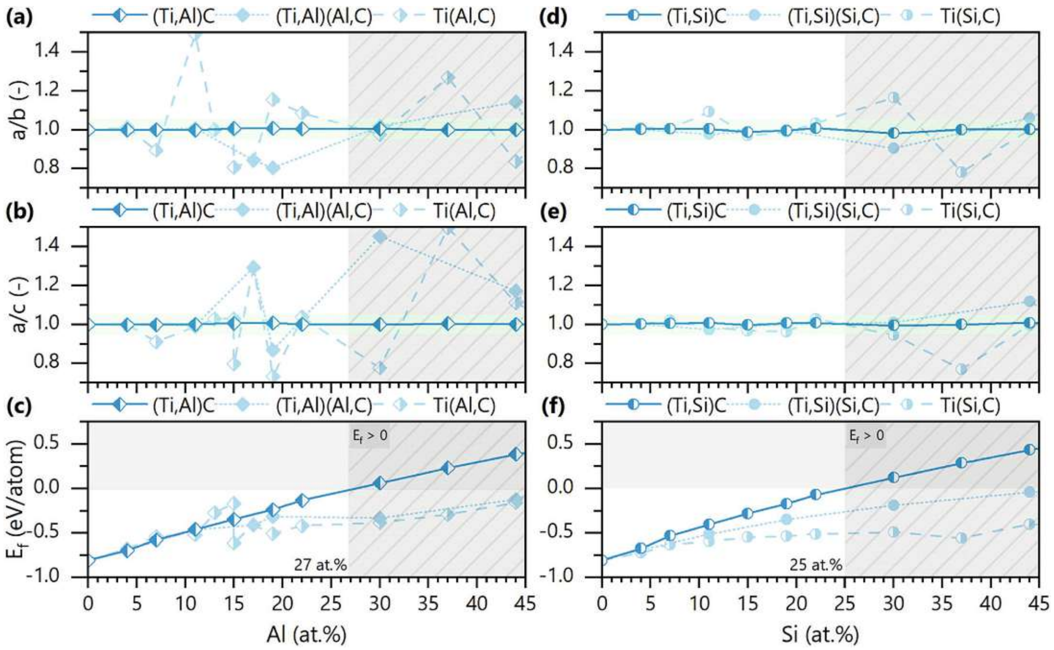

Fig. 1. Evolution of the solubility limit (shaded area) of X=Al/Si in fcc-structured Ti-X-C using E_f as an indicator for chemical stability and the lattice constant ratios as structural indicators. (a) and (b) represent the structural stability for fcc structured Ti-Al-C considering the ratios of lattice constants a/b and a/c, whereas (d) and (e) show the structural modifications of Ti-Si-C, respectively. (c) and (f) represent E_f,of Ti-Al/Si-C with the following labels: (TM,X)C: X is located at a TM site, TM(X, C): X is located at a C site, and (TM,X)(X,C): X is evenly distributed between TM and C sites.

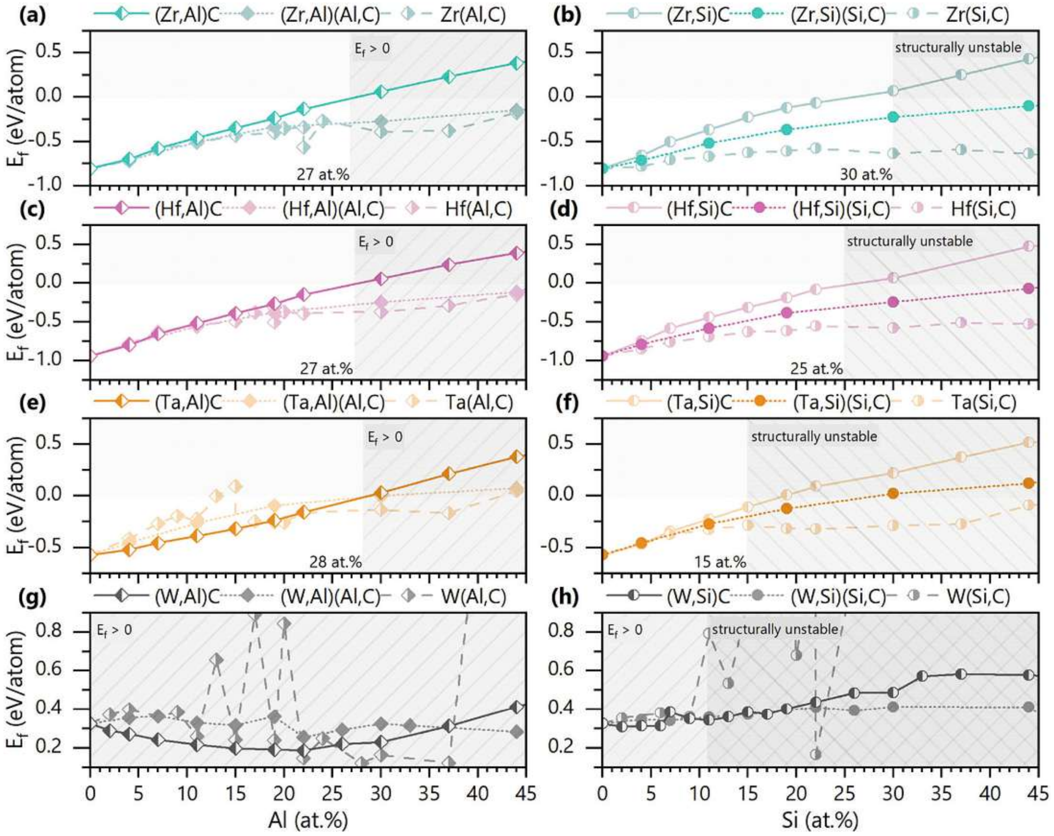

Fig. 2. Energy of formation (E_f) and solubility limit (shaded area) of Al/Si for various ternary fcc TM-Al/Si-C systems (solid solution), including (a) Zr-Al-C, (b) Zr-Si-C, (c) Hf-Al-C, (d) Hf-Si-C, (e) Ta-Al-C, (f) Ta-Si-C, (g) W-Al-C, and (h) W-Si-C, with the following labels: (TM,X)C: X is on a TM site, TM(X,C): X is located at a C site, and (TM,X)(X,C): X is equally distributed between TM and C sites.

metal carbide systems investigated (TM = Zr, Hf, Ta, W) as a function of alloy content (X=Al/Si), with solubility limits indicated based on criteria for structural and chemical instability. Following the methodology outlined in Fig. 1, chemical instability is characterized by an energy of formation exceeding 0 eV/atom, while structural instability occurs when the fcc structure experiences significant deformation. Fig. 2 provides a comprehensive overview of these findings, and additional structural details, including lattice ratios a/b and a/c, can be found in Appendix B.

Fig. 2a, b illustrates the formation energy for the Zr-Al-C and Zr-Si-C systems. In the Zr-Al-C system, investigations of the lattice parameters (Fig. B. 1 in the appendix) showed that (Zr,Al)C retains the fcc structure over the entire composition range (0–45 at.% Al) with the solubility limit defined by chemical stability at around 27 at.% Al where E_f exceeds 0 eV/atom. For the Zr-Si-C system, however, the limit is determined by structural instability, as the (Zr,Si)(Si,C) phase retains fcc symmetry only up to 30 at.% Si. At higher concentrations, the a/c ratio deviates significantly from 1, indicating low stability of an fcc structured compound, even though E_f remains negative at over the whole alloying range.

Fig. 2c–f displays the behavior of the Hf-X-C and Ta-X-C systems, which shows similarities to the Zr-X-C systems. In the Al-alloyed systems, the solubility limit is clearly determined by chemical instability, as fcc symmetry could be sustained over the whole alloying range and set by E_f approaching 0 eV/atom between 25 and 30 at.%. It is noteworthy that Al in these systems preferentially occupies TM sites. In the Si-alloyed systems, however, Si shows a preference for both TM and C sites, with a stronger tendency to occupy C sites. Detailed information on structural stability in the appendix shows that the (TM,Si)(Si,C) phase retain fcc symmetry over a wide range, but at high alloying levels, structural instability becomes apparent: For the Hf-Si-C system, the solubility limit is around 25 at.% Si, while the Ta-Si-C system has a lower solubility limit of around 15 at.%, far beyond which deviations from fcc symmetry are observed.

The W-X-C system stands out as a significant outlier. It exhibits positive formation energy values (0.326 eV/atom) even for binary WC, where the thermodynamically stable phase is hexagonal W_2C. Structural investigations (see Appendix) confirm that in the W-Al-C system Al preferably occupies W sites and is (meta)stable in the fcc structure over the entire composition range from 0 to 45 at.% Al. The energy of formation of (W,Al)C reaches a minimum at about 22 at.% Al. Above this concentration, E_f increases again. In contrast, the fcc structure is only retained up to about 5 at.% Al when Al occupies C sites. The W-Si-C system behaves similarly, with positive values of the formation energy over the entire composition range (up to 45 at.% Si). Structural investigations show that the W-Si-C system is most stable when Si occupies W sites. However, this structural (meta)stability is only maintained up to about 11 at.% Si. Beyond that, the a/b and a/c ratios deviate from 1 (perfect cubic), marking an additional solubility limit beyond the chemical instability ($E_f > 0$ eV/atom).

3.2. Phase formation

Based on theoretical predictions for stoichiometric TM-X-C compositions, the experimental depositions also include a variety of transition metal to carbon (TM:C) ratios, as the sputtering behavior of all involved elements varies accordingly. This approach facilitated a more comprehensive phase analysis within the TM-X-C material family (TM = Ti, Zr, Hf, Ta, W and X = Al, Si).

Fig. 3 shows the chemical compositions obtained in the ternary phase diagram of TM-Al/Si-C systems and illustrates the variety of compositions obtained by the combinatorial sputter deposition process. The samples show a “loss” of carbon with higher alloying content of Al/Si, which is primarily related to the position of the target to the substrate during co-sputtering of ceramic TMC targets together with Al/Si, respectively. This also allows the assessment of varying carbon contents on the fcc phase formation of ternary solid solutions.

In Fig. 3, the distribution of all data points highlights the capabilities of a combinatorial PVD deposition approach, yielding a wide range of chemical compositions. This wide variety is crucial for thoroughly exploring novel TM-X-C systems. Especially for the Ti-X-C, Zr-X-C, and W-X-C systems, a broad domain of Si/Al alloying could be achieved. In general, higher Al contents could be reached (see full diamond symbols), which is related to the inherently higher sputtering rate of metals such as Al. For example, the Al content in the Ti-X-C system reaches 64 at.%, in accordance to the Zr-X-C and W-X-C systems obtaining 71 and 61 at.% Al, respectively. In contrast, the chemical variety was less pronounced in Hf-X-C, where the Al content only hit 44 at.%. The Ta-X-C system exhibited even less chemical diversity, with most thin films containing only 0–10 at.% Al or Si. For all Si alloyed systems, the content reached is lower compared to Al. For the Ti-Si-C system, the Si content hit about 44 at.%, while the Zr-Si-C, Hf-Si-C, Ta-Si-C, and W-Si-C systems obtain maximum Si contents of 57, 43, 18, and 22 at.%, respectively. These high alloying contents of Al/Si in TM-X-Cs already suggest the formation of more metallic coatings, in accordance to TM to C stoichiometry.

In addition, the results in Fig. 3 show a clear trend of increased carbon loss for heavier transition metals (Ti < Zr < Hf < Ta < W). Generally, the sputter yields at i.e. 600 eV (kinetic energy of the striking Ar atom) for the individual metals and C are as follows [51]: 0.6 for Ti, 0.7 for Zr, 0.8 for Hf, 0.6 for Ta, 0.6 for W, 1.2 for Al, 0.5 for Si, and 0.2 for C. It should be noted that the deposition parameters (e.g., applied current) were the same for all TMCs during the combinatorial sputtering process. This trend can be related to scattering effects and different sputtering angles in combination with varying atomic masses of the transition metals. The comparatively light Ti exhibits lower carbon losses compared to Hf-X-C and Ta-X-C, which is reflected in their respective positions in the ternary phase diagram (diverging from the TMC to the Al/Si rich corner line). In more detail, the Ti-X-C data points in Fig. 3 are above the stoichiometric tie line, while the Ta-X-C and Hf-X-C data points are below. An exception to this trend is the W-X-C systems, whose data points are located near Ti-X-C and Zr-X-C. This deviation is attributed to the use of a carbon-enriched WC/C target (70/30 mol%) during deposition, to compensate the expected carbon lose during magnetron sputtering [52].

All synthesized samples (more than 260 different chemical compositions) were subjected to phase analysis using XRD. To streamline the discussion, the phase analysis is presented schematically using the Ti-X-C system as a representative case. The XRD diffractograms for all other TM-X-C thin films (TM = Zr, Hf, Ta, W) are available in Appendix C. Fig. 4 shows the XRD diffractograms of Ti-Al-C thin films with different Al alloy contents ranging from 16 to 64 at.% Al (from top to bottom). In these diffractograms, the hexagonal symbols correspond to the sapphire substrate material. Up to an Al content of 27 at.%, the thin films have a pure fcc-TiC structure. In this domain, slight variations in the intensity and sharpness of the fcc-TiC peaks can be seen, reflecting differences in crystallinity and defect density. In particular, the peaks become sharper as the TM:C ratio approaches the stoichiometric ratio of 1:1, as can be seen for $Ti_{0.24}Al_{0.27}C_{0.49}$, indicating a well-ordered crystalline thin film material. On the other hand, the high C coatings show a peak shift of the fcc-TiC peaks: For example, for the top coating in Fig. 4 ($Ti_{0.25}Al_{0.16}C_{0.59}$), the fcc-TiC peaks are initially shifted to the left compared to the perfect stoichiometric reference fcc-TiC, indicating that C occupies interstitial sites (C super-stoichiometry), leading to a larger lattice parameter and thus a decrease in the 2Θ [53]. Furthermore, the

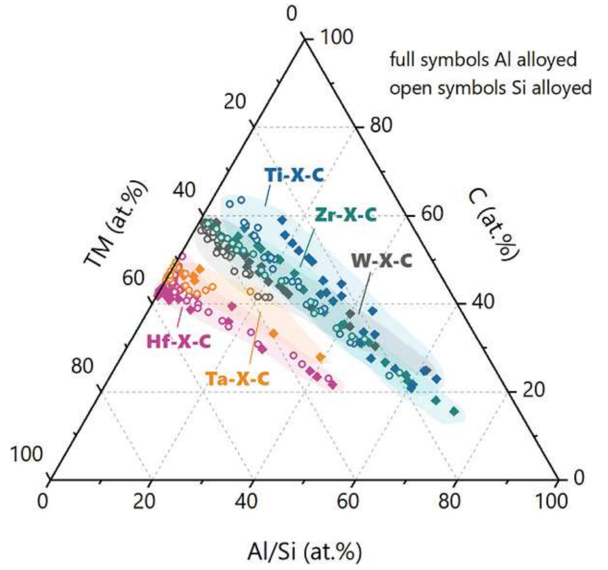

Fig. 3. Ternary phase diagram showing the chemical compositions of Ti-X-C, Zr-X-C, Hf-X-C, Ta-X-C, and W-X-C systems (X = Al or Si) synthesized by co-sputtering a TMC and Al/Si target.

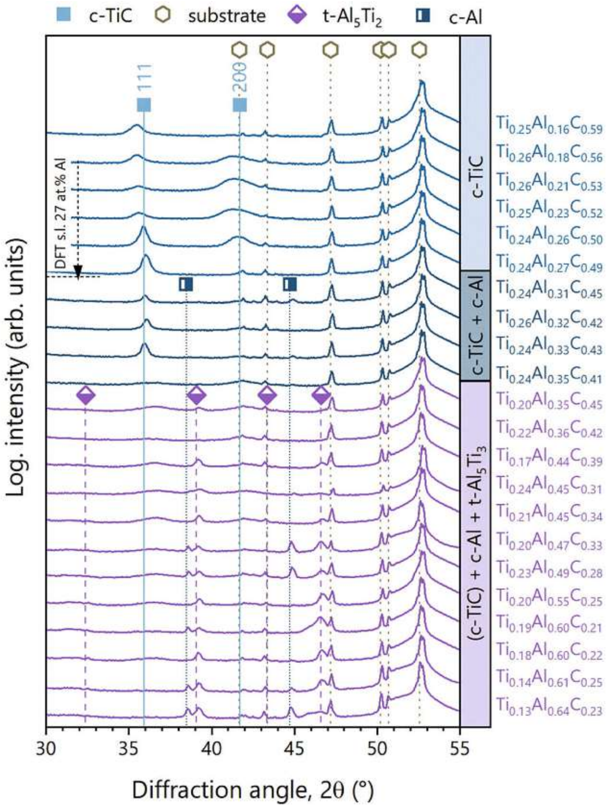

Fig. 4. XRD diffractograms of Ti-Al-C thin films with different chemical compositions. The observed phases include c-TiC [55], c-Al [56] and t-Al_5Ti_2 [57]. The hexagons belong to the substrate (sapphire) [58].

additional carbon can also form C-rich grain boundary domains causing less coherently diffracting domains, and hence weaker intensities (alongside to carbon interstitials) [54]. With increasing Al content and a TM:C ratio of 1:1, the peaks are gradually approaching the stoichiometric reference TiC, as can be seen for $Ti_{0.24}Al_{0.27}C_{0.49}$, suggesting the formation of solid solutions in the NaCl rock salt structure. This is supported by the theoretical results presented in Fig. 1, where the solubility limit is also found around 27 at.% Al content (where Al is occupying Ti lattice sites) indicated by the dashed vertical line.

As the Al content increases above 31 at.%, the metallic cubic (c) Al phase starts to form alongside to fcc TiC. In this compositional range (> 31 at.% Al), the DFT calculations show that the cubic cell remains (meta) stable only when Al sits on TM sites. The energy of formation in this range turns positive, suggesting the formation of second phases such as c-Al. By further increasing in the Al content to 35 at.% (and 45 at.% C), the formation of the metallic Al_5Ti_2 phase becomes more evident. For these high Al containing films, the intensity of the (111) peak of TiC decreases. With further increasing Al contents and decreasing Ti and C contents, the metallic peaks become more pronounced. This corresponds to a decrease in the intensity of the fcc-TiC peaks, indicating a shift in phase formation from TiC to Al-rich phases. In particular, $Ti_{0.13}Al_{0.64}C_{0.23}$ exhibits solely pure metallic phases during XRD analysis, resulting in a dual phase structure of c-Al and t-Al_5Ti_2.

Fig. 5 presents the XRD diffractograms of the Ti-Si-C thin films and the effects of Si alloying on the crystalline cubic TiC structure. The chemical composition of these samples ranges from 4 to 44 at.% Si. Up to about 25 at.% Si, the diffractograms indicate crystalline fcc-TiC thin films. However, when the Si content exceeds this threshold, the intensity and sharpness of the fcc-TiC peaks decrease, indicating a transition to an XRD amorphous structure. This transition is particularly evident between 25 and 26 at.% Si (with about 45 at.% C), where the diffraction peaks become broader and less defined. This experimental observation can, in turn, be supported by theoretical DFT calculations (Fig. 1), which clearly show that Si has a solubility limit of about 25 at.%, after which it inhibits the formation of an ordered crystalline structure (and promotes amorphization). Interestingly, no additional crystalline phases such as silicon carbide (SiC) or other Si-containing phases such as disilicide can be seen in the diffractograms of the Ti-Si-C system. Si is either incorporated into the TiC lattice or contributes to the amorphization as part of a disordered grain boundary phase, especially at higher concentrations, preventing the formation of distinct crystalline Si-containing phases.

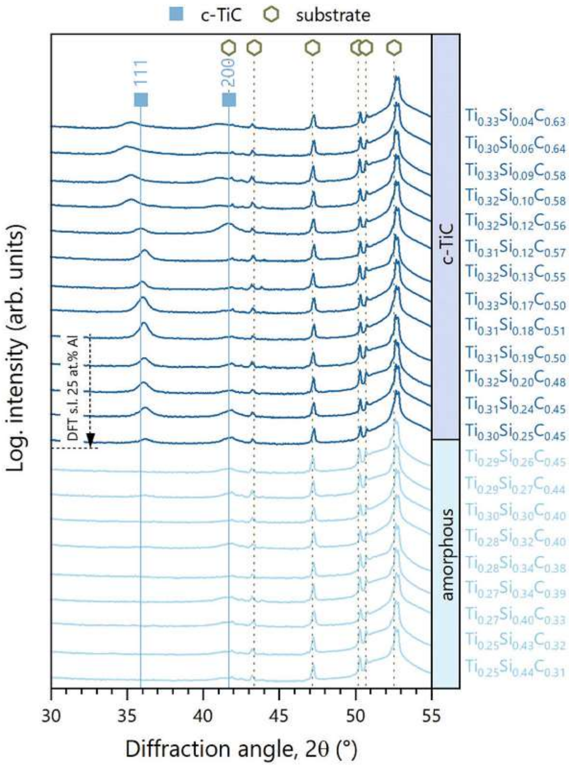

Fig. 5. XRD diffractograms of Ti-Si-C thin films with different chemical compositions. The films show the presence of c-TiC [55]. The hexagons belong to the substrate (sapphire) [58].

Additionally, an important observation in Fig. 5 is the shift to lower 2Θ angles compared to the fcc-TiC peaks, especially for samples with high carbon contents (~ 60 at. %), reflecting a similar trend compared to the Ti-Al-C system in Fig. 4. Again, C can be expected to occupy interstitial sites, resulting in a larger lattice parameter and smaller 2Θ angles. As the Si content increases and the coating compositions become C stoichiometric, the peaks approach the stoichiometric at around 17 at. % Si, reflecting a similar trend to Ti-Al-C. Despite the increasing Si content, the intensity and sharpness of the fcc-TiC peaks remain almost constant up to a Si concentration of about 25 at.% (with a corresponding carbon content of 48 at.%), indicating that the TiC lattice remains well defined.

For a more detailed proof of the solid solution formation in TM-X-C thin films, one material system (Ti-Al-C) out of the ten material families was selected for detailed TEM analysis. Fig. 6a shows a top view BF-TEM image of the $Ti_{0.24}Al_{0.26}C_{0.50}$ coating, reflecting the boundary between the single-phase solid solution and the dual-phased structure (a solubility limit of about 27 at.% Al in TiC was determined by DFT calculation, Fig. 1c, and XRD analysis, Fig. 4). The sample itself shows a dense morphology in Fig. 6a, and the structural analysis by SAED could verify the fcc-TiC structure as the prevalent phase (Fig. 6b and 6c). For a more detailed understanding, chemical mapping (EELS) was employed (Fig. 6d, EELS mapping in the region of about 100 × 100 nm) to determine the distribution of Ti, Al, and C, respectively. Contrary to the case described in [35], where Al alloying in TiC leads to the formation of nanocomposite films ((Ti,Al)C crystals embedded in an amorphous C matrix), we are dealing with a single-phase ternary compound. On a small scale (100 nm), there is no completely homogeneous distribution of Ti, Al, and C (Fig. 6d). Nevertheless, this local inhomogeneous distribution does not negatively affect the formation of a Ti-Al-C solid solution. In addition, a similar investigation was done for $Ti_{0.31}Si_{0.19}C_{0.50}$ obtaining a homogeneous distribution of Ti, Si, and C as well as a clear fcc structure during SAED – see Appendix D.

Fig. 7a provides a comprehensive overview of the phase analysis performed on various TM-X-C thin films, highlighting the 2 big domains in the ternary phase diagram where fcc phases predominate (single phase) versus amorphous or multiphase structures. In Fig. 7a, full symbols represent compositions where fcc structured TM-X-C solid solutions are predominant, while open symbols indicate the presence of additional phases (multi-phase thin films) or amorphous coatings.

From a general perspective, Fig. 7a highlights that fcc TM-X-C solid solutions (single-phase) with Al/Si contents up to around 25 at.% can be formed. Within this compositional range, the C content varies between 33 and 63 at.%, indicating considerable compositional flexibility to maintain the face-centered cubic TMC structure. However, notable exceptions are observed in the Ta-Al-C and Ta-Si-C systems, where the formation of hexagonal Ta_2C is observed at low alloying contents promoting dual phased characters. Furthermore, Hf-Al-C obtains a very limited solubility to Al. In addition, both the Ta-Al-C and Hf-Al-C systems exhibit c-Al peaks even at low alloying contents (1–5 at.% Al). This indicates that fcc structured solid solutions do not form at the prevalent deposition conditions.

When the Al/Si content exceeds 25 at.%, the tendency to form additional phases or amorphous states becomes more pronounced. In the Ti-Si-C system, increasing Si content leads to a gradual transition to an amorphous structure, while in the Ti-Al-C system, increasing Al

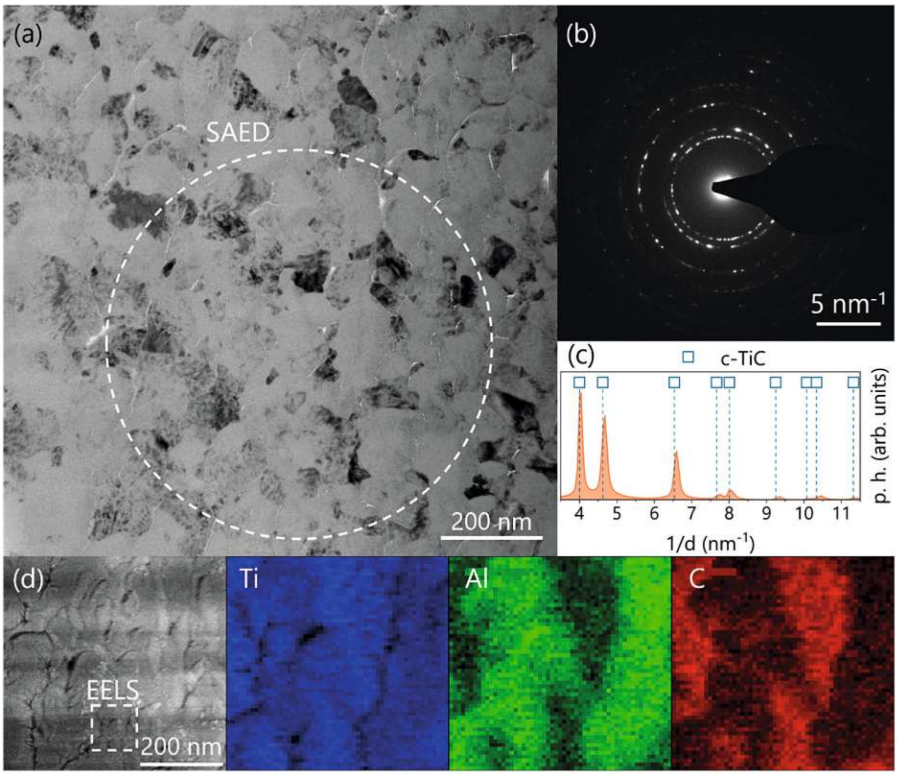

Fig. 6. (a) shows a top view BF-TEM image of the $Ti_{0.24}Al_{0.26}C_{0.50}$ sample (as deposited) with the area for SAED marked. (b) and (c) only show the c-TiC phase [55] determined by SAED. (d) features the STEM HAADF image with the area marked where the chemical mapping was determined by EELS for Ti, Al and C.

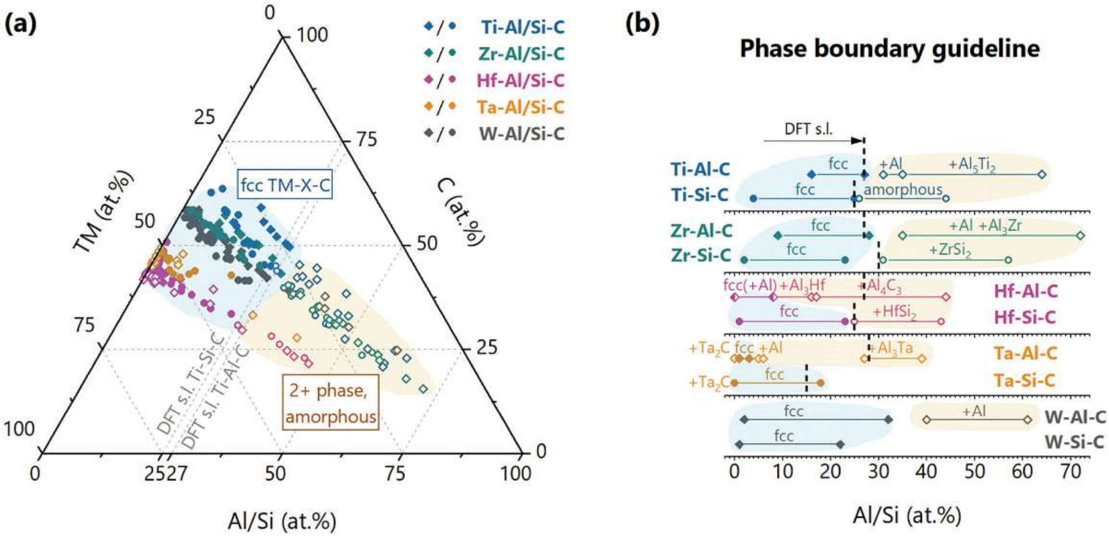

Fig. 7. (a) Ternary phase diagram illustrating the compositional regions where fcc phases (full symbols) are stable and where dual-/multi-phase or amorphous coatings (open symbols) are present in the Ti-X-C, Zr-X-C, Hf-X-C, Ta-X-C, and W-X-C (X = Al or Si) systems. The Al and Si alloyed systems are distinguished by the diamond and circle symbols, respectively. For Ti-Al/Si-C, the DFT solubility limits of 27 and 25 at.% Al/Si are marked as an example. (b) Phase boundary guidelines for comparing the experimental XRD data with the Al/Si solubility limits determined by DFT calculations for all systems.

content leads to the formation of coexisting metallic phases such as c-Al and t-Al_5Ti_2. Similar tendencies can be observed for other TM-X-C systems (the corresponding XRD diffractograms are shown in the Appendix). The comparison of experimentally observed phase regions and theoretically predicted solubility limits is depicted in Fig. 7b. In the Zr-Al-C system, metallic phases such as c-Al and t-Al_3Zr start to form between 28 and 35 at.% Al compared to the DFT predicted solubility limit of 27 at.% Al, see Fig. 7b (and Fig. B. 1 for more details). In the Zr-

Si-C system, $ZrSi_2$ forms between 23 and 31 at.% Si. DFT calculations support these experimental results and showed a solubility limit of about 30 at.% Si, see Fig. 7b and Fig. B. 1. In contrast, the Hf-Al-C system exhibits low Al solubility, which is evident from the presence of metallic phases even at low alloying contents (< 16 at.% Al). In addition, rhombohedral Al_4C_3 is detected at Al contents above 17 at.%. Interestingly, these experimental results differ from the theoretical calculations, as for the Hf-Al-C system a theoretical solubility limit of 27 at.% Al was suggested (see Appendix Fig. B. 2). There may be deviations due to competing phases (whose E_f is lower) that were not considered in the calculation, but the expansion is surprisingly larger. The Hf-Si-C system follows a similar trend as Zr-Si-C and forms the disilicide phase $HfSi_2$ above 23 at.% Si. Again, the result can be supported by DFT analysis, as the solubility limit was also theoretically determined for 25 at.% (see Fig. 7b and Fig. B. 2 in the Appendix). For the Ta-Al-C system there are again deviations between the DFT calculations and the experimental results (as in Hf-Al-C). Here a fcc-TaC phase could only be detected experimentally at low alloying contents (up to 3 at.% Al), while metallic c-Al peaks can be seen from 5 at.% Al. Again, competing phases were not considered in the theoretical calculation. In contrast, the theoretical predictions for Ta-Si-C agree with the actual experimental phase formations: experimentally, the fcc-TaC phase could be stabilized up to 18 at.% Si, while DFT calculations indicate a solubility limit of about 15 at.%, see again Fig. 7b. Finally, in the W-Al-C system, broad peaks associated with the fcc-WC phase could be observed (indicating almost amorphization). For Al contents above 40 at.%, additional c-Al peaks appear. For the W-Al-C system, the formation energy was found to be greater than 0 eV/atom, which also favors amorphization and prevents the formation of an ordered cubic WC crystal structure. The same behavior (almost amorphization and broad WC peaks) was observed for the W-Si-C system, whose E_f was also determined to be above 0 eV/atom. The phase studies carried out so far have shown that for most of the systems the experimentally determined phase solubility can be accurately predicted using DFT. Only the Hf-Al-C and Ta-Al-C systems show significant deviations from the predicted solubility limits.

3.3. *Mechanical properties*

Fig. 8 illustrates the mechanical properties of TM-X-C thin films, determined through nanoindentation using the continuous stiffness measurement (CSM) technique. This method allows ultra-fast mapping of hardness and elastic modulus, which is a key for the combinatorial high-throughput approach investigating more than 260 compositions. Like the previously discussed phase analysis, closed symbols in Fig. 8 represent single-phased fcc TM-X-C thin film materials, while open symbols indicate dual-/multi-phase or amorphous structures.

In Fig. 8a, the hardness of the different TM-X-C systems is plotted against their Al/Si alloy content. A striking trend emerges: the fcc-based TM-X-C systems exhibit a significantly higher hardness compared to their dual-phase/non-cubic or amorphous counterparts. This trend is particularly evident at alloy contents up to about 25 at.%, which is closely related to the previously identified phase boundaries. Among these systems, the Ta-X-C coatings are characterized by the highest hardness values of over 40 GPa. Interestingly, the coatings with these high hardness values exhibit a dual phase structure consisting of cubic TaC and hexagonal Ta_2C phase (indicated by open symbols). This super hardness is consistent with the results of [59], which also found hardness values above 40 GPa for dual phase TaC thin films (c-Ta and h-Ta_2C).

The Ta-X-C thin films are followed in terms of hardness by the low-alloyed Hf-X-C thin films (0–5 at.% Al/Si), which exhibit values around 40 GPa. Beyond 5 at.% Al/Si content, the hardness values scatter significantly due to variations in phase composition and carbon content. These deviations also reflect the difficulties in achieving a prefect homogeneous chemical composition within single samples using combinatorial co-sputtering. The Zr-X-C thin films exhibit hardness values around 35 GPa, especially for alloying contents up to approximately 15 at.%. The relatively constant hardness of about 35 GPa across this range suggest a strong capability to form solid solution formation within the Zr-X-C system. However, this trend weakens as the alloy content increases above 15 at.%, leading to a decrease in hardness. In the Ti-X-C and W-X-C systems, the hardness values reach almost 30 GPa, with both systems showing an almost horizontal trend up to an alloy content of about 25 at.%, where the single-phase fcc structure starts to diminish. Beyond this threshold, the hardness drops to around 20 to 10 GPa as multi-phased structured films strongly differ in their specific properties. This reduction in hardness to approximately 20 to 10 GPa is consistent across all TM-X-C systems when the cubic phase transitions into dual-phase or amorphous structures.

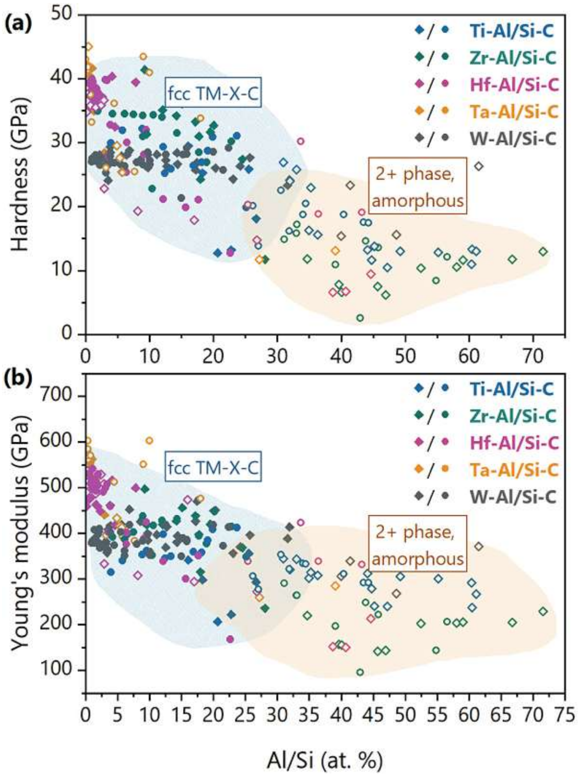

Fig. 8. Shows the (a) hardness and (b) Young's modulus of the different TM-X-C (TM = Ti, Zr, Hf, Ta, W and X = Al, Si) systems determined by nanoindentation. The closed symbols represent fcc phases, and the dual-/multi-phase or amorphous coatings are marked by open symbols.

Fig. 8b presents the Young's modulus as a function of Al/Si alloy content, with similar trends to those observed for the hardness. The Ta-X-C system again exhibits the highest values, with moduli exceeding 550 GPa for the nearly unalloyed coatings. As with hardness, the dual phase coatings consisting of c-TaC and h-Ta_2C have particularly the highest Young's modulus values and are indicated by open symbols (Fig. 7b: Ta-X-C, 0–5 at.% Al/Si). Modulus values above 550 GPa have also been discussed in [59] for $TaC_{0.78}$ thin films (sub-stoichiometric in C, dual phase structure consisting of c-TaC and h-Ta_2C) and are comparable to our results.

The Hf-Al-C system ranks second in terms of Young's modulus with values around 500 GPa for low-alloyed coatings (up to 5 at.%). The other systems, including Zr-X-C, Ti-X-C, W-X-C, shows a similar trend with Young's moduli around 400 GPa up to an Al/Si content of about 25 at.%. Beyond this point, the modulus drops, with values scattering between 150 and 350 GPa due to the different phase composition and carbon content.

The strong correlation between the mechanical properties and phase formation is particularly evident and underlines the importance of fcc TM-X-C solid solutions in achieving excellent mechanical properties over a wide range of stability. Furthermore, the TEM results (Fig. 6, formation of a single-phase solid solution) correlate with the high hardness values for alloying contents up to about 25 at.% Al/Si.

4. Conclusions

This study provides a thorough high-throughput exploration of the prevalent phases in Al and Si alloyed ternary transition metal carbide (TM-X-C) thin film materials, with an emphasis on the formation of fcc solid solutions. The combination of aluminum and silicon, both of which are strong oxide formers, with refractory transition metal carbides (TMCs), is expected to facilitate the development of alternative oxidation resistant ternary TM-X-C ceramics. Using 5 different transition metals (TM = Ti, Zr, Hf, Ta, W), 10 different ternary material systems were systematically investigated in an in-depth phase analysis and mechanical property assessment. In a combinatorial co-sputtering approach with carefully aligned targets, over 260 chemical compositions have been deposited. The prevalent thermodynamic conditions in PVD growth allowed for the alloying of up to 60 to 70 at.% Al/Si and encompassed a broad range of carbon contents (20–60 at.%), enabling a thorough mapping of the ternary phase diagram.

In first-principles DFT calculations, the formation of fcc solid solutions is suggested for all investigated materials systems except the W-X-C system, for which the hexagonal W_2C is the ground state. For all structural and chemical stable systems, the calculations proved that Si preferentially occupies both TM and C sites, while Al preferably replaces TMs. Furthermore, the solubility limits of Si alloyed fcc systems are dominated by their structural limit (symmetry of the fcc cell is maintained when $a/b = a/c = 1 \pm 0.05$), while the TM-Al-Cs are restricted by their thermodynamic stability ($E_f > 0$ eV/atom). Experimentally, fcc solid solutions are validated up to 25–30 at.% Al or Si, as determined by XRD phase analysis of more than 260 different compositions. Only the TaC and HfC systems exhibit limited solubility for Al, leading to the early formation of c-Al at low alloying contents (up to 10 at.%). And, in contrast to all other systems, the XRD analysis of the W-X-C system exhibits a slight tendency towards a nanocrystalline structure or even amorphization, which is in partial agreement with the DFT predictions of forming no fcc solid solutions. The mechanical properties, in particular hardness and Young's modulus, have been investigated by nanoindentation utilizing the continuous stiffness measurement technique. A clear and strong correlation was found: the fcc phases consistently exhibited a higher hardness (30–40 GPa) and a high modulus of elasticity. Conversely, disruption of the fcc structure by higher alloy content (> 25 at.% Al or Si) – whether by the development of more metallic coatings or amorphization – led to a sharp decrease in hardness to around 10 GPa.

In summary, this study combines a theoretical and experimental high-throughput approach to explore X = Al and Si alloyed fcc-structured ternary TM-X-C solid solutions. For both alloying routes 25 to 30 at.% Al or Si limits the formation of single-phased (meta)stable fcc-TM-X-Cs. Preserving the cubic single phase structure in TM-X-C systems is essential for achieving optimal mechanical performance. These insights could lead to significant advancements in high performance materials for various applications and may also open up possibilities for innovative ternary oxidation resistant TM-Al/Si-C ceramics. In particular, Al and Si alloyed fcc structured ternary coatings with their promising mechanical properties are compelling candidates for further oxidation testing. Among them, Ti-Al/Si-C, Zr-Al/Si-C, Hf-Si-C and Ta-Si-C proved to be excellent systems for future oxidation studies, obtaining a wide solubility range (approx. 25 at.%) for the strong oxide formers with promising mechanical properties.

CRediT authorship contribution statement

S. Richter: Writing – original draft, Visualization, Validation, Project administration, Methodology, Investigation, Formal analysis, Conceptualization. **C. Gutschka:** Data curation. **D. Danner:** Investigation, Data curation. **R. Hahn:** Writing – review & editing. **T. Wojcik:** Resources, Data curation. **E. Ntemou:** Resources, Data curation. **C. Jerg:** Resources, Funding acquisition. **J. Ramm:** Resources, Funding acquisition. **P. Polcik:** Resources, Funding acquisition. **S. Kolozsvári:** Resources, Funding acquisition. **D. Primetzhofer:** Resources, Data curation. **H. Riedl:** Writing – review & editing, Supervision, Resources, Project administration, Funding acquisition.

Declaration of competing interest

The authors declare that they have no known competing financial interests or personal relationships that could have appeared to influence the work reported in this paper.

Acknowledgments

The financial support by the Austrian Federal Ministry for Digital and Economic Affairs, the National Foundation for Research, Technology and Development, and the Christian Doppler Research Association is gratefully acknowledged (Christian Doppler Laboratory "Surface Engineering of high-performance Components"). We also thank Plansee SE, Plansee Composite Materials GmbH, and Oerlikon Balzers, Oerlikon Surface Solutions AG for financial support. We also thank the X-ray center (XRC) of TU Wien for beam time and the electron microscopy center—USTEM TU Wien—for using the SEM and TEM facilities. We acknowledge TU Wien Bibliothek for financial support through its Open Access Funding Programme. In addition, the authors thank the RADIATE project for funding our beamtime at the Tandem Laboratory at Uppsala University. Accelerator operation at Uppsala University was supported by the Swedish research council VR-RFI (#2019-00191). Finally, the Theodor Körner Fonds is gratefully recognized for its invaluable support in the completion of this work.

Supplementary materials

Supplementary material associated with this article can be found, in the online version, at doi:10.1016/j.actamat.2025.120839.

References

[1] J.F. Justin, A. Jankowiak, Ultra high temperature ceramics: densification, properties and thermal stability, Aerosp. Lab. 1 (2011).
[2] B.C. Wyatt, S.K. Nemani, G.E. Hilmas, E.J. Opila, B. Anasori, Ultra-high temperature ceramics for extreme environments, Nat. Rev. Mater. (2023) 1–17.
[3] W.G. Fahrenholtz, E.J. Wuchina, W.E. Lee, Y. Zhou, Ultra-High Temperature Ceramics: Materials for Extreme Environment Applications, John Wiley & Sons, 2014.
[4] W.G. Fahrenholtz, G.E. Hilmas, Ultra-high temperature ceramics: materials for extreme environments, Scr. Mater. 129 (2017) 94–99.
[5] O. Cedillos-Barraza, D. Manara, K. Boboridis, T. Watkins, S. Grasso, D. D. Jayaseelan, R.J.M. Konings, M.J. Reece, W.E. Lee, Investigating the highest melting temperature materials: a laser melting study of the TaC-HfC system, Sci. Rep. 6 (2016) 37962.
[6] O. Cedillos-Barraza, S. Grasso, N.A. Nasiri, D.D. Jayaseelan, M.J. Reece, W.E. Lee, Sintering behaviour, solid solution formation and characterisation of TaC, HfC and TaC–HfC fabricated by spark plasma sintering, J. Eur. Ceram. Soc. 36 (2016) 1539–1548.
[7] M.J. Gasch, D.T. Ellerby, S.M. Johnson, Ultra high temperature ceramic composites, in: N.P. Bansal (Ed.), Handbook of Ceramic Composites, Springer US, Boston, MA, 2005, pp. 197–224.
[8] R.A. Andrievskii, N.S. Strel'nikova, N.I. Poltoratskii, E.D. Kharkhardin, V. S. Smirnov, Melting point in systems ZrC-HfC, TaC-ZrC, TaC-HfC, Powder Metall. Met. Ceram. 6 (1967) 65–67.
[9] A.I. Savvatimskiy, S.V. Onufriev, S.A. Muboyadzhyan, Thermophysical properties of the most refractory carbide Ta0.8Hf0.2C under high temperatures (2000–5000 K), J. Eur. Ceram. Soc. 39 (2019) 907–914.

[10] I. Khatri, R.K. Koju, Y. Mishin, First-principles prediction of point defect energies and concentrations in the tantalum and hafnium carbides, Acta Mater. 277 (2024) 120216.

[11] G. Pulci, M. Tului, J. Tirillò, F. Marra, S. Lionetti, T. Valente, High temperature mechanical behavior of UHTC coatings for thermal protection of re-entry vehicles, J. Therm. Spray Technol. 20 (2011) 139–144.

[12] J. Binner, M. Porter, B. Baker, J. Zou, V. Venkatachalam, V.R. Diaz, A. D'Angio, P. Ramanujam, T. Zhang, T.S.R.C. Murthy, Selection, processing, properties and applications of ultra-high temperature ceramic matrix composites, UHTCMCs–a review, Int. Mater. Rev. 65 (2020) 389–444.

[13] S. Shimada, Formation and mechanism of carbon-containing oxide scales by oxidation of carbides (ZrC, HfC, TiC), Mater. Sci. Forum (2001), https://doi.org/10.4028/www.scientific.net/MSF.369-372.377.

[14] M. Sokol, V. Natu, S. Kota, M.W. Barsoum, On the chemical diversity of the MAX phases, Trends Chem. 1 (2019) 210–223.

[15] P. Sharma, K. Singh, O.P. Pandey, Investigation on oxidation stability of V2AlC MAX phase, Thermochim. Acta 704 (2021) 179010.

[16] X. Li, X. Xie, J. Gonzalez-Julian, J. Malzbender, R. Yang, Mechanical and oxidation behavior of textured Ti2AlC and Ti3AlC2 MAX phase materials, J. Eur. Ceram. Soc. 40 (2020) 5258–5271.

[17] M. Haftani, M. Saeedi Heydari, H.R. Baharvandi, N. Ehsani, Studying the oxidation of Ti2AlC MAX phase in atmosphere: a review, Int. J. Refract. Met. Hard Mater. 61 (2016) 51–60.

[18] X. Li, S. Wang, G. Wu, D. Zhou, J. Pu, M. Yu, Q. Wang, Q. Sun, Oxidation and hot corrosion behaviors of MAX-phase Ti3SiC2, Ti2AlC, Cr2AlC, Ceram. Int. 48 (2022) 26618–26628.

[19] N.V. Sevost'yanov, O.V. Basargin, V.G. Maksimov, N.P. Burkovskaya, High-temperature oxidation of Ti3SiC2-based materials prepared by spark plasma sintering, Inorg. Mater. 55 (2019) 9–13.

[20] M. Potoczek, J. Dąbek, T. Brylewski, Oxidation behavior of Ti2AlC MAX-phase foams in the temperature range of 600–1000°C, J. Therm. Anal. Calorim. 148 (2023) 4119–4127.

[21] Synthesis and oxidation behaviour of Ta-Al-C MAX phases, (n.d.). http://resolver.tudelft.nl/uuid:7e055e3c-39f4-49da-990f-939c7ccaf7c7 (accessed November 13, 2024).

[22] C. Tang, M. Steinbrück, M. Große. S. Ulrich, M. Stüber, H.J. Seifert, Improvement high-temperature oxidation resistance Zr alloy cladding surface modification aluminum-containing ternary carbide coatings, 2018.

[23] A. Donchev, M. Schütze, E. Ström, M. Galetz, Oxidation behaviour of the MAX-phases Ti2AlC and (Ti, Nb)2AlC at elevated temperatures with and without fluorine treatment, J. Eur. Ceram. Soc. 39 (2019) 4595–4601.

[24] C. Tang, M. Steinbrück, M. Große, T. Bergfeldt, H.J. Seifert, Oxidation behavior of Ti 2 AlC in the temperature range of 1400°C–1600°C in steam, J. Nucl. Mater. 490 (2017) 130–142.

[25] S. Badie, D. Sebold, R. Vaßen, O. Guillon, J. Gonzalez-Julian, Mechanism for breakaway oxidation of the Ti2AlC MAX phase, Acta Mater. 215 (2021) 117025.

[26] J. Nicolaï, C. Furgeaud, B.W. Fonrose, C. Bail, M.F. Beaufort, Formation mechanisms of Ti2AlC MAX phase on SiC-4H using magnetron sputtering and post-annealing, Mater. Des. 144 (2018) 209–213.

[27] Q.M. Wang, W. Garkas, A.F. Renteria, C. Leyens, H.W. Lee, K.H. Kim, Oxidation behaviour of Ti–Al–C films composed mainly of a Ti2AlC phase, Corros. Sci. 53 (2011) 2948–2955.

[28] X. Sun, W. Li, J. Huang, Z. Ye, J. Yang, S. Chen, X. Zhao, Effect of Si content on the microstructure and properties of Ti–Si–C composite coatings prepared by reactive plasma spraying, Ceram. Int. 47 (2021) 24438–24452.

[29] O. Wilhelmsson, J.P. Palmquist, E. Lewin, J. Emmerlich, P. Eklund, P.O.Å. Persson, H. Högberg, S. Li, R. Ahuja, O. Eriksson, L. Hultman, U. Jansson, Deposition and characterization of ternary thin films within the Ti–Al–C system by DC magnetron sputtering, J. Cryst. Growth 291 (2006) 290–300.

[30] J. Lauridsen, P. Eklund, T. Joelsson, H. Ljungcrantz, Å. Öberg, E. Lewin, U. Jansson, M. Beckers, H. Högberg, L. Hultman, High-rate deposition of amorphous and nanocomposite Ti–Si–C multifunctional coatings, Surf. Coat. Technol. 205 (2010) 299–305.

[31] Z. Qiao, X. Ma, W. Zhao, H. Tang, S. Cai, B. Zhao, A novel (W–Al)–C–Co composite cemented carbide prepared by mechanical alloying and hot-pressing sintering, Int. J. Refract. Hard Met. 26 (2008) 251–255.

[32] J.M. Yan, X.F. Ma, W. Zhao, H.G. Tang, C.J. Zhu, Synthesis, crystal structure, and density of (W1−xAlx)C, J. Solid State Chem. 177 (2004) 2265–2270.

[33] Z. Wang, H. Kang, R. Chen, P. Ke, A. Wang, Enhanced mechanical and tribological properties of V-Al-C coatings via increasing columnar boundaries, J. Alloys Compd. 781 (2019) 186–195.

[34] S. Du, M. Wen, L. Yang, P. Ren, Q. Meng, K. Zhang, W. Zheng, Structural, hardness and toughness evolution in Si-incorporated TaC films, Ceram. Int. 44 (2018) 9318–9325.

[35] M. Lindquist, O. Wilhelmsson, U. Jansson, U. Wiklund, Tribofilm formation and tribological properties of TiC and nanocomposite TiAlC coatings, Wear 266 (2009) 379–387.

[36] C. Tang, M. Steinbrück, M. Große, S. Ulrich, M. Stüber, H.J. Seifert, Evaluation magnetron sputtered protective Zr-Al-C coatings accident tolerant Zircaloy claddings, 2017.

[37] C. Vitelaru, M. Balaceanu, A. Parau, C.R. Luculescu, A. Vladescu, Investigation of nanostructured TiSiC–Zr and TiSiC–Cr hard coatings for industrial applications, Surf. Coat. Technol. 251 (2014) 21–28.

[38] A. Gaydaychuk, S. Linnik, A. Mitulinsky, S. Zenkin, Effect of Al addition on the oxidation resistance of HfC thin films, Coat. World 12 (2021) 27.

[39] J. Jiang, K. He, X. He, H. Huang, X. Pang, Z. Wei, Structure, mechanical and tribological properties of TiSiC films deposited by magnetron sputtering segment target, Mater. Res. Express 4 (2017) 126401.

[40] O. Tengstrand, Me-Si-C (Me= Nb, Ti or Zr) Nanocomposite and Amorphous Thin Films, 2012. https://www.diva-portal.org/smash/get/diva2:572989/FULLTEXT01.pdf.

[41] M. Andersson, S. Urbonaite, E. Lewin, U. Jansson, Magnetron sputtering of Zr–Si–C thin films, Thin Solid Films 520 (2012) 6375–6381.

[42] R. Anton, V. Leisner, P. Watermeyer, M. Engstler, U. Schulz, Hafnia-doped silicon bond coats manufactured by PVD for SiC/SiC CMCs, Acta Mater. 183 (2020) 471–483.

[43] A. Zunger, S. Wei, L.G. Ferreira, J.E. Bernard, Special quasirandom structures, Phys. Rev. Lett. 65 (1990) 353–356.

[44] D. Gehringer, M. Friák, D. Holec, Models of configurationally-complex alloys made simple, Comput. Phys. Commun. 286 (2023) 108664.

[45] G. Kresse, J. Furthmüller, Efficient iterative schemes for ab initio total-energy calculations using a plane-wave basis set, Phys. Rev. B Condens. Matter 54 (1996) 11169–11186.

[46] J.P. Perdew, K. Burke, M. Ernzerhof, Generalized gradient approximation made simple, Phys. Rev. Lett. 77 (1996) 3865–3868.

[47] AJA International, Orion Series Sputtering Systems, AJA International, 2025. https://www.ajaint.com/system-orion. accessed January 22, 2025.

[48] Plansee Composite Materials, Plansee Composite Materials. (2024). https://www.plansee.com/de/unternehmen/kontakt/deutschland.html (accessed February 18, 2025).

[49] P. Ström, D. Primetzhofer, Ion beam tools for nondestructive *in-situ* and in-operando composition analysis and modification of materials at the Tandem Laboratory in Uppsala, J. Instrum. 17 (2022) P04011.

[50] D. Holec, R. Rachbauer, L. Chen, L. Wang, D. Luef, P.H. Mayrhofer, Phase stability and alloy-related trends in Ti–Al–N, Zr–Al–N and Hf–Al–N systems from first principles, Surf. Coat. Technol. 206 (2011) 1698–1704.

[51] Sputtering yields, angstrom sciences (2024). https://angstromsciences.com/sputtering-yields (accessed November 24, 2024).

[52] T. Glechner, C. Tomastik, E. Badisch, P. Polcik, H. Riedl, Influence of WC/C target composition and bias potential on the structure-mechanical properties of non-reactively sputtered WC coatings, Surf. Coat. Technol. 432 (2022) 128036.

[53] W.H. Bragg, W.L. Bragg, The reflection of X-rays by crystals, Proc. R. Soc. Lond. A Math. Phys. Sci. 88 (1913) 428–438.

[54] U. Jansson, E. Lewin, Sputter deposition of transition-metal carbide films–a critical review from a chemical perspective, Thin Solid Films 536 (2013) 1–24.

[55] International Center of Diffraction Data, Powder diffraction file - cubic TiC - 00-032-1383, (1982).

[56] International Center of Diffraction Data, Powder diffraction file - cubic Al - 00-004-0787, (1954).

[57] International Center of Diffraction Data, Powder diffraction file - tetragonal Al5Ti2 - 03-065-9788, (2004).

[58] International Center of Diffraction Data, Powder diffraction file - hexagonal Al2O3 - 00-005-0712, (1955).

[59] H. Riedl, T. Glechner, T. Wojcik, N. Koutná, S. Kolozsvári, V. Paneta, D. Holec, D. Primetzhofer, P.H. Mayrhofer, Influence of carbon deficiency on phase formation and thermal stability of super-hard TaCy thin films, Scr. Mater. 149 (2018) 150–154.

Appendix

A. Supplementary experimental details

This section contains technical and detailed information on the computational details, the coating synthesis as well as the coating characterization.

A.1 Computational details

The Vienna Ab initio Simulation Package (VASP) [1] applies the Projector Augmented Wave (PAW) method [2,3]. The PAW potentials were selected according to the recommended parameters listed in the VASP wiki [4]. The electron-electron exchange-correlation interactions were treated with the GGA in the form proposed by Perdew, Burke and Enzerhof (PBE) [5].

Following experimental results, spin polarization was excluded from the calculations and Spin-Orbit-Coupling (SOC) was not explicitly considered. The Kohn-Sham wave functions were represented using plane waves with a cutoff energy of 520 eV. A Monkhorst Pack k-mesh with the Γ-point as the center was automatically generated, resulting in an 8 × 8 × 8 grid in reciprocal space for the supercells. A Methfessel-Paxton [6] smearing of 0.2 eV was applied. The convergence criterion for the total energy and forces on ions were set to 10^{-5} eV, while structural relaxations were considered convergent when reaching a threshold of 10^{-4} eV.

The following Tab. A.1. provides additional information about the theoretically studied chemical compositions. Tab. A.1. applied to all 10 material systems (TM = Ti, Zr, Hf, Ta, W and X = Al, Si).

Tab. A.1. Chemical compositions theoretically investigated

TM (at.%)	X (at.%)	C (at.%)	Atoms (54 in total)	
46	4	50	$TM_{25}X_2C_{27}$	X occupies TM sites
43	7	50	$TM_{23}X_4C_{27}$	
39	11	50	$TM_{21}X_6C_{27}$	
35	15	50	$TM_{19}X_8C_{27}$	
31	19	50	$TM_{17}X_{10}C_{27}$	
28	22	50	$TM_{15}X_{12}C_{27}$	
20	30	50	$TM_{11}X_{16}C_{27}$	
13	37	50	$TM_7X_{20}C_{27}$	
6	44	50	$TM_3X_{24}C_{27}$	
2	48	50	$TM_1X_{26}C_{27}$	
50	4	46	$TM_{27}X_2C_{25}$	X occupies C sites
50	7	43	$TM_{27}X_4C_{23}$	
50	11	39	$TM_{27}X_6C_{21}$	
50	13	37	$TM_{27}X_7C_{20}$	
50	15	35	$TM_{27}X_8C_{19}$	
50	17	33	$TM_{27}X_9C_{18}$	
50	19	31	$TM_{27}X_{10}C_{17}$	
50	22	28	$TM_{27}X_{12}C_{15}$	
50	30	20	$TM_{27}X_{16}C_{11}$	
50	37	13	$TM_{27}X_{20}C_7$	
50	44	6	$TM_{27}X_{24}C_3$	
50	48	2	$TM_{27}X_{26}C_1$	
48	4	48	$TM_{26}X_2C_{26}$	X occupies TM and C cites (equally distributed)
44	11	44	$TM_{24}X_6C_{24}$	
41	19	41	$TM_{22}X_{10}C_{22}$	
35	30	35	$TM_{19}X_{16}C_{19}$	
28	44	28	$TM_{15}X_{24}C_{15}$	
26	48	26	$TM_{14}X_{26}C_{14}$	

A.2 Deposition process

The substrates used for deposition were single-crystalline Al_2O_3 (sapphire, 1-102 orientation, 10 x 10 x 0.53 mm). Before deposition, the substrates were cleaned in an ultrasonic bath with acetone and ethanol for 5 min each. The substrate holder was set to approx. 80 mm. The base pressure was maintained at less than 2 x 10^{-4} Pa before each deposition process. Prior to deposition, the substrates were subjected to an ion etching step for 20 min, at a bias potential of -750 V and an argon flow rate of 27.8 sccm, resulting in an etching pressure of approximately 4.0 Pa. After etching, the target surfaces were cleaned in a 3 min pre-sputtering step with closed shutters. The parameters for the pre-sputtering were identical to those for deposition: a current of 0.3 A was applied to all TMC targets, resulting in power densities of approximately 2.3 W/cm^2 for TiC, 2.0 W/cm^2 for ZrC, 3.2 W/cm^2 for HfC, 2.5 W/cm^2 for TaC, and 3.2 W/cm^2 for WC/C (70/30 mol%). The 2'' cathodes were operated with a current of 0.2 A for the Al target, resulting in a power density of about 4.1 W/cm^2. The Si target was operated in pulsed mode with a frequency of 150 kHz and a pulse duration of 257 ns, resulting in an average power density of about 3.1 W/cm^2. For all depositions, the substrate temperature was set to 420 °C, the bias potential to -50 V and the argon flow rate to 27.0 sccm, resulting in a deposition pressure of about 0.5 Pa. In relation to different sputter yields, the deposition times varied depending on the TM-X-C system: 120 min for Ti, Zr and Ta systems, 180 min for Hf and 60 min for W. These times were chosen so that layer thicknesses of 500 nm to 1.5 µm were achieved.

A.3 Coating characterization

ToF-ERDA was carried out using $^{127}I^{8+}$ ions with a primary energy of 36 MeV, with an incident angle of 67.5° relative to the surface normal and recoils were detected in an angle of 45° with respect to the incident beam direction. For EBS, 4.35 MeV $^4He^+$ ions were used to employ the $^{12}C(^4He,^4He)$ elastic resonance at ~4.26 MeV [7]. The detection angle was 170° and the incidence angle was 5°. The ToF-ERDA data were processed with the CONTES software [8], while the EBS results were analyzed with the SIMNRA software [9], employing the information on the light species from ERDA as input parameters. The total systematic and statistical uncertainties were estimated to be 5-8 % of the deduced value for the major constituents.

X-ray fluorescence analysis (XRF) was performed using a Panalytical AXIOS system in wavelength dispersive (WDXRF) mode with a rhodium anode under vacuum conditions at room temperature. The ERDA/EBS data were used as standards for the quantification of the elements. In XRF, the estimated systematic uncertainties for these measurements were expected to be around 5 %.

The phase evolution of the as deposited TM-X-C coatings was investigated using a Panalytical X'Pert Pro MPD X-ray diffractometer in Bragg-Brentano geometry with Cu-K_α radiation (wavelength λ = 1.5418 Å).

To further investigate the crystal structure and morphology, transmission electron microscopy (TEM) analysis was performed on an FEI TECNAI F20 microscope with a field emission gun. Prior to this, the TEM lamellas were prepared using a dual-beam focused ion beam (Ga^+ ions)/scanning electron microscope (FIB-SEM) system (Thermo Scientific Scios 2). Using the TEM, bright field (BF) images, selected area electron diffraction (SAED) and EELS Mapping were then obtained.

The Young's modulus and hardness were measured using a FT-I04 Femto-Indenter with a Berkovich diamond tip calibrated against a fused silica reference sample. The continuous stiffness measurement (CSM) technique was used with an applied maximum force of 20 mN, which allowed rapid measurements of the large number of compositions. To reduce the influence of the substrate, data points with indentation depths greater than 10 % of the coating thickness were not considered. The Young's modulus of the coatings was derived by fitting the raw modulus data and extrapolating to a zero indentation depth, in accordance with the guidelines given in references [10,11].

B. Supplementary DFT results

Supplementary DFT results of the TM-X-C systems (TM = Zr, Hf, Ta, W and X = Al, Si) are given in Appendix B. The structural changes of the cubic structure (changes of the lattice parameters considered as ratios a/b and a/c respectively) with increasing alloying element X are shown.

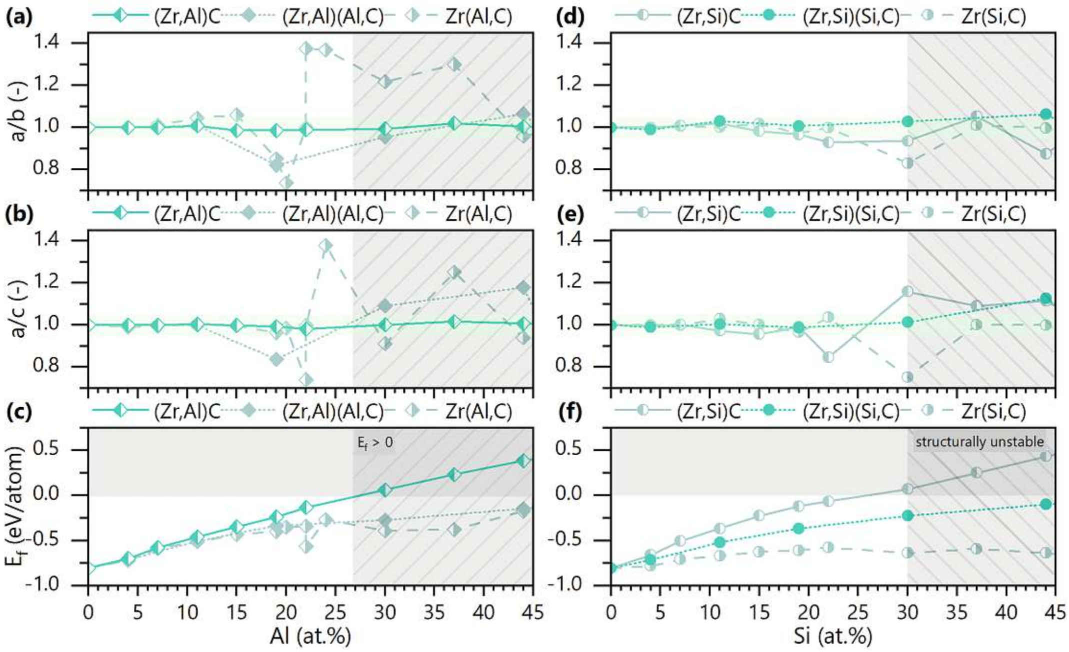

Fig. B. 1. Solubility limit of Al/Si (shaded area) in fcc-structured ZrC. (a) and (b) represent the ratios of lattice constants a/b and a/c, respectively, and (c) reflects the formation energy (E_f) of the Ti-Al-C system. (d) and (e) show the structural modifications of Ti-Si-C (a/b and a/c), respectively, and (f) shows the chemical stability and E_f of Ti-Si-C.

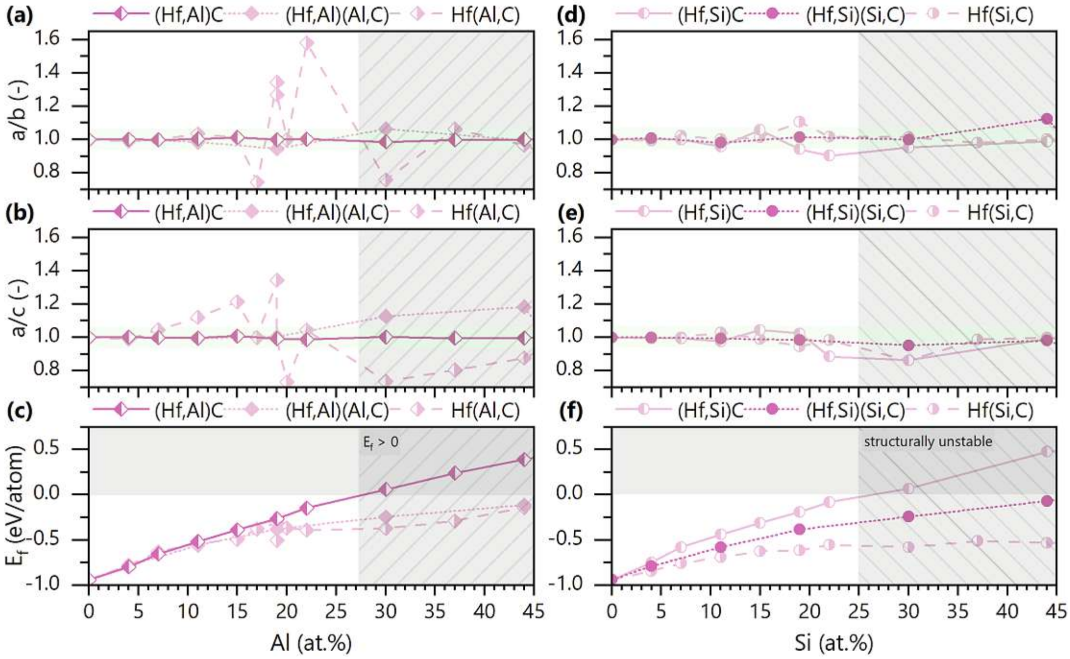

Fig. B. 2. Solubility limit of Al/Si (shaded area) in fcc-structured HfC. (a) and (b) represent the ratios of lattice constants a/b and a/c, respectively, and (c) reflects the formation energy (E_f) of the Hf-Al-C system. (d) and (e) show the structural modifications of Hf-Si-C (a/b and a/c), respectively, and (f) shows the chemical stability and E_f of Hf-Si-C.

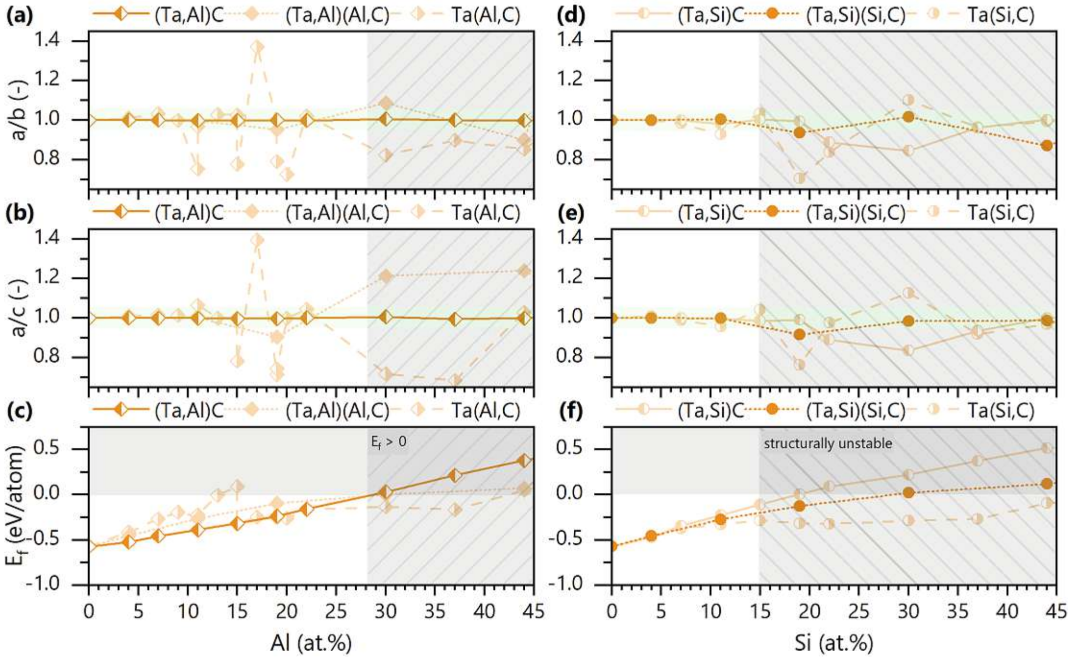

Fig. B. 3. Solubility limit of Al/Si (shaded area) in fcc-structured TaC. (a) and (b) represent the ratios of lattice constants a/b and a/c, respectively, and (c) reflects the formation energy (E_f) of the Ta-Al-C system. (d) and (e) show the structural modifications of Ta-Si-C (a/b and a/c), respectively, and (f) shows the chemical stability and E_f of Ta-Si-C.

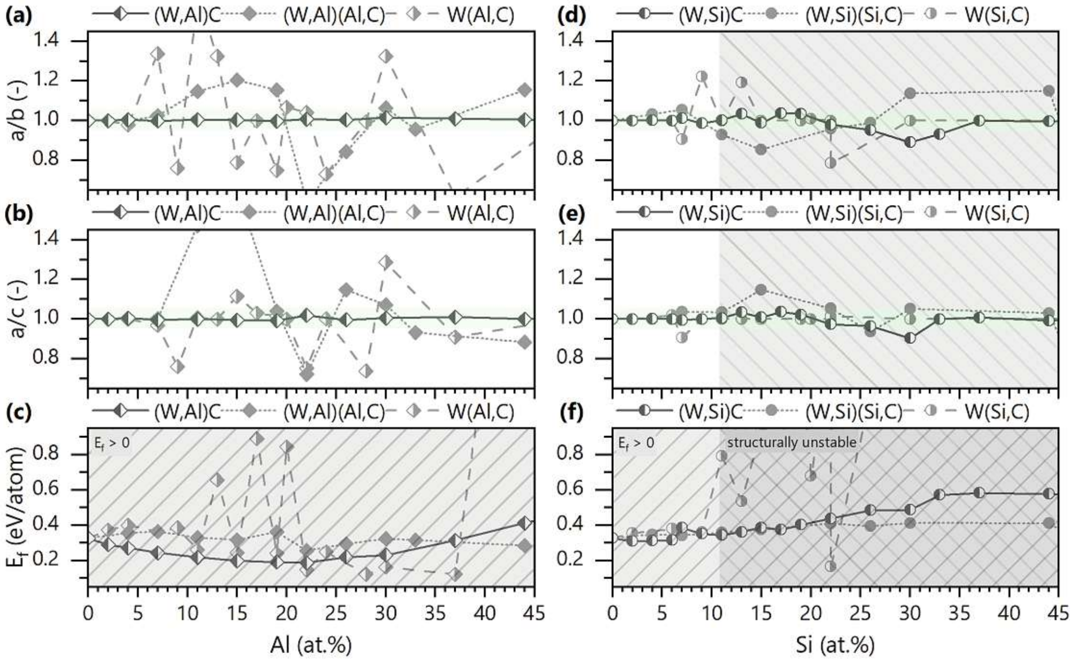

Fig. B. 4. Solubility limit of Al/Si (shaded area) in fcc-structured WC. (a) and (b) represent the ratios of lattice constants a/b and a/c, respectively, and (c) reflects the formation energy (E_f) of the W-Al-C system. (d) and (e) show the structural modifications of W-Si-C (a/b and a/c), respectively, and (f) shows the chemical stability and E_f of W-Si-C.

C. Supplementary phase analysis

Appendix C shows the XRD diffractograms of TM-X-C thin films (TM = Zr, Hf, Ta, W and X = Al, Si).

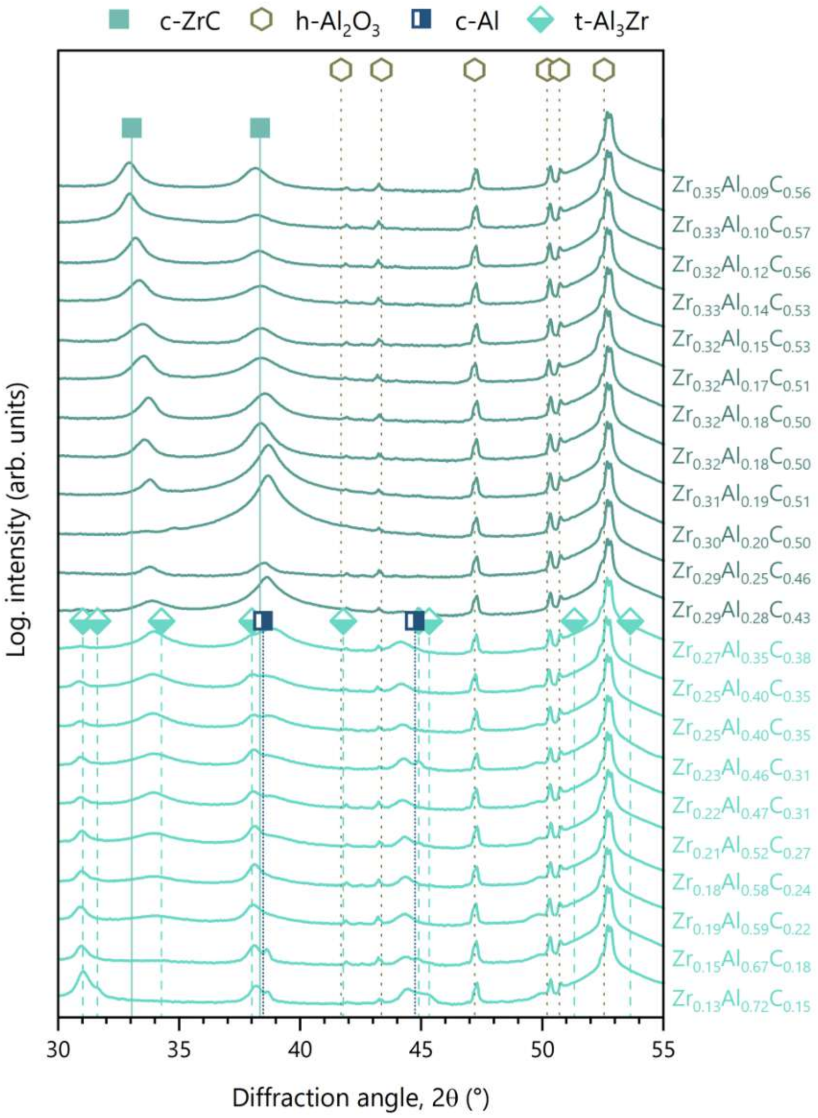

Fig. C.1. XRD diffractograms of Zr-Al-C thin films with different chemical compositions. The observed phases include c-ZrC (00-035-0784), c-Al (00-004-0787), and t-Al_3Zr (04-003-4015). The hexagons belong to the substrate (sapphire, 00-005-0712).

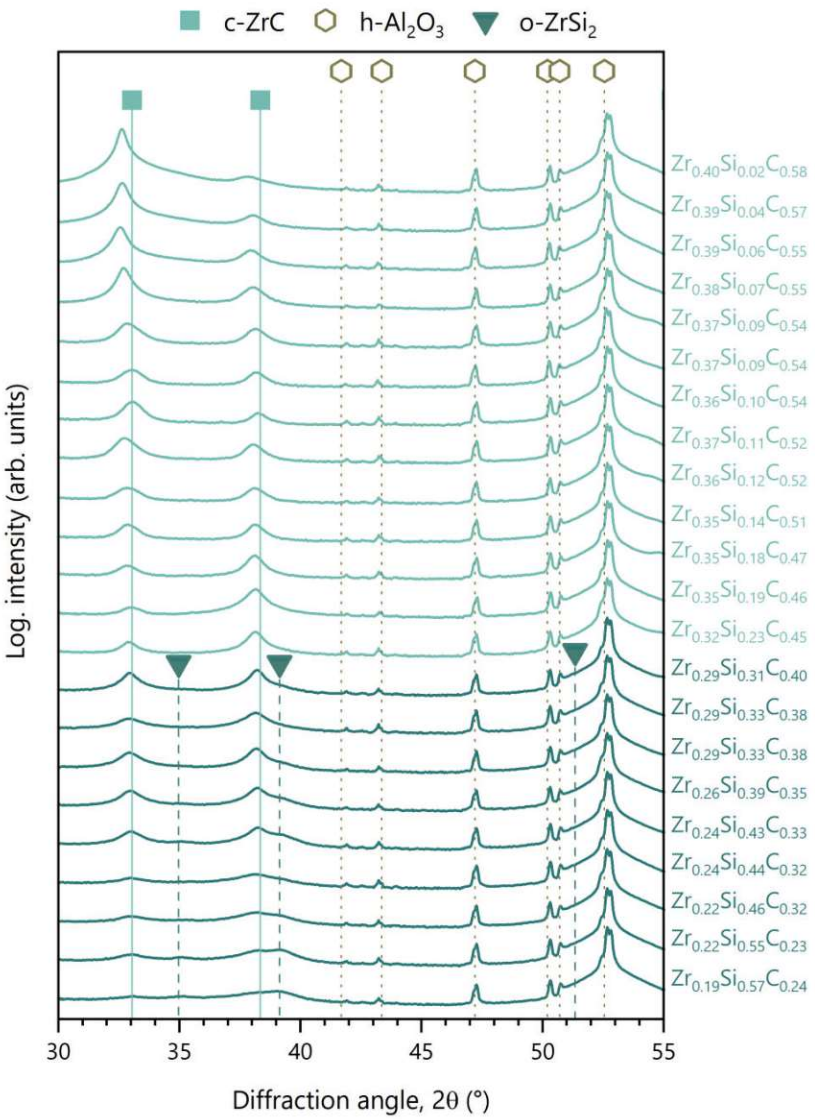

Fig. C.2. XRD diffractograms of Zr-Si-C thin films with different chemical compositions. The observed phases include c-ZrC (00-035-0784) and o-$ZrSi_2$ (00-032-1499). The hexagons belong to the substrate (sapphire, 00-005-0712).

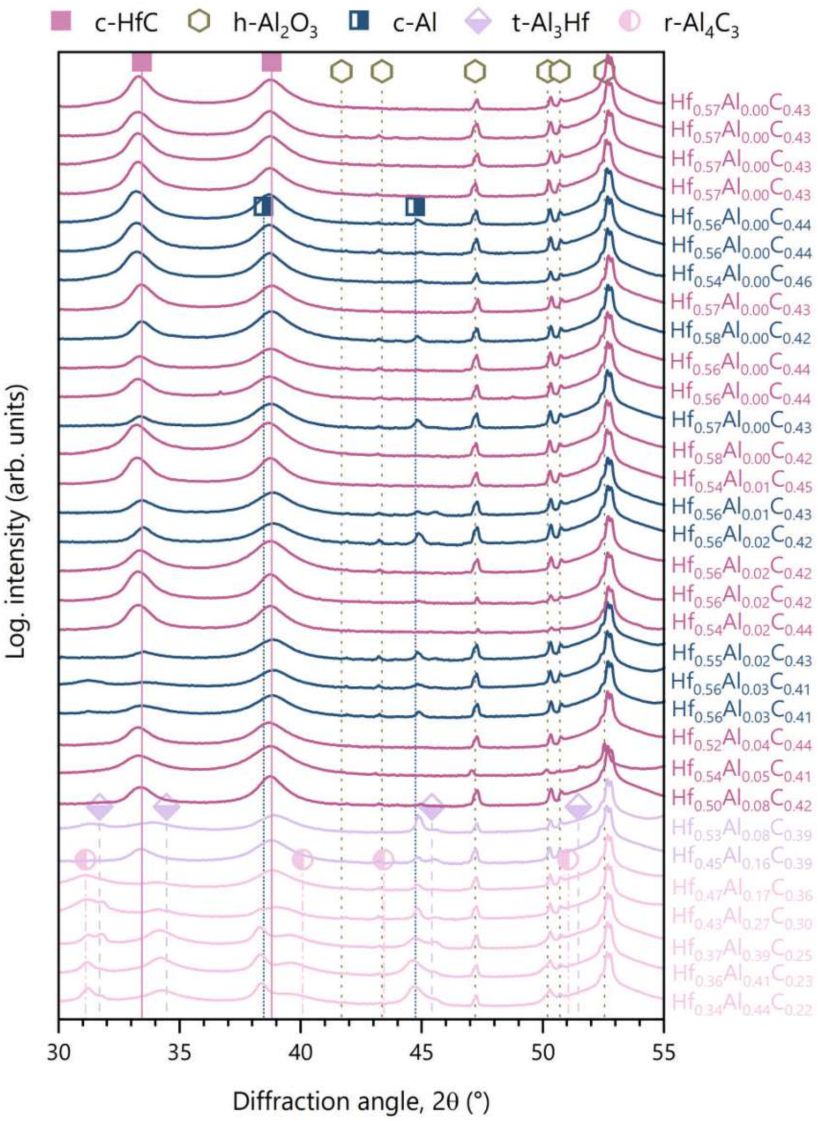

Fig. C.3. XRD diffractograms of Hf-Al-C thin films with different chemical compositions. The observed phases include c-HfC (00-039-1491), c-Al (00-004-0787), t-Al_3Hf (00-037-0891), and r-Al_4C_3 (00-035-0799). The hexagons belong to the substrate (sapphire, 00-005-0712). Based on the total systematic and statistical uncertainties of 5-8 % of the deduced value for the major constituents the chemical composition of very low Al containing films can be misinterpreted – therefore the Hf-Al-C thin films with supposedly 0 at.% Al already show c-Al peaks. Nevertheless, we kept the same labeling as for the other systems and used the following denotation as described above.

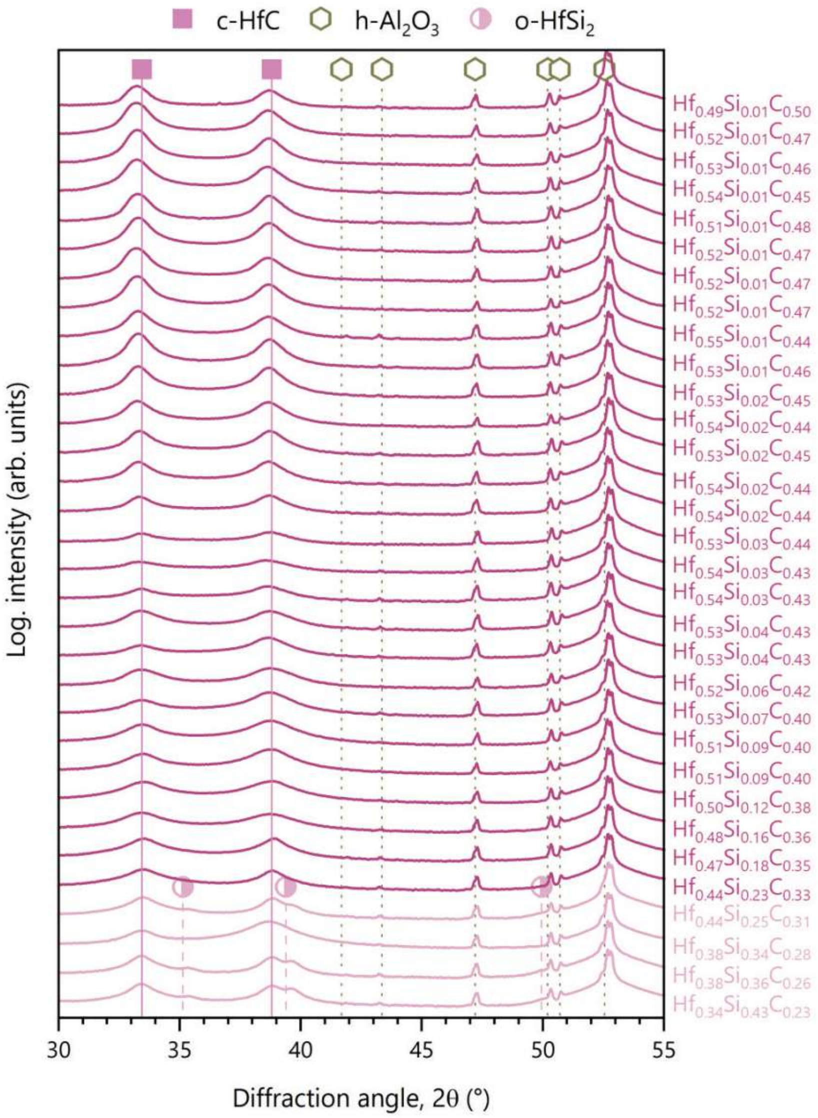

Fig. C.4. XRD diffractograms of Hf-Si-C thin films with different chemical compositions. The observed phases include c-HfC (00-039-1491), and o-HfSi$_2$ (00-038-1373). The hexagons belong to the substrate (sapphire, 00-005-0712).

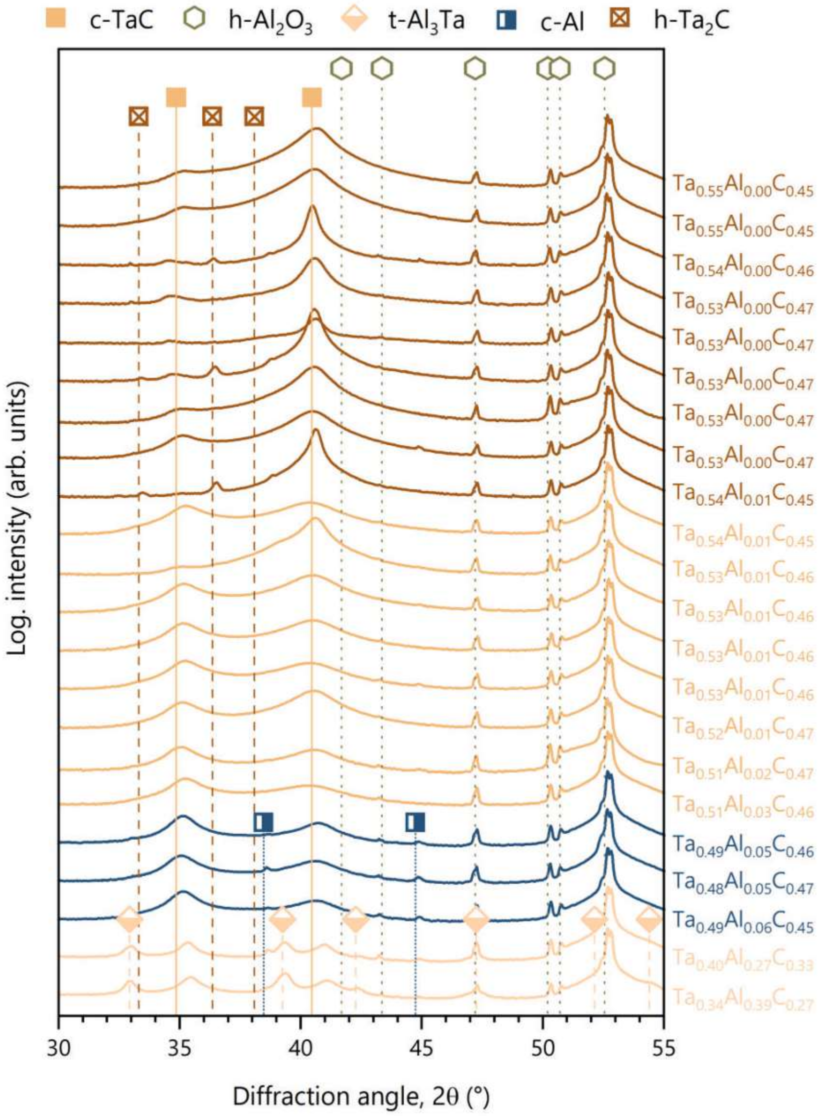

Fig. C.5. XRD diffractograms of Ta-Al-C thin films with different chemical compositions. The observed phases include c-TaC (00-035-0801), t-Al_3Ta (04-014-2301), c-Al (00-004-0787), and h-Ta_2C (01-073-1321). The hexagons belong to the substrate (sapphire, 00-005-0712).

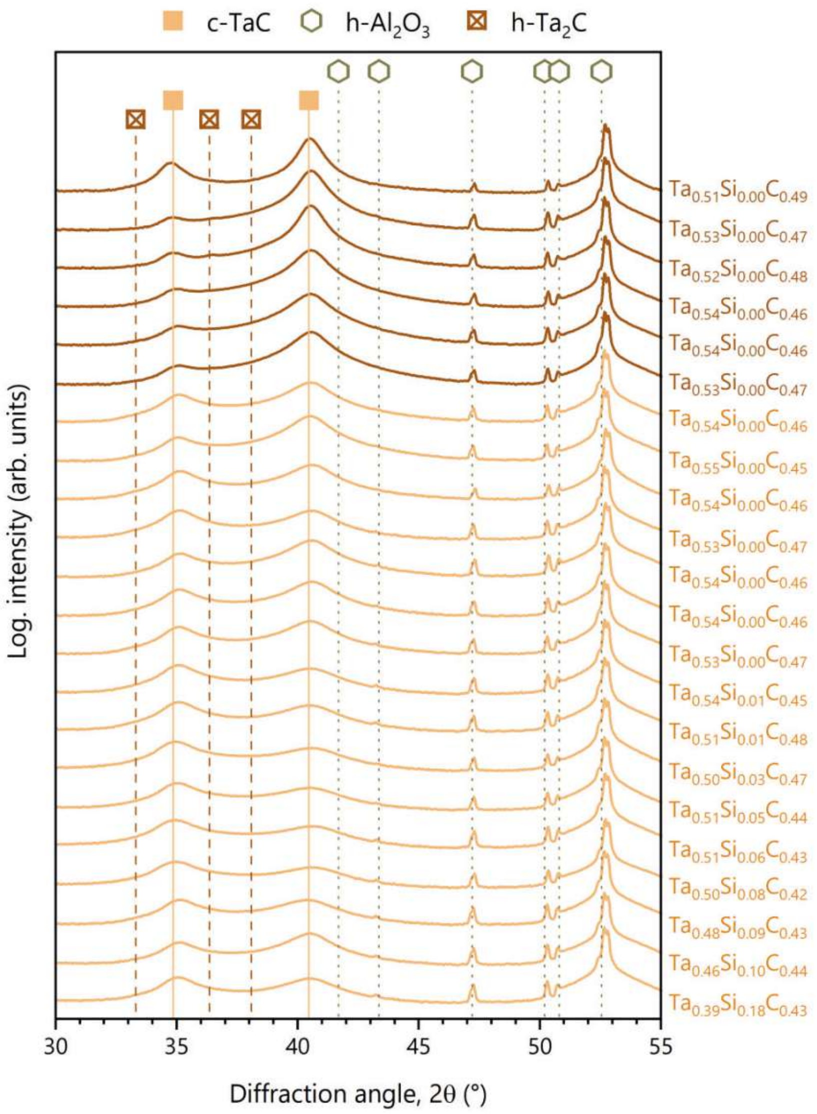

Fig. C.6. XRD diffractograms of Ta-Si-C thin films with different chemical compositions. The observed phases include c-TaC (00-035-0801) and h-Ta_2C (01-073-1321). The hexagons belong to the substrate (sapphire, 00-005-0712).

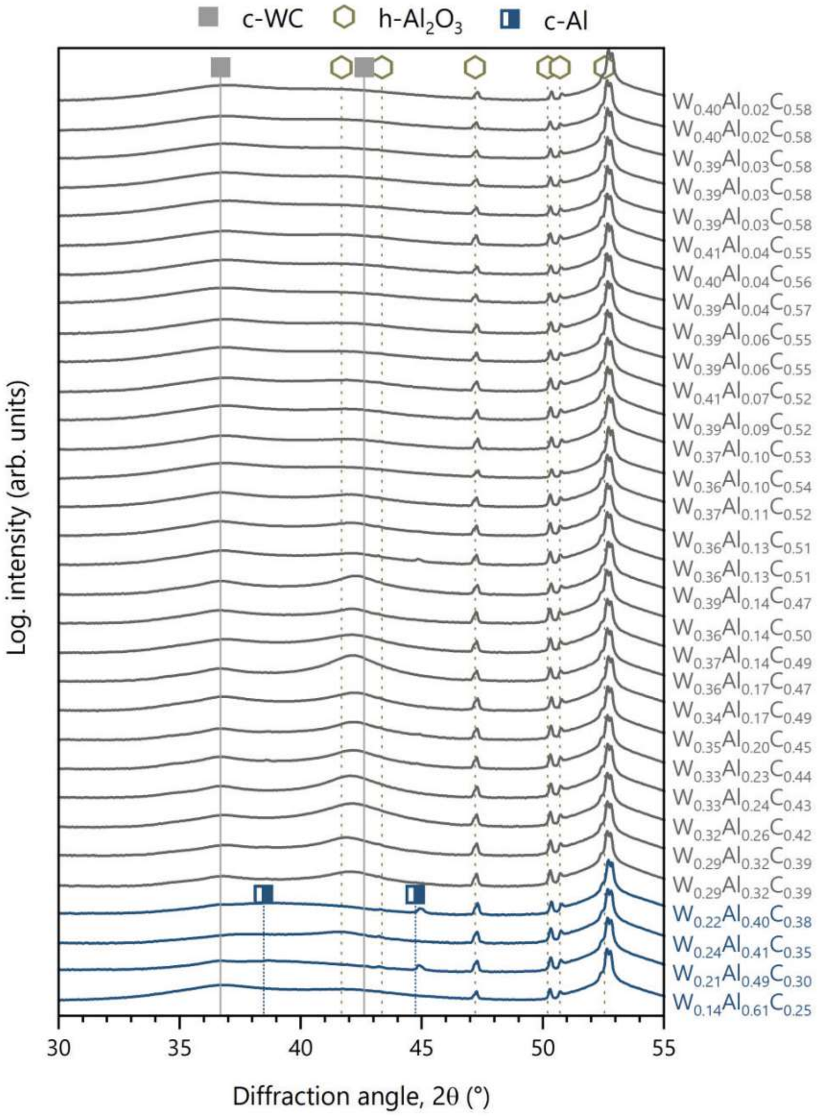

Fig. C.7. XRD diffractograms of W-Al-C thin films with different chemical compositions. The observed phases include c-WC (01-084-4476) and c-Al (00-004-0787). The hexagons belong to the substrate (sapphire, 00-005-0712).

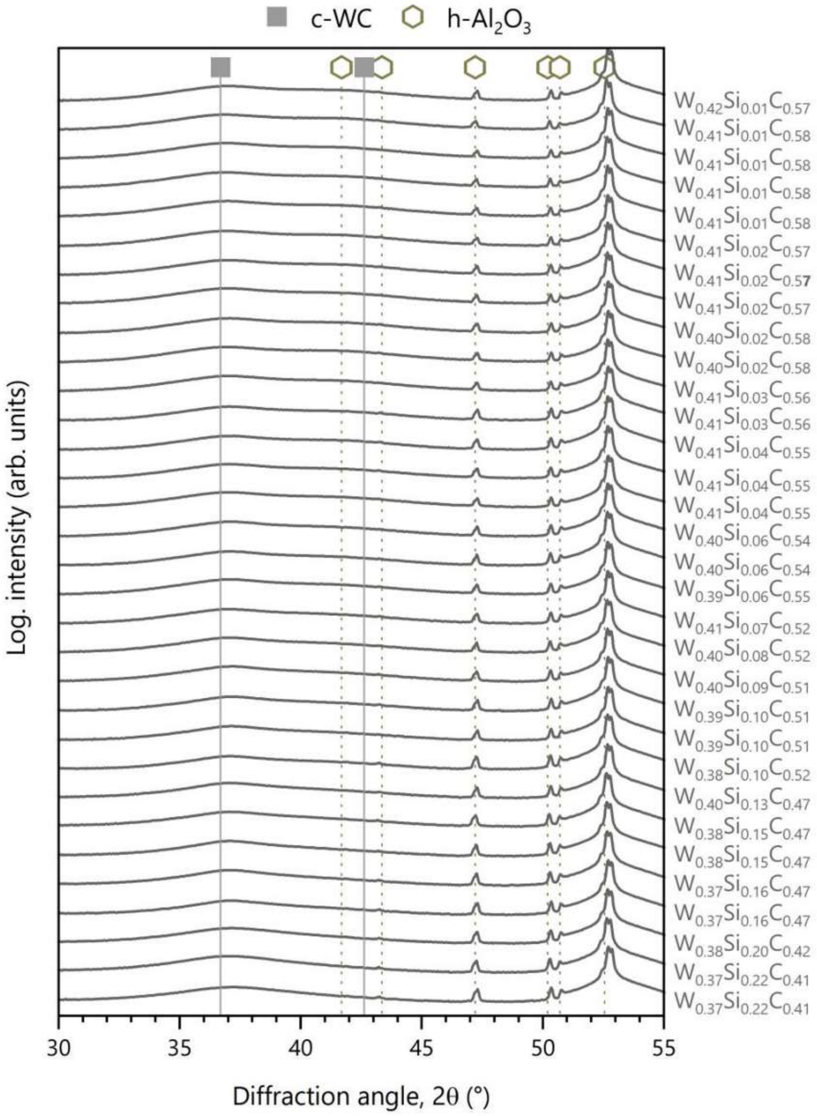

Fig. C.8. XRD diffractograms of W-Si-C thin films with different chemical compositions. The films show the presence of c-WC (01-084-4476). The hexagons belong to the substrate (sapphire, 00-005-0712).

D. Supplementary TEM analysis

Appendix D shows the TEM analysis of fcc structured $Ti_{0.31}Si_{0.19}C_{0.50}$ with a homogeneous distribution of Ti, Si and C.

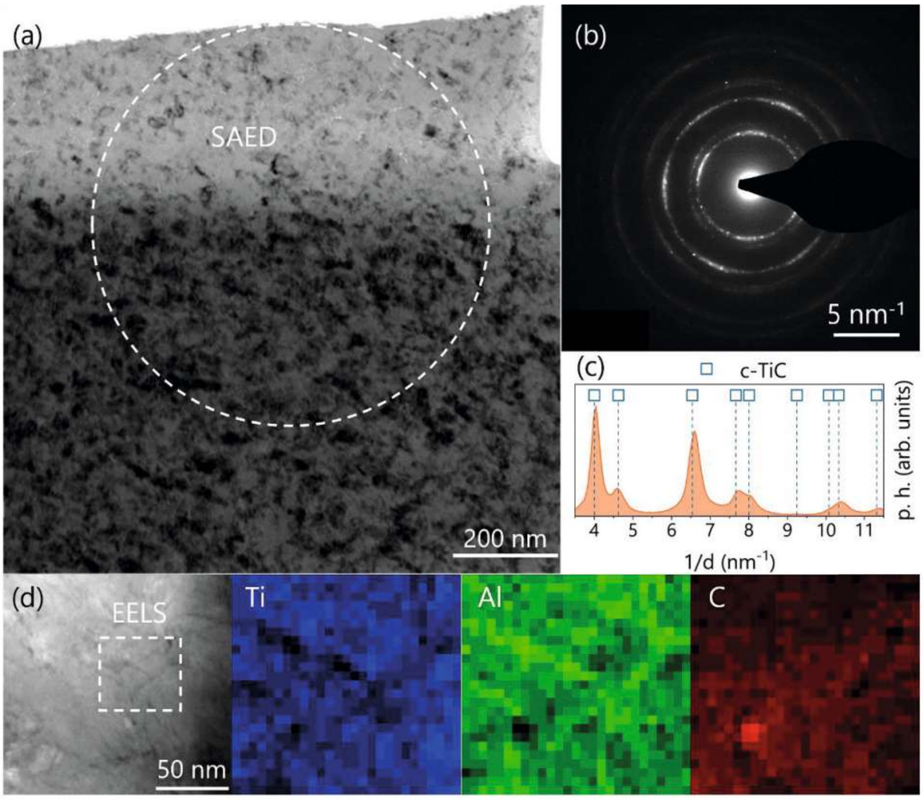

Fig. D.1. (a) shows a top view BF-TEM image of the $Ti_{0.31}Si_{0.19}C_{0.50}$ sample (as deposited) with the area for SAED marked. (b) and (c) only show the c-TiC phase [12] determined by SAED. (d) features the STEM HAADF image with the area marked where the chemical mapping was determined by EELS for Ti, Si and C.

References

[1] G. Kresse et al., Efficient iterative schemes for ab initio total-energy calculations using a plane-wave basis set, Phys. Rev. B Condens. Matter. 54 (1996) 11169–11186.
[2] G. Kresse et al., From ultrasoft pseudopotentials to the projector augmented-wave method, Phys. Rev. B Condens. Matter. 59 (1999) 1758–1775.
[3] P.E. Blöchl, Projector augmented-wave method, Phys. Rev. B Condens. Matter. 50 (1994) 17953–17979.
[4] Available pseudopotentials, VASP Wiki. (2024). https://www.vasp.at/wiki/index.php/Available_pseudopotentials (accessed August 28, 2024).
[5] J.P. Perdew et al., Generalized Gradient Approximation Made Simple, Phys. Rev. Lett. 77 (1996) 3865–3868.
[6] M. Methfessel et al., High-precision sampling for Brillouin-zone integration in metals, Phys. Rev. B Condens. Matter. 40 (1989) 3616–3621.
[7] J.A. Leavitt et al., Cross sections for 170.5 ° backscattering of 4He from carbon for 4He energies between 1.6 and 5.0 MeV, Nucl. Instrum. Methods Phys. Res. B. 40–41 (1989) 776–779.
[8] M.S. Janson, CONTES conversion of time-energy spectra—a program for ERDA data analysis, Uppsala University. (2004).
[9] M. Mayer, Improved physics in SIMNRA 7, Nucl. Instrum. Methods Phys. Res. B. 332 (2014) 176–180.
[10] W.C. Oliver et al., An improved technique for determining hardness and elastic modulus using load and displacement sensing indentation experiments, J. Mater. Res. 7 (1992) 1564–1583.
[11] A.C. Fischer-Cripps, Critical review of analysis and interpretation of nanoindentation test data, Surf. Coat. Technol. 200 (2006) 4153–4165.
[12] International Center of Diffraction Data, Powder Diffraction File - cubic TiC - 00-032-1383, (1982).

Publication IV

PLANSEE
SEMINAR
21 | 2025

Exploring the oxidation characteristics of binary and ternary transition metal carbide coatings

S. Richter, P. Kutrowatz, T. Wojcik, S. Kolozsvári, P. Polcik, C. Jerg, J. Ramm, H. Riedl

Plansee Seminar, Conference Proceeding (2025).

Exploring the oxidation characteristics of binary and ternary transition metal carbide coatings

S. Richter*, P. Kutrowatz*, T. Wojcik*, S. Kolozsvári**, P. Polcik**,
C. Jerg***, J. Ramm***, H. Riedl*,****

* Christian Doppler Laboratory for Surface Engineering of high-performance Components, TU Wien, Austria

** Plansee Composite Materials GmbH, 86983 Lechbruck am See, Germany

*** Oerlikon Balzers, Oerlikon Surface Solutions AG, 9496 Balzers, Liechtenstein

**** Institute of Materials Science and Technology, TU Wien, 1060 Wien, Austria

Abstract

This study explores the oxidation properties of binary and ternary Al/Si alloyed transition metal carbide (TMC) thin films, focusing on group IV to VI metals, specifically Ti, Zr, Hf, Ta, and W. TMCs are classified as ultra-high temperature ceramics (UHTCs) and are recognized for their high melting temperatures, exceeding 3000 °C, along with their exceptional thermal stability. However, they typically suffer from poor oxidation resistance. Binary TMC thin films start to oxidize at temperatures below 600 °C. To expand the application possibilities of TMCs, particularly in high-temperature fields such as aerospace, automotive, and tooling industries, alloying concepts with Al and Si are being explored to enhance their oxidation resistance. In detail, ten different sputter deposited ternary TM-X-C coating families were isothermally oxidized at 750 °C for 1 h and their oxidation kinetics have been benchmarked. For Al alloyed thin films, the best performing systems are Ti-Al-C and Ta-Al-C, forming scales below 750 nm at alloy contents above 25 at.% Al. In contrast, Ti-Si-C only requires around 20 at.% Si to form a dense and adherent scale (below 300 nm). Both $Ti_{0.26}Al_{0.32}C_{0.42}$ and $Ti_{0.29}Si_{0.26}C_{0.45}$ exhibit a two-layered oxide scale, consisting of a metal oxycarbide zone at the interface to the unaffected, nonporous Ti-Al/Si-C coating, followed by a mixed Ti-(Al/Si)-oxide scale on top. Based on detailed TEM analysis Al alloyed TiC obtains a better ability to act as an oxygen diffusion barrier.

Keywords

Transition metal carbides, Aluminum, Silicon, Oxidation resistance, UHTCs, Thin films, Coatings

Introduction

Transition metal carbides (TMCs) are known for their exceptional thermal stability and high melting points, making them ideal candidates among ultra-high temperature ceramics (UHTCs) for high-temperature applications [1]. Not just that, the HfC-TaC material system has been intensively studied and is known for having one of the highest melting temperatures [2,3], various TMCs ceramics are used under extreme conditions [4]. However, TMCs suffer from insufficient oxidation resistance compared to their boride-based counterparts: Bulk diborides, such as ZrB_2 and HfB_2, exhibit oxidation resistance up to 1100 °C due to the formation of dense, glassy oxide scales of B_2O_3 [5]. In contrast, bulk TMC (TM = Ta, Nb, Zr), experience oxidation onset temperatures below 760 °C, and TiC has shown a steadily increasing mass signal indicative of oxidation from room temperature up to 1000 °C [6]. This poor oxidation behavior limits TMCs for potential applications, especially in extreme environments such as in energy and aerospace industries [1,6]. Improving their oxidation behavior would greatly expand their usability in diverse high-temperature applications.

Current research in high-temperature materials is increasingly focused on new material concepts that are both lightweight and capable of withstanding higher operation temperatures (< 1500 °C). Ceramic matrix composites (CMCs) have emerged as a promising alternative to conventional used Ni-based superalloys due to their lower density and superior thermal properties [7–9]. A widely used, promising CMC material is SiC/SiC, which form protective silica scales of 8 µm after 48 h oxidation at 1400 °C [10]. However, for high-temperature applications (> 1200 °C), CMCs with carbon fiber are particularly suitable, as they have higher creep resistance (in contrast to SiC and oxide fibers). These carbon fibers, however, start to oxidize at around 500 °C [11]. To ensure long-term stability, CMCs require effective protection against oxidation and corrosion. In this context, protective coatings play an important role in enhancing oxidation resistance of CMC based substrates/components. Among various coating techniques, physical vapor deposition (PVD) stands out as a powerful and versatile method for efficient synthesis and screening of new coating materials. Additionally, PVD provides precise control over composition, phase formation, and microstructure. It also enables various alloying approaches, allowing for the incorporation and alloying of low-melting metals, such as Al and Si, with ultra-high temperature ceramics (UHTCs) [12].

Previous studies have shown that alloying with strong-oxide forming elements, such as Cr, Al or Si, can drastically improve the oxidation resistance of various material systems and thin films (e.g., borides, carbides, nitrides). HfC-SiC ceramics, for example, showed extreme high-temperature oxidation resistance above 2500 °C [13]. In the context of improving the oxidation resistance of CMC-based components, TMCs are particularly well-suited based on their similar coefficients of thermal expansion with CMCs, providing good coating adhesion [7]. By alloying Al and Si into face centered cubic (fcc) structured TMCs (TM-X-C, X = Al, Si), the formation of silica (SiO_2) or alumina (Al_2O_3) based scales is expected to act as a protective barrier against (oxygen) diffusion and further accelerated oxidation. Ternary fcc-structured TM-X-C solid solutions differ from their ordered counterparts, known as MAX phases. Due to the preference of the PVD process to stabilize fcc structures, these solid solutions are anticipated to be easier to stabilize using plasma-based growth techniques. This stabilization offers significant advantages for synthesis and industrial applications.

In this study, a combinatorial sputter deposition approach comprising 10 different TM-X-C material systems is performed to screen their oxidation resistance in relation to their binaries. Furthermore, a detailed microstructural analysis of the formed oxide scales was performed using transmission electron microscopy (TEM) to gain insight into the oxidation mechanism and appearance of the scales.

Experimental

All binary and ternary TMC (TM = Ti, Zr, Hf, Ta, W) thin films were synthesized in an AJA Orion 5 [14] deposition system. The binary systems were magnetron sputtered from 3'' TiC, ZrC, HfC, TaC, and WC/C (70/30 mol%) targets, respectively (provided by Plansee Composite Materials GmbH [15]). During sputtering, argon with a purity of 99.999% was used as the working gas. For the ternary systems, the same TMC targets were co-sputtered with pure 2'' Al or Si targets. The targets were confocally aligned for co-sputtering. In order to deposit a chemical variety and different alloying states, a combinatorial deposition approach was chosen for this study, i.e. no substrate rotation was applied during co-sputtering. Thus, a chemical gradient along the substrate holder could be achieved. All detailed deposition parameters can be found in [12]. For the binary carbide coatings, the same deposition parameters were used as in [12], but without co-sputtering Al and Si.

To determine the chemical composition of the binary and ternary TMC thin films, standards were measured using Time-of-Flight Elastic Recoil Detection Analysis (ToF-ERDA) and Elastic Backscattering Spectrometry (EBS) at the 5 MV Pelletron Tandem accelerator at Uppsala University [16]. These standards have been used for further chemical analysis using X-ray fluorescence analysis (XRF) at the TU Vienna. All details for measuring the chemistry are described in more detail in [12].

To study the phase formation of the binary and ternary TMC thin films, X-ray diffraction (XRD) was performed using a Panalytical X'Pert Pro MPD X-ray diffractometer. The measurements were carried out in Bragg-Brentano geometry with Cu-Kα radiation (wavelength $\lambda = 1.5418$ Å).

To investigate the oxidation characteristics of the binary TMC thin films, dynamic oxidation tests were conducted in a combined differential scanning calorimetry (DSC)-thermogravimetric analysis (TGA) system (Netzsch STA 449 F1) equipped with a Rhodium furnace. Only the TGA data was recorded from coatings deposited on sapphire (single crystalline Al_2O_3) substrates. The dynamic tests were performed from room temperature up to 1400 °C (heating rate of 10 °C/min), in a mixture of synthetic air (50 ml/min) and helium (protective gas, 20 ml/min). Before each measurement, a baseline measurement was performed with an empty crucible with the same testing conditions. Based on the fact that the substrate material is inert against oxidation in the investigated temperature range [17], the mass change detected can be directly related to the oxidation effects of the coating material. Additional isothermal oxidation tests were performed for the ternary coatings. The coatings were oxidized in a DSC/TGA Mettler Toledo system in lab-air at 650, 700 or 750 °C (depending on the TMC) for 1 h.

After the oxidation experiment, focused ion beam (FIB) cross sections were prepared using a FIB-scanning electron microscope (SEM) configuration (ThermoFisher Scientific Scios 2). The cross sections were prepared using Ga^+ ions with a current between 7 and 17nA for fine milling, at an acceleration voltage of 30kV. Using the FIB cross sections, the oxide scale thickness was measured. In addition, energy-dispersive X-ray spectroscopy (EDX) line scans were performed.

To study the oxidation characteristics more detailed, transmission electron microscopy (TEM) was performed using a FEI TECNAI F20 (S)TEM system, operated at 200 kV acceleration voltage. The TEM lamellae were prepared via a standardized FIB lift out procedure on a ThermoFisher Scios 2. Additional electron energy loss spectroscopy (EELS) line scans were used to further determine the chemical composition and coating architecture.

Results and Discussion

A comprehensive structural analysis is essential to evaluate the oxidation behavior of binary and ternary TM-X-C thin films. All binary thin films, except TaC, display a single-phase face-centered cubic (fcc) structure in their as-deposited state, as determined by XRD illustrated in Figure 1. Additionally, Figure 1 presents the chemical composition of the binary systems. Besides fcc-TaC, the hexagonal Ta_2C coexists, which can be related to the sub-stoichiometry in C (46 at.% C), being in accordance to other studies [18]. In addition, $W_{0.41}C_{0.59}$ and $Hf_{0.50}C_{0.50}$ obtains a very fine-grained morphology, as the XRD peaks appear relatively broad. The same applies to the $Ti_{0.25}C_{0.75}$ thin films, which have a super stoichiometry in C.

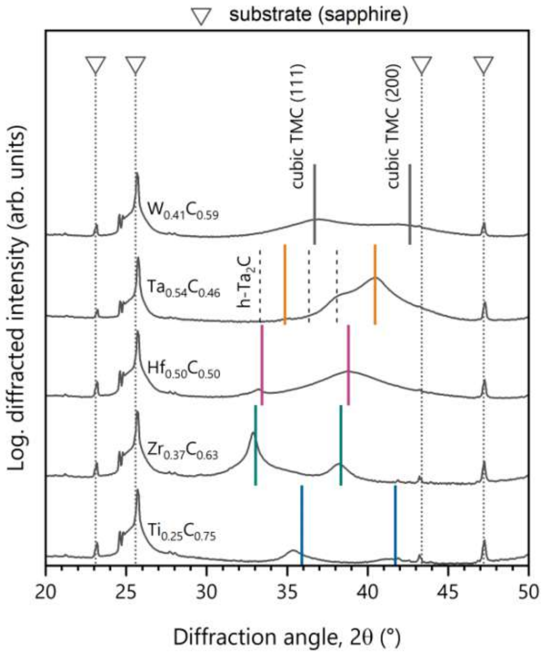

Figure 1: XRD diffractograms of binary TMC thin films. The solid vertical lines represent the reference lines of each TMC system (fcc-TiC [19], fcc-ZrC [20], fcc-HfC [21], fcc-TaC [22], fcc-WC [23]). TaC appears dual phased, with the co-existence of hexagonal Ta_2C (dashed reference line, [24]). The triangles belong to the substrate (sapphire, [25]).

The oxidation behavior and onset temperature ($T_{Ox,onset}$) for the binary transition metal carbides (TMCs) have been evaluated using thermogravimetric analysis (TGA). The coatings were dynamically oxidized in synthetic air at temperatures up to 1400 °C, and the mass change was recorded as a function of temperature, as shown in Figure 2. Unfortunately, the measurement for TiC failed, and after 1400 °C, the sample was no longer present, indicating a complete oxidation of the thin film. For this reason, the TGA curve for TiC is not shown in Figure 2 and reference is made to literature data. For both, bulk TiC [26] as well as TiC thin films [27], a parabolic oxidation behavior between 600 and 800 °C has been described – therefore indicated with an oxidation onset of 600 °C in Figure 2 (see blue vertical line). $Zr_{0.37}C_{0.63}$ presents a stable mass signal up to 550 °C, after which a mass increase can be recognized. The oxidation is complete at around 680 °C indicated by the dotted vertical line $T_{ox,saturated}$ in Figure 2. The subsequent slight decrease in mass can be related to the volatilization of CO and CO_2 [2]. Furthermore, the formation of ZrO_2 is associated with significant volume changes, which can lead to oxide layer cracking and thus underlying ZrC is unprotected and gets oxidized. In this sense, a constant mass signal is established after approximately 700 °C up to about 1400 °C. A similar behavior is observed for $Hf_{0.50}C_{0.50}$. The increase in mass/oxidation also appears around $T_{Ox,onset}$ = 550 °C, and reaches its peak at around $T_{Ox\_saturated}$ = 800 °C. The subsequent decrease in mass is again related to the volatilization of carbon. $Ta_{0.54}C_{0.46}$ demonstrates a consistent increase in mass between 150 °C and 700 °C. Subsequently, a substantial mass increase occurs at approximately 750 °C, which aligns with existing literature [2]. Ta_2O_5 is well known for its significant increase in volume, which can lead to cracking of the scale and further oxidation of the underlying material. $W_{0.41}C_{0.59}$ shows a constant TGA signal up to about $T_{Ox,onset}$ = 550 °C, followed by a continuous increase in mass up to about 1100 °C, followed by a drop due to a suggested volatilization of both W and C.

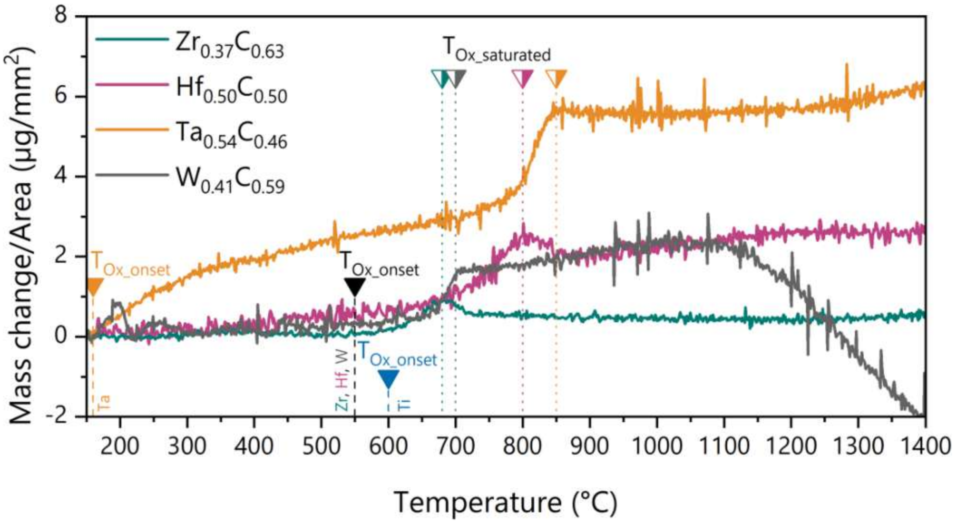

Figure 2: TGA signals for dynamic oxidation experiments on $Zr_{0.37}C_{0.63}$, $Hf_{0.50}C_{0.50}$, $Ta_{0.54}C_{0.46}$, and $W_{0.41}C_{0.59}$ up to 1400 °C. The oxidation onset temperatures for the different TMCs are given as T_{Ox_onset} (full triangle symbols with dashed vertical lines). Literature data were used for TiC [26,27], T_{Ox_onset} = 600 °C. For TaC T_{Ox_onset} is already at about 150 °C. ZrC, HfC, WC start to oxidize at approx. 550 °C. Furthermore, half-filled triangles with dotted vertical lines represent the fully oxidized state ($T_{Ox\_saturated}$).

For the oxidation tests of the 10 different ternary TM-X-C material systems, 3 different alloying states each in correspondence to our previous study [12] have been selected. All ternary Al/Si alloyed TMC thin films were isothermally oxidized at the same temperature for 1 h to compare their oxidation behavior. Based on the TGA results, the oxidation experiments were performed at 750 °C, representing an interesting range based on the oxidation behavior of the binaries. However, for Ta-Si-C, an oxidation temperature of 700 °C was chosen, since the films were fully oxidized at 750 °C. The same applies to the W-Al/Si-C thin films, which were oxidized at 600 °C. In this context, both TaC and WC also showed the poorest oxidation behavior after TGA.

Figure 3a shows the XRD diffractograms of the selected three compositions for Ti-Al-C: $Ti_{0.24}Al_{0.26}C_{0.50}$, $Ti_{0.26}Al_{0.32}C_{0.42}$, and $Ti_{0.24}Al_{0.45}C_{0.31}$, both in the as deposited and oxidized state, respectively. In the as deposited state, $Ti_{0.24}Al_{0.26}C_{0.50}$ indicates a single-phase fcc structured coating (solid solution). For higher Al contents (> 32 at.%), dual-phased structured coatings are representative, which additionally comprise the tetragonal Al_5Ti_2 phase – such as for $Ti_{0.26}Al_{0.32}C_{0.42}$ and $Ti_{0.24}Al_{0.45}C_{0.31}$. After oxidation, the $Ti_{0.24}Al_{0.26}C_{0.50}$ sample still shows the fcc TiC structure. The higher alloyed samples also withstood the oxidation experiment and exhibit fcc TiC peaks next to fractions of the metallic Al_5Ti_2 phase. For all three compositions no oxide based structures could be identified after oxidation at 750 °C for 1h.

Figure 3b presents the XRD diffractograms of the as deposited and oxidized Ti-Si-C thin films with the compositions: $Ti_{0.32}Si_{0.20}C_{0.48}$, $Ti_{0.29}Si_{0.26}C_{0.45}$, $Ti_{0.27}Si_{0.40}C_{0.33}$. $Ti_{0.32}Si_{0.20}C_{0.48}$ shows a single-phase fcc structure in the as-deposited state. For higher Si contents, the films tend to become XRD amorphous, as described in more detail in [12]. The same trend applies to the oxidized states, $Ti_{0.32}Si_{0.20}C_{0.48}$ also obtains fcc peaks after oxidation, whereas the coatings with higher Si alloying contents (> 26 at.%) appear fully amorphous after oxidizing at 750 °C for 1 h. Similar to the Al alloyed TiC, no oxides could be indexed after oxidation at 750 °C for 1h.

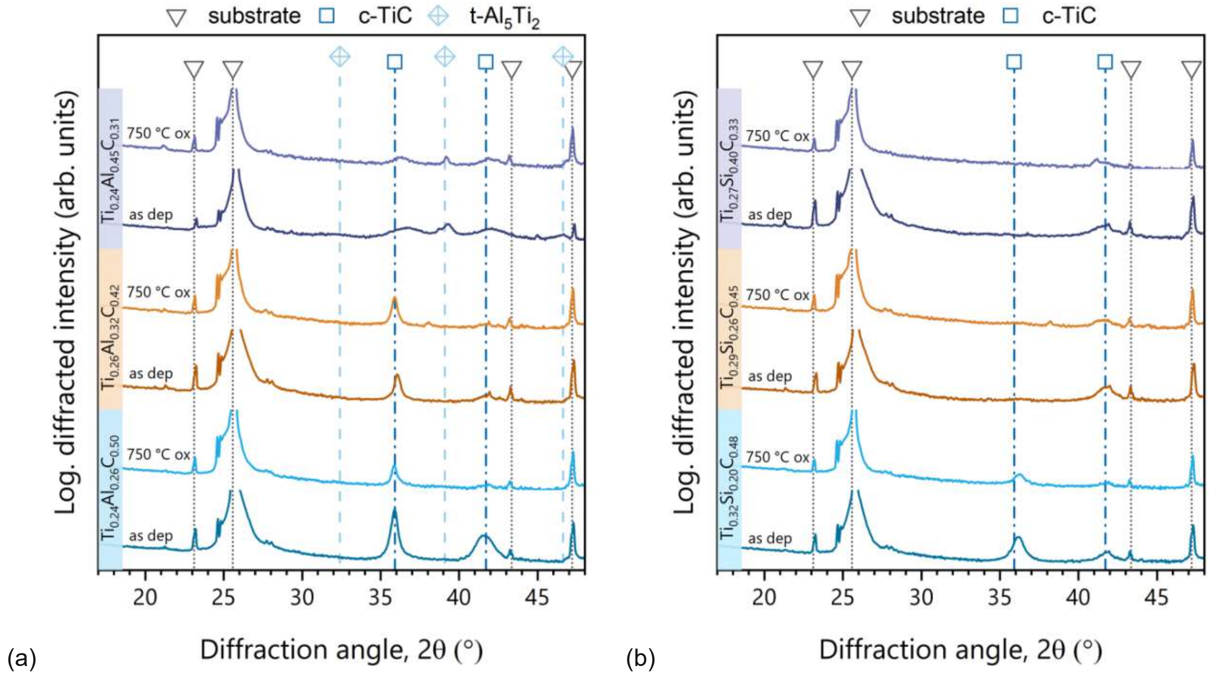

Figure 3: XRD diffractograms of (a) Ti-Al-C and (b) Ti-Si-C thin films in their as deposited and oxidized state (750 °C, 1h). The triangles belong to the substrate (sapphire, [25]). The squares and the crossed squares belong to cubic TiC [19] and tetragonal Al_5Ti_2 [28], respectively. The as deposited XRD diffractograms have already been published in [12].

For the other TM-X-C systems (TM = Zr, Hf, Ta, W), the XRD diffractograms can be found in the appendix (Figure A.1 to A.4). In summary, it can be stated that for the Zr-Al/Si-C systems, only the highest alloyed variants ($Zr_{0.23}Al_{0.46}C_{0.31}$ and $Zr_{0.22}Si_{0.46}C_{0.32}$, both thin films being dual-phased) withstood oxidation at 750 °C for 1 hour. In contrast, the lower alloyed Zr-X-C thin films (with aluminum content less than 24 at.% and silicon content less than 33 at.%) were completely oxidized after the oxidation test. X-ray diffractograms showed an amorphous structure, and EDX line scans along the film growth revealed an oxygen content of 40-45 at.% throughout the entire coating thickness. For Hf-X-C, only $Hf_{0.36}Al_{0.41}C_{0.23}$ resisted the oxidation test and was not fully oxidized after 1 h at 750 °C. All Hf-Si-C thin films and all Al alloyed coatings with Al < 27 at.% appear XRD amorphous after annealing, while $Hf_{0.36}Al_{0.41}C_{0.23}$ still exhibits peaks corresponding to the fcc HfC and metallic tetragonal $HfAl_3$ phase. For Ta-Al-C, thin films having Al > 27 at.% withstood the annealing experiments and fcc TaC and metallic tetragonal $TaAl_3$ were detectable in the oxidized state. In contrast, the Ta-Si-C thin films only withstood annealing temperatures at 700 °C for 1 h. However, for two alloy contents investigated ($Ta_{0.46}Si_{0.10}C_{0.44}$ and $Ta_{0.39}Si_{0.18}C_{0.43}$) XRD peaks corresponding to o-Ta_2O_5 were already detected after oxidation. The W-X-C coatings were oxidized at 650 °C for 1 h; the thin films did not withstand higher oxidation temperature. $W_{0.24}Al_{0.41}C_{0.35}$ was completely oxidized after the annealing test, $W_{0.29}Al_{0.32}C_{0.39}$ showed hexagonal WAl_2 and tetragonal WO_3 peaks after oxidation, and $W_{0.24}Al_{0.41}C_{0.35}$ withstood the oxidation test (no t-WO_3 phase visible in the XRD). However, the coating appears XRD amorphous in both the as deposited as well as the oxidized states.

Figure 4 summarizes the scale formation and respective oxide scale thicknesses of the various Al- and Si- alloyed TM-X-C systems. The solid symbols represent coating systems that passed the oxidation test based on the XRD (prevalent fcc structures) and oxygen content evaluated during cross sectional analysis in the SEM/EDX. Cross symbols indicate that the coating was completely oxidized. Open symbols indicate the systems Ta-Si-C and W-Al/Si-C, as they only withstood the oxidation temperatures of 700 and 650 °C. For Al alloyed TM-X-C coatings an alloying content higher than 25 at.% is necessary to withstand the oxidation treatment at 750 °C for 1 h – see Figure 4a. In contrast, for Si alloying only the Ti-Si-C and the highly alloyed Zr-Si-C thin film (Si > 45 at.%) withstood 750 °C – see Figure 4b. Based on these tests, Ti-Al/Si-C shows highly promising results in terms of scale thickness and oxidation resistance at 750 °C. Also Ta-Al-C obtains an interesting behavior. Based on the structure-mechanical properties [12] the oxidation characteristics of $Ti_{0.26}Al_{0.32}C_{0.42}$ and $Ti_{0.29}Si_{0.26}C_{0.45}$ were examined in more detail using TEM analysis. The two selected coatings are single phase fcc structured in the as deposited state and exhibit hardness values > 20 GPa [12].

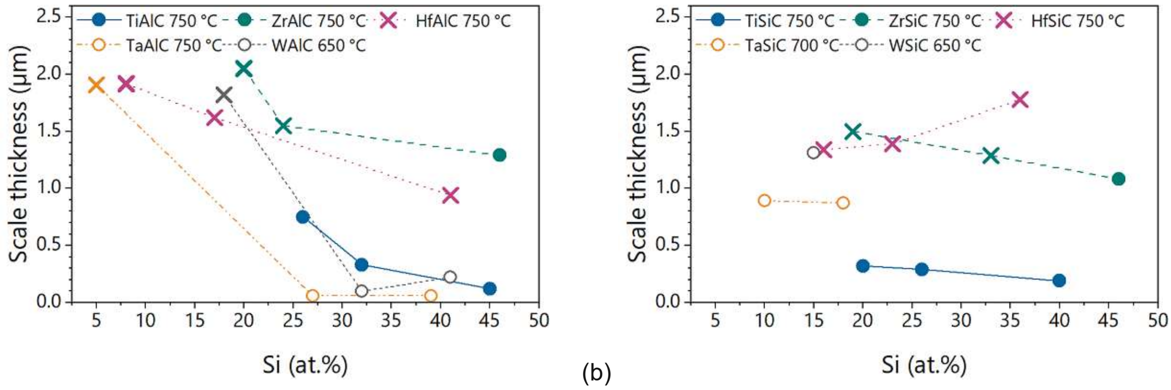

(a) (b)

Figure 4: represents the scale thickness in relation to the (a) Al and (b) Si alloying content in ternary transition metal carbide thin films TM-X-C after the isothermal oxidation test (1h). The data were taken from FIB cross sections after the oxidation experiment. The crosses symbolize samples that were completely oxidized but still present after the annealing test. Open symbols indicate TM-X-C systems that only withstood lower oxidation temperatures (e.g., 700 °C or 650 °C).

Figure 5a presents a bright field (BF)-TEM cross section of the oxidized $Ti_{0.26}Al_{0.32}C_{0.42}$ thin film at 750 °C after 1 h. From bottom to top, the sapphire substrate, the Ti-Al-C film with an oxide scale can be recognized, topped with a W protection layer from FIB lamella preparation. The cross section already indicates an oxide scale consisting of two different layers. The two layered scale formation is also reflected in the EELS line scan taken from bottom to top along thin film growth (see Figure 5b) containing the substrate, followed by the non-oxidized Ti-Al-C coating, and the layered scale, respectively. This layered scale is similar to what is described in the literature for oxidized TMCs [29]. At the interface to the unaffected coating, a metal oxycarbide ($MC_{1-x}O_x$) is formed, and a carbon depleted oxide scale develops on top towards the surface. In more detail, the C content in the first oxide layer is about 40 at.% (at a distance between 700 and 800 nm in Figure 5b), whereas in the second region of the oxide (from a distance of 800 nm in Figure 5b) the C content decreases to below 20 at.% and the oxygen content increases to about 60 at.% - being in good relation to the abovementioned literature. Furthermore, the $MC_{1-x}O_x$ based region is dominated by Ti, whereas the outermost region obtains a more mixed Ti-Al-based oxide. In Figure 5a and 5b, the oxide scale thickness (comprising both zones) is approximately 300 nm, which differs from the film thickness determined using FIB cross sections. This is due to the inaccuracy of thickness measurements by FIB/SEM cross sections and the fact that the coating thickness may differ at different locations on the coated substrate.

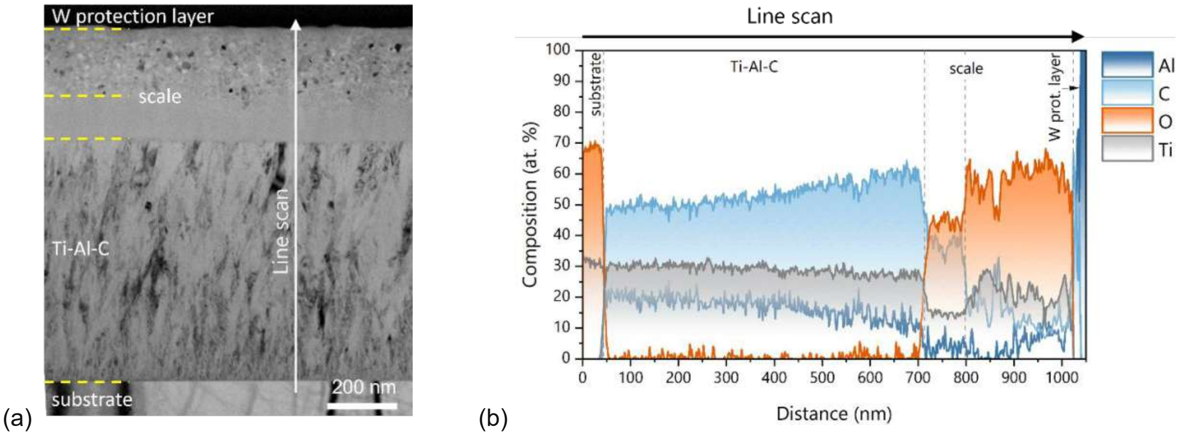

Figure 5: TEM analysis of an oxidized $Ti_{0.26}Al_{0.32}C_{0.42}$ thin film. The sample was annealed in ambient air at 750 °C for 1h. (a) shows a Bright-field (BF) image of the sample cross section. The arrow in (a) indicates the position and direction of the (b) EELS line scan.

Figure 6a shows the BF-TEM image of the oxidized $Ti_{0.29}Si_{0.26}C_{0.45}$ thin film after 1 h at 750 °C. In principle, the appearance after oxidation is similar to $Ti_{0.26}Al_{0.32}C_{0.42}$ presented in Figure 5, containing the sapphire substrate, followed by an unaffected Ti-Si-C zone, and an approx. 300 nm thick oxide scale topped with the W protection layer. Again, a closer look at the BF image reveals a layered oxide scale containing two different zones, which is also represented in the EELS line scan in Figure 6b. Again, a transition between a metal oxycarbide towards a carbon depleted oxide scale can be identified.

Interestingly, the outermost part of the scale is dominated by Ti and oxygen, and the added strong oxide former (Si) is not prevalent. However, small additions of Si can be recognized. Please note also that the high Si signal at the end of the EELS line scan is assigned to the W protection layer. In contrast to $Ti_{0.26}Al_{0.32}C_{0.42}$, the EELS line scan reveals residual oxygen inward diffusion into the Ti-Si-C zone. Nevertheless, both coating systems $Ti_{0.26}Al_{0.32}C_{0.42}$ and $Ti_{0.29}Si_{0.26}C_{0.45}$ clearly withstand the oxidation test and show no pore formation, indicating that the oxide formers enhance the oxidation resistance.

Based on these initial studies, the oxidation resistance of Al alloying seems to work better for most of the TMC thin films. Al-alloyed TiC thin films exhibit enhanced capabilities to act as a diffusion barrier for oxygen. Based on the line scans in Figure 5b and 6b, Ti-Al-C obtains a sharp interface at the coating/scale interface, proving a suppressed oxygen inward diffusion/oxidative attack. In contrast, for Ti-Si-C minor oxygen diffusion into the unaffected zone can be seen.

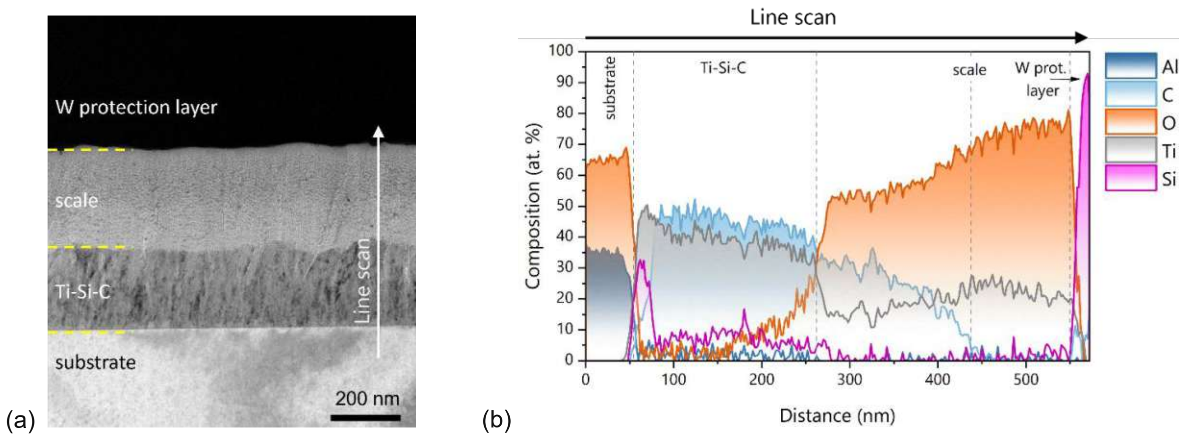

Figure 6: TEM analysis of an oxidized $Ti_{0.29}Si_{0.26}C_{0.45}$ thin film. The sample was annealed in ambient air at 750 °C for 1h. (a) shows a Bright-field (BF) image of the sample cross section. The arrow in (a) indicates the position and direction of the (b) EELS line scan.

Conclusions

Within this study, Al/Si alloyed ternary transition metal carbides are investigated with respect to their oxidation resistance. The oxidation properties were first investigated for all binary TMC thin films, obtaining predominantly fcc structure. Only $Ta_{0.42}C_{0.46}$ (sub-stoichiometric in C) was dual phased with the coexistence of hexagonal Ta_2C. Dynamic oxidation tests for the binary systems yielded oxidation onset temperatures of around 150°C for TaC, as well as 550 °C for ZrC, HfC, and WC. For TiC, reference data were taken from the literature, which indicate oxidation starts from 600 °C. To investigate the oxidation properties of the ternary TM-X-Cs, isothermal oxidation experiments were performed at 750 °C for 1 h. Only Ta-Si-C and W-Al/Si-C did not withstand these temperatures (no coating was left after the oxidation experiment). In general, the results of these oxidation experiments highlighted that an alloying content of about 25 at.% Al is crucial to sufficiently protect TM-Al-Cs at these conditions. The best systems were Ta-Al-C and Ti-Al-C, which were characterized by a thin oxide scale (less than 750 nm). Among the Si alloyed TM-X-Cs, Ti-Si-C (studied between approximately 20 to 40 at.%) was able to withstand the oxidation test at 750 °C. Detailed TEM analysis of $Ti_{0.26}Al_{0.32}C_{0.42}$ and $Ti_{0.29}Si_{0.26}C_{0.45}$ revealed layered oxide scale architectures with a metal oxycarbide at the interface to the pore-free Ti-Al/Si-C, and a Ti-

(Al/Si)-based oxide scale on top. For $Ti_{0.26}Al_{0.32}C_{0.42}$ no oxygen inward diffusion could be identified after the scale region. In summary, the study identifies Al as a more effective scale former (i.e., for Ti-Al-C and Ta-Al-C), whereas Si requires lower contents to form adherent but not so dense scales (i.e. Ti-Si-C).

Acknowledgments

The financial support by the Austrian Federal Ministry for Digital and Economic Affairs, the National Foundation for Research, Technology and Development, and the Christian Doppler Research Association is gratefully acknowledged (Christian Doppler Laboratory “Surface Engineering of high-performance Components”). We also thank Plansee SE, Plansee Composite Materials GmbH, and Oerlikon Balzers, Oerlikon Surface Solutions AG for financial support. We also thank the X-ray center (XRC) of TU Wien for beam time and the electron microscopy center—USTEM TU Wien—for using the SEM and TEM facilities. We acknowledge TU Wien Bibliothek for financial support through its Open Access Funding Programme. In addition, the authors thank the RADIATE project for funding our beamtime at the Tandem Laboratory at Uppsala University. Accelerator operation at Uppsala University was supported by the Swedish research council VR-RFI (#2019-00191). Finally, the Theodor Körner Fonds is gratefully recognized for its invaluable support in the completion of this work.

References

[1] B.C. Wyatt et al., Ultra-high temperature ceramics for extreme environments, Nature Reviews Materials. (2023) 1–17.
[2] C. Zhang et al., Thermal analysis of tantalum carbide-hafnium carbide solid solutions from room temperature to 1400 °C, Coatings. 7 (2017) 111.
[3] R.A. Andrievskii et al., Melting point in systems ZrC-HfC, TaC-ZrC, TaC-HfC, Powder Metall Met Ceram. 6 (1967) 65–67.
[4] W.G. Fahrenholtz et al., Ultra-high temperature ceramics: Materials for extreme environments, Scr. Mater. 129 (2017) 94–99.
[5] W.G. Fahrenholtz et al., Oxidation of ultra-high temperature transition metal diboride ceramics, Int. Mater. Rev. 57 (2012) 61–72.
[6] Z. Huang et al., High-temperature oxidation behaviors of dense TMC (TM= Ta, Nb, Ti and Zr) ceramics in air, Ceram. Int. 49 (2023) 38036–38046.
[7] S.V. Raj, M. Singh, R. Bhatt, High Temperature Lightweight Self-Healing Ceramic Composites Aircraft Engine Applications, NASA NTRS. (2014). https://ntrs.nasa.gov/citations/20140017309 (accessed February 12, 2024).
[8] P. Spriet, CMC Applications to Gas Turbines, in: Ceramic Matrix Composites, John Wiley & Sons, Inc., Hoboken, NJ, USA, 2014: pp. 591–608.
[9] National Aeronautics and Space Administration, Agency Licensing Concierge, Glenn Research Center, Environmental Barrier Coatings for Ceramic Matrix Composites, NASA Technology Transfer Program. (n.d.). https://technology.nasa.gov/patent/LEW-TOPS-136 (accessed February 23, 2024).
[10] N.A. Nasiri et al., Oxidation behaviour of SiC/SiC ceramic matrix composites in air, J. Eur. Ceram. Soc. 36 (2016) 3293–3302.
[11] F. Lamouroux et al., Oxidation-resistant carbon-fiber-reinforced ceramic-matrix composites, Compos. Sci. Technol. 59 (1999) 1073–1085.
[12] S. Richter, C. Gutschka, D. Danner, R. Hahn, T. Wojcik, E. Ntemou, C. Jerg, J. Ramm, P. Polcik, S. Kolozsvári, D. Primetzhofer, and H. Riedl, High-throughput phase exploration of ternary transition metal carbide TM-X-C (X=Al/Si) thin films, Under Review at Acta Materialia. (2025).
[13] Y.-H. Seong et al., Evaluation of oxidation behaviors of HfC-SiC ultra-high temperature ceramics at above 2500 °C via oxyacetylene torch, Ceram. Int. 44 (2018) 8505–8513.
[14] AJA International, Orion Series Sputtering Systems, AJA International. (2025). https://www.ajaint.com/system-orion (accessed January 22, 2025).
[15] Plansee Composite Materials, Plansee Composite Materials. (n.d.). https://www.plansee.com/de/unternehmen/kontakt/deutschland.html (accessed January 10, 2023).
[16] P. Ström et al., Ion beam tools for nondestructive in-situ and in-operando composition analysis and modification of materials at the Tandem Laboratory in Uppsala, J. Instrum. 17 (2022) P04011.
[17] T. Glechner et al., Influence of Si on the oxidation behavior of TM-Si-B2±z coatings (TM = Ti, Cr, Hf, Ta, W), Surf. Coat. Technol. 434 (2022) 128178.
[18] H. Riedl et al., Influence of carbon deficiency on phase formation and thermal stability of super-hard TaCy thin films, Scr. Mater. 149 (2018) 150–154.
[19] International Center of Diffraction Data, Powder Diffraction File - cubic TiC - 00-032-1383, (1982).
[20] International Center of Diffraction Data, Powder Diffraction File - cubic ZrC - 00-035-0784, (1985).
[21] International Center of Diffraction Data, Powder Diffraction File - cubic HfC - 00-039-1491, (1989).
[22] International Center of Diffraction Data, Powder Diffraction File - cubic TaC - 00-035-0801, (1985).
[23] International Center of Diffraction Data, Powder Diffraction File - cubic WC - 01-084-4476, (2016).
[24] International Center of Diffraction Data, Powder Diffraction File - hexagonal Ta2C - 01-073-1321, (1998).
[25] International Center of Diffraction Data, Powder Diffraction File - hexagonal Al2O3 - 00-005-0712, (1955).
[26] L. Boatemaa et al., The effect of the TiC particle size on the preferred oxidation temperature for self-healing of oxide ceramic matrix materials, J. Mater. Sci. 53 (2018) 5973–5986.
[27] A. Mitsuo et al., Improvement of high-temperature oxidation resistance of titanium nitride and titanium carbide films by aluminum ion implantation, Surf. Coat. Technol. 103–104 (1998) 98–103.
[28] International Center of Diffraction Data, Powder Diffraction File - tetragonal Al5Ti2 - 03-065-9788, (2004).
[29] S. Shimada, Formation Mechnism Carbon-Containing Oxide Scales Oxidation Carbides (ZrC, HfC, TiC), Materials Science Forum. (2001). https://doi.org/10.4028/www.scientific.net/MSF.369-372.377.

Appendix

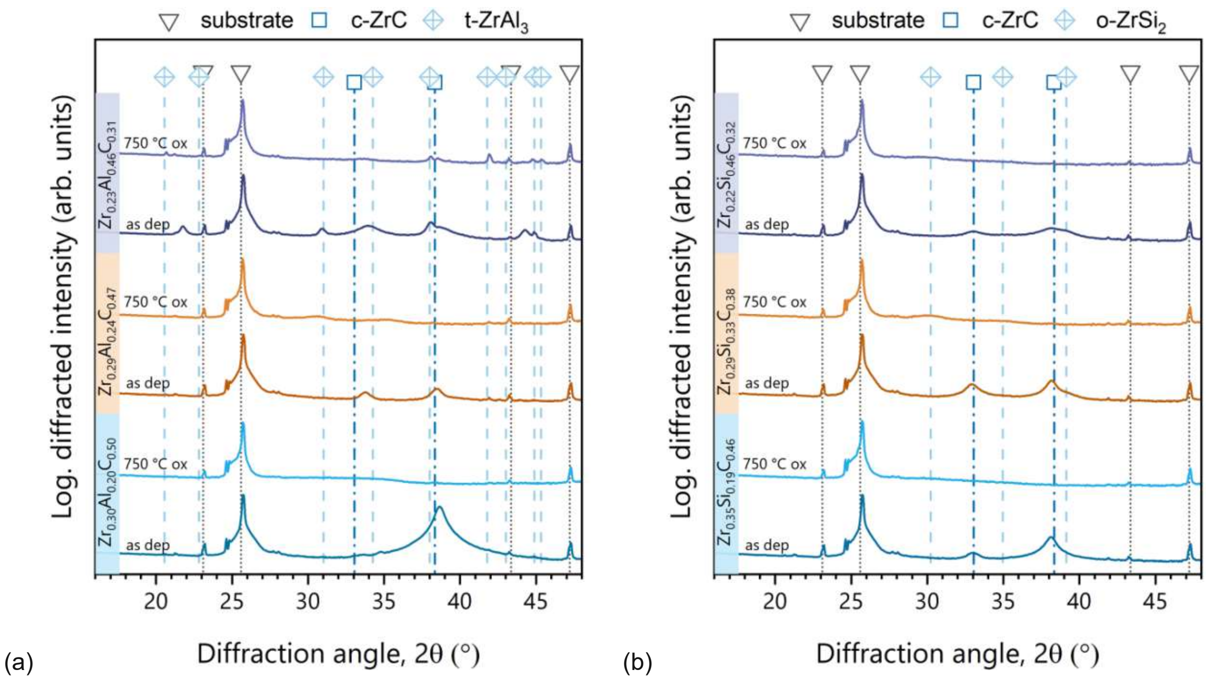

Figure A.1: XRD diffractograms of (a) Zr-Al-C and (b) Zr-Si-C thin films in their as deposited and oxidized state. The triangles belong to the substrate (sapphire, 00-005-0712). The squares belong to cubic ZrC (00-035-0784). In (a) the crossed squares represent tetragonal ZrAl$_3$ (04-003-4015). In (b) the crossed squares highlight orthorhombic ZrSi$_2$ (00-032-1499). The as deposited XRD diffractograms have already been published in [12].

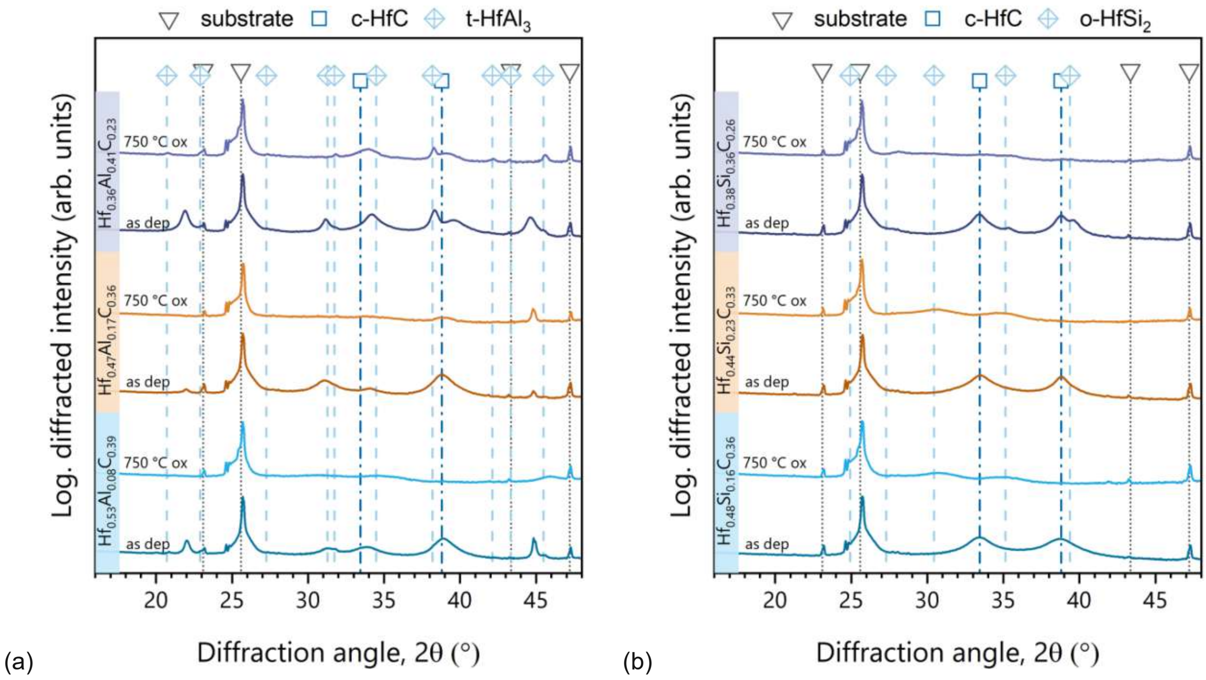

Figure A.2: XRD diffractograms of (a) Hf-Al-C and (b) Hf-Si-C thin films in their as deposited and oxidized state. The triangles belong to the substrate (sapphire, 00-005-0712). The squares belong to cubic HfC (00-039-1491). In (a) the crossed squares represent tetragonal $HfAl_3$ (04-027-9400). In (b) the crossed squares highlight orthorhombic $HfSi_2$ (00-038-1373). The as deposited XRD diffractograms have already been published in [12].

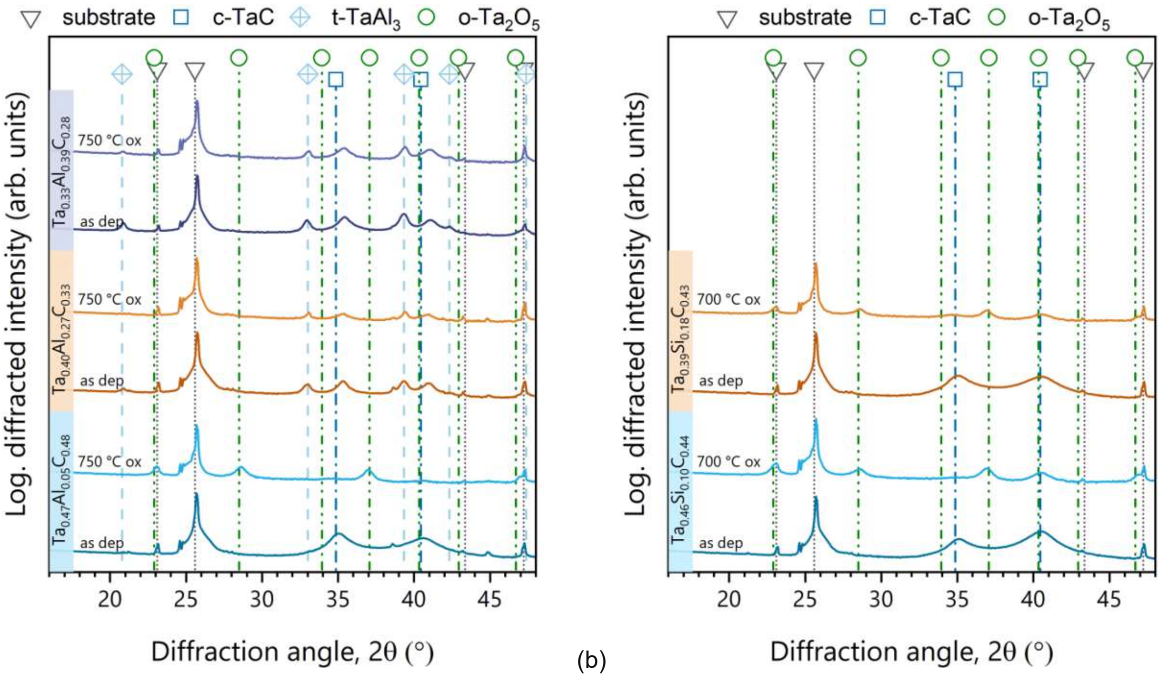

(a) (b)

Figure A.3: XRD diffractograms of (a) Ta-Al-C and (b) Ta-Si-C thin films in their as deposited and oxidized state. The triangles belong to the substrate (sapphire, 00-005-0712). The squares, crossed squares, and circles represent cubic TaC (00-035-0801), tetragonal $TaAl_3$ (04-004-2211), and orthorhombic Ta_2O_5 (00-025-0922), respectively. The as deposited XRD diffractograms have already been published in [12].

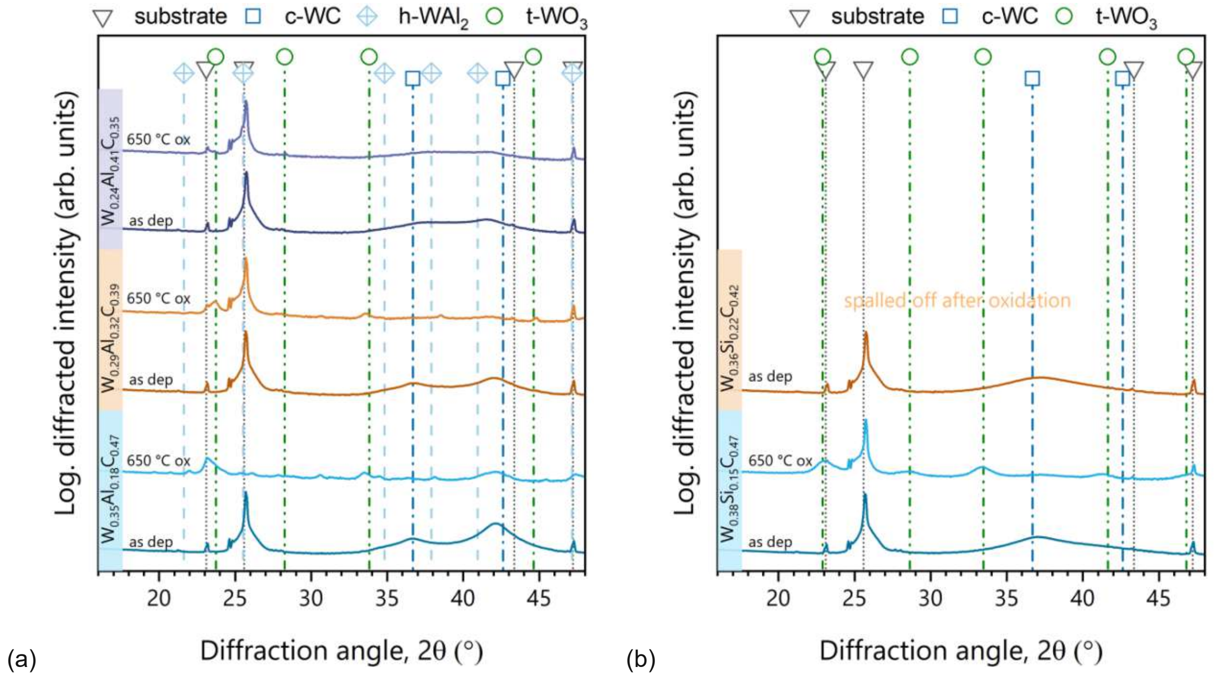

Figure A.4: XRD diffractograms of (a) W-Al-C and (b) W-Si-C thin films in their as deposited and oxidized state. The triangles belong to the substrate (sapphire, 00-005-0712). The squares, crossed squares, and circles represent cubic WC (01-084-4476), hexagonal WAl_2 (04-015-6886), and tetragonal WO_3 (04-025-0268), respectively. The as deposited XRD diffractograms have already been published in [12].

Publication V

Assessing the effectiveness of strong oxide formers (Cr, Si, Al) in diboride thin films

S. Richter, A. Bahr, T. Wojcik, E. Ntemou, S. Kolozsvári, P. Polcik, J. Ramm, D. Primetzhofer, H. Riedl

Manuscript draft for *Materials Research Letters*, (2025).

Assessing the effectiveness of strong oxide formers (Cr, Si, Al) in diboride thin films

Sophie Richter[1], Ahmed Bahr[1], Tomasz Wojcik[1], Eleni Ntemou[2], Szilárd Kolozsvári[3], Peter Polcik[3], Jürgen Ramm[4], Daniel Primetzhofer[2], Helmut Riedl[1,5]

[1] Christian Doppler Laboratory for Surface Engineering of high-performance Components, TU Wien, 1060 Wien, Austria
[2] Department of Physics and Astronomy, Uppsala University, 75120 Uppsala, Sweden
[3] Plansee Composite Materials GmbH, 86983 Lechbruck am See, Germany
[4] Oerlikon Balzers, Oerlikon Surface Solutions AG, 9496 Balzers, Liechtenstein
[5] Institute of Materials Science and Technology, TU Wien, 1060 Wien, Austria

Abstract

This study focuses on phase screening of strong oxide formers, particularly Al and Si, in CrB_2 thin films. Various chemical compositions were explored using a high-throughput combinatorial PVD deposition approach, including hexagonal structured ternary (Cr-Al-B and Cr-Si-B) and quaternary (Cr-Al-Si-B) films – all below 2 µm thickness. Dynamic thermogravimetry showed excellent oxidation resistance for $Cr_{0.34}Si_{0.18}B_{0.48}$ and $Cr_{0.29}Al_{0.18}Si_{0.10}B_{0.43}$ thin films up to 1300 °C. Isothermal oxidation tests at 1200 °C for 1 hour indicated no film decomposition and a reduced recrystallization in the quaternary system, compared to Cr-Si-B. Interestingly, small amounts of silicon (8 at.%) could enhance the formation of protective aluminum oxide scales, highlighting the key effect of Si. Transmission electron microscopy revealed a layered scale architecture featuring Si-O on the diboride surface, followed by Cr-O and Al-O, for the quaternary system, towards the surface.

Key words

Diborides; Oxide formers; Chromium; Aluminum; Silicon

Impact statement

Screening strong oxide formers (Cr, Al, Si) in diborides reveals that Si significantly enhances the protective properties, with the additional characteristics to promote the formation of alumina.

Introduction

Transition metal (TM) diborides, such as TiB_2 [1], ZrB_2 [2,3], and CrB_2 [4] are known for their high melting points, phase stability, and exceptional mechanical properties, including high hardness, wear resistance, and moderate fracture toughness [3,5,6]. These properties make them ideal for demanding applications in industries such as aviation and aerospace, where performance under extreme conditions is critical [1–3,6]. However, their oxidation resistance is often considered as a weak point [7–9]. Specifically, boron typically forms B_2O_3, which undergoes a temperature-dependent transition to a volatile state. This transition competes with the formation of the corresponding metal oxide [10]. This oxidation mechanism exhibits distinct morphological and kinetic characteristics for bulk and thin film diborides. For bulk diborides, a glassy, amorphous B_2O_3 layer is typically formed in a lower temperature regime – also known for self-healing effects based on the partly viscous state [11] – while in the high temperature regime, the volatile B_2O_3 predominates the formation of a non-protective, porous TM oxide skeleton [3]. This transition temperature is reported to be between 900 to 1000 °C [3,11,12]. In comparison, for thin film diborides the volatilization of B_2O_3 predominates already at low temperatures – i.e. at 500 to 600 °C for $TiB_{2\pm z}$ varying with the presence of boric acid [13] – resulting in the formation of porous TM oxide structures. In thin film materials, the boron concentration also plays a crucial role, as super-stoichiometric films form B-rich tissue phases, which accelerate the oxidation kinetics and hence shift the oxidation onset to lower temperatures [12,14].

To enhance the oxidation resistance of TM diborides, the use of strong metal oxide formers is crucial, as they promote the formation of dense, slow-growing protective scales which generally obtain parabolic or logarithmic growth trends [15]. This protective layer effectively prevents progressive oxidation by inhibiting the volatilization of B_2O_3 [16]. Among these, Cr, Al, and Si are particularly effective due to their high stability as indicated by the Ellingham diagram [17] and their favorable Pilling-Bedworth ratios [15]. In general, these factors ensure the formation of stable, dense, non-porous oxide scales that are free from unfavorable residual stresses that could cause breakaway oxidation [15,16]. Bulk CrB_2 is known to oxidize around 1000 °C [18], while for physical vapor deposited thin films the oxidation onset is around 600 °C [8] due to accelerated B_2O_3 formation caused by B-rich grain boundaries [12,19]. To overcome the pronounced oxygen transfer through the porous TMO_2 scales, bulk TM diborides are typically alloyed with secondary phases such as SiC [20–22]. For thin film materials various concepts are discussed in literature, whereas Cr [23], Si [8,24,25] and Al [26–28] containing transition metal diborides thin films represent the most promising approaches enhancing the oxidation resistance. For example, Lellig et al. was able to increase the oxidation behavior of TiB_2 thin films up to 900 °C by alloying

21 at.% Al (pure TiB_2 initially oxidizes between 400 and 500 °C [11,29,30]), since Al promotes the formation a passivating oxide scale [31] – mainly composed of Al, O, and B, respectively. At 700 °C, these oxide scales are amorphous, but after 8 hours at 900 °C, a (nano-)crystalline aluminoborate layer forms. In this context, also Thörnberg et at. [32] investigated the oxidation behavior of Ti-Al-B thin films. It has been shown that a thinner oxide layer is obtained with lower B contents and again Al promotes the formation of an Al_2O_3-TiO_2 based scale which acts as a diffusion barrier against further oxidation at 600 °C. In contrast to this, also Si-alloyed diboride systems show promising results with regard to improved oxidation behavior: For example, the oxidation resistance of Cr-Si-B with 8-16 at.% Si alloying content could be increased to 1300 °C (compared to 600 °C for CrB_2) [8,25] due to the formation of a protective silica beneath a Cr_2O_3 scale. This drastic improvement is related to the enhanced diffusivity of Si and the tendency to form Si and TM-Si rich clusters during oxidation [8,33]. Furthermore, Kiryukhantsev-Korneev et al. [34] showed the oxidation resistance of $Cr_{0.51}Al_{0.06}Si_{0.02}B_{0.40}N_{0.01}$ at 1200 °C. Nevertheless, the existing studies lack a comprehensive overview of the oxidation behavior of Cr, Al and Si in transition metal diborides.

This study examines the effectiveness of Cr, Al, and Si as oxide formers in diboride thin films grown by physical vapor deposition (PVD). Using CrB_2 as a base material, the research evaluates how alloying with Al and/or Si influences oxidation mechanisms while minimizing structural effects (strong AlB_2 prototype stabilizer during magnetron sputtering). Ternary (Cr-Al-B, Cr-Si-B) and quaternary (Cr-Al-Si-B) compositions are synthesized via combinatorial co-sputtering. The films are subjected to phase analysis (XRD), oxidation testing (dynamic thermogravimetry up to 1400 °C and isothermal oxidation at 1200 °C for 1h), and transmission electron microscopy (TEM) analysis to investigate the detailed scale formation and oxide layer architecture. Especially alloys with Al could be of interest for high temperature applications in water vapor [35,36], in comparison to the already described Cr-Si-B system.

Materials and methods

All Al and/or Si alloyed CrB_2 thin films were deposited in an AJA Orion 5 deposition system using Ar (99.999 % purity) as the working gas, and a 3" CrB_2, a 2" AlB_2 and a 2" Si target, provided by Plansee Composite Materials GmbH [37]. A combinatorial deposition approach was chosen in which the targets were operated in co-sputtering mode. No substrate rotation was applied so that a chemical gradient was deposited across the substrate holder. The coatings were grown on polycrystalline Al_2O_3 substrates (20 × 7 × 0.38 mm) which were pre-cleaned in an ultrasonic bath for 5 min each in acetone and ethanol. Prior to the deposition process, a base pressure of $1 \cdot 10^{-4}$ Pa was reached, the substrate temperature was set to 420 °C, and the substrates were subjected to an Ar ion etching step at a bias voltage of -800 V, an etching pressure of 6.0 Pa (20 sccm Ar flow rate) for 10 min. In addition, all targets were pre-sputtered with closed shutters and the same parameters as for the actual deposition process to remove surface contaminants. The substrate to target distance was set to approximately 80 mm. For the deposition of the films, a current of 0.4 A was applied to the CrB_2 target, resulting in a power density of 4.5 W/cm^2. The AlB_2 target was operated at 0.2 A resulting in a power density of 6.1 W/cm^2. The Si target was operated in pulsed mode (150 kHz frequency, 257 ns pulse duration), resulting in an average power density of 3.1 W/cm^2. The bias potential during deposition was set to -40 V, the argon ion flow was set to 10 sccm to maintain a deposition pressure of 0.4 Pa. The deposition time for all coatings was 150 min.

For chemical analysis, ion beam analytical techniques at the 5 MV Pelletron tandem accelerator at Uppsala University [38] were selected to provide standards for further X-ray fluorescence (XRF) analysis: Time-of-Flight Elastic Recoil Detection Analysis (ToF-ERDA) and Rutherford backscattering spectrometry (RBS). ToF-ERDA was performed with $^{127}I^{8+}$ ions at a primary energy of 36 MeV and an 67.5° angle of incidence relative to the surface normal. The angle of recoil detection relative to the incident beam was 45°. RBS was performed with 3 MeV $^{4}He^{+}$ ions and a detection angle of 170 °. ToF-ERDA data was analyzed using the CONTES software [39], while RBS was analyzed using the SIMNRA software [40,41]. The total systematic and statistical uncertainties were estimated to be 5-8 % of the deduced value for the major constituents. XRF measurements were performed on a Panalytical AXIOS system with a rhodium anode in wavelength dispersive mode und vacuum conditions at room temperature. For XRF, the systematic and statistical uncertainties were expected to be around 5 %.

Phase analysis was conducted using X-ray diffraction (XRD) and a Panalytical X'Pert Pro MPD X-ray diffractometer in Bragg-Brentano geometry with a Cu-K_α source (wavelength $\lambda = 1.5418$ Å).

To study the oxidation characteristics, dynamic oxidation tests (continuous temperature increase from room temperature to 1400 °C) were performed using a Netzsch STA 449 F1 Thermo-Gravimetric Analysis (TGA) system equipped with a rhodium furnace. For these experiments, a heating rate of 10 °C/min was provided during a steady flow of synthetic air (50 ml/min) and helium (20 ml/min) to protect the scales. Moreover, isothermal oxidation experiments in ambient air were carried out in a conventional box furnace. The coatings were placed in the preheated furnace at 1200 °C for 1 h.

For detailed investigation of the coating morphology and scale formation, transmission electron microscope (TEM, FEI TECNAI F20) analysis was used. The TEM lamellas were prepared using a standardized focused ion beam (FIB) lift out in a dual-beam FIB/scanning electron microscope (FIB-SEM) system (ThermoFisher Scios II). The FIB was operated with Ga+ ions. The TEM was equipped with a field emission gun and employed at an accelerating voltage of 200 kV to perform bright field TEM (BF-TEM) imaging. Electron energy loss spectroscopy (EELS) was performed in scanning TEM (STEM) mode to gain insight into the chemical composition. For EELS, a Gatan GIF Tridiem energy filter was used. Elemental quantification was performed at the Si K, Al K, Cr L, O K, and B K edges. Additional FIB cross sections were prepared in the same FIB-SEM dual beam system. The system was performed at currents from 7 to 17 nA (for fine milling) at an accelerating voltage of 30 kV.

Results and discussion

Fig. 1 summarizes the chemical compositions of all ternary (Cr-Al-B and Cr-Si-B) and quaternary (Cr-Al-Si-B) thin films derived from ERDA-calibrated XRF. The exact compositions for the quaternary systems can be found in the Appendix A (see Fig. A3). In the Cr-Si-B system, Si could be alloyed up to approximately 24 at.% while maintaining a boron content of at least 44 at.%. For the Cr-Al-B system, Al could be alloyed up to 31 at.%. In the quaternary Cr-Al-Si-B system, the Al and Si content reached up to 34 at.% in total (25 at.% Al and 9 at.% Si). This dissimilarity is likely due to different sputtering rates during co-sputtering of CrB_2, AlB_2, and Si. Despite these variations, the combinatorial deposition approach allowed the synthesis of a wide range of chemical compositions.

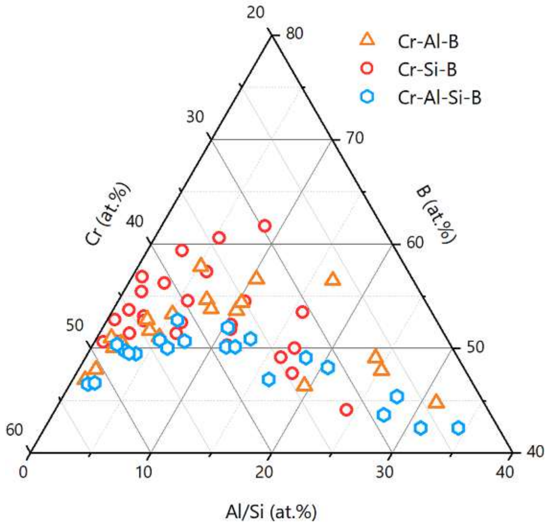

Fig. 1. Ternary chemical composition map of the Al and/or Si alloyed CrB_2 thin films – please note, that the axes are zoomed in.

Phase analysis confirmed that the coatings in all systems predominantly adopt the preferred hexagonal AlB_2 structure (corresponding XRD diffractograms are included in the Appendix). No additional phases were identified for the Cr-Al-B system, as confirmed by XRD patterns (see Appendix A1). A notable shift in thin film growth orientation was observed, moving from (001) for low or no alloying to (101) with increasing Al content. This trend is consistent with the findings of Dorri et al. who reported a (001) orientation in binary CrB_2 thin films deposited by magnetron sputtering [42]. For the Cr-Si-B system (XRD data in Appendix A2), h-$CrSi_2$ peaks emerge in the diffractograms with increasing Si content, indexable at about 3 to 5 at.%, but with relatively small intensities. The quaternary Cr-Al-Si-B system showed similar behavior (Appendix A3), with the h-$CrSi_2$ phase appearing at approximately 4 at.% Si and an increase in $CrSi_2$ peaks with higher Si contents. Also, for the quaternary system, increasing Al content induced a shift in the preferred growth orientation from (001) to (101). The solubility limit of Si within the AlB_2 prototype structure, about 4 at.%, is in agreement with the findings of Zauner et al. [25], who determined this limit experimentally using atom probe tomography.

To evaluate the impact of oxide formers (Cr, Al, Si) on oxidation behavior, TGA was conducted in synthetic air up to 1400 °C, as shown in Fig. 2. Fig. 2a illustrates the oxidation behavior of the Cr-Al-B coatings. The low-alloyed CrB_2 based coatings ($Cr_{0.52}Al_{0.01}B_{0.47}$) exhibit an oxidation onset at approximately 600 °C. However, as the Al alloying content increases, the oxidation resistance improves. For coatings with Al contents above 20 at.%, the oxidation onset temperature increases to about 800 °C. Fig. 2b displays the effect of Si alloying in the Cr-Si-B coatings. Also, with small Si addition (1 at.%), the oxidation onset temperature is near 600 °C. With increasing Si alloying to 18 at.% the oxidation resistance improves significantly. The stable mass increase up to about 1300 °C reflects outstanding oxidation resistance of Cr-Si-B, consistent with previous findings reporting excellent oxidation stability above 11 at.% Si alloying [8,25]. This distinct improvement correlates with the role of Si in forming protective silica-based oxide scales. Fig. 2c shows the oxidation performance of quaternary Cr-Al-Si-B coatings. Notably, the coating with a composition of $Cr_{0.27}Al_{0.24}Si_{0.04}B_{0.45}$ achieves excellent oxidation resistance despite having lower Al and Si contents than the ternary coatings in Fig. 2a and 2b, respectively. Increasing the Si content from 4 to 10 at.% further suppresses the mass gain (while having only 18 at.% Al), suggesting the effectiveness of Si for the scale formation. Similar behavior has been observed in Ni-based superalloys, where small Si additions promote protective alumina scale formation during oxidation at 1200 °C [16].

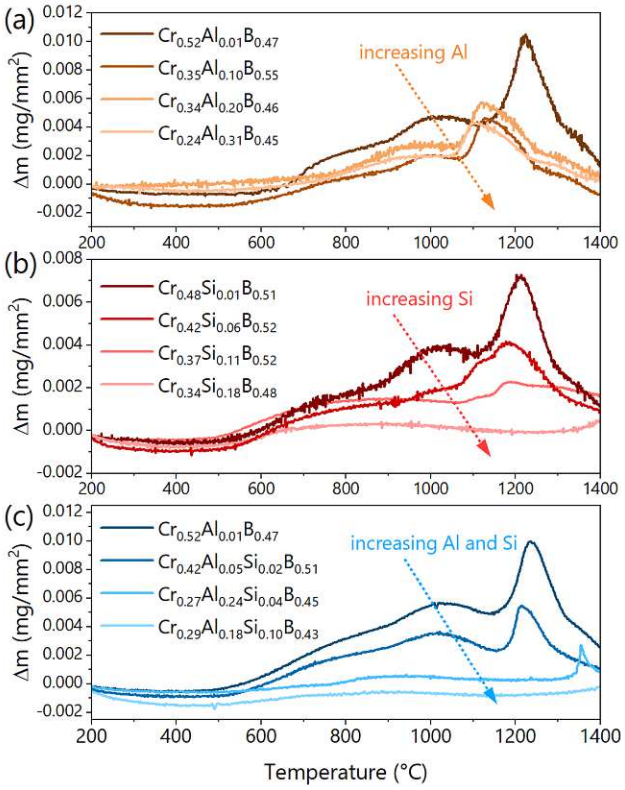

Fig. 2. TGA curves (mass change Δm over temperature) in synthetic air up to 1400 °C showing the oxidation behavior of (a) Cr-Al-B, (b) Cr-Si-B, and (c) Cr-Al-Si-B thin films.

To thoroughly evaluate scale formation and oxidation resistance under high-temperature conditions, one coating system was selected from each alloy system based on the dynamic oxidation tests. Each thin film demonstrated a similar phase formation and chemical composition in relation to the best performers during dynamic oxidation. These films were then isothermally annealed at 1200 °C for 1 hour in ambient air. TEM analyses were conducted to investigate scale formation, concentrating on the architecture and protective properties of the scale.

The Cr-Al-B system already showed limited oxidation resistance during dynamic thermogravimetry, with partially improved oxidation properties up to 800 °C, even for Al alloying contents above 31 at.%. Consistent with these results, the isothermal oxidation test at 1200 °C showed that the $Cr_{0.27}Al_{0.25}B_{0.48}$ sample was completely oxidized after 1 h. Corresponding EELS line scans and a cross section of this sample are shown in Appendix B (Fig. B1).

In contrast, $Cr_{0.35}Si_{0.16}B_{0.49}$ (Fig. 3) and $Cr_{0.27}Al_{0.22}Si_{0.09}B_{0.42}$ (Fig. 4) showed exceptional oxidation resistance at 1200 °C for 1 h, due to the formation of non-porous, protective scales. The STEM images of the two systems (Figs. 3a and 4a) reveal differences in scale morphology and thin film recrystallization. The Cr-Si-B system exhibits enhanced recrystallization compared to the Cr-Al-Si-B system. Additionally, EELS line scans along the thin film growth (see Appendix B, Fig. B2) indicate also Si clustering and a concentration of Si towards the substrate in the Cr-Si-B coating. However, the Si clusters might protect the underlying thin film from further oxidation. Here, an intact coating is present under the Si clusters [33] (hardly any oxygen could be detected in the EELS line scan, see Fig. B2). Furthermore, the outward diffusion of Si facilitates the formation of a silica-based protective scale [43], as can be seen in Fig. 3c and d, respectively. In the Cr-Al-Si-B, no Si clustering was observed, although B-rich regions were detected (Appendix B, Fig. B3), appearing as darker areas in the coating (Fig. 4a).

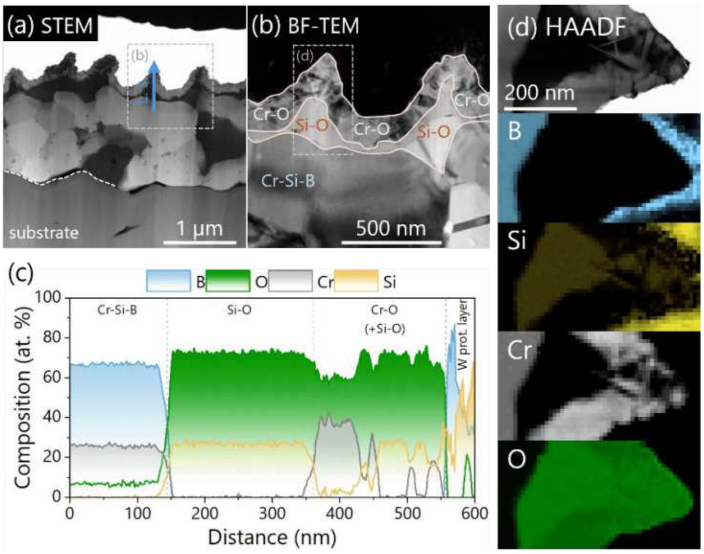

Fig. 3. TEM analysis of the oxidized $Cr_{0.35}Si_{0.16}B_{0.49}$ thin film after 1h at 1200 °C in ambient air. (a) shows the sample cross section (STEM image, overview) with the marked area for the detailed (b) BF-TEM image of the scale formation and the position of the (c) EELS line scan. (d) shows a detailed HAADF image (position marked in (b)) and an EELS mapping of B, Si, Cr and O.

When comparing the scale formation, Cr-Si-B shows a more pronounced sharp triangular scale structure while Cr-Al-Si-B shows a less sharp, more homogeneous scale morphology. Detailed examination of the oxide layers revealed layered scale growth in both systems. For Cr-Si-B, the EELS line scan (Fig. 3c) as well as the EELS mapping in Fig. 3d indicated that the scale consisted of a Si-O-based layer above the boride, followed by a Cr-O-based layer on the outer surface. The Cr-O layer on top appears crystallized, whereas the Si-O layer beneath is amorphous [33]. Similarly, the Cr-Al-Si-B system exhibited a Si-O scale directly above the boride (see Fig. 4c and 4d), followed by a Cr-O scale, with an Al-based oxide forming on the outmost region. This layered oxide growth align with previous studies [34], which reported Al-based oxide formation atop Cr-based oxide in Cr-Al-Si-B coatings. However, the current results of this study and a comparison of the three systems and their chemical compositions suggest that small amounts of Si (about 8 at.%) promote the formation of additional protective alumina scales. It can therefore be seen that Si has a key effect on the oxidation resistance of diboride thin films, even for Al-containing coatings. Si, with a low solubility in diboride structures, and, as shown here, a tendency to dual-phased structures (formation of $CrSi_2$), seems to be readily available for scale formation, favorable for the formation of protective oxide scales.

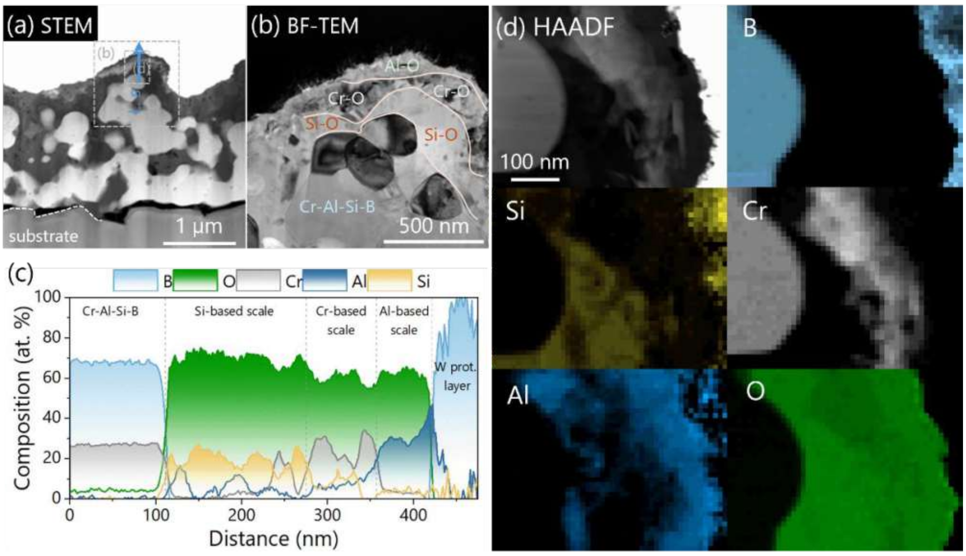

Fig. 4. TEM analysis of the oxidized $Cr_{0.27}Al_{0.22}Si_{0.09}B_{0.42}$ thin film after 1 h at 1200 °C in ambient air. (a) shows the sample cross section (STEM image, overview) with the marked area for the detailed (b) BF-TEM image of the scale formation and the position of the (c) EELS line scan. (d) shows a detailed HAADF image (position marked in (a)) and an EELS mapping of B, Si, Cr, Al and O.

Both coatings, Cr-Si-B and Cr-Al-Si-B, showed excellent oxidation resistance at 1200 °C for 1 h, despite their relatively thin film thickness (1.5-2 µm). However, the oxidation behavior at higher temperatures (1300-1400 °C) showed limitations. At 1300 °C, Cr-Si-B withstood oxidation without significant degradation at the first glance of FIB cross sections (Appendix C, Fig. C1a). In contrast, Cr-Al-Si-B exhibited significant delamination from the substrate (Appendix C, Fig. C1b). None of the two coating systems were able to withstand 1400 °C, as both coatings were completely oxidized at the end of the test.

Conclusions

In this paper, a combinatorial deposition technique has been used to synthesize a chemical variety of Si and/or Al alloyed CrB_2 thin films. This study focuses on the effectiveness of the strongest oxide formers on the scale formation and oxidation resistance of AlB_2 structured diborides. The ternary system Cr-Si-B as well as the quaternary system Cr-Al-Si-B show small peaks of the $CrSi_2$ phase in the as deposited state (starting from about 3-4 at.% Si), which is due to the low Si solubility in hexagonal CrB_2. Nevertheless, all thin films have a clear hexagonal AlB_2 dominated structure. After an initial screening by dynamic thermogravimetry, the oxidation behavior of different Cr/Al/Si ratios was investigated. The oxidation resistance of CrB_2 could be increased from 600 °C to 800 °C by adding about 20 at.% Al. But with an additional increase in the Al content to 31 at.%, an oxidation onset at 800 °C could not be avoided. In contrast, Si alloyed CrB_2 coatings exhibit excellent oxidation properties due to the formation of a protective silica scale. In our study, the threshold value was between 11 and 18 at.% Si content, where the oxidation behavior up to 1300 °C was significantly improved. Interestingly, for the quaternary Cr-Al-Si-B system, the combination of (lower) Si and Al alloying (compared to the two ternary systems) could also lead to significantly improved oxidation behavior up to 1300 °C. In both cases, a layered scale was formed consisting of a Si-oxide based scale (on top of the diboride), followed by a Cr-oxide based scale, and an Al-oxide based scale (for the quaternary system). At oxidation testing at higher temperatures (1300 and 1400 °C), significant spalling of the quaternary coating from the alumina substrate occurred and only the Cr-Si-B system could withstand temperatures up to 1400 °C. In summary, while the Cr-Si-B system exhibits excellent resistance to high-temperature oxidation, the quaternary system also shows promising results, particularly for high-temperature applications involving water vapor, taking into account the instability of SiO in these environments.

Acknowledgments

The financial support by the Austrian Federal Ministry for Digital and Economic Affairs, the National Foundation for Research, Technology and Development and the Christian Doppler Research Association is gratefully acknowledged (Christian Doppler Laboratory “Surface Engineering of high-performance Components”). We also thank Plansee SE, Plansee Composite Materials GmbH, and Oerlikon Balzers, Oerlikon Surface Solutions AG for financial support. We also thank the X-ray center (XRC) of TU Wien for beam time and the electron microscopy center - USTEM TU Wien - for using the SEM and TEM facilities. Finally, we acknowledge TU Wien Bibliothek for financial support through its Open Access Funding Programme. In addition, the authors thank the REMADE project for funding our beamtime at the Tandem Laboratory at Uppsala University.

Declaration of interest statement

No potential conflict of interest was reported by the author(s).

References

[1] Y.L. Krutskii et al., Diborides of some transition metals: Properties, application and production. Review. Part 1. Titanium and vanadium diborides, Steel Transl. 51 (2021) 93–106.

[2] B. Mohammadzadeh et al., Manufacturing ZrB2-SiC-TaC composite: Potential application for aircraft wing assessed by frequency analysis through finite element model, Materials (Basel). 13 (2020) 2213.

[3] W.G. Fahrenholtz et al., Oxidation of ultra-high temperature transition metal diboride ceramics, Int. Mater. Rev. 57 (2012) 61–72.

[4] R.D. Bedse et al., Processing and characterization of CrB_2-based novel composites, High Temp. Mater. Processes. 34 (2015) 683–687.

[5] A.A. Goncharov et al., Structure, composition, and mechanical properties of thin films of transition metals diborides, J. Superhard Mater. 37 (2015) 422–428.

[6] M. Magnuson et al., Review of transition-metal diboride thin films, Vacuum. 196 (2022) 110567.

[7] W.G. Fahrenholtz et al., Ultra-high temperature ceramics: Materials for extreme environments, Scr. Mater. 129 (2017) 94–99.

[8] T. Glechner et al., Influence of Si on the oxidation behavior of TM-Si-B2±z coatings (TM = Ti, Cr, Hf, Ta, W), Surf. Coat. Technol. 434 (2022) 128178.

[9] D.J. Young, High Temperature Oxidation and Corrosion of Metals, Elsevier, 2016.

[10] T.A. Parthasarathy et al., A model for the oxidation of ZrB2, HfB2 and TiB2, Acta Mater. 55 (2007) 5999–6010.

[11] X. Cai et al., Unmasking the anomalous rapid oxidation of refractory TiB2 at low temperatures, J. Eur. Ceram. Soc. 41 (2021) 5100–5108.

[12] S. Dorri et al., Oxidation kinetics of overstoichiometric TiB2 thin films grown by DC magnetron sputtering, Corros. Sci. 206 (2022) 110493.

[13] R. Naraparaju et al., Effect of moisture on the oxidation behavior of ZrB2, J. Am. Ceram. Soc. 104 (2021) 1058–1066.

[14] C. Fuger et al., Tissue phase affected fracture toughness of nano-columnar TiB2 + z thin films, Materials Research Letters. 11 (2023) 613–622.

[15] W.D. Callister et al., Materialwissenschaften und Werkstofftechnik: Eine Einführung, John Wiley & Sons, 2012.

[16] S. Ma et al., The effects of alloying elements Cr, Al, and Si on oxidation behaviors of Ni-based superalloys, Materials (Basel). 15 (2022) 7352.

[17] Transactions and communications, J. Soc. Chem. Ind. 63 (1944) 125–160.

[18] M.L. Emiliani, Characterization and oxidation resistance of hot-pressed chromium diboride, Mater. Sci. Eng. A Struct. Mater. 172 (1993) 111–124.

[19] J. Thörnberg et al., Improved oxidation properties from a reduced B content in sputter-deposited TiBx thin films, Surf. Coat. Technol. 420 (2021) 127353.

[20] I.G. Talmy et al., Oxidation of ZrB2 ceramics modified with SiC and group IV--VI transition metal diborides, in: Elec. Chem. Soc. Proc, books.google.com, 2001: pp. 144–158.

[21] R. Guo et al., Oxidation behavior of high-entropy (Zr0.2Hf0.2Ta0.2Nb0.2Ti0.2)B2 ceramic with 20% SiC addition, J. Eur. Ceram. Soc. 44 (2024) 5181–5189.

[22] J.W. Hinze et al., The high-temperature oxidation behavior of a HfB2 + 20 v / o SiC composite, J. Electrochem. Soc. 122 (1975) 1249–1254.

[23] B. Bakhit et al., Multifunctional ZrB2-rich Zr1-xCrxBy thin films with enhanced mechanical, oxidation, and corrosion properties, Vacuum. 185 (2021) 109990.

[24] T. Glechner et al., High temperature oxidation resistance of physical vapor deposited Hf-Si-B2±z thin films, Corros. Sci. 205 (2022) 110413.

[25] L. Zauner et al., Role of Si segregation in the structural, mechanical, and compositional evolution of high-temperature oxidation resistant Cr-Si-B2±z thin films, J. Alloys Compd. 944 (2023) 169203.

[26] A.H. Navidi Kashani et al., Synthesis and oxidation behavior of Ti0.35Al0.65By (y = 1.7–2.4) coatings, Surf. Coat. Technol. 442 (2022) 128190.

[27] P. Kümmerl et al., Improved oxidation behavior of Hf0.11Al0.20B0.69 in comparison to Hf0.28B0.72 magnetron sputtered thin films, Sci. Rep. 14 (2024) 21653.

[28] A.H.N. Kashani et al., Morphology, mechanical properties, and oxidation behavior of stoichiometric Ti0.33-xAlxB0.67 coatings (x = 0.04, 0.15, 0.21, and 0.28), Acta Mater. (2024) 119829.

[29] B. Bakhit et al., Improving the high-temperature oxidation resistance of TiB2 thin films by alloying with Al, Acta Mater. 196 (2020) 677–689.

[30] A. Tampieri et al., Oxidation of monolithic TiB2 and of Al2O3-TiB2 composite, J. Mater. Sci. 28 (1993) 649–653.

[31] S. Lellig et al., Passivating oxidation behavior of Ti0.12Al0.21B0.67 coatings investigated by scanning transmission electron microscopy and chemical environment dependent density functional theory simulations, Acta Mater. 285 (2025) 120662.

[32] J. Thörnberg et al., Oxidation resistance and mechanical properties of sputter-deposited Ti0.9Al0.1B2-y thin films, Surf. Coat. Technol. 442 (2022) 128187.

[33] A. Bahr et al., High-temperature oxidation resistance of ternary and quaternary Cr-(Mo)-Si-B2-z coatings — Influence of Mo addition, Surf. Coat. Technol. 468 (2023) 129733.

[34] P.V. Kiryukhantsev-Korneev et al., Hard Cr-Al-Si-B-(N) coatings with oxidation resistance up to 1200°C, Glas. Phys. Chem. 37 (2011) 411–417.

[35] E.J. Opila, Volatility of common protective oxides in high-temperature water vapor: Current understanding and unanswered questions, Mater. Sci. For. 461–464 (2004) 765–774.

[36] E.J. Opila et al., Predicting oxide stability in high-temperature water vapor, JOM (1989). 58 (2006) 22–28.

[37] Plansee Composite Materials, Plansee Composite Materials. (n.d.). https://www.plansee.com/de/unternehmen/kontakt/deutschland.html (accessed January 10, 2023).

[38] P. Ström et al., Ion beam tools for nondestructive in-situ and in-operando composition analysis and modification of materials at the Tandem Laboratory in Uppsala, J. Instrum. 17 (2022) P04011.

[39] M.S. Janson, CONTES conversion of time-energy spectra—a program for ERDA data analysis, Uppsala University. (2004).

[40] M. Mayer, Improved physics in SIMNRA 7, Nucl. Instrum. Methods Phys. Res. B. 332 (2014) 176–180.

[41] M. Mayer, SIMNRA user's guide, (1997). https://pure.mpg.de/rest/items/item_2130938/component/file_3260821/content.

[42] M.M. Dorri et al., Synthesis and characterization of CrB2 thin films grown by DC magnetron sputtering, Scr. Mater. 200 (2021) 113915.

[43] A. Bahr et al., Oxidation behaviour and mechanical properties of sputter-deposited TMSi2 coatings (TM = Mo, Ta, Nb), J. Alloys Compd. 931 (2023) 167532.

Appendices

A. Phase analysis (XRD)

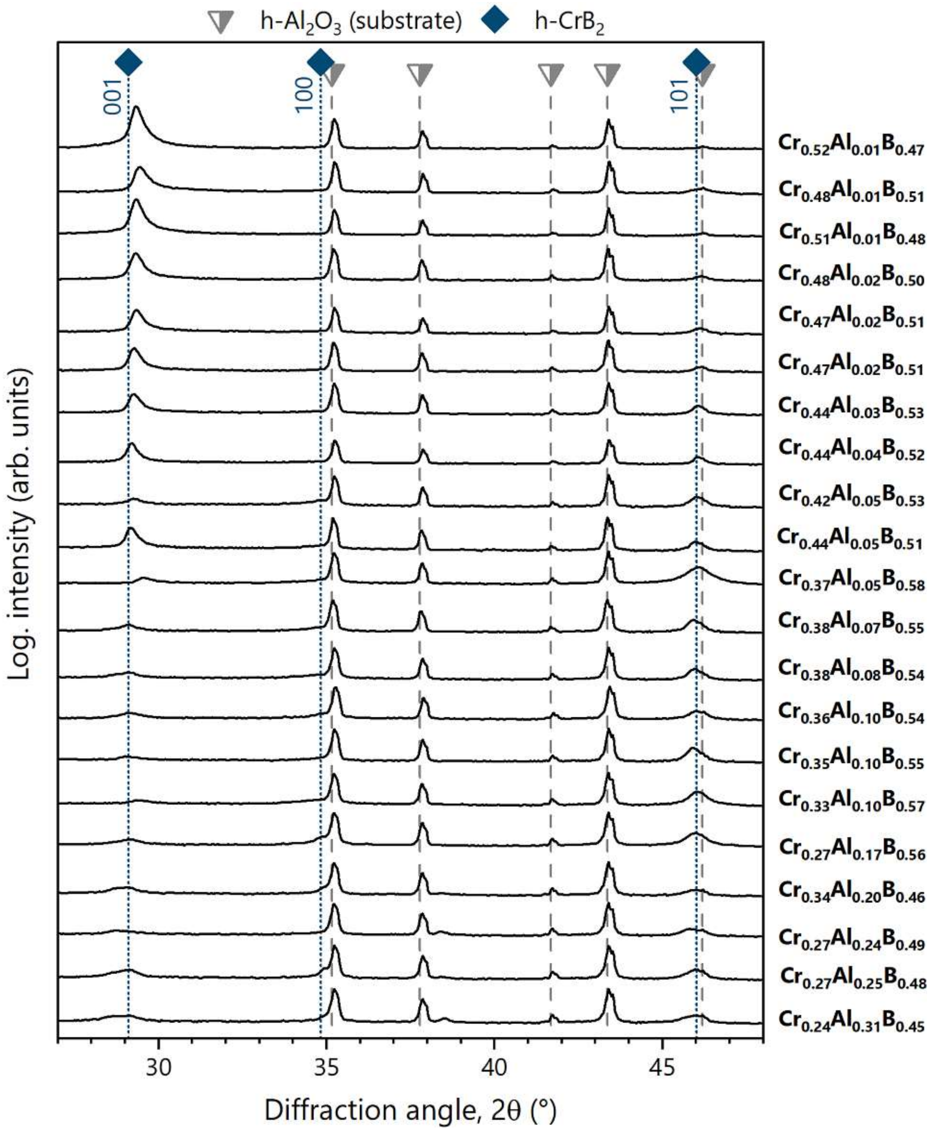

Fig. A1. X-ray diffraction patterns of all Cr-Al-B thin films. The chemical composition of the films is shown to the right of the diffractograms, which are arranged from top to bottom with increasing Al content. The peaks are correlated to standardized reference patterns: the squares represent hexagonal CrB_2 (space group 191, AlB_2 prototype, 04-003-6127) and the triangles represent the polycrystalline Al_2O_3 substrate material (00-046-1212).

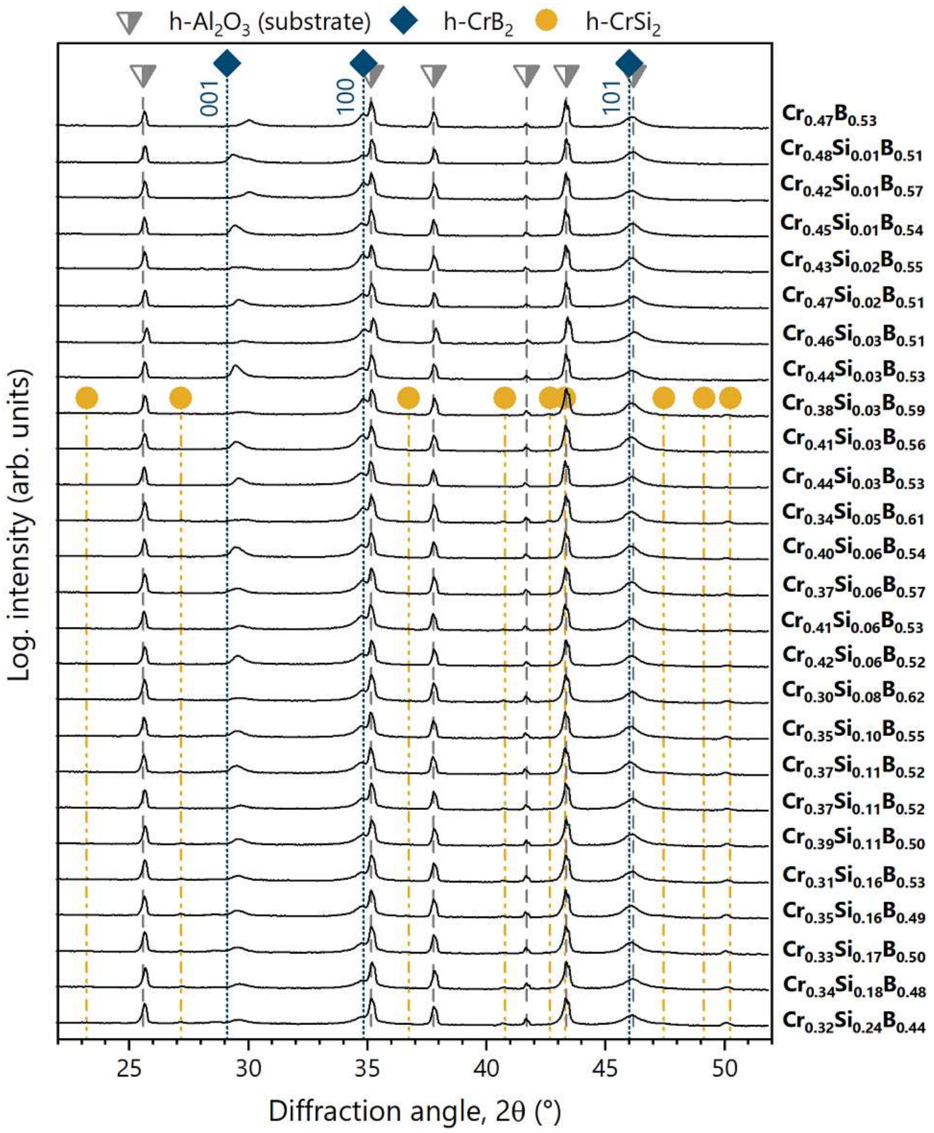

Fig. A2. X-ray diffraction patterns of all Cr-Si-B thin films. The chemical composition of the films is shown to the right of the diffractograms, which are arranged from top to bottom with increasing Si content. The peaks are correlated to standardized reference patterns: the squares represent hexagonal CrB$_2$ (space group 191, AlB$_2$ prototype, 04-003-6127), the circles represent hexagonal CrSi$_2$ (03-065-9705), and the triangles represent the polycrystalline Al$_2$O$_3$ substrate material (00-046-1212).

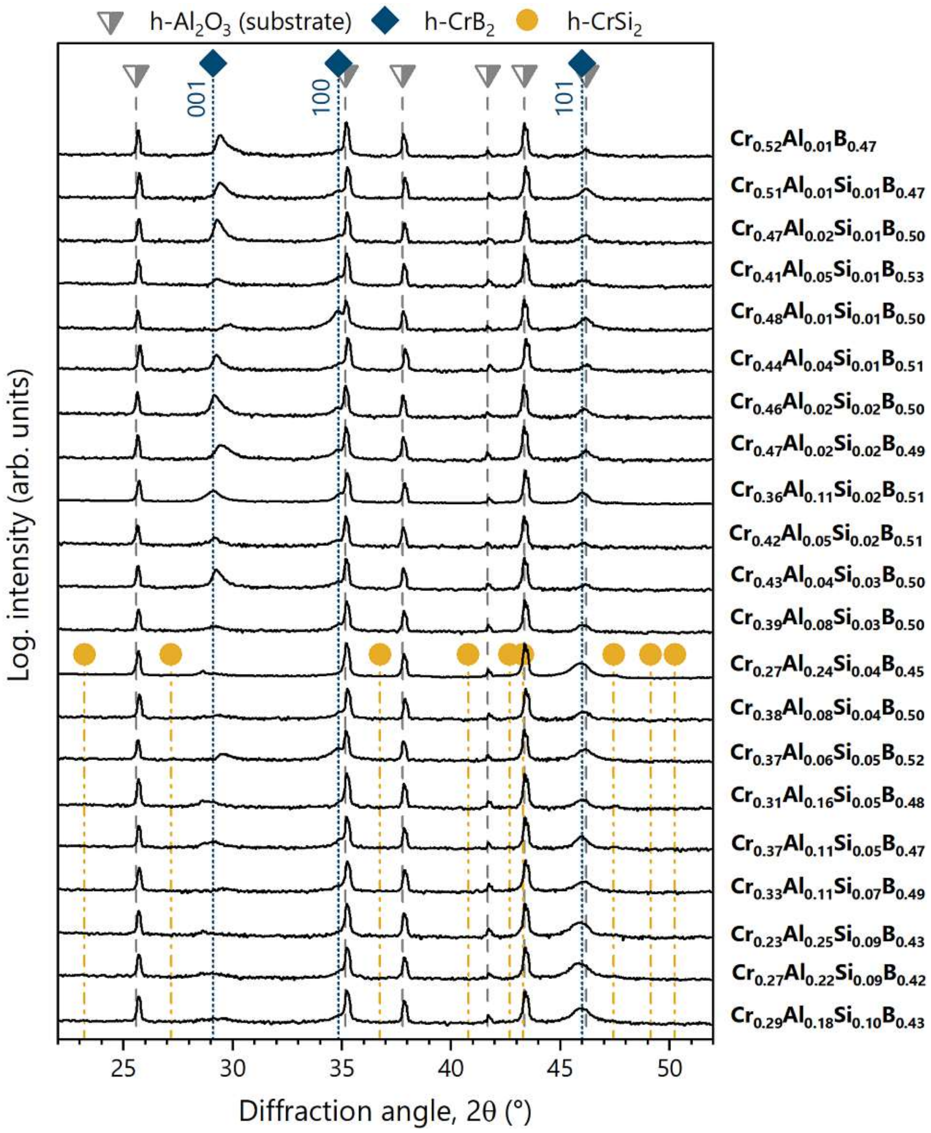

Fig. A3. X-ray diffraction patterns of all Cr-Al-Si-B thin films. The chemical composition of the films is shown to the right of the diffractograms, which are arranged from top to bottom with increasing Si content. The peaks are correlated to standardized reference patterns: the squares represent hexagonal CrB_2 (space group 191, AlB_2 prototype, 04-003-6127), the circles represent hexagonal $CrSi_2$ (03-065-9705), and the triangles represent the polycrystalline Al_2O_3 substrate material (00-046-1212).

B. Additional TEM analysis

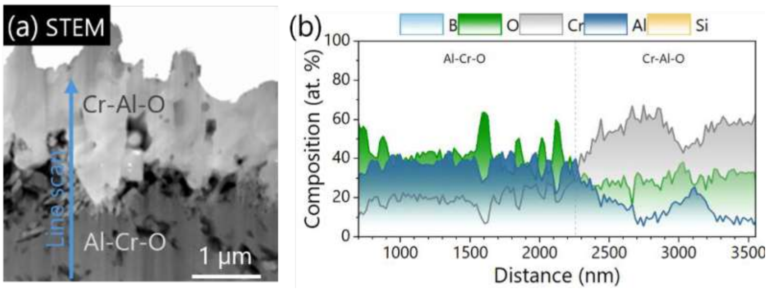

Fig. B1. (a) STEM cross section of the oxidized $Cr_{0.27}Al_{0.25}B_{0.48}$ thin film after 1 h at 1200 °C in ambient air with the marked area for the (b) EELS line scan. The coating is completely oxidized after the oxidation test.

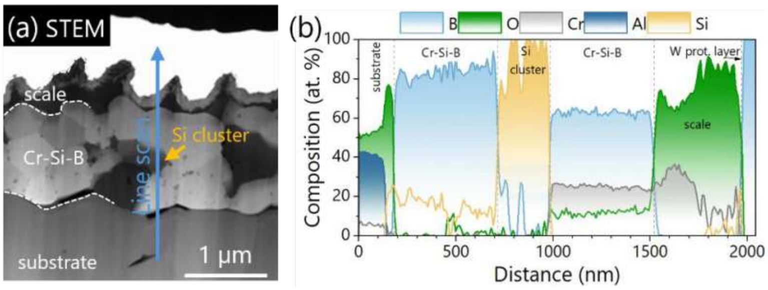

Fig. B2. (a) STEM cross section of the oxidized $Cr_{0.35}Si_{0.16}B_{0.49}$ thin film after 1 h at 1200 °C in ambient air with the marked area for the (b) EELS line scan. After the oxidation test, Si accumulates towards the substrate and Si precipitates form.

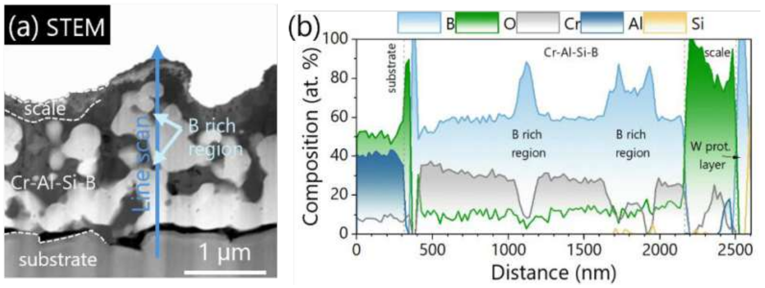

Fig. B3. (a) STEM cross section of the oxidized $Cr_{0.27}Al_{0.22}Si_{0.09}B_{0.42}$ thin film after 1 h at 1200 °C in ambient air with the marked area for the (b) EELS line scan. No segregation occurs after the oxidation test. The dark areas in the STEM image (between substrate and scale) indicate B-rich regions.

C. Oxidations tests at higher temperatures (1300 and 1400 °C)

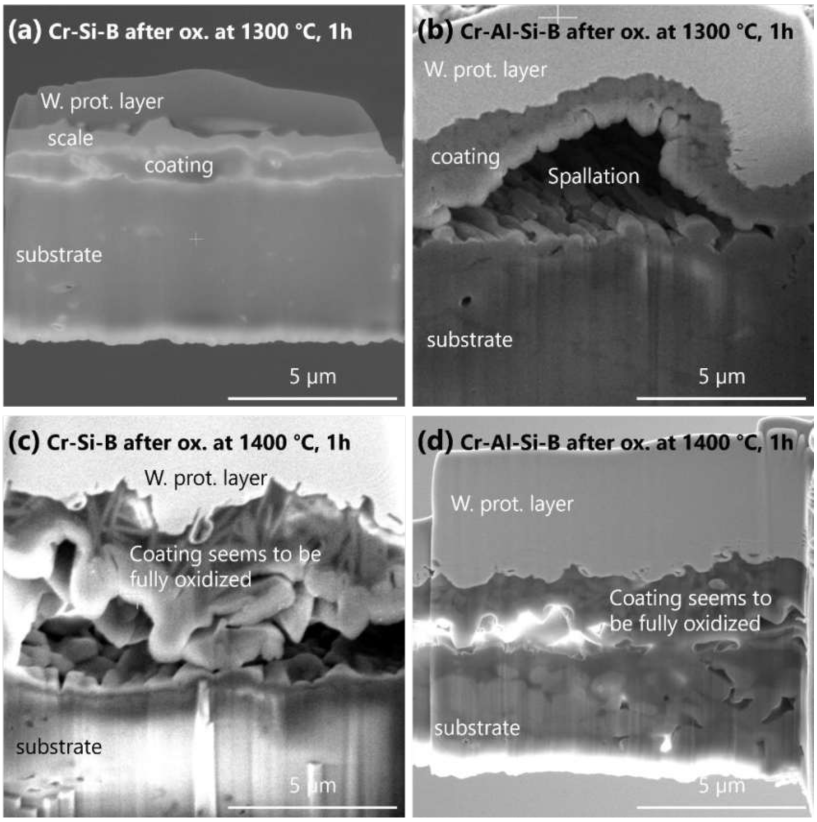

Fig. C1. FIB cross section of the oxidized (a) $Cr_{0.35}Si_{0.16}B_{0.49}$ coating after 1 h at 1300 °C, (b) $Cr_{0.27}Al_{0.22}Si_{0.09}B_{0.42}$ coating after 1 h at 1300 °C, (c) $Cr_{0.35}Si_{0.16}B_{0.49}$ coating after 1 h at 1400 °C, and (d) $Cr_{0.27}Al_{0.22}Si_{0.09}B_{0.42}$ coating after 1 h at 1400 °C. The coating in (a) appears to be intact after the oxidation test, (b) has suffered spallation, (c) and (d) appear to be completely oxidized.